STABILITY OF TOKAMAK AND RFP PLASMAS WITH AN EXTENDED REGION OF LOW MAGNETIC SHEAR

THÈSE N^{O} 6636 (2015)

PRÉSENTÉE LE 16 JUILLET 2015
À LA FACULTÉ DES SCIENCES DE BASE
CRPP - THÉORIE
PROGRAMME DOCTORAL EN PHYSIQUE

ÉCOLE POLYTECHNIQUE FÉDÉRALE DE LAUSANNE

POUR L'OBTENTION DU GRADE DE DOCTEUR ÈS SCIENCES

PAR

Daniele BRUNETTI

acceptée sur proposition du jury:

Prof. H. M. Rønnow, président du jury
Dr J. Graves, Dr W. A. Cooper, directeurs de thèse
Dr H. Christopher, rapporteur
Dr S. Medvedev, rapporteur
Dr H. Reimerdes, rapporteur

ÉCOLE POLYTECHNIQUE
FÉDÉRALE DE LAUSANNE

Suisse
2015

Ad augusta per angusta

To my family

Abstract

It has been observed experimentally that magnetically confined plasmas, characterised by the safety factor q with a small or slightly inverted magnetic shear, have good confinement properties. Such plasmas typically have no internal transport barrier, operate with $q_{95} \sim 4$ and are good candidates for long pulse operation at high fusion yield in the reactor ITER. These *"hybrid"* scenarios are an intermediate step between the reference *standard* H-mode (high confinement) scenario with monotonic q and inductive current, and *advanced* scenarios with strongly reversed magnetic shear in which the entire plasma current is ideally generated non-inductively. This thesis focuses on the study of the dynamics of hybrid plasmas, with weak or almost zero magnetic shear, in tokamak and Reversed Field Pinch (RFP) configurations, when q in the central region assumes values close to one (tokamaks) or to a rational number (tokamaks, RFPs), though the exact resonance is avoided.

The first part of this thesis is focused on the study of tokamak and RFP equilibria with slightly reversed shear when an extremum in the safety factor is close to a low order rational. These equilibria are characterised by the possible presence of internal helical cores, although the plasma edge is symmetric in the toroidal direction. Such 3-D structures can be understood as the result of the nonlinear saturation of ideal MHD modes. The amplitude of large scale $m = 1$ helical displacements in tokamak and RFP plasmas is investigated using contrasting approaches, namely 3-D equilibrium and non-linear stability codes. The non-linear amplitude of such saturated modes obtained with the stability code is compared both with the helical core structure resulting from equilibrium numerical calculations, and with analytic predictions which extend the nonlinear treatment of reversed q plasmas to arbitrary toroidal mode numbers. A preliminary study of the impact of a $n = 1$ RMP on the equilibrium helical distortion is also presented.

The second part of the thesis is devoted to the analytical and numerical study of the stability of an initially axisymmetric tokamak configuration when the safety factor is almost flat and very close to a rational value over a macroscopically extended region in the plasma centre. Such conditions typically occur either in hybrid scenarios or following reconnection of a global instability such as a sawtooth. This configuration is characterised by non-negligible coupling between a fundamental mode and its Fourier adjacent modes. A dispersion relation has been derived both for ideal and resistive modes, with additional non-MHD effects such as plasma diamagnetism, viscosity and equilibrium velocity flows. The analytical results show that the resistive sidebands coupled to a core kink-like mode exhibit extremely fast growth, though additional non-MHD effects tend to moderately reduce the extreme growth rate of the resistive modes. The existence of such modes has been confirmed numerically, where the sensitivity of the growth rate to changes in resistivity and two-fluid effects has been demonstrated, and thus in turn provides generally good agreement with the analytical theory developed. A family of modes are obtained, including modes with novel scaling against plasma resistivity, some of which rotate in the electron diamagnetic direction, and others in the ion diamagnetic direction, consistent with experimental observations in e.g. TCV during hybrid-like operation.

Key words: Magnetohydrodynamics, TOKAMAK, RFP, Hybrid, Kink, Tearing, Infernal

Résumé

Il a été observé expérimentalement que les plasmas confinés magnétiquement, caractérisés par le facteur de sécurité q avec un cisaillement magnétique faible ou légèrement inversé, ont de bonnes propriétés de confinement. Ces plasmas, qui n'ont généralement pas de barrière de transport interne, fonctionnent avec $q_{95} \sim 4$ et sont de bons candidats pour produire des choc de longue durée avec un taux élevé de reactions de fusion dans le réacteur ITER. Ces scénarios *"hybrides"*, sont une étape intermédiaire entre le scénario *standard* de référence fonctionnant en mode H (haut confinement) avec un profil de q monotone et courant inductif, et les scénarios *avancés* avec cisaillement magnétique fortement inversé dans lesquels tout le courant plasma est idéalement généré de manière non-inductive. Cette thèse discute de la dynamique des plasmas hybrides, avec cisaillement magnétique faible ou presque nul, pour des configurations tokamak et Reversed Field Pinch (RFP), lorsque la valeur de q dans la région centrale s'approche de l'unité (tokamak) ou d'un nombre rationnel (tokamak, RFP), bien que la résonance exacte soit évitée.

La première partie de cette thèse est donc centrée sur l'étude des équilibres tokamaks et RFP, lorsque le cisaillement est faiblement inversés, et quand l'extrême du facteur de sécurité (maximum ou minimum) est proche d'un nombre rationnel. Ces équilibres sont caractérisés par la présence éventuelle de structures internes hélicoïdales, bien que le bord du plasma soit symétrique dans la direction toroïdale. Ces structures tridimensionnelles peuvent être comprises comme le résultat de la saturation non linéaire des modes idéaux magnétohydrodynamiques (MHD). L'amplitude des déplacements macroscopiques hélicoïdaux avec nombre d'onde poloïdal $m = 1$ dans des plasmas de tokamak et RFP, est analysée en utilisant différentes méthodes, soit l'aide de codes d'équilibre 3-D ou codes de stabilité non linéaire. L'amplitude non linéaire de tels modes saturés, obtenus avec les codes de stabilité, est comparée avec les structures hélicoïdales calculé grâce aux codes d'équilibre, et les prédictions analytiques, qui généralisent, à des valeurs arbitraires du nombre d'onde toroïdal, la description non linéaire des plasmas dont le profil de q est inversé. Enfin, l'impact des perturbations magnétiques résonnantes (RMP) avec nombre toroïdal $n = 1$ sur la distorsion hélicoïdale de l'équilibre, est présenté de manière préliminaire.

La deuxième partie de la thèse se concentre sur l'étude analytique et numérique de la stabilité des configurations tokamak initialement axisymétriques, pour lesquelles le facteur de sécurité est presque plat et très proche d'une valeur rationnelle dans une région étendue du centre du plasma. Ces conditions se produisent généralement dans les scénarios hybrides, ou après la reconnexion d'une instabilité globale comme une dent de scie (sawtooth). Cette configuration est caractérisée par un couplage non négligeable entre un mode fondamental et des modes de Fourier adjacents. Une relation de dispersion a été dérivée à la fois pour les modes idéaux et résistifs, avec l'inclusion d'autres effets non-MHD, comme le diamagnétisme du plasma, la viscosité et une vitesse d'équilibre non-nulle. Les résultats de l'analyse montrent que les bandes latérales résistives couplée à un mode interne, ont une croissance extrêmement rapide, et les effets supplémentaires non-MHD ont tendance à réduire modérément ce taux. L'existence de ces modes a été confirmée numériquement, et la sensibilité du taux de croissance par rapport aux variations de la résistivité et les effets dûs au modèle à deux fluides, a été démontrée avec un bon accord avec la théorie analytique développée. Une famille de modes a été obtenue, ainsi qu'une nouvelle loi d'echelle en fonction de la résistivité du plasma, dont certains tournent dans le sens diamagnétique électronique, et d'autres dans la direction diamagnétique ionique. Ces résultats sont cohérents avec les observations expérimentales, par exemple dans le tokamak TCV pendant les opérations hybride.

Mots clefs : Magnétohydrodynamique, TOKAMAK, RFP, Hybride, Kink, Tearing, Infernal

Sinossi

É stato osservato sperimentalmente che plasmi confinati magneticamente, caratterizzati da un fattore di sicurezza q con shear magnetico piccolo o leggermente invertito, presentano un buon confinamento. Generalmente questi plasmi non hanno barriere di trasporto interne, operano con q al bordo prossimo a 4 ($q_{95} \sim 4$) e sono un candidato molto promettente per scariche di lunga durata ad alto rendimento nel reattore di prossima generazione ITER. Questi scenari *ibridi* si collocano a metà strada tra lo scenario *standard* di riferimento in modo H-mode (alto confinamento) con q monotono e corrente induttiva, e gli scenari *avanzati* a shear magnetico fortemente invertito in cui idealmente l'intera corrente di plasma è generata in maniera non induttiva. La presente tesi è focalizzata sullo studio della dinamica di plasmi di tipo tokamak e Reversed Field Pinch (RFP) in condizioni ibride, tali per cui q nella regione centrale assume valori prossimi a uno (tokamak) oppure a un valore razionale (tokamak, RFP), pur mantenendosi sempre leggermente lontano dalla risonanza.

La prima parte di questa tesi è dunque incentrata sullo studio di equilibri tokamak e RFP, in condizioni di shear debolmente invertito, quando un estremo (massimo o minimo) del fattore di sicurezza è vicino a un numero razionale di ordine basso. Questi equilibri sono caratterizzati dalla possibile presenza di strutture elicoidali interne, benché il bordo del plasma sia simmetrico nella direzione toroidale. Tali strutture tridimensionali possono essere intese come il risultato della saturazione non lineare di modi magnetoidrodinamici (MHD) ideali. Pertanto l'ampiezza delle perturbazioni elicoidali macroscopiche con numero d'onda poloidal $m = 1$ in plasmi tokamak e RFP è analizzata metodi differenti, ovvero tramite codici sia di equilibrio 3-D che di stabilità non lineare. L'ampiezza risultante dalla saturazione non lineare di tali modi, ottenuta con codici stabilità, è confrontata con le strutture elicoidali calcolate sia tramite i codici di equilibrio, che con le previsioni analitiche, le quali generalizzano a valori arbitrari del numero d'onda toroidale la descrizione non lineare di plasmi con q a shear invertito. Infine è presentato uno studio preliminare sull'impatto di perturbazioni magnetiche risonanti (RMP) con numero toroidale $n = 1$ sulla distorsione elicoidale d'equilibrio.

La seconda parte della tesi è dedicata allo studio analitico e numerico della stabilità di una configurazione tokamak inizialmente assialsimmetrica quando il fattore di sicurezza è pressoché piatto e molto vicino a un valore razionale in una regione macroscopicamente estesa nel centro plasma. Tali condizioni si verificano in genere in scenari ibridi o dopo la riconnessione di instabilità globali come un sawtooth. Questa configurazione è caratterizzata da un accoppiamento non trascurabile tra un modo fondamentale e i suoi modi di Fourier adiacenti. É stata derivata una relazione di dispersione per modi sia ideali che resistivi, con l'inclusione di altri effetti non-MHD quali il diamagnetismo di plasma, la viscosità e le velocità di equilibrio non nulle. I risultati analitici mostrano che le sideband resistive, accoppiate ad modo interno, presentano una crescita estremamente veloce, anche se gli effetti non-MHD tendono a ridurre moderatamente il tasso di crescita estremamente rapido di tali instabilità. L'esistenza di tali modi è stata confermata numericamente, dove è stata dimostrata la sensitività del tasso di crescita rispetto a variazioni nella resistività e negli effetti a due fluidi e con un accordo generalmente buono con la teoria analitica sviluppata. É stata ottenuta una famiglia di modi, inclusi nuovi scaling in funzione della resistività di plasma, alcuni dei quali ruotano in direzione diamagnetica elettronica e altri in direzione diamagnetica ionica, in linea con le osservazioni sperimentali per esempio nel tokamak TCV durante operazioni in configurazione ibrida.

Parole chiave: Magnetoidrodinamica, TOKAMAK, RFP, Ibrido, Kink, Tearing, Infernal

Contents

Abstract (English/French/Italian) **i**

1 Introduction **1**
- 1.1 The magnetic confinement concept . . . 3
- 1.2 Tokamak modes of operation . . . 6
- 1.3 Focus of this thesis . . . 7
- 1.4 Outline of the thesis . . . 9

2 MHD plasma model description of tokamaks and RFP plasmas **11**
- 2.1 The ideal MHD model . . . 11
- 2.2 Plasma equilibrium and the Grad-Shafranov equation . . . 14
- 2.3 The Tokamak and the Reversed Field Pinch concepts . . . 15
- 2.4 Ideal MHD stability . . . 19
  - 2.4.1 The normal mode problem and the energy principle . . . 20
  - 2.4.2 The linear and nonlinear internal kink mode in tokamak geometry 21
- 2.5 Resistive internal modes with finite magnetic shear . . . 28
- 2.6 Introduction to stability in plasmas with low magnetic shear . . . 33
  - 2.6.1 Experimental motivation for investigations of ideal and resistive instabilities in low shear plasmas . . . 35

3 Ideal MHD helical structures in hybrid-like (low shear) scenarios **41**
- 3.1 Introduction . . . 42
- 3.2 Linear theory of the $m = 1$ mode (arbitrary n) with reversed shear . . 44
- 3.3 Nonlinear internal kink mode for arbitrary n and reversed shear . . . 47
- 3.4 Ideal saturated $m = 1$ kinks in tokamaks . . . 49
  - 3.4.1 Ideal kink instabilities in ITER-like scenarios . . . 49
  - 3.4.2 Helical state response to RMP fields in MAST-like hybrid plasmas . . . 53
  - 3.4.3 Analytic characterisation of equilibrium helical 3D structures in tokamaks . . . 58
- 3.5 Comparison of equilibrium and non-linear simulations for RFX . . . 63
- 3.6 Summary . . . 70

4 Fast growing modes in low-shear tokamaks with non-MHD effects 71
4.1 Introduction . . . 72
4.2 Equilibrium . . . 73
4.3 Physical model and drift MHD equations . . . 75
4.4 Derivation of the equations for $(\Phi,\ \psi,\ f,\ p)$ . . . 78
4.5 Low-shear region . . . 81
4.6 Sheared region . . . 84
4.6.1 WKB approach for more general q profiles . . . 86
4.7 Resonant $(m_0+1)/n$ layer region . . . 87
4.8 Eigenfunctions and eigenvalues . . . 90
4.8.1 Case $m_0 = n$ . . . 91
4.8.2 Case $m_0 > n$ . . . 92
4.9 Analysis of the dispersion relation . . . 93
4.9.1 Resistive infernal modes with diamagnetic effects . . . 95
4.9.2 Visco-Resistive infernal modes . . . 101
4.9.3 Rotating-Resistive infernal modes . . . 104
4.10 Summary . . . 108

5 XTOR-2F numerical simulations of infernal modes and comparison with analytic results 111
5.1 Introduction . . . 112
5.2 XTOR-2F physical model for low shear plasmas with diamagnetic effects 113
5.2.1 Choice of equilibrium profiles parametrisation of analytic solutions for comparison against XTOR-2F . . . 114
5.3 Numerical simulations for a low-shear MAST-like configuration . . . 116
5.3.1 Ideal simulations . . . 119
5.3.2 Resistive simulations . . . 123
5.3.3 Evolution of the island width . . . 128
5.4 Summary . . . 135

6 Conclusions 137

A Mathematical derivations 141
A.1 Curvilinear coordinate systems . . . 141
A.2 Derivation of equations (4.19), (4.24) and (4.25) . . . 143
A.3 Finite β corrections to Eq. (4.31) . . . 145
A.4 Effects of density gradients on the infernal mode . . . 146

B Coupled internal modes in tokamaks with a helical core 151
B.1 Geometry and fluxes with equilibrium helical cores . . . 151
B.2 Interior and exterior eigenfunctions . . . 154
B.2.1 Interior region . . . 154
B.2.2 Exterior region . . . 156
B.3 Dispersion relation for ideal and resistive modes . . . 157

B.3.1 Ideal modes 157
B.3.2 Resistive modes 157

C Numerical codes 161
C.1 VMEC 161
C.2 XTOR-2F 165
C.3 VMEC/XTOR-2F interface 168

Bibliography 169

Acknowledgements 177

Curriculum Vitae 179

1

Introduction

According to the standard textbook there are three states of matter, solid, liquid and gaseous states. However if temperatures are large enough, the excitation of the atoms is so high that electrons are separated from the nuclei, moving free through the medium. Such a new state is called plasma, the fourth state of matter. Although plasmas constitute a population of single charged particles, each with relatively long mean free path, the plasma exhibits a collective behaviour and appears globally neutral when it is observed on a scale larger than the Debye length λ_D [1]:

$$\lambda_D = \sqrt{\varepsilon_0 T / e^2 n},$$

where T is the plasma temperature (in eV), e the electric charge and n the density. The presence of charge carriers makes plasma electrically conductive so that it responds strongly to electromagnetic fields.

Plasmas are by far the most common state of ordinary matter in the universe. Stars, for example, are giant plasma balls with a temperature of million degrees in the core. The intergalactic medium, which constitutes the largest part of the matter in the universe, is also a plasma. This state is reached when temperatures are $\sim 1eV$ ($1eV \sim 1 \times 10^4 K$). Plasmas on Earth are observed during lightning and during the aurora (borealis or australis) phenomena.

Laboratory plasmas can be created by heating a gas or subjecting it to a strong electromagnetic field applied with a laser or microwave generator. Technical applications which involve the use of plasmas are neon lamps, plasma torches (employed for cutting), material treatment and plasma film deposition.

The main application in which plasmas play a crucial role is nuclear fusion. If the temperature is sufficiently high, the kinetic energy of the ions is large enough to overcome the Coulomb barrier and the two reacting nuclei can fuse together thus producing a heavier element. The fusion chain is energetically convenient for atoms with lower mass than iron. Since the mass of the product is slightly less than the mass of the colliding nuclei, an amount of energy corresponding to the mass difference is released according to the well known formula $E = mc^2$ (c is the speed of light and m is the mass which is converted into energy).

There are many possible fusion reactions, and the most promising in the near future is the reaction between Deuterium (${}^2_1D$) and Tritium (${}^3_1T$), which has the largest cross-section with relatively "*low*" temperatures ($\sim 50KeV$):

$$ {}^2_1D +^3_1 T \longrightarrow^4_2 He(3.5MeV) +^1_0 n(14.1MeV). $$

The energy release is contained in the kinetic energy of the reaction products. Such a reaction is several thousand times more energetic than standard chemical reactions involving fossil fuels and it is clear why so much interest over the last fifty years has been applied to developing a reliable technology capable of extracting such an enormous amount of energy.

The burning plasma regime is achieved if the *Lawson triple product criterion* is fulfilled, i.e. for a D-T reaction [2]:

$$ nT\tau_E \geq 3 \times 10^{21} m^{-3} KeVs, $$

where τ_E is the energy confinement time, i.e. the ratio of the plasma total energy and the power losses from fusion reactions. For D-T reactions at $T \approx 20KeV$, we have $n\tau_E \geq 1.5 \times 10^{20} m^{-3} s$ and this condition is fulfilled when we have e.g. plasma density $n > 10^{20} m^{-3}$ and confinement time $\tau_E > 1.5s$. The Lawson criterion simply states that for larger densities we have larger reaction rate, for higher temperatures we have bigger reaction probabilities, and a sufficiently long confinement time guarantees that the energy which is produced is not lost.

Maintaining a sufficiently large triple product is an extremely challenging task and several methods have been developed in the last decades to maintain burning plasma conditions. There are two main approaches developed in mainstream fusion research: the first consists of reaching extremely high densities but with a low confinement time. This is the so called *inertial confinement fusion* approach, where powerful lasers are employed to compress fuel capsules of $1mm$ in diameter up to very high densities, around one-hundred times the density of lead, namely $\sim 1000gcm^{-3}$. The other approach is to confine a rarefied (i.e. low density $\sim 10^{20}m^{-3}$) plasma, whose temperature is around few $KeVs$, by means of strong magnetic fields in a toroidally shaped chamber. This approach is the so called *magnetic confinement fusion* approach. The next section describes in more detail some aspects of how magnetically confined plasmas behave in toroidal configurations.

1.1 The magnetic confinement concept

The magnetic confinement system is based on the application of strong magnetic fields in order to enclose the hot plasma in a magnetic bottle. The basic idea is that a charged particle, with velocity $\boldsymbol{v}$ which undergoes the effect of an external electric and magnetic field, experiences a force:

$$\boldsymbol{F} = q(\boldsymbol{E} + \boldsymbol{v} \times \boldsymbol{B}).$$

This tells us that to lowest approximation the particle gyrates along the magnetic field, essentially being "glued" to the field lines (this is shown in Fig. 1.1). Several confinement concepts have been developed during the last fifty years: the two main categories are open configurations and closed configurations.

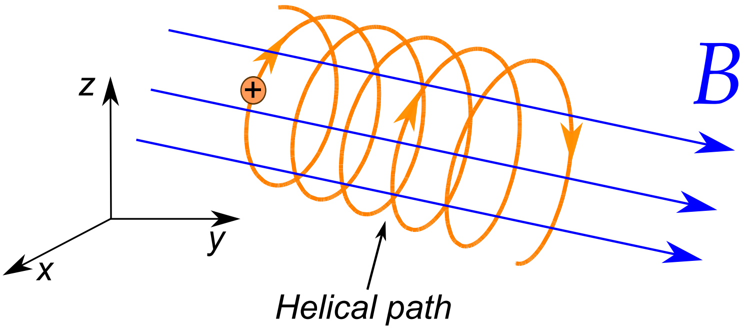

Figure 1.1: Motion of a positively charged particle in the presence of a magnetic field.

Open configurations are so called *mirror configurations* [3]: these consist of two parallel coils separated by a small distance, carrying the same current in the same direction, producing a magnetic bottle between them. Invoking energy conservation $E = \frac{1}{2}mv_{||}^2 + \mu B = const.$ and the adiabatic invariance of the magnetic moment $\mu = \frac{mv_{\perp}^2}{2B} = const$ (with a vanishing electric field), particles near the coils of the bottle, where the magnetic field is stronger, must drop their velocity parallel to the magnetic field. If the parallel velocity goes negative, the particle is reflected by the large magnetic field, and thus the particle experiences a magnetic force towards the plasma centre; particles with appropriate speeds spiral repeatedly from one end of the region to the other and back. This physical mechanism is used to temporarily trap charged particles up to temperatures of the order of 10^6K. Such configurations are however affected by loss cones for particles which fulfil the condition $v_{||}/v_\perp > \sqrt{B_{max}/B_{min} - 1}$ [3]. The "*Van Allen radiation belts*" (doughnut shaped regions around the Earth), are a natural mirror confinement system analogous to laboratory mirror machines, which occur due to the non-uniformity of the Earth's magnetic field (see Fig. 1.2).

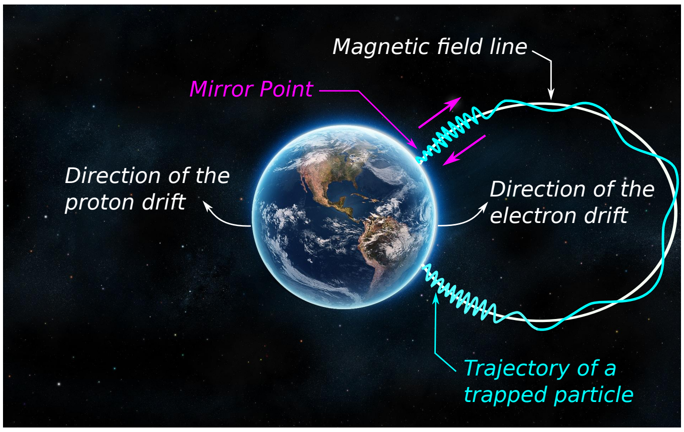
Magnetic field line
Mirror Point
Direction of the proton drift
Direction of the electron drift
Trajectory of a trapped particle

Figure 1.2: Pictorial view of the Van Allen belt.

In contrast to mirror systems, examples of *closed* configurations include tokamaks, stellarators and reversed field pinches (RFPs) (a more detailed description of the tokamak and reversed field pinch closed configurations is given in Chapter **2**). By *closing* the system, particle losses along the field lines are eliminated. These configurations are characterised by a doughnut-shaped toroidal chamber with the presence of a strong toroidal field. Since the toroidal field alone is not sufficient to confine the particles (due to gradients of the field which produces charge separation and hence self generated electric fields which in turn produce secular loss orbits), an additional poloidal field (generated by a toroidally flowing current or by modular toroidally deformed coil configuration) is added. The magnetic field lines become helical, winding around the interior of the reactor. It is convenient to define an important physical quantity related to this helicity, the safety factor, labelled q, which represents the ratio of the times a particular magnetic field line travels around a toroidal confinement area's "long way" (toroidally) to the "short way" (poloidally) (for a more detailed definition of q see Chapter **2**). The particles which gyrate around the field lines, slowly drift vertically up and down. Charge separation is therefore reduced and individual particles are confined. Figure 1.3 shows examples of the open and closed magnetic configurations. The plasma current is also used to heat the plasma via Ohmic heating. This method is more effective at low temperatures since the plasma resistivity decreases with temperature according to the Spitzer law

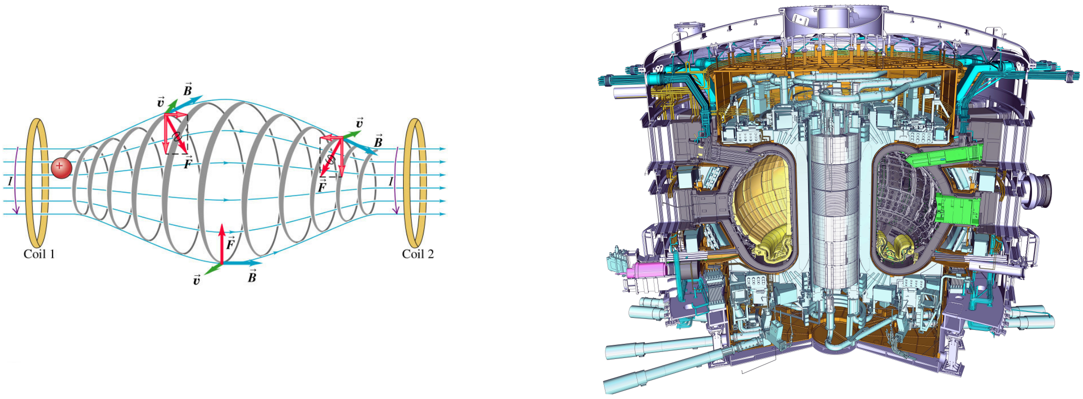

Figure 1.3: Schematic drawing of the magnetic mirror confinement system (open field configuration, left) and cutout of the ITER tokamak (closed field configuration right).

$\eta \sim T^{-3/2}$. Other heating systems that are efficient at high plasma temperatures are required, for example injection of radio frequency or neutral particles whose physics is not discussed here, since it is beyond the scope of the present thesis.

The macroscopic features of the plasmas of open and closed field line systems are well described by the magnetohydrodynamic (MHD) model, whose detailed description is given in Chapter **2**. Plasmas in general and toroidally closed configurations in particular, are affected by the presence of macroscopic MHD instabilities which strongly degrade the confinement. Such instabilities develop around *fragile* surfaces, called rational surfaces, where the safety factor assumes rational values, namely $q = m/n$. On these surfaces, the magnetic field lines close on themselves after m toroidal turns and n poloidal turns (if q is irrational the surface is densely covered by a field line). The perturbations (which are periodic in their angular arguments of the form $\boldsymbol{\xi} = \boldsymbol{\xi}(r)\exp[im\vartheta - in\varphi]$, ϑ and φ are the poloidal and toroidal angles respectively) are *resonant*, i.e. their parallel wave vector vanishes, and on these surfaces instabilities can develop. These instabilities, which can be ideal (perfectly conducting plasma) or resistive (due to finite resistivity which allows the rejoining of the magnetic field lines) in character, are destabilised by current and pressure gradients. Ideal internal $m = 1$ modes, which correspond to a rigid shift and tilt of the plasma core, are often encountered in tokamak and RFP plasmas. In tokamaks the main core MHD instabilities are sawteeth oscillations, which are linked to $m = n = 1$ mode activity associated with a $q = 1$ surface corresponding to a periodic reorganisation of the core plasma, and tearing modes which are resistive in character. Much effort has been put in the last decades in order to develop scenarios in which this deleterious MHD activity is reduced and fusion efficiency is maximised. This produced three different regimes which are now analysed in relation to the central theme of this thesis is the characterisation of reactor relevant plasma regimes, in particular their equilibrium and stability properties against macroscopic fluid instabilities.

1.2 Tokamak modes of operation

In the last decade there was increasing interest in plasmas characterised by ELM-free, H-mode (high confinement) and with internal transport barrier (ITB) operation. Such conditions were achieved by maintaining high values of plasma kinetic pressure (high β, see the definition of β in Chapter **2**). The ultimate aim of fusion research is to obtain fusion in steady state conditions. The parameters needed for steady state operation are the following: lower current to minimise the need for non-inductive drive, high confinement to maximise the fusion production and high pressure operation to maximise the bootstrap current fraction.The steady state scenario aims at producing discharges where the current is driven fully non-inductively.

One of the main parameters in the present development of advanced scenarios is the plasma current profile. Since the shape of the current density (and consequently the safety factor) determines most of the stability properties of the plasma, much effort has been put in the last few years in tailoring the current density profile, in particular trying to avoid the development of dangerous core MHD instabilities (see Chapter **2**) such as sawteeth and *Neoclassical Tearing modes* (NTMs). The sawtooth instability manifests itself as a regular periodic reorganisation of the core plasma surrounding the magnetic axis when there is a region in the plasma where $q < 1$ [4]. NTMs, driven by helical current deficits arising as a result of reduced pressure gradients, take the form of island structures on surfaces characterised by a rational value of q (viz. $q = m/n$, with m and n integers) [5].

Most of the experimental scenarios use a substantial amount of heating and/or current drive in the current ramp-up phase, when the β of the plasma is still low, in order to freeze the current profile [6]. The shape of the current density profile is locally related to the magnetic shear, which is the radial gradient of the rotational transform. A very large variety of current profiles, from deep reversed shear to low positive shear, have been generated and sustained. The shape of the current density profile (i.e. the magnetic shear) determines the operating regime.

There are three main tokamak reactor relevant scenarios considered for the next generation reactor ITER [6]:

- The (**standard**) inductive H-mode scenario (the most promising for obtaining $Q = 10$ in ITER) is characterised by a centrally peaked, predominantly ohmic current density profile (inductively driven) and a monotonic q profile featuring a $q = 1$ surface (hence the plasma is unstable to sawteeth). This scenario has the disadvantage that it is short-pulsed (due to the induced current) and it is prone to major internal and *"external"* magnetohydrodynamic instabilities (sawteeth, NTMs, ELMs) which could cause a plasma disruption and significantly damage the vessel.

- One of the interesting developments of the recent years is the achievement of stationary tokamak H-modes with zero or low magnetic shear and $q(0)$ around 1 (both in ASDEX Upgrade and DIII-D) [6]. These are the so called **advanced hybrid scenarios** (often simply called *hybrid scenarios*). Such configurations are very promising candidates for near steady state operation characterised by a long burn time ($> 1000\ s$), high fluence/shot and $Q > 5$. A significant part of the plasma current is driven non-inductively, off-axis, and a centrally flat, broad q-profile with $q > 1$ everywhere can be obtained with a large region of low magnetic shear. This scenario aims at producing high fusion yield and features a higher β limit with an optimised current profile, a lower current and a lower loop voltage ($Q > 5$, long pulse duration). Furthermore, the increased central pressure increases the bootstrap current (see Chapter **2** § 2.5) which can contribute significantly to the total plasma current (typically up to $\sim 30\%$). The absence of a $q = 1$ surface generally ensures that these scenarios are sawteeth-free. Nevertheless NTMs are still observed in these scenarios, as are ideal internal kink modes. The plasma current in this scenario is lower than the reference H-mode scenario but higher than steady state scenarios [6].

- **Advanced scenarios** are created by driving more than 50% of the current non-inductively. The q-profile reverses giving a region of strong negative magnetic shear, with an internal transport barrier (ITB) (a region of locally reduced transport). The locally reduced transport causes a steep gradient in the plasma pressure, and driving as a consequence large amounts of off-axis bootstrap current which can sustain, together with other non-inductively driven currents, even up to 100% of the total current. In configurations with strong shear reversal, long, steady high performance discharges with almost no current at the centre have been achieved [6]. However, such discharges present problems in steady state operation such as low fusion yield due to low current operation, impurity accumulation due to the density peaking, poor confinement of alphas and other energetic particles (again due to low current), leading to power deposition outside the ITB, as well as an increased diffusion.

The safety factor and the corresponding toroidal current density profile are shown in figure 1.4 for the three scenarios listed above. Similar modes of operation having weakly reversed safety factor with an off axis extremum characterised by an improved confinement, are also developed in RFP configurations.

1.3 Focus of this thesis

The present thesis focuses mainly on the MHD properties of tokamak hybrid-like scenarios. The primary goal of hybrid scenarios in tokamaks is to enable high

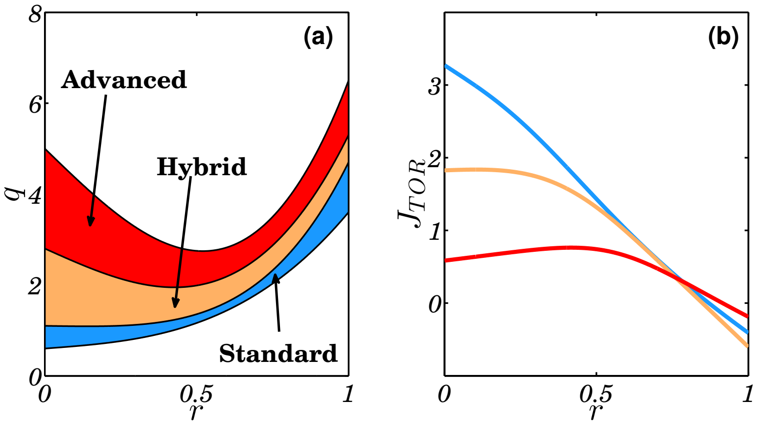

Figure 1.4: Sketches of the safety factor profiles (a) and current density profiles (b) for the three reactor relevant tokamak operating scenarios (the variable r is a normalised radial variable which extends from the plasma centre to the edge). Inspired by Ref. [6]

performance operation with large plasma currents while at the same time trying to avoid MHD instabilities. However, if a local minimum in the safety factor is allowed to approach unity in low or weak shear configurations, magnetic field line bending stabilisation is lost and large MHD structures can be created, with typically dominant $m = n = 1$ helical component. Previous three dimensional numerical equilibrium calculations showed the possibility of the existence of such structures in tokamak hybrid like plasmas as well as standard axisymmetric equilibrium states. Similar structures with $m = 1$ dominant harmonic are often observed also in Reversed Field Pinches (RFPs), leading to improved plasmas performance [7]. In tokamaks however, strong MHD activity during hybrid scenario development has been observed to impair plasma performance in MAST, TCV and JET plasmas [8, 9, 10]. This is a major concern related to future ITER operating regimes.

This work thus addresses the methods of characterisation of $m = 1$ structures in tokamaks and RFPs ($n = 1$ in tokamaks and $n = 7$ in reversed field pinch), analysing the equilibrium properties via 3D equilibrium codes, and the linear and non-linear ideal MHD stability via initial value stability calculations. It will be shown that the helical features of a 3D equilibrium code are essentially the same as that from a non-linear ideal MHD code (departing from an initially axisymmetric equilibrium). While this is a significant advance developed in this thesis, providing a uniform base in our understanding of large scale 3D magnetic structures, it also motivates investigation into the relevance of the ideal MHD model in tokamak observations. Indeed, experimentally it is seen in high elongation experiments in TCV that resistivity may play an important role in further weakening the ability of the tokamak core to remain axisymmetric, producing island structures in the plasma. The separate dynamics of electrons and ions (via diamagnetic drifts) are also observed. Such measurements in TCV and other machines therefore demonstrate the importance of developing extended MHD models for such instabilities.

1.4 Outline of the thesis

In this chapter a brief introduction on nuclear fusion and the basic concepts of magnetic confinement have been presented. Our goal is to investigate plasma behaviour (in particular macroscopic magnetohydrodynamic instabilities) in fusion reactor relevant conditions. The main thesis chapters are organised as follows.

- Chapter **2** provides an introductory description of the main tools (both analytical and numerical) used in the framework of this thesis. First the magnetohydrodynamical equations governing macroscopic plasma dynamics are presented, followed by a description of toroidally symmetric equilibria, where a general overview of the tokamak and reversed field pinch configurations is presented. A section on ideal stability is presented, where the energy principle and the normal mode approach are used to describe linear and nonlinear kink instability in tokamak plasmas. Then the ideal constraint is relaxed and general information about the classical theory of tearing instabilities and the underlying physics governing NTM dynamics are given. The derivation of the modified Rutherford equation is presented and the connection between fast growing NTMs and pressure driven instabilities in a low-shear tokamak configuration is outlined.

- Chapter **3** investigates kinked saturated $m = 1$ helical structures both in tokamaks and in reversed field pinches (RFPs). Linear and non-linear (numerical and novel analytic) stability calculations which evaluate the departure from an axisymmetric plasma state are used to assess the behaviour of such instabilities, together with equilibrium calculations using a 3D equilibrium code. The configurations studied include ITER, MAST and RFX-like plasmas all characterised by a slightly reversed safety factor. The main themes of this chapter have been published in the following journal publications: [D. Brunetti et al., *"Ideal saturated MHD helical structures in axisymmetric hybrid plasmas"*, Nucl. Fusion **54**, 064017 (2014)] and [J. P. Graves, D. Brunetti et al., *"Magnetohydrodynamic helical structures in nominally axisymmetric low-shear tokamak plasmas"*, Plasma Phys. Control. Fusion **55**, 014005 (2013)].

- Chapter **4** presents a derivation of the dispersion relation for linear modes in tokamaks with low magnetic shear in the core. This is the first attempt to write a dispersion relation with the inclusion of plasma resistivity and other effects such as plasma diamagnetism for plasmas with an extended region of low magnetic shear. Estimates of the transition point between tearing-like behaviour and infernal-like behaviour are given. Various new scalings against plasma resistivity are found also with the inclusion of toroidal flows and viscosity. The main themes of this chapter have been published in a journal publication: [D. Brunetti et al., *"Fast growing* *resistive two fluid instabilities in hybrid-like tokamak configuration"*, Plasma Phys. Control. Fusion **56**, 075025 (2014)].

- Chapter **5** presents a numerical study of pressure driven magnetohydrodynamic instabilities in a low-shear tight aspect ratio configuration with the initial value code XTOR-2F. The numerical predictions of the growth rate and on the rotation frequency of the modes are compared with the estimates of the linear theory computed in Chapter **4**. In addition, a comparison of the nonlinear evolution of the magnetic island between numerical simulations and Rutherford's analytic theory is presented. The main themes of this chapter have been published in a journal publication: [D. Brunetti et al., *"Extended MHD simulations of infernal mode dynamics and coupling to tearing modes"*, Plasma Phys. Control. Fusion **57**, 054002 (2015)].

Extensive appendices are found at the end of the thesis: these appendices contain general information about curvilinear coordinate systems and the technical details of the mathematical derivations and some additional physics effects (finite β, mass density gradients) which were not taken into account in the main body of the thesis. A small appendix on the behaviour of tearing mode coupling driven by the presence of helical cores is given. Finally a brief description of the numerical scheme of the VMEC and XTOR-2F codes is given.

2

MHD plasma model description of tokamaks and RFP plasmas

The main goal of this chapter is to provide the essential information concerning the model equations and the numerical tools employed in the analysis presented in the next chapters. We first start to describe the physical plasma model widely used in tokamak physics, followed by a general description of an axisymmetric equilibrium. Subsequently the problem of ideal magnetohydrodynamic stability is addressed and the basic information about the internal kink mode and its linear and nonlinear behaviour are given (this will be extensively used in Chapter **3**). After this, the problem of reconnecting modes is described and the implications on low-shear tokamak operation regimes with finite resistivity are presented. Eventually the description of the numerical procedures employed in the VMEC and XTOR-2F codes (which are used for obtaining the numerical results in Chapters **3** and **5**) is outlined at the end of the present chapter.

2.1 The ideal MHD model

The ideal magnetohydrodynamic (MHD) model gives a description of a macroscopic single fluid, long-wavelength, low-frequency plasma. The fundamental equations which constitute the ideal MHD model are the following [11]:

$$\frac{\partial \varrho}{\partial t} + \boldsymbol{\nabla} \cdot (\varrho \boldsymbol{v}) = 0, \tag{2.1}$$

$$\varrho \left(\frac{\partial \boldsymbol{v}}{\partial t} + \boldsymbol{v} \cdot \boldsymbol{\nabla} \boldsymbol{v} \right) = -\boldsymbol{\nabla} p + \boldsymbol{J} \times \boldsymbol{B}, \tag{2.2}$$

$$\frac{d}{dt} \left(\frac{p}{\varrho^{\Gamma}} \right) = 0, \tag{2.3}$$

$$\boldsymbol{E} + \boldsymbol{v} \times \boldsymbol{B} = 0, \tag{2.4}$$

$$\boldsymbol{\nabla} \times \boldsymbol{E} = -\frac{\partial \boldsymbol{B}}{\partial t}, \tag{2.5}$$

$$\boldsymbol{\nabla} \times \boldsymbol{B} = \mu_0 \boldsymbol{J}, \tag{2.6}$$

$$\boldsymbol{\nabla} \cdot \boldsymbol{B} = 0, \tag{2.7}$$

where ϱ is the plasma mass density, $\boldsymbol{E}$ and $\boldsymbol{B}$ the electric and magnetic field respectively, $\boldsymbol{J}$ the current density, p the plasma pressure with $\Gamma = 5/3$, and $d/dt = \partial/\partial t + \boldsymbol{v} \cdot \boldsymbol{\nabla}$ is the convective derivative. The plasma velocity is given by $\boldsymbol{v} = \partial \boldsymbol{\xi}/\partial t$, where $\boldsymbol{\xi}$ is the plasma displacement. Eq. (2.4) indicates that the plasma is a perfect conductor, i.e. that the electric field in the moving plasma frame is zero. Equations (2.5)-(2.7) are pre-Maxwell equations, indicating low frequency electromagnetic behaviour. Thus, displacement currents and net charges ($\varepsilon_0 \boldsymbol{\nabla} \cdot \boldsymbol{E}$) are zero within the MHD framework. The first implying that electromagnetic waves of interest have $\omega/k \ll c$ and the characteristic thermal velocities of ion and electron species are non-relativistic ($V_{T_\alpha} = (2T_\alpha/m_\alpha)^{1/2} \ll c$, the subscript $\alpha = i, e$ indicates the species ions or electrons), and the second implying that the characteristic frequency of plasma behaviour is much lower than the plasma frequency ($\omega \ll \omega_{pe}$, $\omega_p = (n_0 e^2/m_e \varepsilon_0)^{1/2}$) and with a characteristic length much longer than the Debye length $\lambda_D = V_{T_e}/\omega_{pe}$. For sake of simplicity we assume a fully ionised plasma consisting of electrons and positive hydrogen or isotopes (H,D,T) ions for which the ion charge number is $Z_i = 1$. From neglecting the net charge, one has $n_e = Z_i n_i = n$ (*quasi-neutrality approximation*). The mass density equation (2.1) implies that the number of particles is conserved (no ionisation, recombination, etc.). In the single fluid approximation, the electron inertia is neglected ($m_e \to 0$), thus the mass density is defined as $\varrho = m_i n$. The momentum of the fluid is carried by the ions, so that $\boldsymbol{v} = \boldsymbol{v}_i$. The current density is given by $\boldsymbol{J} = en(\boldsymbol{v}_i - \boldsymbol{v}_e)$ and $p = nT = p_i + p_e$, $T = T_i + T_e$.

The ideal MHD model assumes a collision-dominated plasma, for which:

$$V_{T_i} \tau_{ii}/a \sim V_{T_e} \tau_{ee}/a \ll 1,$$

where $\tau_{\alpha\alpha}$ is the $\alpha - \alpha$ particle collision time, and a is the characteristic length of the system (much longer than the Debye length). This implies that the distribution function both for ions and electrons is nearly Maxwellian and that the macroscopic scale length is much longer than the mean path. The validity of the ideal MHD model can be summarised by the following conditions [11]:

$$\begin{aligned}
&1-\text{High collisionality, } \left(\frac{m_i}{m_e}\right)^{1/2}\frac{V_{T_i}\tau_{ii}}{a} \ll 1\\
&2-\text{Small gyroradius, } \frac{r_{L_i}}{a} \ll 1\\
&3-\text{Small resistivity, } \frac{r_{L_i}^2}{a}\left(\frac{m_e}{m_i}\right)^{1/2}\frac{1}{V_{T_i}\tau_{ii}} \ll 1
\end{aligned}$$

where $r_{L_i} = V_{T_i}/\Omega_{ci}$ is the ion gyro radius ($\Omega_{ci} = q_i B/m_i$ is the ion cyclotron frequency). The third condition implies that resistive diffusion is negligible, despite the high collisionality. In fusion relevant plasmas, the high collisionality assumption is never fulfilled. Nevertheless empirical evidence during many years of fusion plasma research has shown that the ideal MHD theory provides a very good description of most macroscopic plasma behaviour. This suggests that there are subtle physics issues at play that can be explained by introducing a modified collisionless MHD model, that is however beyond the scope of the present thesis. The ideal MHD equations (2.1)-(2.7) form the basis for studying plasma equilibrium and macroscopic perturbation dynamics.

An important concept of the MHD model is the frozen in theorem. In particular, it demonstrates the peculiarity of this particular plasma model insofar as the marriage of fluid dynamics and electromagnetism. Considering a moving surface $\boldsymbol{S}$ crossed by a magnetic field $\boldsymbol{B}$, the flux Φ_M which passes through the surface is defined as:

$$\Phi_M = \int_S \boldsymbol{B}\cdot\boldsymbol{n}dS,$$

where $\boldsymbol{n}$ is the normal vector to the surface. Substituting Eq. (2.5) into Φ_M and using the Stoke's theorem we obtain:

$$\frac{d\Phi_M}{dt} = -\oint d\boldsymbol{l}\cdot(\boldsymbol{E}+\boldsymbol{u}\times\boldsymbol{B}),$$

where $\boldsymbol{u}$ is the velocity of the moving surface $\boldsymbol{S}$. Therefore, using (2.4) and assuming that the velocity $\boldsymbol{u}$ coincides with the plasma velocity $\boldsymbol{v}$, one has that $d\Phi_M/dt = 0$. This demonstrates that in ideal MHD the total magnetic flux is conserved, i.e. the magnetic field lines move with the plasma frozen into the fluid. Relaxing the ideal constraint, viz. assuming a small amount of plasma resistivity, the flux conservation can be violated. This concept will help us to interpret the instabilities investigated in this thesis. In the next sections the problem of the MHD equilibrium and stability is analysed.

2.2 Plasma equilibrium and the Grad-Shafranov equation

Before introducing instabilities, we first examine states of plasma equilibrium which are of particular importance in toroidal plasmas. By setting the full (convective) time derivatives equal to zero in Eq. (2.2), since rotating stationary equilibria are not in the scope of this thesis, magnetostatic equilibrium is described by the following equation:

$$\boldsymbol{\nabla} p = \boldsymbol{J} \times \boldsymbol{B}, \tag{2.8}$$

where Eqs. (2.6) and (2.7) can be imposed in order to eliminate $\boldsymbol{J}$ from (2.8). From the equations above, it follows immediately that p must be constant along the magnetic field lines and the current density lines, i.e. the magnetic field lines and the current density lines lie on constant p surfaces ($\boldsymbol{J} \cdot \boldsymbol{\nabla} p = \boldsymbol{B} \cdot \boldsymbol{\nabla} p = 0$). If we take now the usual right handed cylindrical coordinate system (R, φ, Z), the condition (2.7) is written as:

$$\frac{1}{R}\frac{\partial\left(RB_R\right)}{\partial R} + \frac{\partial B_Z}{\partial Z} = 0,$$

where the axisymmetric constraint ($\partial/\partial\varphi = 0$) has been imposed. It is therefore useful to introduce a stream function ψ, such that $B_R = -\frac{1}{R}(\partial\psi/\partial Z)$ and $B_Z = \frac{1}{R}(\partial\psi/\partial R)$, so that the magnetic field can be written as:

$$\boldsymbol{B} = B_\varphi \boldsymbol{e}_\varphi + \boldsymbol{B}_P = T\boldsymbol{\nabla}\varphi + \boldsymbol{\nabla}\psi \times \boldsymbol{\nabla}\varphi, \tag{2.9}$$

with $T = RB_\varphi$ and $\boldsymbol{\nabla}\varphi = \boldsymbol{e}_\varphi/R$ where $\boldsymbol{e}_\varphi$ is the unit vector in the toroidal direction. The shear function Ψ_P can be related to the flux of the poloidal magnetic field, namely $\Psi_P = \int \boldsymbol{B}_P \cdot d\boldsymbol{A}$. Thus by taking the integration area $\boldsymbol{A}$ to be the surface lying in the $Z = 0$ plane, extending from the magnetic axis located at $R = R_0$ to an arbitray contour defined by $\psi = \psi(R_b, 0)$, we have [11]:

$$\Psi_P = \int_0^{2\pi} d\varphi \int_{R_0}^{R_b} dRRB_Z(R, Z = 0) = 2\pi\psi,$$

where the integration constant has been chosen such that $\psi(R_0, 0) = 0$.

Since $\boldsymbol{B} \cdot \boldsymbol{\nabla} p = 0$ and the field is assumed symmetric with respect to the toroidal direction, we must have that $\boldsymbol{\nabla}\psi \times \boldsymbol{\nabla} p = 0$, so that $p = p(\psi)$. From the condition $\boldsymbol{J} \cdot \boldsymbol{\nabla} p = 0$, it follows that also the quantity T is constant on the constant pressure surfaces, so that $T = T(\psi)$.

From Ampére's law (Eq. (2.6)) we express the toroidal current density in the following manner:

$$J_\varphi = -\frac{\boldsymbol{\Delta}^*\psi}{R}, \tag{2.10}$$

where

$$\boldsymbol{\Delta}^*\psi = R^2\boldsymbol{\nabla}\cdot\left(\frac{\boldsymbol{\nabla}\psi}{R^2}\right) = R\frac{\partial}{\partial R}\left(\frac{1}{R}\frac{\partial\psi}{\partial R}\right) + \frac{\partial^2\psi}{\partial Z^2}.$$

The standard two dimensional tokamak equilibrium is described by the well known Grad-Shafranov equation, which is obtained by taking the $\nabla\psi$ projection of (2.8) and using (2.9) and (2.10). Since $p = p(\psi)$, and $T = T(\psi)$ the Grad-Shafranov equation is [12, 13]:

$$\boldsymbol{\Delta}^*\psi = -\mu_0 R^2\frac{dp}{d\psi} - T\frac{dT}{d\psi}. \tag{2.11}$$

This second order nonlinear differential equation describes a two dimensional equilibrium (i.e. axisymmetric), where the configuration is determined by the choice of p and T. It can be solved analytically for particular choices of the pressure and the toroidal magnetic field [14]. Nominally axisymmetric devices include tokamaks and Reversed Field Pinches (RFPs). The equilibrium equation (2.11) is the usual starting point for the analysis of the plasma properties in both tokamak and RFP configurations.

2.3 The Tokamak and the Reversed Field Pinch concepts

The tokamak is a toroidal plasma confinement system, where confinement is achieved by applying magnetic fields to the plasma. As already described in Chapter **1**, the main magnetic field is the toroidal field, produced by the toroidal coils surrounding the plasma. A poloidal magnetic field is also needed for plasma confinement. This field is produced by inducing a plasma current in the toroidal direction. The resulting magnetic field lines have a helical trajectory around the torus, as shown in Fig. 2.1. The magnetic field lines lie on isobaric surfaces, where the plasma pressure is given by $p = nT$ (n is the density and T the temperature where an hydrogen-like plasma is assumed). The cross section of the plasma for a given toroidal angle on a constant pressure surface is typically approximately circular (cf. Eq. (2.8)). Slight deviations are caused by the plasma pressure and the configuration of the vacuum magnetic field. These distorsions are accounted for by the Shafranov shift and elliptic and triangular perturbations. The flux surfaces can be conveniently parametrised in the following approximate manner [15]:

$$
\begin{aligned}
R &= R_0 - \Delta(r) + r\cos(\theta + \delta\sin\theta),\\
Z &= r\kappa\sin\theta,
\end{aligned}
$$

where $\Delta(r)$ is the so called Shafranov shift, while δ is linked to the plasma triangularity and κ to the ellipticity and in addition R_0 represents the position of the magnetic axis. When the magnetic field is axisymmetric, as assumed in section 2.2, the equilibrium parameters (e.g. R, Z, Δ, q, κ, δ, etc.) do not depend on the toroidal angle φ. Hence the equilibrium is also called *"two dimensional"* [11].

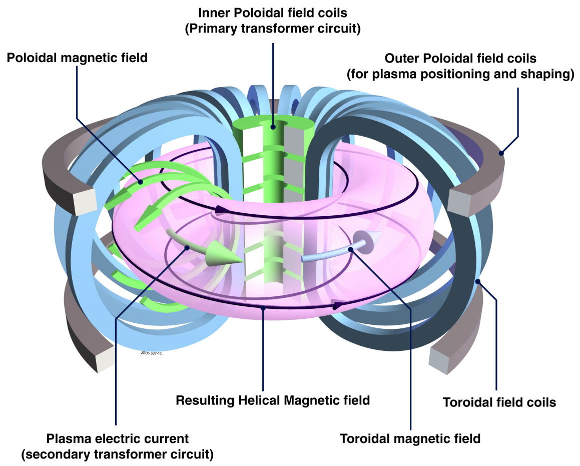
Inner Poloidal field coils
(Primary transformer circuit)
Poloidal magnetic field
Outer Poloidal field coils
(for plasma positioning and shaping)
Resulting Helical Magnetic field
Toroidal field coils
Plasma electric current
(secondary transformer circuit)
Toroidal magnetic field

Figure 2.1: Schematic diagram of the tokamak principle. *Image: EUROfusion*

In burning plasmas, since the fuel reactivity ($\langle\sigma v\rangle$, σ is the fusion cross section v is the relative velocity between ions and the angular brackets indicate an average over Maxwellian distributions), defined as the probability of reaction per unit time per unit density, increases when n and T increase, p must be sufficiently high. In addition, the generation of the magnetic field is one of the major costs of running a plasma device. Hence an important tokamak figure of merit related to machine efficiency is the ratio between the kinetic pressure p and the magnetic pressure, namely [11]:

$$
\beta = \frac{2\mu_0\langle p\rangle}{B^2} \approx \frac{2\mu_0\langle p\rangle}{B_\varphi^2},
$$

where the angular brackets denote the volume average, $\langle\ \cdot\ \rangle = 1/V \int \sqrt{g}(\ \cdot\ )drd\theta d\varphi$. The poloidal beta is defined by [16]:

$$
\beta_p = \frac{\int p dS / \int dS}{B_a^2/(2\mu_0)},
$$

where the integrals represent surface integration over the poloidal cross section with

$B_a = \mu_0 I_\varphi / l$ where l is the length of the poloidal plasma perimeter and I_φ is the plasma current. An alternative definition uses the volume average instead of the surface average.

Now it is useful to introduce some tokamak parameters. We define the smallness parameter ε as the ratio between the minor (a) and the major (R_0) radius of the machine, i.e. $\varepsilon = a/R_0 \ll 1$. The ratio of the poloidal field B_P over the toroidal field B_φ scales with the smallness parameter ε, i.e.:

$$B_P/B_\varphi \sim \varepsilon,$$

where the toroidal magnetic field varies according to $B_\varphi \sim 1/R$. Therefore we have:

$$\beta \sim \frac{2\mu_0 p}{B_\varphi^2} \sim \varepsilon^2, \quad \beta_p \sim \frac{2\mu_0 p}{B_P^2} \sim \varepsilon^{-2}\beta \sim 1.$$

An important parameter is the *safety factor* q which denotes the ratio of toroidal to poloidal turns of the magnetic field on a given magnetic field surface and is defined as:

$$q(\psi) = \frac{T(\psi)}{2\pi} \oint \frac{dl_p}{R^2 B_P} \sim 1,$$

where the integral is carried over a poloidal circuit around the magnetic surface labelled by ψ. As discussed briefly in Chapter **1**, if the numerical value of q is an irrational number, then the magnetic field line densely covers the magnetic surface. The rational surfaces are the surfaces for which q is a rational, namely $q = m/n$. On such surfaces, the magnetic field line closes on itself after m toroidal and n poloidal turns. In the cylindrical limit, making use of (2.9), we can approximate:

$$q = \frac{T(\psi)}{2\pi d\psi/dr} \oint \frac{d\vartheta\sqrt{g}}{R^2} \approx \frac{rB_\varphi}{R_0 B_P},$$

where r is the radial coordinate and labels the flux surface, ϑ is a poloidal-like angle and $\sqrt{g}$ is the Jacobian of the toroidal coordinate system (r, ϑ, φ). The edge value of q is linked to the total toroidal plasma current I_φ via $q(a) \approx (2\pi a^2 B_\varphi)/(\mu_0 I_\varphi R)$. The shape of the safety factor is thus related to the current density profile, which is given in a cylinder by:

$$\mu_0 J_\varphi \simeq \frac{1}{r}\frac{d}{dr}\left(\frac{r^2}{q}\right).$$

Typical profiles of the tokamak magnetic fields and q profile are shown in Fig. (2.2)-a.

Reversed field pinches (RFPs) like tokamaks are nominally axisymmetric config-

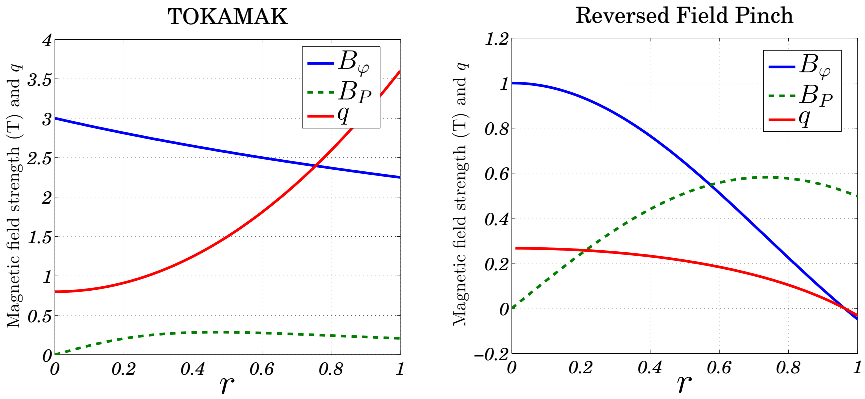

Figure 2.2: Magnetic field (toroidal and poloidal) strength and safety factor q, for Tokamak (a) and RFP (b) configuration at $\vartheta = 0$.

urations (note as we shall see in this thesis, both tokamak and RFP plasmas can develop stationary states which are strongly non-axisymmetric). This configuration relies on currents flowing in the plasma for the generation of both poloidal and toroidal components of the magnetic field. The poloidal field B_P is produced by the toroidal component of the plasma current while the toroidal field B_φ is produced by the external toroidal field coil and the poloidal component of the plasma current. Unlike in a tokamak, the magnitude of B_φ and B_P is comparable. Typical profiles of RFP magnetic fields are shown in Fig. (2.2)-b. The peculiar characteristic of an RFP plasma is that its toroidal magnetic field has a reversal in its sign close to the edge. The volume averaged toroidal field is typically much weaker than the toroidal field of a similarly sized tokamak device (two to ten times smaller). In this way, in principle, a highly sheared magnetic configuration can be obtained which is stable with respect to MHD modes at low values of the safety factor and high values of β. The ordering for the relevant physical quantities reads:

$$B_P/B_\varphi \sim 1, \quad q \sim \frac{rB\varphi}{R_0 B_P} \sim \varepsilon, \quad \beta \sim 1, \quad \beta_p \sim 1,$$

Therefore in principle, we could expect high-beta ($\beta = 10 \sim 20\%$) plasmas to be confined in an MHD stable way. Since the plasma current can be larger than the Kruskal–Shafranov limit ($q < 1$), it was hoped that RFP would reach the ignition condition by ohmic heating alone. However it is important to note that RFP plasma dynamics are generally highly turbulent and in addition near the edge stochastic regions form due to the overlapping of rational surfaces.

Generally the Grad-Shafranov equation (2.11), valid both for tokamaks and RFPs, is solved numerically. There are however a few cases for which the Grad-Shafranov equation can be solved analytically [14]. The standard procedure for tackling the analytic solution of (2.11) is to expand in powers of the smallness parameter ε certain relevant plasma quantities such as the poloidal flux ψ, p, etc. Such analytic expansion will be used as a basis for the analytic calculations of stability in Chapters **3** and **4**. Nevertheless, for accurate calculation of plasma stability (e.g. Chapter **3**), numerically resolved equilibria are required. The Grad-Shafranov equation (2.11), as shown earlier, is obtained by imposing that the equilibrium is axisymmetric ($\partial_\varphi = 0$). It is possible however to have plasma equilibrium configurations in which the axisymmetric constraint is relaxed. Clearly stellarator equilibria can not be solved assuming (2.11) since the plasmas are naturally strongly non-axisymmetric due to the vessel and coil geometry. Moreover, it is possible to have particular conditions in axisymmetric machines, for which helical equilibria can develop. This has been confirmed numerically for tokamak plasmas [17] and experimentally in RFPs (RFX-SHAx states) [7]. It is clear that Eq. (2.11) is not appropriate anymore for describing such plasma states. Therefore we must abandon such an approach and use an alternative method [18]. We start with writing the expression for the plasma energy:

$$W = \int d\boldsymbol{x} \left(\frac{B^2}{2\mu_0} + \frac{p}{\Gamma - 1} \right), \tag{2.12}$$

where $\Gamma = 5/3$. The new approach for finding an equilibrium configuration is based on a variational principle, in which the integral expression above is minimised. The lowest energy state corresponds to the equilibrium state. Such an approach is used for the determination of the equilibrium in the VMEC code [18] (the numerical procedure is described in section C.1). It can be shown that minimisation of Eq. (2.12) reduces exactly to the Grad-Shafranov equation (2.11) in the limit of axisymmetry ($\partial_\varphi = 0$).

2.4 Ideal MHD stability

In laboratory generated plasmas, the plasma equilibrium is spontaneously broken by the presence of small perturbations which alter the balance of the forces acting on the system. Such perturbations can develop in different ways: they can either restore the plasma to its starting equilibrium state or they can grow. Their growth can eventually saturate, thereby leading to the formation of a new equilibrium state, or it can continue to grow until the plasma confinement is completely destroyed. Ideal (non resistive) perturbations of this kind are very dangerous, since disruptions can occur within a few milliseconds or less. This demonstrates that ideal MHD stability is of extreme importance for good confinement of fusion devices.

2.4.1 The normal mode problem and the energy principle

Let us begin this section by examining the normal mode method to the assessment of ideal MHD stability. The starting point of the normal mode approach is the linearisation of the MHD equations (Eqs. (2.1)-(2.7)) about the equilibrium state, giving [19]:

$$\begin{aligned}
&\varrho_0\partial_t\boldsymbol{v}_1 = -\boldsymbol{\nabla}p_1 + (\boldsymbol{\nabla}\times\boldsymbol{B}_1)\times\boldsymbol{B}_0 + (\boldsymbol{\nabla}\times\boldsymbol{B}_0)\times\boldsymbol{B}_1, && (2.13)\\
&\partial_t\boldsymbol{B}_1 = \boldsymbol{\nabla}\times(\boldsymbol{v}_1\times\boldsymbol{B}_0), && (2.14)\\
&\partial_t p_1 = -\boldsymbol{v}_1\cdot\boldsymbol{\nabla}p_0 - \Gamma p_0\boldsymbol{\nabla}\cdot\boldsymbol{v}_1, && (2.15)\\
&\partial_t\varrho_1 = \boldsymbol{\nabla}\cdot(\boldsymbol{v}\varrho_0), && (2.16)
\end{aligned}$$

where the subscript 0 indicates equilibrium quantities and the subscript 1 perturbed ones. Combining these equations together and assuming that the perturbations have a normal mode time dependence of the form $\exp(-i\omega t)$, we obtain the following expression written in terms of the fluid displacement $\boldsymbol{\xi}$:

$$\begin{aligned}
&-\omega^2\varrho_0\boldsymbol{\xi} = \boldsymbol{F}(\boldsymbol{\xi}) = \\
&(\boldsymbol{\nabla}\times\boldsymbol{B}_1)\times\boldsymbol{B}_0 + (\boldsymbol{\nabla}\times\boldsymbol{B}_0)\times\boldsymbol{B}_1 + \boldsymbol{\nabla}(\boldsymbol{\xi}\cdot\boldsymbol{\nabla}p_0 + \Gamma p_0\boldsymbol{\nabla}\cdot\boldsymbol{\xi}), \qquad (2.17)
\end{aligned}$$

where the differential operator $\boldsymbol{F}$ has the property of being self adjoint [11, 20], namely:

$$\int\boldsymbol{\eta}\cdot\boldsymbol{F}(\boldsymbol{\xi})d^3\boldsymbol{x} = \int\boldsymbol{\xi}\cdot\boldsymbol{F}(\boldsymbol{\eta})d^3\boldsymbol{x}.$$

Dotting Eq. (2.17) with $\boldsymbol{\xi}^*$ and integrating over the plasma volume, one has [20, 21]:

$$\omega^2\frac{1}{2}\int d^3\boldsymbol{x}\varrho_0|\boldsymbol{\xi}|^2 + \frac{1}{2}\int d^3\boldsymbol{x}\boldsymbol{\xi}^*\cdot\boldsymbol{F}(\boldsymbol{\xi}) = \delta K + \delta W = \text{const}, \qquad (2.18)$$

where

$$\begin{aligned}
&\delta K = -\omega^2\frac{1}{2}\int\varrho_0|\boldsymbol{\xi}|^2d^3\boldsymbol{x} = -\omega^2K, \text{ with } K = \frac{1}{2}\int\varrho_0|\boldsymbol{\xi}|^2d^3\boldsymbol{x}, && (2.19)\\
&\delta W = -\frac{1}{2}\int\boldsymbol{\xi}^*\cdot\boldsymbol{F}(\boldsymbol{\xi})d^3\boldsymbol{x}. && (2.20)
\end{aligned}$$

δW can be interpreted as the work done against the force $\boldsymbol{F}$, when the plasma is displaced by a quantity $\boldsymbol{\xi}$. By integration by parts, after some algebra, we can write:

$$\delta W = \frac{1}{2}\int\left[|\boldsymbol{B}_1|^2 + \Gamma p_0|\boldsymbol{\nabla}\cdot\boldsymbol{\xi}|^2 - \boldsymbol{\xi}_\perp^*\cdot(\boldsymbol{J}_0\times\boldsymbol{B}_1) + (\boldsymbol{\xi}_\perp\cdot\boldsymbol{\nabla}p_0)\boldsymbol{\nabla}\cdot\boldsymbol{\xi}_\perp^*\right]d^3\boldsymbol{x}, \qquad (2.21)$$

where the integration is carried over the plasma volume, having assumed vanishing contributions from the surface term and the vacuum field.

From the self adjointness property of $\boldsymbol{F}$, it can be easily shown that the eigenvalues ω^2 in Eq. (2.18) are purely real. This means that we must have either an oscillation around the equilibrium state ($\omega^2 > 0$) or an exponential growth of the perturbation ($\omega^2 < 0$). Indeed if we write Eq. (2.18) as $\omega^2 = \delta W/K$, this immediately shows that if $\delta W > 0$ for all the possible displacements $\boldsymbol{\xi}$, the system is stable. This condition is the so called *energy principle* [20] and δW is the *energy integral*.

This is a powerful tool widely used in plasma physics, in particular in magnetic confinement fusion. Usually linear stability is analysed by minimising the quantity $\delta K + \delta W$ via the Euler-Lagrange equations. It turns out that we can write the total energy in the form [22]:

$$\delta K + \delta W = \int_0^a \mathcal{L}\left(\xi_r, \frac{d\xi_r}{dr}, r\right) dr, \tag{2.22}$$

thus the extremum of the quantity above with respect to a variation over ξ_r at constant ω^2 is obtained by the Euler-Lagrange equation:

$$\frac{\partial \mathcal{L}}{\partial \xi_r} - \frac{d}{dr}\left(\frac{\partial \mathcal{L}}{\partial(\partial_r \xi_r)}\right) = 0,$$

which, crucially, coincides identically with the equation of motion (2.13). The minimisation procedure consists of deducing from Eq. (2.18) the Euler-Lagrange equations in the form (2.22), and then expanding all quantities in a power series in the inverse aspect ratio $\varepsilon = a/R_0$ (a and R_0 are the plasma minor and major radius respectively). Now we are ready to apply the energy principle and the minimisation procedure to the practical physical case of the internal kink mode.

2.4.2 The linear and nonlinear internal kink mode in tokamak geometry

An instability can develop more easily as a result of the weakening of the field line bending stabilisation in response to a plasma displacement. The field line bending stabilising effect is significantly weakened when the pitch of the unperturbed magnetic field lines becomes sufficiently small i.e. almost perpendicular to the wave vector:

$$|\delta B_\perp| \sim \boldsymbol{k}_{||} \cdot \boldsymbol{B}_0 \sim (nq(r) - m)B_0/R_0 \approx 0.$$

This occurs when the value of the safety factor is sufficiently close to m/n (as we shall see later it is not necessary to have exact resonance) as previously mentioned.

The $m = n = 1$ internal mode is one of the simplest and most important to analyse. The stability of this mode can be assessed assuming various shapes of the q profile [23] as shown in Fig. 2.3. Since all the three cases shown in figure 2.3 have regions where q is close to unity, $m = n = 1$ modes are expected to be unstable. When the safety factor is monotonic and presents a $q = 1$ surface located at $r = r_1$, it gives rise to the so called internal kink mode, whose results on linear and nonlinear theory are summarised in the next section.

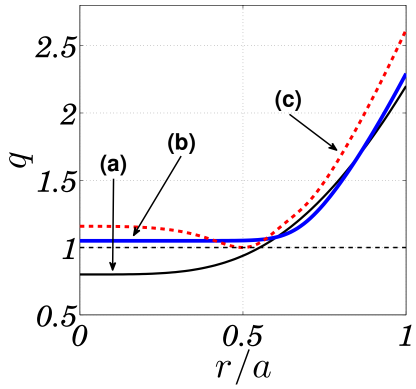

Figure 2.3: Various shapes of the safety factor which are prone to the ideal internal kink instability [24]: monotonic (a), flat (b), hollow (c)

However it turns out that the $m = n = 1$ internal kink instability can develop also for non-monotonic q profiles which have an off axis minimum close to unity. If q_{min} is sufficiently close to one, though the exact resonance is avoided, the field line bending stabilisation is reduced in the narrow region around that point, therefore the instability can occur. Nevertheless, the distorsion of the magnetic flux surfaces is similar for cases (a) and (c) in Fig. 2.3, but is different for cases where the exact resonance is avoided (see Fig. 2.6). Chapter **3** analyses the linear and nonlinear behaviour of the $m = 1$ internal kink mode with hollow q (cf. Fig. 2.3), where the theory is extended to $n > 1$ modes (which are of particular importance in RFP plasmas).

If q is close to unity over a large portion of the plasma core, i.e. with vanishing shear in the central region, unstable $m = 1$ internal modes can develop. The shape of the flux surfaces due to the perturbation is rather different from the one found for the case of monotonic and hollow safety factors (see Fig. 2.6 in section 2.6). Considerations on the stability of this configuration and the implication on resistive stability will be discusses in section 2.6, while the analytic theory and the numerical characterisation of such perturbations will be addressed in Chapters **4** and **5** respectively.

Linear theory of the $m = 1$ internal kink mode with finite magnetic shear

In this section we overview the stability of the internal kink mode for plasmas with finite magnetic shear (case (a) in Fig. 2.3). These stability conditions are in some respects more easily described than the low shear or reverse shear cases of particular interest in this thesis. The internal kink mode is particularly dangerous since it can trigger sawteeth oscillations which eventually lead to a disruption of the plasma discharge. This instability corresponds to a rigid shift of the plasma column, as it will be shown later, and it occurs when the safety factor drops below unity close to the magnetic axis. An internal-kink unstable monotonic safety factor is shown in Figs. 2.3-(a) and 2.4.

In order to simplify the analysis, we initially assume a cylindrical equilibrium described by the coordinate system (r, ϑ, z), where r is the radial variable, ϑ is the poloidal angle and z is the azimuthal direction. The safety factor is taken to be increasing monotonically with respect to r, with $q_0 < 1$ (q_0 is the value of the safety factor on the magnetic axis).

We apply now the minimisation procedure described in the previous section. Equation (2.21) is cast in the form $\delta W = \delta W_0 + \varepsilon^2 \delta W_2 + \varepsilon^4 \delta W_4 + ...$, where we normalised potential energy in the following manner $\widehat{\delta W} = \delta W/(2\pi^2 a^2 R_0 B_0^2/\mu_0)$. $\widehat{\delta W}_0$ is minimised by imposing $\boldsymbol{\nabla} \cdot \boldsymbol{\xi}_\perp = 0$ where $\boldsymbol{\xi}_\perp = \xi_r \boldsymbol{e}_r + \xi_\vartheta \boldsymbol{e}_\vartheta$, so that $\widehat{\delta W}$ is written in the following form [19, 25]:

$$\widehat{\delta W} = \int_0^a dr \left(f \left| \frac{d\xi}{dr} \right|^2 + g |\xi|^2 \right), \tag{2.23}$$

$$f = r \frac{(mB_\vartheta/r + k_z B_z)^2}{k^2 B_0^2}, \tag{2.24}$$

$$g = \frac{2k_z^2}{k^2 B_0^2} \frac{dp_0}{dr} + \left(\frac{m^2 - 1}{r^2} + k_z^2 \right) f + \frac{2k_z^2}{rk^4 B_0^2} \left(k_z^2 B_z^2 - \left(\frac{m}{r} \right)^2 B_\vartheta^2 \right), \tag{2.25}$$

where $\xi = \xi_r/a$ (a is the plasma minor radius), $k_z = -n/R$, $k^2 = (m/r)^2 + k_z^2$, having used the ansatz $\xi = \xi(r) \exp[im\vartheta + ik_z z]$. At leading order we assume $B_z \sim B_0 = \text{const.}$, where $\varepsilon = r/R \ll 1$. The functions f and g are thus expanded in powers of $rk_z \sim \varepsilon$ up to second order (valid when $n \ll \varepsilon^{-1}$), leading to the following expression for $\widehat{\delta W}_2$ [19, 25, 26]:

$$\widehat{\delta W}_2 = \frac{1}{R^2} \int_0^a r dr \left(\frac{n}{m} - \frac{1}{q} \right)^2 \left[r^2 \left| \frac{d\xi}{dr} \right|^2 + (m^2 - 1)|\xi|^2 \right]. \tag{2.26}$$

It is immediate to recognise that for the special case $m = 1$ (the *internal kink mode*), the energy integral is minimised by the singular function (see also Fig. 2.4) [25]:

$$\xi = \begin{cases} \xi_0, & r < r_1 \\ 0, & r > r_1, \end{cases} \tag{2.27}$$

where r_1 denotes the position where $q = 1$.

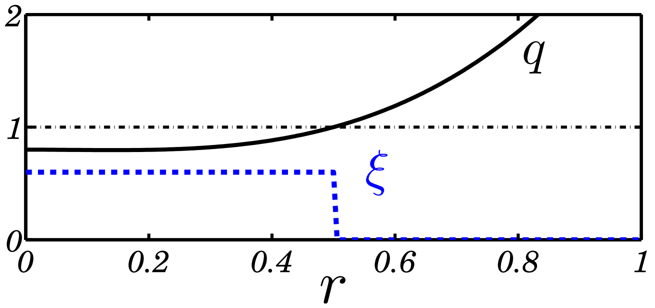

Figure 2.4: Safety factor and corresponding eigenfunction for the internal kink mode.

For the special case of the $m = 1$ mode, regardless of the magnetic shear, the field line cannot bend in the poloidal plane in response to the rigid shift of the $m = 1$ mode. Both $\widehat{\delta W}_0$ and $\widehat{\delta W}_2$ have been minimised to zero, implying that the internal kink is marginally stable to order ε^2. Fourth order terms in (2.23) are therefore required for the determination of the stability of the internal kink. Going further to fourth order expansion in the calculation of $\widehat{\delta W}$, we have for the special case $m = 1$ in (2.26):

$$\widehat{\delta W}_4 = \delta W_C = \frac{n^2}{R^2}\int_0^a r dr \left[\frac{2r}{B_0^2}\frac{dp_0}{dr} + \frac{r^2}{R^2}\left(n - \frac{1}{q}\right)\left(3n + \frac{1}{q}\right)\right] |\xi|^2 = \xi_0^2 \int_0^{r_1} g dr. \tag{2.28}$$

This cylindrical derivation, valid to order ε^4, is correct only when modes with $n > 1$ are considered. For $n = 1$ [26] the toroidicity of the system (in particular the Shafranov shift) becomes important and the coupling which occurs between the $m = 1$ and the $m = 2$ mode plays a crucial role for the correct determination of the energy integral. Under the assumption $\beta_p \sim s \sim 1$ (where s is the magnetic shear defined as $s = r d \ln q/dr$), $\widehat{\delta W}$ is expanded up to fourth order in ε, and the energy minimisation procedure leads to the following replacement:

$$\widehat{\delta W} = \left(1 - \frac{1}{n^2}\right)\widehat{\delta W}_C + \frac{1}{n^2}\widehat{\delta W}_T. \tag{2.29}$$

The cylindrical contribution is entirely cancelled by the inclusion of toroidal effects. For a current profile of the form $J_z(r) \sim 1 - (r/a)^\nu$ with $\nu < 4$, $q(r_j) = j$ and

$1-q_0 \ll 1$, the toroidal contribution to the energy integral reads [19, 26]:

$$\widehat{\delta W}_T \simeq 3\frac{r_1^4}{R^4}(1-q_0)\left(\frac{13}{48}\times\frac{4-\nu}{4+\nu}-\tilde{\beta}_p^2\right)\xi_0^2, \tag{2.30}$$

where $\tilde{\beta}_p = -2/B_\vartheta(r_1)^2 \int_0^{r_1} \frac{r_1^2}{r_2^2}\frac{dp}{dr}dr$, with $q(r_2)=2$.

A special treatment is required close to the rational surface, since equation (2.28) is a valid description of the total energy $\widehat{\delta W}+\delta K$ everywhere except close to the rational surface. Near the rational surface, we have also to consider the inertia in the total energy $\widehat{\delta W}+\delta K$, which we are permitted to treat in slab geometry. Here $\delta K = -2\pi^2 R_0\omega^2 \int_0^a r\varrho(|\xi_r|^2+|\xi_\vartheta|^2)dr$. By varying this quantity with respect to ξ we obtain at leading order the Euler-Lagrange equation for the fluid displacement near the rational surface (for sake of simplicity we omit to write the subscript 0 in the equilibrium magnetic field $\boldsymbol{B}$) [25]:

$$\frac{d}{dr}\left[r^3\left(\mu_0\varrho_0\gamma^2+(\boldsymbol{k}\cdot\boldsymbol{B})^2\right)\frac{d\xi}{dr}\right]=0, \tag{2.31}$$

where $\gamma=-i\omega$ and $\boldsymbol{k}\cdot\boldsymbol{B}=B_\vartheta(1-q)/r$ with $n=1$. Note that the inertia term removes the singular point at the rational $q=1$ surface in the expression above where $\boldsymbol{k}\cdot\boldsymbol{B}$ vanishes. Near the singular layer we write $\boldsymbol{k}\cdot\boldsymbol{B}\approx(\boldsymbol{k}\cdot\boldsymbol{B})'_{r_1}x$, where $'\equiv d/dr$ and $x=r-r_1\sim r\varepsilon$ (we recall tha ε is the inverse aspect ratio). The energy conservation requires (for $n=1$):

$$\delta K_{r_1}+\widehat{\delta W}_{r_1}=-\widehat{\delta W}_T, \tag{2.32}$$

$$\delta K_{r_1}+\widehat{\delta W}_{r_1}=\left(\frac{r_1}{R}\right)^2\frac{r_1^3[(\boldsymbol{k}\cdot\boldsymbol{B})'_{r_1}]^2}{B_0^2}\int_{-\infty}^{\infty}dx\left[x^2+\left(\frac{\gamma\sqrt{\varrho_0\mu_0}}{|(\boldsymbol{k}\cdot\boldsymbol{B})'_{r_1}|}\right)^2\right]\left(\frac{d\xi}{dr}\right)^2. \tag{2.33}$$

The layer solution of (2.31), where inertia is important, is:

$$\xi=\tfrac{1}{2}\xi_0\{1-(2/\pi)\arctan[((|\boldsymbol{k}\cdot\boldsymbol{B})_{r_1}|'x)/\gamma\sqrt{\mu_0\varrho}]\}, \tag{2.34}$$

where boundary conditions $\xi(r\ll r_1)=\xi_0$, and $\xi(r\gg r_1)=0$, have been imposed. Substituting the above expression in (2.33) we obtain from the dispersion relation (2.32), the estimate for the growth rate γ. Using $|(\boldsymbol{k}\cdot\boldsymbol{B})'_{r_1}|\sim q'_{r_1}B_z/R$ we have:

$$\gamma=-\frac{\pi R}{r_1^3 B_z q'_{r_1}\sqrt{\mu_0\varrho_0}}\frac{B_0^2\widehat{\delta W}_T}{\varepsilon_1^2\xi_0^2}, \tag{2.35}$$

where $\varepsilon_1=r_1/R$, which shows that the system becomes unstable when $\delta W_T<0$.

Nonlinear calculation of the saturation of the $m = 1$ internal kink mode with finite magnetic shear

In order to calculate the static nonlinear helical equilibrium we simplify the analysis setting ourselves in cylindrical geometry described by the coordinate system (r, ϑ, z), where we assume a constant toroidal field in the narrow layer where $q \approx 1$. Even though a cylindrical approximation is chosen for the non-linear treatment, the analysis is capable of non-linearly continuing the toroidal linear stability analysis just derived. In a static helical equilibrium, all the quantities must depend only upon the radial variable r and the helical angle $\chi = \vartheta + k_z z$. We introduce a helical flux function ψ_* defined by $\psi_* = \psi - (nB_0 r^2)/(2mR)$, where ψ is linked to the poloidal field as shown previously ($\boldsymbol{B}_p = \boldsymbol{e}_z \times \boldsymbol{\nabla}\psi$), such that $\partial\psi_*/\partial r = B_\vartheta(1-q)$. Since the plasma is considered ideal, both poloidal and toroidal magnetic fluxes are conserved. Moreover ψ_* fulfils the equation $\partial\psi_*/\partial t + \boldsymbol{v} \cdot \boldsymbol{\nabla}\psi_* = 0$, so that the helical flux ψ_* is preserved while following the plasma motion. Thus if the flux surfaces are shifted by a small amount ξ_0, then the helical flux is linked to the initial cylindrical equilibrium flux ψ_0 by the relation $\psi_*(r, \vartheta) = \psi_0(r - \xi_0(r, \vartheta))$ (fo sake of simplicity here we set $z = 0$). By Taylor-expanding the previous expression in series of x in a neighbourhood of the singular $q = 1$ surface, we get [19, 25]:

$$\psi_* = \psi_0 + \tfrac{1}{2}x^2 r_1 [r(\boldsymbol{k} \cdot \boldsymbol{B})]'_{r_1} + \dots. \tag{2.36}$$

It is important to note that the expansion above is not valid in the case of reversed shear when the exact resonance $q = 1$ is avoided, since in this particular case $(\boldsymbol{k} \cdot \boldsymbol{B})_{r_1} \sim (1-q) \neq 0$ and $(\boldsymbol{k} \cdot \boldsymbol{B})]'_{r_1} = 0$, so that we must retain the $\mathcal{O}(x^3)$ term. This case will be analysed in the next chapter.

By taking the curl of Eq. (2.8) and choosing the projection along the magnetic field, we have at leading order:

$$\boldsymbol{\nabla}^2\psi_* = J_z(\psi_*), \quad \boldsymbol{\nabla}^2 = \frac{1}{r}\frac{\partial}{\partial r} r \frac{\partial}{\partial r} + \frac{1}{r^2}\frac{\partial^2}{\partial\vartheta^2}. \tag{2.37}$$

The plasma is assumed incompressible ($\boldsymbol{\nabla} \cdot \boldsymbol{\xi} = 0$), so that the area in the $r - \vartheta$ plane enclosed by a flux surface is constant when the surface is moved, i.e.:

$$\int_{\psi_*} r dr d\vartheta = \int_{\psi_0} r dr d\vartheta. \tag{2.38}$$

By assuming strong radial excursions, Eq. (2.37) is integrated over the radial variable r and eventually becomes [19, 25]:

$$\left(\frac{d\psi_*}{dr}\right)_\vartheta = \pm\sqrt{\tilde{F}(\psi_*) + \tilde{G}(\vartheta)}, \tag{2.39}$$

with F and G are unknown functions to be determined. The ± sign indicates the formation of a current sheet at the resonant surface. In the unperturbed cylindrical equilibrium, we take a surface labelled by the quantity x, which represents the distance from the singular surface located in r_1. The fluid displacement $\xi(r,\vartheta)$ shifts the surface labelled x to $r(x,\vartheta)$, according to:

$$r(x,\vartheta) = r_1 + x + \xi(r,\vartheta).$$

Differentiating Eq. (2.36) and the expression above with respect to x and inserting the result into (2.39), after integration in x, we obtain:

$$\xi(x,\vartheta) = \pm \int dx' \left(\frac{x'}{[\tilde{f}(x) + \tilde{g}(\vartheta)]^{1/2}} - 1 \right) + h(\vartheta), \tag{2.40}$$

with the normalisation $\tilde{f} = \tilde{F}/[r(\boldsymbol{k} \cdot \boldsymbol{B})]_{r_1}$. Differentiating (2.40) with respect to x and integrating over the poloidal angle, yields to the following expression:

$$\frac{1}{2\pi} \oint \frac{x}{[\tilde{f}(x) + \tilde{g}(\vartheta)]^{1/2}} d\vartheta = 1, \tag{2.41}$$

from which it follows that $\tilde{f} \to x^2$ for large x. The asymptotic expansion of ξ reads:

$$\xi(x,\vartheta) \sim \begin{cases} \displaystyle\int_0^\infty dx' \left(\frac{x'}{[\tilde{f}(x) + \tilde{g}(\vartheta)]^{1/2}} - 1 \right) + \frac{1}{2}\frac{\tilde{g}(\vartheta)}{x} + h(\vartheta), & x \to +\infty \\ \displaystyle -\int_0^\infty dx' \left(\frac{x'}{[\tilde{f}(x) + \tilde{g}(\vartheta)]^{1/2}} - 1 \right) + \frac{1}{2}\frac{\tilde{g}(\vartheta)}{x} + h(\vartheta), & x \to -\infty, \end{cases} \tag{2.42}$$

from which we have that $\lim_{x\to-\infty} \xi(x,\vartheta) = \xi_0 \cos\vartheta$ and $\lim_{x\to+\infty} \xi(x,\vartheta) = 0$. The displacement of (2.42) can be connected to the displacement (2.34) resolved in the linear analysis of the last section (which depends on γ, and hence on δW_T):

$$\xi(x,\vartheta) \sim \begin{cases} \xi_0[1 + (\gamma\tau_A r_1/\pi x)]\cos\vartheta, & x < 0 \\ \xi_0(\gamma\tau_A r_1/\pi x)\cos\vartheta, & x > 0, \end{cases} \tag{2.43}$$

where $\tau_A = B_0/\sqrt{\mu_0\varrho_0}$. Hence from (2.42) and (2.43) with the boundary conditions given above we have $h(\vartheta) = -\int_0^\infty dx' \left(\frac{x'}{[\tilde{f}(x)+\tilde{g}(\vartheta)]^{1/2}} - 1 \right)$ and we are left with the following expression:

$$\xi_0 \cos\vartheta = -2 \int_0^\infty dx' \left(\frac{x'}{[\tilde{f}(x) + \tilde{g}(\vartheta)]^{1/2}} - 1 \right).$$

By using Eq (2.41), we can transform the equation above into an integral equation for $\tilde{g}(\vartheta)$, namely [25] (for the sake of simplicity we omit the dependence of $\tilde{f}$ and $\tilde{g}$

upon their arguments):

$$\xi_0 \cos\vartheta = -2\int_0^\infty d\tilde{f}\frac{\oint(\tilde{f}+\tilde{g})^{-3/2}d\vartheta/2\pi}{(\oint(\tilde{f}+\tilde{g})^{-1/2}d\vartheta/2\pi)^3}\left(\frac{1}{\sqrt{\tilde{f}+\tilde{g}}}-\oint\frac{d\vartheta/2\pi}{\sqrt{\tilde{f}+\tilde{g}}}\right) \tag{2.44}$$

This equation can be solved by means of a variational principle, and provides an expression for the function $\tilde{g}(\vartheta)$. Matching asymptotically Eq. (2.42) with Eq. (2.43) we obtain:

$$-\frac{\xi_0}{r_1^3[(\boldsymbol{k}\cdot\boldsymbol{B})_1']^2}\int_0^{r_1}\hat{g}dr = \int_0^{2\pi}\cos\vartheta\tilde{g}(\vartheta)d\vartheta,$$

and solving numerically (2.44) are able to write the amplitude of the non-linearly saturated helical kink as a function of the linear growth rate in the following manner [19, 25]:

$$\xi_0 = \frac{13.3}{q_1'\pi}\gamma\tau_A, \tag{2.45}$$

where the toroidal effects are contained inside the expression for the growth rate γ. These results show that the ideal internal kink mode has a saturated nonlinear solution of amplitude given by (2.45) and radial and poloidal structure given by the linear analysis, i.e. by (2.43). In the next chapter the amplitude of this solution is compared with simulations performed with the initial value code XTOR-2F (see Appendix **C** C.2). Note however that in practise current sheets develop on the $q = 1$ surface, so that (2.45) would be modified strongly by resistivity [19]. However, in the next chapter we will derive a similar non-linear solution for the $m = 1$ internal kink, but with a hollow safety factor, namely $q_{min} > 1$. For such a calculation the resistivity can be safely neglected on the m/n surface. Similar rigid displacements for $m = 1$ modes can be found also in RFP plasmas as it will be shown in Chapter **3**, where an analogous derivation is employed for calculating the shift of a $m = 1$ mode when the q profile presents an off axis minimum. The theory of the nonlinear saturation is also extended to general toroidal mode numbers.

2.5 Resistive internal modes with finite magnetic shear

We now allow for plasma resistivity in the MHD equation. Resistive effects are taken into account by modifying Eq. (2.4) in the following manner:

$$\boldsymbol{E} + \boldsymbol{v}\times\boldsymbol{B} = \eta\boldsymbol{J}, \tag{2.46}$$

where η is the plasma resistivity and $\boldsymbol{J}$ the current density. The most simple expression for η is given by Spitzer resistivity [27]:

$$\eta = \frac{1}{\pi^{3/2}} \frac{m_e^{1/2} Z e^2 \ln \Lambda}{12\sqrt{2}\varepsilon_0^2 T_e^{3/2}} \sim T_e^{-3/2},$$

where Z is the ionisation of the nuclei, and $\Lambda \approx 10 \sim 20$ is the Coulomb logarithm where $\Lambda \sim (12\pi/Z)n\lambda_D^3$ [27].

When plasma resistivity is allowed in the MHD equations, new types of instabilities occur. At present we focus our attention on the so called *tearing instability*. The tearing instability is closely related to the kink instability described in the previous section. Tearing modes are driven by current density gradients and by the presence of a small amount of resistivity (due to electron-ion collisions) on surfaces which are resonant with the safety factor whose value is a rational, i.e. $q = m/n$. On these *"fragile"* surfaces, the forces preventing magnetic reconnection become sufficiently small that plasma resistivity can no longer be neglected and the field lines are allowed to break, implying that magnetic reconnection can take place. If resistivity is not permitted, non physical current sheets (singular spikes of current) occur on rational surfaces, as mentioned just previously for the non-linear internal kink mode [1].

Hence the flux surfaces are deformed from their initial nested configuration and *"island"* structures appear in the poloidal plane, as shown in figure 2.5. When the magnetic island is formed, the original $q = m/n$ surface is transformed into a separatrix, and as the island becomes larger, forms the external edge of the island. The magnetic field lines inside the island lie on helical surfaces with their own magnetic axis labelled by the O-point (see Fig. 2.5). The two parts which divide the separatrix meet at the X-points. Although a tokamak plasma can form a stationary state in the presence of magnetic islands, these structures enhance the radial energy transport along the magnetic field lines. In practice, the width of an island can be 10% $\sim$ 20% of the minor radius, with the result that temperature gradients are flattened in this region. Density profiles are also flattened across the island structure, although typically its flattening is less pronounced than the temperature.

---

[1] Let us take a simple example: consider helical perturbations in cylindrical approximation with a Lagrangian fluid displacement in the coordinate system (r, θ, z) given by $\boldsymbol{\xi}(r, \theta, z, t) = \boldsymbol{\xi}(r) \exp[i(m\theta - nz/R) + \gamma t]$, such that $\boldsymbol{v} = \partial\boldsymbol{\xi}/\partial t$. By using Eq. (2.4) we can write the radial component of the displacement:

$$\xi_r = \delta B_r / \left[\frac{imB_\theta}{r} \left(1 - \frac{n}{m} q(r)\right) \right],$$

where δB_r is the perturbed radial magnetic field. It is clear that the displacement above diverges on the rational $q = m/n$ surface, i.e. is singular on this surface. In proximity of such surface, if the plasma resistivity η is non vanishing, the component of the magnetic field orthogonal to the equilibrium surfaces can grow so that the magnetic diffusion becomes important and changes in the magnetic topology are permitted.

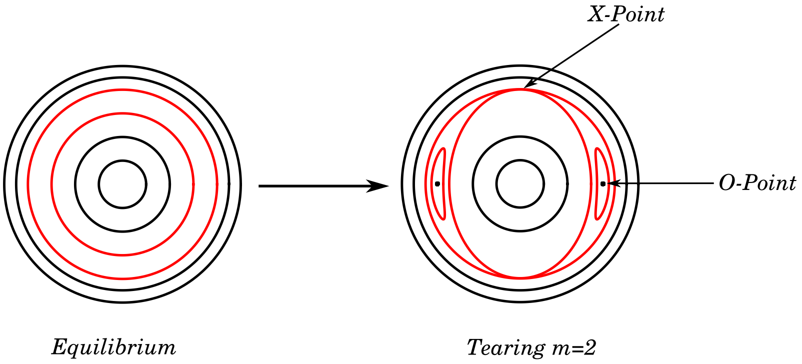

Figure 2.5: Magnetic flux surfaces for an equilibrium nested configuration (left) and reconnected configuration with an island with poloidal wave number $m = 2$ (right).

Tearing instabilities limit the plasma β at significantly lower values than the ideal limits [28]. These instabilities are a major concern for a future operating reactor, since they degrade substantially the plasma confinement (and hence fusion reactivity) and they can eventually lead to a disruption affecting the integrity of the machine. Tearing modes have been extensively studied theoretically and experimentally over the years and the understanding of the underlying physics has rapidly expanded. The next two sections present a simple mathematical description of such instabilities in the linear and nonlinear regime.

Basic linear classical tearing mode dynamics

Since the growth of the instability is sufficiently slow, inertial effects are negligible over a large portion of the plasma volume and the plasma can be assumed ideally conducting ($\eta = 0$). However, close to a rational resonant surface (whose position is denoted here by r_s), plasma resistivity and inertia (although small) have an important effect upon the plasma behaviour. Thus the theory of tearing modes involves solving two sets of equations, one far from the resonant surface r_s *"outer region"*, and another set close to this resonant layer *"inner region"*. The solutions for the eigenfunction obtained separately in these two regions are matched, and the matching procedure determines the growth rate (eigenvalue).

The equation describing the plasma state in the outer region is given by (2.8). The large aspect ratio approximation is employed to order the magnetic field and the currents [16], both equilibrium and perturbed (the equilibrium quantities are denoted by the subscript 0 and the perturbed ones by a tilde):

$$B_{\vartheta 0} \sim \frac{dB_{\varphi 0}}{dr} \sim \varepsilon B_{\varphi 0}, \qquad J_{\vartheta 0} \sim \varepsilon J_{\varphi 0} \qquad \tilde{B}_{\varphi} \sim \varepsilon \tilde{B}_r \sim \varepsilon \tilde{B}_{\vartheta}, \qquad \tilde{B}_r \sim \varepsilon \tilde{J}_{\vartheta} \sim \varepsilon \tilde{J}_{\varphi},$$

with $\varepsilon = a/R_0 \ll 1$. In the ordering adopted, the perturbed magnetic field can be expressed in terms of a flux function $\tilde{\psi}$, defined by:

$$\tilde{B}_r = -\frac{1}{r}\frac{\partial\tilde{\psi}}{\partial\vartheta}, \quad \tilde{B}_\vartheta = \frac{d\tilde{\psi}}{dr}.$$

By taking the toroidal projection of the curl of Eq. (2.8) and using Ampére's law, after linearisation one has in cylindrical geometry the *tearing equation* for the perturbed magnetic flux, which reads:

$$\boldsymbol{\nabla}_\perp^2\tilde{\psi} = \frac{1}{r}\frac{d}{dr}\left(r\frac{d\tilde{\psi}}{dr}\right) - \frac{m^2}{r}\tilde{\psi} = -\frac{dJ_{\varphi 0}/dr}{\frac{B_{\vartheta 0}}{\mu_0}\left(1-\frac{nq}{m}\right)}\tilde{\psi}, \tag{2.47}$$

where the perturbation has been assumed to be of the form $\exp[i(m\vartheta - n\varphi)]$. This equation has a singularity in $r = r_s$, where the resonance with the safety factor occurs, i.e. where $q = m/n$.

It can be shown that the change in the magnetic energy, due to this perturbation, is given by [29]:

$$W = \tfrac{1}{2}\int d\boldsymbol{x}\left(|\boldsymbol{\nabla}_\perp\psi|^2 + \frac{dJ_{\varphi 0}/dr}{\frac{B_{\vartheta 0}}{\mu_0}\left(1-\frac{nq}{m}\right)}|\tilde{\psi}|^2\right) = -\tfrac{1}{4}r_s|\tilde{\psi}(r_s)|^2\Delta',$$

where the integration is carried over the plasma volume and:

$$\Delta' = \frac{\tilde{\psi}'}{\tilde{\psi}}\Big|_{r_s-\delta}^{r_s+\delta}, \text{ with } \delta \to 0. \tag{2.48}$$

Hence the free energy available for the development of the instability, is proportional to the jump of $\tilde{\psi}$ across $r = r_s$.

The equation for the jump Δ' calculated without resistivity has to be matched to the jump Δ' calculated near the surface $q = m/n$ (this including inertia and resistivity). This procedure give a dispersion relation for the growth rate γ. The relevant resistive equations are obtained by taking the radial projection of the curl of the Ohm's law Eq. (2.46):

$$\gamma\tilde{\psi} + B_\vartheta\left(1-\frac{nq}{m}\right)\tilde{v}_r = \frac{\eta}{\mu_0}\boldsymbol{\nabla}^2\tilde{\psi}, \tag{2.49}$$

which highlights the dominant contribution of the resistive term in the layer region, where the perturbation is assumed varying in time as $e^{\gamma t}$. Equation (2.47), augmented by the inertial term, is solved simultaneously with Eq. (2.49) and matched with the solution from the outer region via Δ', yielding the following eigenvalue relation for the growth rate [16]:

$$\gamma = 0.55 \left(n \frac{a}{R} \frac{aq'}{q} \right)^{2/5} \tau_R^{-3/5} \tau_A^{-2/5} (a\Delta')^{4/5},$$

where $\tau_R = \mu_0 a^2/\eta$, $\tau_A = a\sqrt{\mu_0 \varrho}/B_\varphi$ and where Δ' is that of the external region, i.e. the solution of Eq. (2.47). Hence the *"classical"* tearing mode becomes unstable when $\Delta' > 0$, and it grows on relatively slow time scales. Indeed for a deuterium JET-like plasma with $B_\varphi \sim 5T$, $n_e \sim 10^{20} m^{-3}$, $T_e \sim 5KeV$ and the minor radius $a = 1m$, the tearing mode is expected to grow within 70 ms [16], which is a much longer time than typical ideal instabilities which grow within few milliseconds or less. It can be shown analytically that high poloidal wave number ($m \gg 1$) modes are intrinsically stable, since $\Delta' < 0$. Therefore only moderately low m ($m = 2 \sim 5$) modes are expected to be unstable.

Essential nonlinear classical tearing mode dynamics

Once the end of the linear phase is reached, a resistive mode grows non-linearly according to the Rutherford equation [30]. A tearing mode is called classical when neoclassical effects, e.g. bootstrap contributions, are neglected. Choosing sheet pinch geometry, i.e. in a coordinate system $(x, y, \varphi \to z)$ [30] Eq. (2.4) is recast in terms of the helical flux ψ, i.e.:

$$(\partial_t + \boldsymbol{v} \cdot \boldsymbol{\nabla})\psi = \eta J_\varphi - E_\varphi, \tag{2.50}$$

where ψ is such that $B_x = -\partial\psi/\partial y$ and $B_y = \partial\psi/\partial x$. Inertia can be neglected inside the reconnecting layer in the nonlinear phase [30], therefore from the curl of (2.2) we have $\boldsymbol{B} \cdot \boldsymbol{\nabla} J_\varphi = 0$ implying that $J_\varphi = J_\varphi(\psi)$. The flux is decomposed in the following manner $\psi(x, y, t) = \psi_0(x) + \tilde{\psi}_1(y, t)$ (constant ψ-approximation [30, 31]), with only one dominant mode where $\tilde{\psi}_1 = \psi_1(t)\cos ky$.

The evolution equation for the island width in the nonlinear phase is obtained by matching the logarithmic-derivative discontinuities in the outer solution to those arising from the asymptotic solution in the nonlinear singular layer. The current density in the nonlinear layer is given by [30]:

$$J_z(\psi) = J_{z,0} + \eta^{-1} \langle \partial_t \tilde{\psi}_1 / [\psi - \tilde{\psi}_1]^{1/2} \rangle_y / \langle [\psi - \tilde{\psi}_1]^{-1/2} \rangle_y, \tag{2.51}$$

with $\langle f \rangle_y = \int_0^{2\pi/k} f k dy/2\pi$. Approximating $\boldsymbol{\nabla}^2\psi \approx \partial^2\psi/\partial x^2$ and integrating over the variable x, we obtain the evolution equation for the island width $w = 4\sqrt{\psi_1/\psi_0''}$

[30]:

$$\frac{\partial w}{\partial t} = 1.22\eta\Delta', \tag{2.52}$$

which shows that the nonlinear growth is proportional to the linear growth rate. Eventually the classical tearing mode saturates to a critical value, according to the following expression [32]:

$$\frac{\partial w}{\partial t} = 1.66\eta(\Delta'(w) - \alpha w), \tag{2.53}$$

where $\Delta'(w) = \psi'/\psi|_{r_s-w/2}^{r_s+w/2}$ and α is a complicated expression related to the local plasma properties (see [16, 32]) and the factor 1.66 comes from a more exact calculation [32]. Note that the tearing parameter Δ' in Eq. (2.52) is not a function of w, whereas in Eq. (2.53) we have $\Delta'(w)$ due to the effect of an island on the current profile [33].

2.6 Introduction to stability in plasmas with low magnetic shear

As briefly described in Chapter **1**, hybrid plasmas are configurations where the safety factor is almost resonant with a rational number in the central region, i.e. $q = m/n + \delta q$ with $\delta q \ll 1$, and are of particular interest both in tokamak and RFP configurations as it will be described in Chapter **3**. The theoretical study of low shear plasmas dates back to the mid 80's when JET sawtooth collapses were experimentally reported to be characterised by a radial displacement $\xi(r)$ which was smoother compared to the rigid displacement typical of the $m = 1$ internal kink (cf. Eq. (2.27)) [34, 35, 36]. Numerical computations of equilibria with very flat q in the central region of the plasma showed an approximately parabolic radial displacement [23], in agreement with experimental measurements in Ref. [36], suggesting an extended region of extremely low magnetic shear. A sketch of the displaced flux surfaces of a $m = n = 1$ mode in a finite and reversed shear configuration is shown in Fig. 2.6.

Tokamak hybrid plasmas are characterised by the absence of a $q = 1$ surface with a vanishing or weak magnetic shear and $q(0) \gtrsim 1$. Nevertheless, although this configuration usually ensures sawteeth-free discharges which is one of the key ingredients for long pulse discharges, MHD activity, both ideal and resistive, is still observed. As it will be shown in the next section, the ideal MHD activity in low shear plasmas, usually associated with pressure driven $m = 1$ modes, very often saturates to persistent Long Lived Modes (LLMs) which are experimentally observed

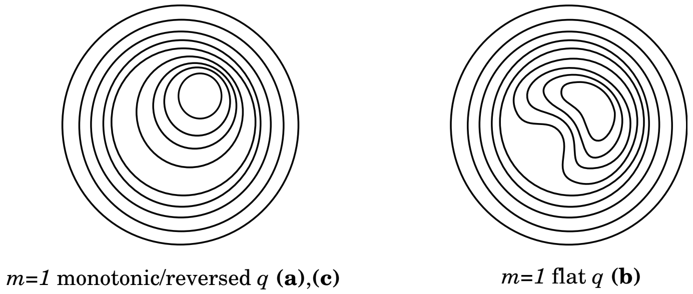

Figure 2.6: Shape of the flux surfaces corresponding to the monotonic and reversed q profiles (left, (a) and (c) in Fig. 2.3) and flat q (right, (b) in Fig. 2.3).

both in tokamaks and RFPs. A significant degradation of performance and braking of the core rotation is found to occur simultaneously with the appearance of the LLM [8]. The anomalous fast ion diffusion rate is enhanced and is increased by nearly a factor of two during the LLM phase and the loss rate of fast ions increases steadily after LLM onset [8].

Low shear plasmas are also prone to develop *Neoclassical Tearing Modes* (NTMs). For NTMs neoclassical effects play a crucial role in their dynamics. These modes are a high-β phenomenon, classically linear tearing stable ($\Delta' < 0$) [33, 37] and non-linearly unstable [33]. They are driven by helical holes in the bootstrap current arising from the local pressure profile flattening in the region of the island.[2] The onset of NTMs, which is one of the most serious concerns for future tokamaks, is the principal β limit in baseline scenarios such as ELMy H-modes in today's tokamaks. These modes occur on present tokamaks at normalised pressure values comparable to those envisaged for baseline scenarios in future devices, such as ITER, reducing confinement and sometimes causing disruptions [38]. We have generally two types of NTMs [5]: at intermediate β_N ($\beta_N = \langle\beta\rangle a B_\varphi / I_\varphi$, where $a[m]$ is the minor radius, $I_\varphi[MA]$ the plasma current, $B_\varphi[T]$ the toroidal field and $\langle\beta\rangle[\%]$ is the volume averaged normalised plasma pressure [6]) a 3/2 mode which degrades confinement is often observed. If β is increased, a 2/1 NTM is observed, which often causes disruptions [38, 39].

The evolution of NTMs is well described by the modified Rutherford equation, which reads [32, 40, 41] (classical and neoclassical/other effects are highlighted)[3]:

---

[2] The bootstrap current is a neoclassical toroidal current caused by the poloidal non-uniformity of the axisymmetric field which leads to an imbalance between passing and trapped particles which generates a net current proportional to the pressure gradient, namely $j_{bs} \approx -\varepsilon^{1/2} B_P^{-1} dp/dr$ [21, 42, 43].

$$\frac{\tau_R}{r_s}\frac{dw}{dt} = \underbrace{\Delta' - \alpha w}_{\text{Classical}} + \underbrace{\Delta'_{BS} + \Delta'_{GGJ} + \Delta'_{Pol} + \dots}_{\text{Neoclassical and other effects}}. \tag{2.54}$$

Low m modes, for which Δ' is not too negative, are more likely to be unstable, while high m modes require more field line bending for instability. The *"bootstrap"* contribution is contained in Δ'_{BS}. Additional effects such as localised heating and current deposition are not considered here.

At small island sizes the polarisation and the GGJ terms act to oppose the bootstrap drive, leading to the requirement of a critical island size or *"seed"* perturbation required in order to obtain neoclassical growth. If a *"seed"* island is formed and it has a width which exceeds a critical value w_{crit}, then the island is driven neoclassically and it increases its amplitude. The physical mechanism of the seeding of the island is not completely understood. The seed can be due to another MHD instability such as sawteeth, fishbones and Edge Localised Modes (ELMs) or further physical mechanisms, such as coupling to the NTM resonant surface [5, 40] (for example nonlinear three wave coupling has been invoked for the seeding of the island [46]).

2.6.1 Experimental motivation for investigations of ideal and resistive instabilities in low shear plasmas

In this section we present some experimental observations which underline the importance of studying the stability of hybrid-like plasmas. As we have seen in the previous sections, hybrid discharges, both in tokamaks and RFPs, are characterised by having an almost shear free or weakly reversed shear core region, where the extremum of the safety factor is close to a low order rational. In such discharges, it frequently occurs that ideal MHD instabilities eventually saturate giving rise to LLMs as shown in Fig. 2.7 [8]. The most commonly observed LLM in tokamaks is the saturated $m = n = 1$ mode which occurs when the q-profile is resonant or nearly resonant with $m/n = 1$, either with monotonic or shear reversed or flat q profiles (see Fig. 2.3). Similar regimes have also been reported in RFP hybrid plasmas (q slightly inverted) [7], where a dominant $m/n = 1/7$ mode develops for sufficiently high currents in

---

[3] The bootstrap, Glasser-Greene-Johnson (GGJ) and polarisation terms are given by

$$\Delta'_{BS} \sim \beta_P \frac{w}{w^2 + w_d^2}, \quad \Delta'_{GGL} \sim -\frac{\beta}{\sqrt{w^2 + 0.2 w_d^2}}, \quad \Delta'_{Pol} \sim -\frac{w}{w^4 + w_p^4},$$

where w_d and w_p account for small island width effects. The Glasser-Greene-Johnson term (Δ'_{GGJ}) [44] is always stabilising and it describes the geometrical effects due to the magnetic field curvature and it becomes relevant in low aspect ratio tokamaks. Finally the effects of the polarisation current, caused by perturbations in the electrostatic potential, are contained in Δ'_{Pol} [45].

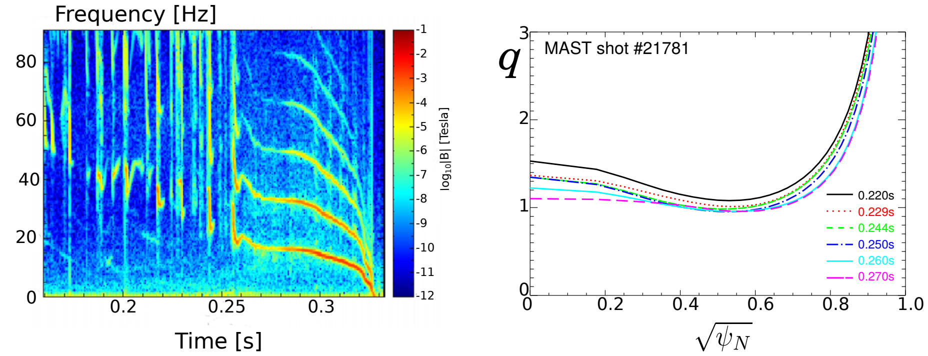

Figure 2.7: MAST frequency spectrogram of the MHD activity measured by Mirnov coils (left) and q-profile evolution (EFIT and MSE measurements) during the LLM phase (from $t \approx 0.25s$ to $t \approx 0.33s$). ψ_N is the normalised poloidal flux. Courtesy of I. T. Chapman et al. (2010).

RFX-mod. These non-linearly saturated ideal MHD modes can be regarded as a new equilibrium. These saturated equilibrium states have been modelled numerically by employing 3D equilibrium codes showing the possibility of the existence, besides the usual axisymmetric state and under particular conditions, of an internally kinked 3D helical equilibrium [17, 47]. A complete study of the behaviour of such instabilities has not yet been performed. Part of this thesis is therefore dedicated to comparing various approaches, both numerical and analytical, for the study of 3D helical kinked states, and consequently for improving our understanding of these near-resonant modes in both tokamak and RFP configurations [48, 49].

Fast growing NTMs are frequently observed experimentally directly after a major sawtooth crash (in particular the 2/1 and 3/2 mode) in JET (Joint European Torus) and in TCV (Tokamak á Configuration Variable) [40, 50]. This is clearly shown in Figs. 2.8 and 2.9.

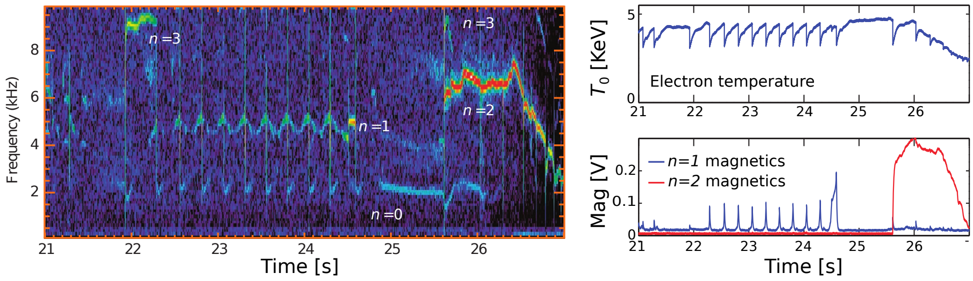

Figure 2.8: Spectrogram, central temperature and magnetic signal temporal evolution in JET shot #78772 showing the rapid rise of a $m/n = 3/2$ NTM right after the sawtooth collapse. Courtesy of J. P. Graves [50].

In JET and TCV plasmas the underlying mechanism for the seeding of (3/2) NTMs via sawteeth is speculated to be the toroidal coupling to $n = 2$ harmonics of the sawtooth precursor or the post cursor [40, 51]. We note that *hybrid-like* conditions

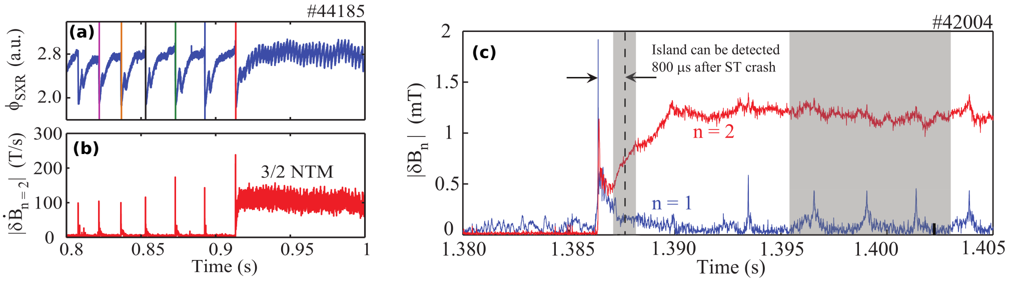

Figure 2.9: Soft X-ray emission (a)-(b) and $n = 2$ amplitude of the magnetic perturbations in TCV shot #44185. (c): $n = 1$ and $n = 2$ components of the magnetic fluctuation generated by the sawtooth crash in TCV shot #42004. Courtesy of G. P. Canal [40].

probably occur for a brief time after a sawtooth crash in baseline scenarios where it is found than $q = 1$ over a large region of the core following a fully reconnected sawtooth crash [52, 53]. Such types of NTMs are reported to grow within few milliseconds, almost on ideal timescales [40, 50]. Hence they are not compatible with the slow growth predicted by the linear tearing theory. Hence, we must go beyond standard tearing mode theory in order to explain the fast growth of these resistive instabilities In particular, NTMs have been experimentally observed without being seeded by another instability under plasma conditions with highly peaked currents [54] or large β [55]. The toroidal coupling between a fundamental helical (m, n) harmonic with its $(m \pm 1, n)$ sidebands could provide a feasible explanation for the triggering of NTMs [40], making unstable an otherwise stable mode with a negative Δ'. Usually the coupling is due to pressure gradients, implying that the threshold of these modes is dependent upon the plasma β, according to experimental measurements of the seeding of NTMs [40]. However, the measured fast growth of NTMs requires the additional ingredient of low shear in the core region.

We note in particular that if full reconnection occurs, the q profile is flattened over a large portion of the core plasma a sawtooth crash, so that the plasma is in hybrid-like conditions. Low-shear plasmas are prone to develop instabilities called *"infernal modes"* [56, 57]. These modes and are closely related to the quasi-interchange modes described by Wesson for the special $m = n = 1$ case [34]. This instability, in contrast to the conventional internal kinks, appears as a global mode which is not confined within the $q = 1$ surface [56]. As shown in Ref. [35], in low shear plasmas neighbouring Fourier harmonics couple non-locally, due to toroidicity and pressure gradients, to the fundamental mode in the region of vanishing magnetic shear (this coupling is stronger than for internal kinks). It will be shown in Chapters **4** and **5** that when resistive effects are taken into account, the poloidal harmonics coupled to the fundamental mode show a tearing character on the resonant $q = (m + 1)/n$ surface [58]. However, because of the inertia of the driving mode in the low-shear region, the growth of these tearing-like islands is on extremely fast timescales, much faster compared to the standard tearing mode ($\gamma \sim S^{-3/13}$ at ideal stability boundary see Chapter **4**) [58]. These sideband perturbations could be relevant for the NTM triggering by sawteeth, thus providing the required sufficiently fast growing seed island.

The hypothesis of the coupling between adjacent Fourier modes is also supported by measurements in recent TCV experiments, where the coexistence of an ideal 1/1 and a resistive 2/1 mode after a sawtooth crash in an EC-dominated scenario has been reported [59]. Regularly repeated internal $m = n = 1$ bursts located where the safety factor approaches unity, alternating with sawtooth crashes, have been measured. These bursts, whose lifetime is approximately $2ms$, are neither a pre- nor a post-cursor modes linked to crashes since they are events which are well separated in time (by $\sim 1ms$). A persistent $m/n = 2/1$ mode, whose amplitude varies irregularly, remains in the magnetics (see Fig. 2.10). The mode frequency of the 1/1 and the 2/1 perturbations is the same, so that we infer a coupling between these two modes. Because of the EC-heating, the suprathermal electron pressure rises rapidly during a phase in which the q profile is still flat in the centre after the sawtooth crash. The destabilisation of the 1/1 mode appears to be closely connected to the fast rise of p_e before a burst. These conditions are similar to those encountered in hybrid plasmas, thus leading us to invoke the existence of an *infernal-like* coupling (see Chapter **4**). Here the role of the driving and driven modes is exchanged with respect to what happens in the sawtooth triggering of NTMs [40].

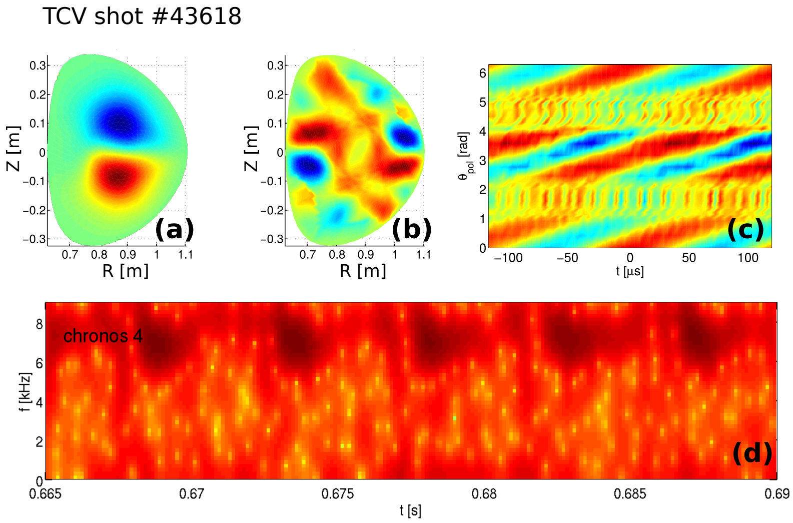

Figure 2.10: TCV shot #43618 ECRH-dominated: Spatial tomographic reconstruction from soft X-ray emission of the mode structure revealing the presence of a 1/1 and 2/1 harmonics (a)-(b); Mode period from conditional averaging of the poloidal Mirnov coil array (c); Spectrogram of the temporal reconstructed signal from soft X-ray emission (d). In ECCD scenarios, the time evolution and spatial structure are found to be similar, while the amplitude of the mode is increased. Courtesy of J. Kamleitner [59].

In conclusion, it is of extreme interest to develop a theory which accounts for toroidal coupling in hybrid plasmas under conditions in which resistive effects are taken into account. Inclusion of additional non-MHD effects such as two-fluid effects, resistivity and viscosity enable us to connect better with experimental measurements, and in addition provide novel scalings of the growth rate with resistivity.

3

Ideal MHD helical structures in hybrid-like (low shear) scenarios

In the present chapter we investigate kinked saturated $m = 1$ helical structures [49]. These structures are frequently observed in tokamak hybrid plasmas and in reversed field pinches (RFPs), occurring when an extremum in the safety factor is close to, but necessarily resonant with, a low order rational (typically $q_{min} \approx 1/1$ in tokamaks, and $q_{max} \approx 1/n$ in RFPs). If the exact resonance can be avoided, the essential [1] character of these modes can be modelled assuming ideal nested magnetic flux surfaces. The RFX-SHAx state is a typical example of a saturated $m = 1$ ideal mode [7], with helicity (1/7). The methods used in this chapter to characterise these structures include linear and non-linear ideal MHD stability calculations which evaluate the departure from an axisymmetric plasma state, or instead equilibrium calculations using a 3D equilibrium code. An analytic attempt for describing these helical states is also presented. The equilibrium calculations are performed by using the equilibrium VMEC code, while the XTOR-2F code is used in the ideal frame with diamagnetic effects switched off for studying ideal MHD stability and the nonlinear saturation of the modes. Three configurations are considered: ITER and MAST-like hybrid plasmas, together with RFX like configuration, all characterised by a slightly reversed safety factor [48, 49]. The extent to which these approaches agree in tokamaks and reverse field pinches are investigated, and compared favourably for the first time with an analytic non-linear treatment that is valid for arbitrary toroidal mode number.

---

[1] We will see that toroidal sidebands, which have their own rational surface in the plasma even if the rational surface of the main mode is avoided , are sensitive to resistivity, and the stability of the main mode is modified via toroidal coupling.

3.1 Introduction

As reported in the previous chapters, recent experiments have achieved good confinement and high beta limit in hybrid tokamak configurations [60, 61], where a large part of the plasma volume is characterised by low or weak reversed magnetic shear, in contrast with the standard tokamak operation with a monotonic q. Hybrid discharges however, are frequently affected by MHD activity becoming eventually ideal saturated modes [8]: the simplest of these Long Lived Modes (LLM), is the saturated $m = n = 1$ mode which requires high β and a q-profile which is resonant or nearly resonant with $m/n = 1/1$ (see Fig 2.7), as shown in Fig. 2.7 in Chapter **2** § 2.6.1 (cf Ref. [8]). As shown in the previous chapter, internal kink modes occur either with monotonic increasing safety factors [25, 26] (with a rational $q = 1$ in the plasma), or in shear reversed configurations where the minimum of the safety factor is close to unity [62, 63] or with an ultra-flat q-profile [34, 35] with $q \approx 1$ over an extended region.

Non-linearly saturated states of such 1/1 modes in tokamaks are conjectured as being novel kinds of equilibria [25, 62, 63]. Regimes similar to Long Lived Modes with dominant $m = 1,\ n = 7$ Fourier components, have also been experimentally found in non-tokamak machines, namely in RFPs [7], for sufficiently high values of the toroidal current density, in a reversed q configuration having the maximum of the safety factor close to the 1/7 resonance. Instead of treating such tokamak and RFP $m = 1$ modes as instabilities, the eventual stationary states have in recent years been modelled primarily using 3D equilibrium codes, such as VMEC [17, 18, 47], which minimises the plasma energy $\delta W = \delta \int \left(\frac{|B|^2}{2\mu_0} + \frac{p}{\Gamma - 1} \right) d^3x = 0$, where B is the modulus of the magnetic field, p the plasma pressure and Γ the adiabatic constant (a detailed description of the equations solved and the numerical procedure adopted in VMEC is given in Appendix **C** § C.1). These calculations demonstrate the presence of two distinct neighbouring equilibria. In addition to the usual axisymmetric state, a novel equilibrium has been found with an internally kinked 3D helical structure [17, 47], even when an axisymmetric plasma boundary is imposed.

The recently employed equilibrium approach for analysing 3D saturated states, and the approach of non-linear stability calculations of the 70's and 80's [24, 25, 62, 63] based on an originally axisymmetric equilibrium, have not yet been compared in detail, though initial attempts have been made [48, 49, 64]. Regarding the analytic approach to the problem, the theory of nonlinear saturated internal kink modes in the ideal MHD approximation was first studied by Rosenbluth *et al.* [25] who considered a monotonically increasing q profile, with a resonant $q = 1$ surface in cylindrical geometry. However hybrid discharges in tokamaks are characterised by having an almost shear free or weakly reversed shear core region, where the minimum of the safety factor is above unity ($q_{min} > 1$ so that there is no resonant $q = 1$ surface). The analytic linear theory for reversed q configurations for the internal (1/1) kink mode, which correctly includes toroidal correction to the plasma potential energy [26], was derived by Hastie *et al.* [23], while Avinash and Bussac [62, 63, 65] considered the analytical extension of the nonlinear theory for ideal saturated kinks ($m = n = 1$) for such configurations. Previous results hold also for configurations with non-monotonic safety factors and q_{min} less than unity providing that the $q = 1$ surface is not split into two distinct resonant layers. These analytic approaches to nonlinear stability have not been previously compared in detail to the two numerical approaches just mentioned.

The aim in this thesis is to develop a framework for comparing the various approaches to attaining 3D helical kinked states, and thereby improve our understanding of these near-resonant modes in both tokamak and RFP configurations [48, 49]. Fundamental to this is to extend the non-linear analytic treatment of $m = 1$ kink modes to arbitrary toroidal mode number n. A new resulting relation between potential energy δW, linear growth rate and non-linear kink displacement amplitude will enable the mechanisms of 3D saturated states to be identified (e.g. pressure, current or toroidal effects). This is especially true for cases where analytic growth rates agree with those from full simulations codes, and where the resulting displacement amplitudes also agree. In addition to this, it is important to analyse in detail the conditions for which the non-linear stability problem, just described, agrees and disagrees with the 3D equilibrium approach. While preliminary studies [48, 49, 64] have indicated good agreement for 1/1 tokamak cases when $q_{min} > 1$, the poor agreement for $q_{min} < 1$ is not properly understood. In this vein, by pursuing the 3D equilibrium free boundary approach for $q_{min} < 1$, and by perturbing the edge of the plasma with an $n = 1$ resonant magnetic perturbation, it is possible to see if this triggers a helical equilibrium branch that agrees better with the initial value 3D stability approach. The philosophy is to see if it is possible to obtain a helical state by adding an infinitesimally small perturbation when $q_{min} < 1$ (one would expect a helical equilibrium state for $q_{min} < 1$, since the axisymmetric equilibrium is classically Bussac-unstable for sufficient high β [26]). Here we attempt a basic variation of the resonant magnetic perturbation (RMP) edge perturbation amplitude. Finally, previous studies of helical states in RMPs have solely employed the 3D equilibrium code approach. We examine for the first time the agreement with stability calculations that commence from an axisymmetric equilibrium, and therefore naturally the mechanisms that ultimately lead to a saturated helical state, especially when compared to the analytic treatment.

The chapter is divided in four sections. Sections 3.2 and 3.3 present a brief review of the linear and nonlinear results, namely the derivation of the growth rate and the helical displacement amplitude for the $m = 1$ mode, with novel extensions to include arbitrary toroidal mode numbers. In the section 3.4 numerical equilibrium calculations are performed using the 3D equilibrium codes VMEC, while the nonlinear stability code XTOR-2F [66] is employed to assess the nonlinear behaviour of the $m = 1$ mode in the ideal frame (for the numerical procedure adopted in XTOR-2F see Appendix **C** § C.2). First we analyse the behaviour of the nonlinear saturation of the internal kink mode in an ITER hybrid configuration, comparing the results from XTOR-2F with VMEC predictions [48]. Then we focus on the study of the behaviour and the response of the saturated $m = n = 1$ mode for a MAST hybrid scenario, when a non axisymmetric external field is applied, whose amplitude is taken much smaller than the equilibrium magnetic fields. At the end of section 3.4 we present an analytic expansion of a 3D helical equilibrium. The results of which produce existence conditions of the equilibria observed in VMEC calculations.

Finally, we investigate the saturated $m = 1$ perturbations in RFP-like configurations, namely SHAx-like equilibria. Analytical results derived for large aspect ratio tokamak configurations are used for predicting the nonlinear state of the SHAx equilibrium using for the first time the three approaches outlined earlier.

3.2 Linear theory of the $m = 1$ mode (arbitrary n) with reversed shear

In this section we extend the linear internal kink calculation, summarised in Chapter **2** § 2.4.2, to include arbitrary n and reversed shear. The linear theory of the $m = n = 1$ mode in a reversed shear configuration (see Fig. 3.1-a), was first addressed by Hastie and Hender [23], in large aspect ratio approximation ($\varepsilon \ll 1$) for a circular cross section plasma. The approach is based on equating the plasma potential energy with

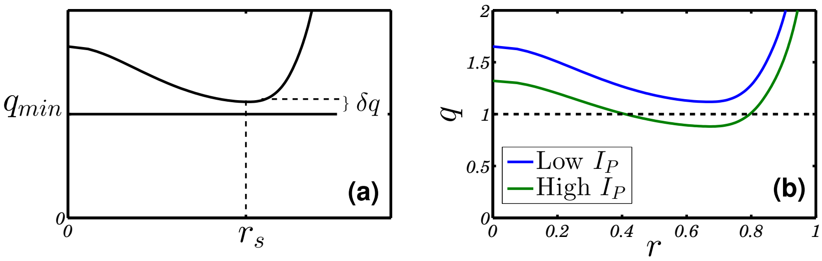

Figure 3.1: Typical shape of the safety factor of a hybrid tokamak configuration.

the kinetic energy of the perturbation, evaluated in the thin almost resonant $q = 1$ layer. It is known that in a tokamak, assuming a monotonic q, the plasma potential energy $\widehat{\delta W}$ can be expressed as a sum of cylindrical and toroidal contributions [26], i.e. (see Eq. (2.29) in Chapter **2** § 2.4.2):

$$\widehat{\delta W} \sim \left(1 - \frac{1}{n^2}\right)\widehat{\delta W}_C + \frac{1}{n^2}\widehat{\delta W}_T,$$

where we normalised $\delta W = \frac{2\pi^2 R_0 B_0^2 |\xi|^2}{\mu_0}\widehat{\delta W}$ [23, 63] (R_0 is the major radius, B_0 is the magnetic field on axis and ξ is the radial fluid displacement) and $\widehat{\delta W}_C$ and $\widehat{\delta W}_T$ are the cylindrical and toroidal contributions to the total energy respectively, which read [11] (valid for arbitrary n and q):

$$\widehat{\delta W}_C = B_0^{-2}\int_0^{r_s} dr \left[\frac{2(kr)^2\mu_0}{1+(kr)^2}\frac{dp_0}{dr} + \right.$$
$$\left. \frac{k^2r^3(\boldsymbol{k}\cdot\boldsymbol{B})^2}{1+k^2r^2} + \frac{2k^2r^3(\boldsymbol{k}\cdot\boldsymbol{B})}{(1+k^2r^2)^2}(kB^{\varphi} - B_\theta/r)\right], \tag{3.1}$$

$$\widehat{\delta W}_T = \frac{1}{16(b-c)}[8\sigma(b-c) + \frac{9}{4}(b-1)(1-c)$$
$$- 6(b-1)(c+3)(\beta_p+\sigma) - 4(c+3)(b+3)(\beta_p+\sigma)^2], \tag{3.2}$$

with:

$$\beta_p = -2\mu_0/B_\theta^2\int_0^{r_s}(r/r_s)^2 p' dr,$$

where $\boldsymbol{k}\cdot\boldsymbol{B} = B_\theta/r - nB_\varphi/R$, $k = -n/R_0$, p_0 is the equilibrium profile of the plasma pressure, a the plasma edge minor radius, $\sigma = \int_0^{r_s} dr(r/r_s)^3(1/q^2-1)$, $b = r_s d\log\xi/dr|_{r_s-}$ and $c = r_s d\log\xi/dr|_{r_s+}$. r_s is the radius closest to, or at, the rational surface, so that $q(r_s) \approx 1/n$ ($m = 1$ is always assumed). For $n = 1$, in order to get the correct growth rate, it is crucial to evaluate the toroidal contribution of the MHD potential energy, since the cylindrical contribution to δW vanishes. However for higher toroidal wave number which is relevant for $m = 1$ modes in RFPs, δW is well approximated by its cylindrical expression.

Near the rational surface, as seen in Chapter **2** § 2.4.2, the plasma inertia has to be considered. In this region it is sufficient to include only field line bending and inertia effects. Minimising the corresponding total energy $\delta W + \delta K$ in this region, we obtain (see Eq. (2.31)):

$$\frac{d}{dr}\left[\left(\frac{(1+2q^2)\gamma^2}{\omega_A^2} + (n/q(q-1/n))^2\right)\frac{d\xi}{dr}\right] = 0,$$

where we have used $\boldsymbol{k}\cdot\boldsymbol{B} = B_\varphi/R(1/q-n)$, $\omega_A = v_A/R_0$ is the Alfvén frequency and $1+2q^2$ is the Glasser-Greene-Johnson inertial enhancement factor [68]. Again following the matching procedure of Chapter **2** § 2.4.2, we obtain [23]:

$$\left(\int_{-\infty}^{\infty} \frac{dx}{(1+2q^2)\gamma^2/\omega_A^2 + \Delta q^2}\right)^{-1} = -\widehat{\delta W}$$

where $x = (r - r_s)/r_s$ and $\Delta q = |q_s - 1/n|$ (the subscript s indicates that the quantity is evaluated at $r = r_s$ which is the position of the shear reversal). We note that the expression above is valid also when the rational surface is avoided. This leads to the following expression for the growth rate for a non-monotonic q profile:

$$\bar{\gamma}\left[1 + \Delta q/\bar{\gamma}\right]^{1/3} = (r_s^2|q_s''|)^{-1/3}\left[-\pi\widehat{\delta W}\right]^{2/3}, \tag{3.3}$$

where $\bar{\gamma}^2 = [(1+2q^2)\gamma^2/\omega_A^2 + \Delta q^2]$. For a generic toroidal mode number n we have to perform the replacements $\gamma \to \gamma/n^2$ and $\delta W \to \delta W_C/(n^4 r_1^2/a^2)$. The formula above holds for q profiles having either $q_s'' > 0$ and $\Delta q > 0$, or $q_s'' < 0$ and $\Delta q < 0$: the first case refers to reversed shear tokamaks without an exact resonance, while the second is applied in RFPs configurations again without an exact resonance. Setting $\gamma = 0$ one finds:

$$\Delta q_c = 1/(2r_s^2|q_s''|)^{1/3}[-\pi\widehat{\delta W}]^{2/3} \tag{3.4}$$

which is the critical value of Δq below which the mode is unstable.

The expressions above can be used also to estimate the growth rate of $m = 1$ modes in RFPs configurations. Usually these modes have a large toroidal number n, simplifying significantly the algebra involved. Unlike the tokamak internal kink $m = n = 1$, if large toroidal mode numbers are considered ($n \gg 1$) the toroidal corrections $\widehat{\delta W}_T$ of Eq. (3.2) are higher order with respect to the cylindrical contribution ($(\delta W - \delta W_C)/\delta W \sim n^{-2}$). If the perturbed displacement is vanishing at the plasma edge, the plasma MHD potential energy δW_C is given by (2.23). Under the assumption that the leading order linear perturbed displacement ξ is a step function [21], we have for an $m = 1$ mode [21]:

$$\begin{aligned}\widehat{\delta W}_C = &B_0^{-2}\int_0^{r_s} dr\Big[\frac{2(kr)^2\mu_0}{1+(kr)^2}\frac{dp_0}{dr} + \frac{(kr)^2 B_\vartheta^2/r}{(1+(kr)^2)^2}(kQ+1)\times \\ &\times(kQ(3+k^2r^2) + k^2r^2 - 1)\Big],\end{aligned} \tag{3.5}$$

having defined $Q = R_0 q$ and $k = -n/R_0$. The value of the normalised plasma MHD energy $\widehat{\delta W}_C$ is evaluated numerically by integrating the formulae above with the input profiles for pressure and poloidal field. The corresponding growth rate is obtained from equations (3.3) and (3.5). This results allow us to examine the linear properties of both tokamak and RFP configurations.

3.3 Nonlinear internal kink mode for arbitrary n and reversed shear

In a thin layer close to r_s nonlinear effects are evaluated in the cylindrical approximation. By following the same steps presented in the previous chapter, we introduce a coordinate system (r, ϑ, φ) were r is the radial variable and ϑ and φ are the poloidal and toroidal angles. The toroidal projection of the curl the pressure balance equation $\boldsymbol{\nabla} p = \boldsymbol{J} \times \boldsymbol{B}$ gives $\boldsymbol{B} \cdot \nabla J_\varphi = 0$ (cf. Eq. (2.37)) which leads to $\psi_*'' = J_\varphi(\psi_*)$ [25, 62, 63], where J_φ is the toroidal component of the current density and ψ_* is the helical flux defined as $\psi_* \sim \int (q/q_s - 1)dr$. For sake of simplicity we set $\varphi = 0$. Integrating the equation for ψ_* we recover Eq. (2.39), i.e.:

$$\frac{d\psi_*}{dr} = [f(\psi_*) + g(\vartheta)]^{1/2}. \tag{3.6}$$

The uncompressibility constraint $(\boldsymbol{\nabla} \cdot \boldsymbol{\xi} = 0)$, implies the area conservation in the poloidal plane, i.e. $\int r dr d\vartheta = const.$ (cf. Eq. (2.38)). The ordering of the relevant quantities is $(\varepsilon = r_s/R_0 \ll 1)$:

$$a_0^2 q_s'' \sim 1, \quad \widehat{\delta W} \sim \varepsilon^2, \quad \Delta q \sim \varepsilon^{4/3}, \quad \delta/a_0 \sim \varepsilon^{2/3},$$

where δ is the width of the layer and a_0 is the minor radius. As in the previous chapter, assuming that $r(x, \vartheta) = r_s + x + \xi(r, \vartheta)$, we expand the perturbed helical flux in a neighbourhood of r_s, so that at leading order rescaling ψ_* we have $(x \sim \delta)$:

$$\frac{\partial \psi_*}{\partial x} = (a^2 + x^2),$$

where $a^2 = 2\Delta q / q_s''$. The equation for the area conservation (cf. Eq. (2.38)) is now written in terms of the functions f and g in Eq. (3.6):

$$\frac{1}{2\pi} \int \frac{a^2 + x^2}{\sqrt{f(x) + g(\vartheta)}} d\vartheta = 1. \tag{3.7}$$

For large x, the equation above implies that $f \to x^4$. Thus the function f is expanded as $f(x) = x^4 + c_1 x^3 + c_2 x^2 + c_1 x + c_4 + ...$ Expanding (3.7) we have that $c_1 = c_3 = 0$, while $c_2 = 2a^2$ and $c_4 = a^4 - \frac{1}{2\pi} \int_0^{2\pi} g d\vartheta$. We do not consider the $m = n = 0$ mode, hence $\int_0^{2\pi} g d\vartheta = 0$. Following the same steps presented in Chapter **2** § 2.4.2 for the calculation of the nonlinear displacement with a monotonic q, using the results just obtained for the function f, we obtain for large x:

$$\xi(x, \vartheta) = \pm \int_0^\infty d\tilde{x} \left(\frac{a^2 + \tilde{x}^2}{\sqrt{f(\tilde{x}) + g(\vartheta)}} - 1 \right) + h(\vartheta) + \frac{g(\vartheta)}{6x^3}, \tag{3.8}$$

where the sign $+(-)$ stands for $x \to +(-)\infty$.

The expression above is matched with the linear eigenfunction in the outer region, which is obtained integrating Eq. (2.31) twice after dropping inertia, whose behaviour in the limit $r \to r_s$ and with a generic φ is given by (here $x = r - r_s$):

$$\xi = \begin{cases} \left[\xi_0 - \dfrac{4}{3}\dfrac{\xi_0}{r_s}\dfrac{\widehat{\delta W}/n^4}{(q_s'')^2}\dfrac{1}{x^3}\right]\cos(\vartheta - n\varphi), \quad r < r_s \\ -\dfrac{4}{3}\dfrac{\xi_0}{r_s}\dfrac{\widehat{\delta W}/n^4}{(q_s'')^2}\dfrac{1}{x^3}\cos(\vartheta - n\varphi), \quad r > r_s. \end{cases} \tag{3.9}$$

Equation (3.9) is now matched with (3.8), providing a matching condition for g. Hence we obtain $g(\vartheta)/6 = -\frac{4}{3}\frac{\xi_0}{r_s}\frac{\widehat{\delta W}/n^4}{(q_s'')^2}\cos\vartheta$. This yields the following equations (here $\hat{x} = x/a$, $\hat{f} = f/a^4$ and $\hat{g} = g/a^4$) [63]:

$$\int_0^\infty dx\left(\frac{1+\hat{x}^2}{\sqrt{\hat{f}(\hat{x}) + \hat{g}(\vartheta)}} - 1\right) = -\mu\cos\vartheta, \tag{3.10}$$

$$\tfrac{1}{2\pi}\oint d\vartheta(\hat{f}(\hat{x}) + \hat{g}(\vartheta))^{-1/2} = (1+\hat{x}^2)^{-1}, \tag{3.11}$$

$$\tfrac{1}{2\pi}\oint d\vartheta\hat{g}(\vartheta)\cos\vartheta = -\frac{\xi_0\widehat{\delta W}/n^4}{r_s\Delta q^2}, \tag{3.12}$$

where $\mu^2 = \frac{\xi_0^2 q_s''}{8\Delta q}$. Since $\mu^2 \sim \xi_0^2 q_s''/\Delta q \ll 1$, we expand $\hat{f}$ and $\hat{g}$ in a power series in μ, i.e. $\hat{f} = \hat{f}_0 + \mu\hat{f}_1 + ...$ and $\hat{g} = \mu\hat{g}_1 + ...$ up to order μ^3. Hence from (3.11) we obtain ($\langle(\;\cdot\;)\rangle = 1/2\pi\oint(\;\cdot\;)d\vartheta$):

$$\hat{f} = (1+\hat{x}^2)^2 + \tfrac{3}{4}\frac{\langle\hat{g}_1^2\rangle}{(1+\hat{x}^2)^2}\mu^2 + \tfrac{3}{2}\frac{\langle\hat{g}_1\hat{g}_2\rangle}{(1+\hat{x}^2)^2}\mu^3 + ...,$$

where we used the constraint $\int_0^{2\pi} g d\vartheta = 0$ and the assumption that $\langle g_i^{2n+1}(\vartheta)\rangle = 0$ with $n = 1, 2, 3, ...$. Using (3.10), the terms of the same order in μ are grouped together, so that:

$$\begin{aligned} g_1(\vartheta) &= \tfrac{8}{\pi}\cos\vartheta, \\ g_2(\vartheta) &= \tfrac{15}{32}(\hat{g}_1^2 - \langle\hat{g}_1^2\rangle), \\ g_3(\vartheta) &= -\tfrac{3}{1024}[105\hat{g}_1^3 - 189\hat{g}_1\langle\hat{g}_1^2\rangle + 320(\langle\hat{g}_1\hat{g}_2\rangle - \hat{g}_1\hat{g}_2)]. \end{aligned}$$

It is easy to see that equation (3.12) implies that $\langle(\hat{g}_1 + \mu^2\hat{g}_3)\cos\vartheta\rangle = \frac{4}{\pi}(\Delta q_c/\Delta q)^{3/2}$, which can be written in the following form:

$$\xi_0^2\frac{q_s''}{\Delta q} = \frac{8}{71}\left(\frac{8\pi}{3}\right)^2\left[\left(\frac{\Delta q_c}{\Delta q}\right)^{3/2} - 1\right], \tag{3.13}$$

where Δq_c is defined in terms of δW by Eq. (3.4).

In order to estimate the $m = 1$ shift when q approaches unity, it is convenient to express the equation above in terms of the growth rate γ. There are two regimes of interest: in one case we have $\gamma \ll \Delta q$ (marginal stability) and another where $\gamma \gg \Delta q$ (strong instability). Expanding in the parameter $\gamma/\Delta q$ by means of (3.3) for both cases, we obtain the following relation:

$$\frac{\xi_0^2|q_s''|}{\Delta q} \approx \begin{cases} \frac{5}{71}\left(\frac{8\pi}{3}\right)^2 \frac{(1+2q_s^2)\gamma^2}{n^4\Delta q^2\omega_A^2}, & \gamma \ll \Delta q, \qquad (3.14a) \\ \frac{8}{71}\left(\frac{8\pi}{3}\right)^2 \left(\frac{\sqrt{1+2q_s^2}\gamma}{n^2\Delta q\omega_A}\right)^{3/2}, & \gamma \gg \Delta q. \qquad (3.14b) \end{cases}$$

We note that Eq. (3.14b) diverges when $\Delta q = 0$. Following the same steps used before, but setting $a = 0$, the displacement for the case $\Delta q = 0$ reads;

$$\xi_0 = \frac{1}{\pi^{1/3}}\sqrt{\frac{\Delta q_c}{2q_s''}}\langle\tilde{g}\cos\vartheta\rangle^{-1/3}, \tag{3.15}$$

where $\langle\tilde{g}\cos\vartheta\rangle$ is found via a variational principle and a simple numerical estimate gives $Max(\langle\tilde{g}\cos\vartheta\rangle) = 0.0089$ [63]. The formulae above will be used for the estimate of the nonlinear helical displacement of a MAST $n = 1$ hybrid scenario and compared with XTOR-2F nonlinear simulation. These results will be also used to examine the nonlinear properties of $n = 7$ SHAx equilibrium in RFX configurations.

3.4 Ideal saturated $m = 1$ kinks in tokamaks

3.4.1 Ideal kink instabilities in ITER-like scenarios

The simplest long lived mode, in hybrid scenarios, is the saturated internal kink. In this section we focus our attention to the numerical study of such MHD activity investigating the relation which occurs between MHD modes and the shape of q profile (i.e. density current profile). The amplitude of the helical distorsion computed by VMEC (the typical profiles for pressure, safety factor and current density which correspond to such situation for an ITER-like equilibrium are shown in Fig. 3.2) depends on the value of the total plasma current which is related to the value of the edge safety factor and consequently to q_{min} (the minimum of the safety factor decreases when the current is increased as shown in Fig. 3.1-b). The key parameter for determining the strength of the helical state is the displacement of the magnetic axis δ_h: in the VMEC equilibrium code this distorsion is quantified by:

$$a\delta_h = \sqrt{R_{01}^2 + Z_{01}^2}, \tag{3.16}$$

where a is the plasma minor radius and the subscripts indicate the $m = 0$ and $n = 1$ Fourier components. It is found that if q_{min} drops below a critical value, the equilibrium helical state merges with the axisymmetric state (see Fig. 3.4).

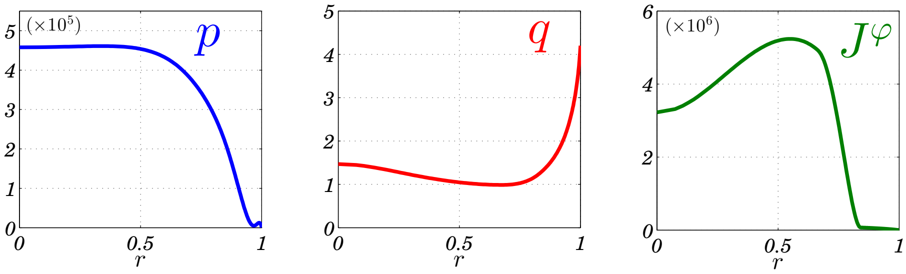

Figure 3.2: Pressure (Pascal) and q profiles for ITER-like hybrid plasma VMEC simulations. The corresponding profile of the toroidal current density (Ampére/m^2) is also shown, with $r = \sqrt{\psi/\psi_{edge}}$ (ψ is the toroidal flux).

Our aim in this section is to compare 3D equilibrium VMEC numerical simulations [47] for ITER like equilibria with hollow q, with the results computed by the nonlinear MHD stability code XTOR-2F [66] in the ideal frame. XTOR-2F simulations are performed starting from a given 2D (i.e. axisymmetric) ITER like equilibrium ($\beta \approx 3\%, 0.96 < q_{min} < 1.03$), with the same profiles which give rise to the 3D helical cores [47] prepared with the 2D equilibrium code CHEASE [69]. A scan in the current, ranging from 13.2 to 13.8 MA, is performed and the associated saturated state is shown in figure 3.3.

In order to quantify the displacement of the magnetic axis in the XTOR-2F simulations and compare it with δ_h given by Eq. (3.16), we adopt the following definition for the helical displacement of the flux surfaces in XTOR-2F::

$$a\delta_h = \sqrt{\left[R_{ax}\left(\varphi = 0\right) - R_{ax}\left(\varphi = \frac{\pi}{2}\right)\right]^2 + Z_{ax}^2\left(\varphi = \frac{\pi}{2}\right)}, \tag{3.17}$$

where $R_{ax}(Z_{ax})$ is the $R(Z)$ position of the magnetic axis and φ denotes the toroidal angle (in XTOR-2F we have $Z_{ax}(\varphi = 0) = 0$). If we decompose in Fourier harmonics the R and Z coordinates of the magnetic axis, it is immediate to see that the expression above reduces to Eq. (3.16), indeed:

$$R = R_0 + R_{0,1}\cos\varphi + R_{0,2}\cos 2\varphi + ...$$
$$Z = Z_0 + Z_{0,1}\sin\varphi + Z_{0,2}\sin 2\varphi + ...,$$

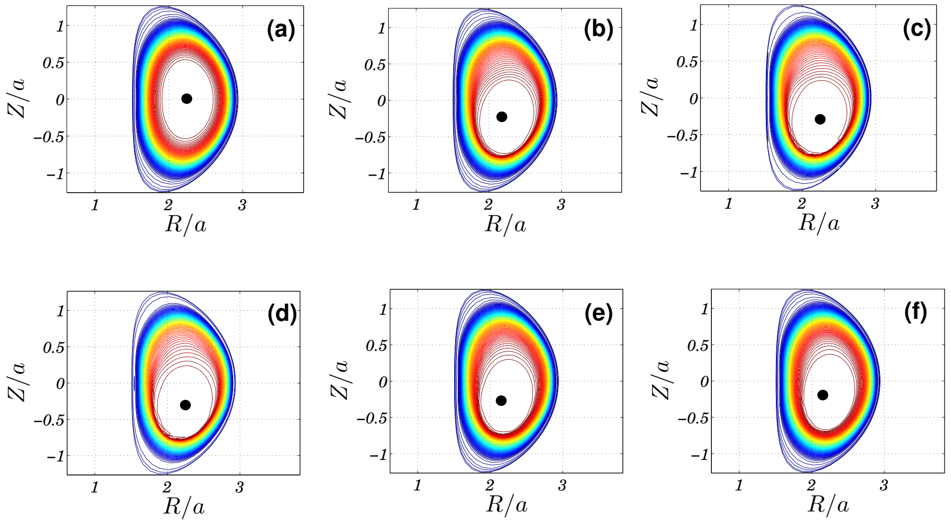

Figure 3.3: Contour of constant pressure surfaces at fixed toroidal angle $\varphi = 3/2\pi$ for saturated internal kink mode evaluated by XTOR-2F starting from a VMEC equilibrium, with toroidal plasma current (a) 13.0 MA, (b) 13.3 MA,(c) 13.4 MA, (d) 13.5 MA, (e) 13.7 MA, (f) 13.8 MA; a denotes the plasma minor radius. The position of the magnetic axis is marked by the thick black dot.

so that, assuming that $Z_0 = 0$ and $R_{0,n}/R_{0,1} \sim \varepsilon$ for $n > 1$, we have at leading order $R_0 = R(\varphi = \pi/2)$, $R_{0,1} = (R - R_0)(\varphi = 0)$ and $Z_{0,1} = Z(\varphi = \pi/2)$.

It is found that both VMEC and XTOR-2F results predict the presence of kink-like 3D structures. When the minimum of q is above the unity (low currents), the helical distorsion δ_h computed numerically with XTOR-2F shows good agreement with the results provided by the 3D equilibrium simulations performed using VMEC and presents a reasonable agreement with the analytical predictions for the non-linearly saturated kink given by Eq. (3.13) [63] (here $' \equiv \partial/\partial_r$):

$$\xi_h^2 q''(r_1) = \frac{8}{71}\left(\frac{8\pi}{3}\right)^2 \Delta q \left(\sqrt{\frac{1}{2}\left(\frac{3\gamma^2}{\omega_A \Delta q^2} + 1\right)\left[\sqrt{\frac{3\gamma^2}{\omega_A \Delta q^2} + 1} + 1\right]} - 1\right)_{r_1}, \quad (3.18)$$

or the Rosenbluth (cf. Eq. (2.45)) result which was obtained for a monotonic q [25]:

$$\xi_h q'(r_1) = \frac{13\sqrt{3}}{\pi} \frac{\gamma}{\omega_A}\bigg|_{r_1}, \quad (3.19)$$

where we recall that ξ_h is the radial displacement, $\omega_A = v_A/R_0$ with v_A the Alfvén velocity, R_0 the major radius, γ is the linear growth rate of the internal kink mode, $\Delta q = |q_{min} - 1|$ and r_1 is the position of the resonant $q = 1$ surface. In the above equations, we included the Glasser-Greene-Johnson inertia enhancement factor.

Equation (3.18) derives from the calculation of the nonlinear $m = n = 1$ saturated kink mode for non-monotonic q profiles with reversed shear having $q_{min} \approx 1$ at $r = r_1$, i.e. equation (3.13) [63]. By expanding Eq. (3.18) in terms of γ, we recover Eqs. (3.14a), (3.14b) and (3.15). Equation (3.19) is nominally valid for the $m = 1$ mode for monotonic safety factor profiles with the $q = 1$ surface at $r = r_1$ [25]. However, this equation can be used also for non-monotonic safety factors with two resonant $q = 1$ surfaces at $r = r_1$ and $r = r_2$ with $r_1 < r_2$: if $q'(r_1) < 0$, it follows that the $m = 1$ mode at that position is stable. This is because the growth rate of the $m = 1$ mode located at $r = r_1$ scales as $\gamma \sim (dq/dr)_{r_1}^{-1}[-\delta W^T]$ [26]. Hence the mode is unstable at $r = r_2$ where $q' > 0$, so that Eq. (3.19) can be used. However, when $q_{min} < 1$ we found that the analytical predictions almost agree with the nonlinear results, but there is a significant deviation between the 3D equilibrium calculations and the nonlinear simulations: while the helical distorsion predicted by VMEC decreases to 0 when $q_{min} \approx 0.96$, XTOR-2F gives a residual distorsion in this region (as shown in figure 3.4) which is consistent with earlier [70, 71] linear stability calculations performed with the TERPSICHORE code. Indeed this is to be expected because the analytic linear internal kink mode of Bussac [26] is unstable. A convenient value for

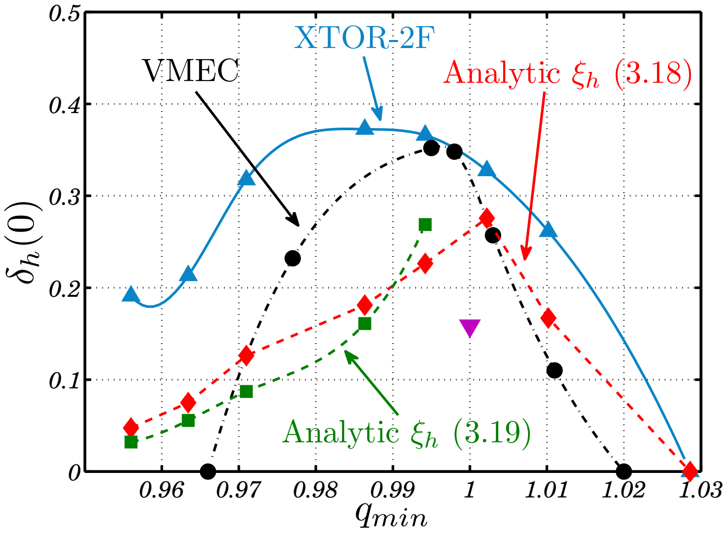

Figure 3.4: Helical distorsion of the magnetic axis for an ITER like scenario as a function of the minimum of the safety factor q. The black line shows the VMEC results , while the blue curve refers to the nonlinear XTOR-2F simulations. The red and green lines correspond to the analytical predictions given respectively by (3.18) and (3.19). The magenta upside down triangle is the theoretical prediction of ξ_h given by Eq. (3.15) when $q_{min} = 1$.

the viscosity was chosen in order to avoid numerical instabilities in the core region; however, even if the growth rate for the $m = n = 1$ mode is not so sensitive to variations in the viscosity ν [72], we should take care of this parameter, since its value can affect significantly the behaviour of $n \neq m$ modes, allowing unphysical modes to grow, as shown in Fig 3.5 (the unphysical modes are the $n = 5$ and $n = 4$).

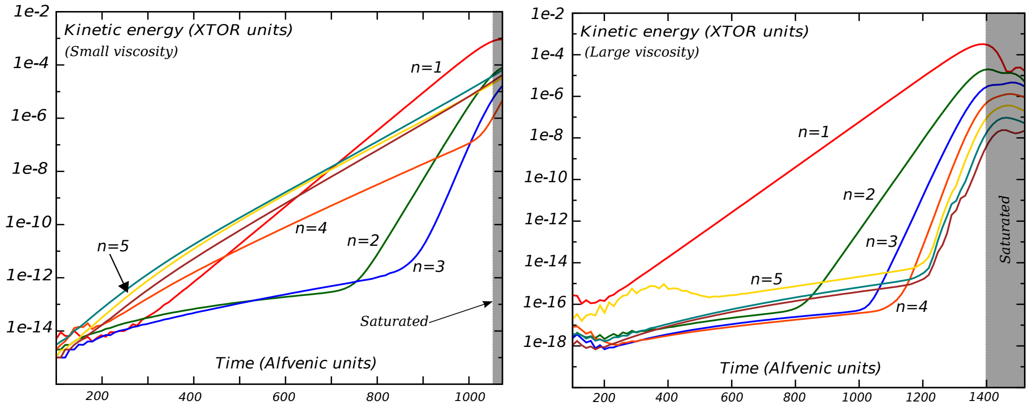

Figure 3.5: Behaviour of the kinetic energy for $n = (1, ..., 9)$ modes for two different values of the viscosity ($\nu = 3 \times 10^{-6}$(XTOR-2F units) in the left picture and $\nu = 5 \times 10^{-5}$(XTOR-2F units) in the right one); the other equilibrium parameters were kept the same for both simulations. We can clearly see that the $n = (4, 5)$ is strongly suppressed in the linear phase. We notice also that (around 1000 alfvenic times in the picture on the right) the growth rate γ for $n > 1$ modes is given by $\gamma_{n>1} = n\gamma_{n=1}$ [73] as expected by toroidal couplings.

3.4.2 Helical state response to RMP fields in MAST-like hybrid plasmas

In this section we present numerical simulations from VMEC and XTOR-2F for a MAST-like plasma (all VMEC runs are performed in stellarator symmetric geometry, i.e. with two up-down symmetric toroidal planes at $\varphi = 0$ and at $\varphi = \pi$). For the VMEC equilibrium simulations we provide as input the vacuum magnetic field configuration, pressure and either current or iota profiles: a careful choice of the rotational transform, defined as $\iota = 1/q$, is required in order to prevent unphysical negative currents. The profiles used in the simulations are shown in figure 3.6: the pressure profile is chosen to be approximately parabolic with respect to the square root of the normalised toroidal flux denoted by s. The iota profile is modelled in order to be consistent with realistic MAST discharges. The value of q_{min} is modified by shifting the safety factor up and down rigidly. The minimum value of the safety factor has been chosen to vary between 0.92 and 1.06 corresponding to a variation of the total plasma current I_p between 0.5 (large q_{min}) and 0.8 (small q_{min}) MA. The total β is about 5% while $\beta_p \approx 0.5$. The normalised β is given by $\beta_N = \langle\beta\rangle[\%]a[m]B_T[T]/I_p[MA] \sim 3$, where B_T is the toroidal magnetic field calculated on the magnetic axis and the angular brackets indicate the volume average. The plasma edge is approximately axisymmetric for all the values of the current. All simulations are performed having a discretisation in the radial direction of 210 grid points, while in the poloidal and toroidal angles we take 41 and 25 grid points

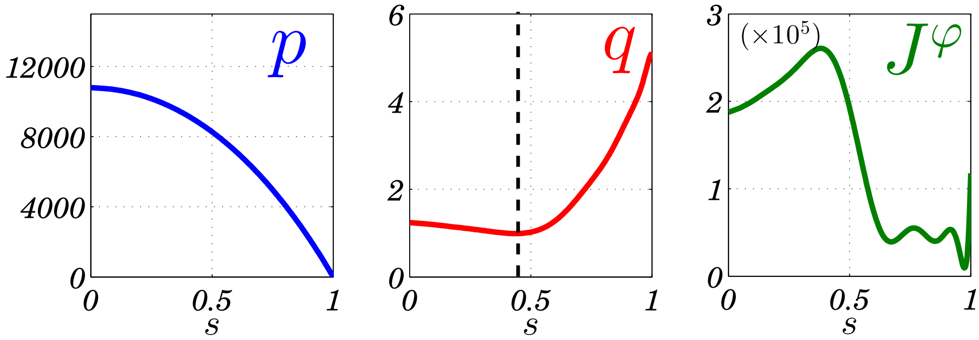

Figure 3.6: Pressure (Pascal) and q profiles used as input for the VMEC simulations. The corresponding profile of the toroidal current density (Ampére/m^2) is also shown. Here $s = \sqrt{\Phi/\Phi_{edge}}$ where Φ is the toroidal flux. The radial position of q_{min} is indicated by the vertical dashed line.

respectively. The Fourier spectrum is composed of 8 poloidal modes and 4 toroidal modes.

In order to run the nonlinear stability code XTOR-2F [66], we prepared a MAST 2D VMEC equilibrium where the pressure and iota (current profiles) are those which produced the equilibrium helical state. The simulation is performed in a free boundary configuration with an axisymmetric vacuum field; afterwards the VMEC output is interfaced with the 2D equilibrium solver code CHEASE [48, 69]. All the non-linear simulations with the code XTOR-2F are performed in the ideal MHD frame: non-ideal effects like resistivity, diamagnetism, neoclassical corrections etc., are switched off. We point out that even when the dominant rational surface is avoided ($q_{min} > 1$), resistivity may play an important role on the smaller sidebands. In this chapter we drop resistive effects, which will be analysed in detail in Chapters **4** and **5**. In particular, and in connection with experimental interest, future work is planned to assess the plasma behaviour in a resistive frame, even when the dominant rational surface is avoided, so that resistivity plays a role only on the smaller sidebands. The effects of viscosity are however necessarily retained in XTOR-2F in order to smooth out numerically induced structures. Viscosity (μ) is kept sufficiently small in order to have, for a strongly unstable mode, a weak dependence of the growth rate on the viscosity [66]. The chosen value for the normalised viscosity is $\bar{\mu} = \tau_A \mu / a^2 = 2 \times 10^{-5}$, where τ_A is the Alfvén time and a is the plasma minor radius. The results of nonlinear XTOR-2F saturated state and 3D equilibrium simulations (with an axisymmetric vacuum field) are shown in figure 3.7 for the case $q_{min} \approx 1$ (0.99). The agreement is good providing $q_{min} \geq 1$, but equilibrium calculations do not predict helical states if q_{min} is sufficiently less than unity [64]. Therefore it has been chosen to apply an external $n = 1$ RMP field in order to assess the behaviour of the internal $m = 1$, $n = 1$ kink mode. The idea is to see whether the equilibrium code will jump to a strong helical solution if it is perturbed slightly at the edge. Indeed, it is believed that for $q_{min} < 0.94$ the equilibrium code approach is incorrect

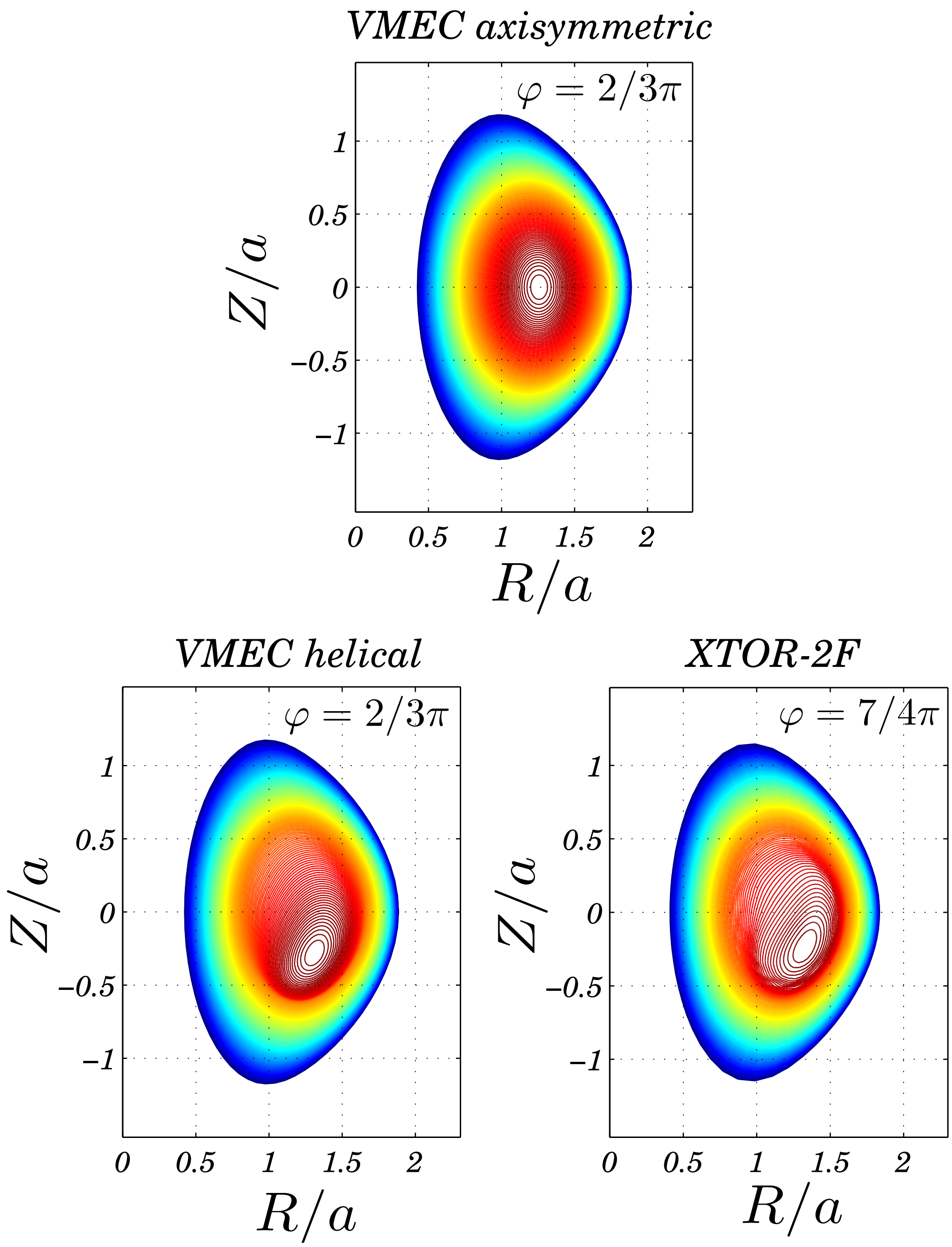

Figure 3.7: Contour of the constant pressure surfaces for MAST case. The top figure shows the VMEC axisymmetric configuration; the figures on the bottom left and on the bottom right show the VMEC helical branch and the non-linearly saturated internal kink from XTOR-2F respectively. Here $q_{min} \approx 0.99$, a value for which the helical displacement reaches its maximum value.

in giving only an axisymmetric solution. Indeed when $q_{min} \ll 1$, the ideal internal kink mode is always strongly linearly unstable (for sufficiently large β) [26], and we expect a large helical displacement. However, VMEC does not produce 3D equilibria for $q_{min} \ll 1$. The discrepancy between VMEC and XTOR occurs when there is a $q = 1$ resonance in the plasma. The solution in XTOR includes inertia, while VMEC does not, and as a result, the current sheets occurring at $q = m/n = 1/1$ will be handled differently. XTOR eigenfunctions in particular are smoothed by inertia.

The nominal amplitude of the external perturbation in MAST is $\delta B_{RMP}/B_{vac} \sim 10^{-4}$, and it is controlled by the current in the RMP coils (I_{RMP}). B_{vac} represents the strength of the axisymmetric vacuum magnetic field. Figure 3.8 shows the displacement of the magnetic axis as a function of the minimum value of the safety factor q. The red curve shows the VMEC displacement with an axisymmetric external field, while the predicted δ_h with an $n = 1$ RMP field at nominal current value is represented by the blue curve. With no RMP external perturbation, i.e. with axisymmetric boundary, previous results analogous to ITER fixed axisymmetric boundary are recovered [48, 64]. We note that the window in q_{min} in which helical states are produced with VMEC (for RMP off), is wider than for the ITER case presented in [48], mainly due to the fact that MAST has a tighter aspect ratio. Table

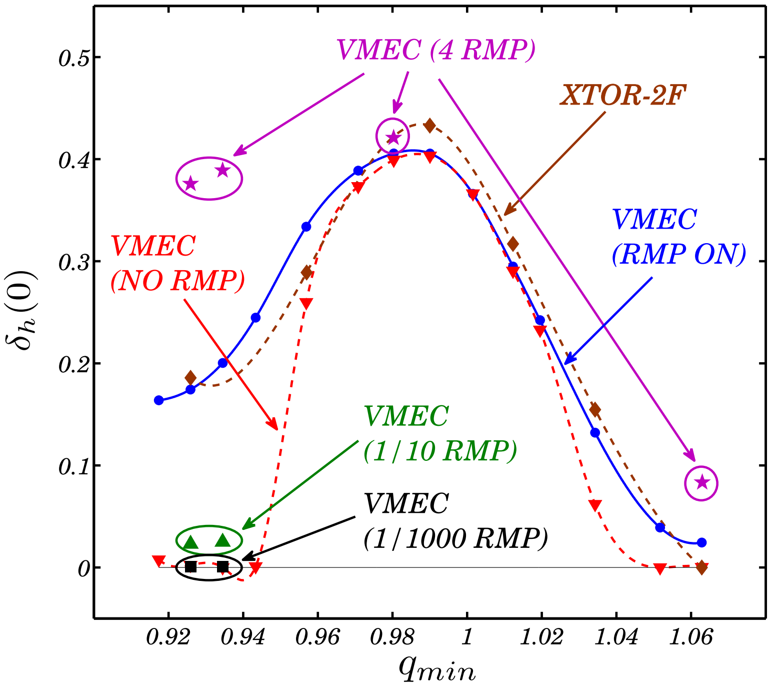

Figure 3.8: Amplitude of the helical displacement computed with VMEC with RMP off (red curve) and RMP on (blue curve). The scattered points have either the RMP perturbation increased or reduced.The results of the nonlinear simulations performed using XTOR-2F are represented by the brown dashed curve.

q_{min}	0.93	0.96	0.99	1.00	1.01	1.03	1.06
ξ_h/a [Eq. 3.18, 3.15]	5×10^{-2}	0.093	0.21	0.23	0.21	0.075	0
ξ_h/a [Eq. 3.19]	0.027	0.091	0.338	-	-	-	-

Table 3.1: Analytic values for ξ_h/a [25, 62, 63]

3.1 shows the analytic estimates of the nonlinear displacement ξ/a obtained using Eq. (3.14a) (Eq. (40) in Ref. [63]).

With an RMP perturbation present, δ_h agrees well with the nonlinear XTOR-2F results, having a persistent displacement even when q_{min} drops below unity. However the amplitude of the VMEC displacement depends on the strength of the external field applied. By varying the coil current I_{RMP} we induce a variation in the external perturbation. By reducing the RMP current by a factor 10 and 1000, the displacement δ_h decreases and eventually the results obtained in an axisymmetric boundary configuration are recovered. On the other hand, by increasing I_{RMP} the value of δ_h increases strongly for $q_{min} < 1$. It is important to note that an asymmetry in the regions $q_{min} > 1$ and $q_{min} < 1$ occurs if the RMP current is either increased or decreased. For $q_{min} \geq 1$ the displacement is not strongly affected by the external perturbation. Conversely for $q_{min} < 1$ the VMEC δ_h can either disappear or it can become unphysically large with external perturbations too big. This strong dependence on the RMP amplitude suggests that the helical state produced by VMEC is not assisted by an infinitesimal perturbation of the edge for $q_{min} < 1$. Nevertheless, the RMP can be used to produce a helical core of the desired amplitude for secondary studies such as fast ion confinement [74], where the correct helical amplitude would be identified by e.g. XTOR-2F.

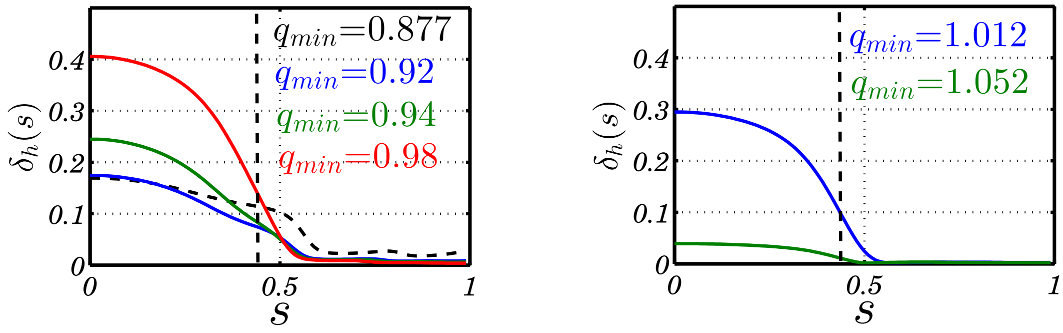

Figure 3.9: Radial profile of the helical displacement $\delta_h(s)$ deduced from VMEC with RMP-on at nominal value. The location of the minimum of the safety factor is located in position $s = 0.44$ as indicated by the thick dashed vertical line.

Employing the nominal RMP amplitude, figure 3.9 shows the profile δ_h from VMEC as a function of the radial variable s for different values of q_{min}. We regard δ_h as a measure of the fluid displacement of the flux surfaces with respect to a axisymmetric configuration. Thus δ_h is directly proportional to the radial fluid displacement ξ_r [26]. It is important to note here that the shape of the *eigen-displacement* δ_h is smoother than the classical top-hat function expected for a kink instability, resembling more a saturated quasi-interchange mode rather than an internal kink [34, 35]. The fact that the mode departs strongly from a step function has implications on the validity of the analytic treatment of sections 3.2 and 3.3. However, in the next section it is seen that good agreement is found for a weakly kinked (virtually top-hat) RFP $n = 7$, $m = 1$ mode.

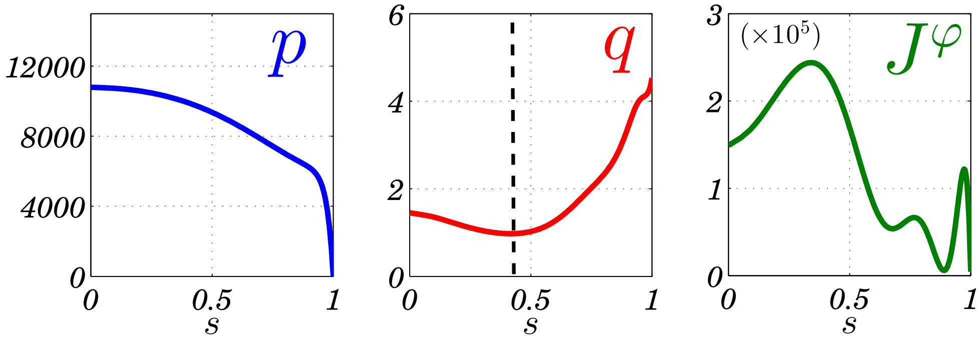

Figure 3.10: Pressure (Pascal) and current density (Ampére/m^2) profiles used as input for the VMEC simulations. The corresponding profile of the safety factor is also shown. The radial position of q_{min} is indicated by the vertical dashed line.

Finally in Figs. 3.10 and 3.11 we present 3D free boundary equilibrium simulations of a MAST H-mode plasma, with profiles shown in Fig. 3.10. The result differs from what has been shown so far because very strong edge displacements are caused by a helical core which can propagate to the edge because of sharp pressure and current gradients at the edge. The results are from a VMEC run in a MAST H-mode like scenario with a total toroidal current $I_p \approx 0.6\ MA$ and $\beta \sim 7\%$. The current density profile includes a bootstrap contribution which takes into account the strong pressure gradient seen in Fig. 3.10. The current and pressure produce the extreme free boundary edge shaping seen in figure 3.11. No RMPs were employed, where only a weak nominal toroidal field ripple was present.

3.4.3 Analytic characterisation of equilibrium helical 3D structures in tokamaks

In the previous sections, we found that in tokamak configurations with a weak reversed shear safety factor with an off axis minimum, the VMEC code predicts two distinct equilibrium solutions [47], depending on the choice of the guess of the magnetic axis. The code can predict either the axisymmetric solution (corresponding to Eq. (2.11)) or a 3D equilibrium state with a helical core . This helical solution presents similarities with saturated internal kinks, as shown previously.

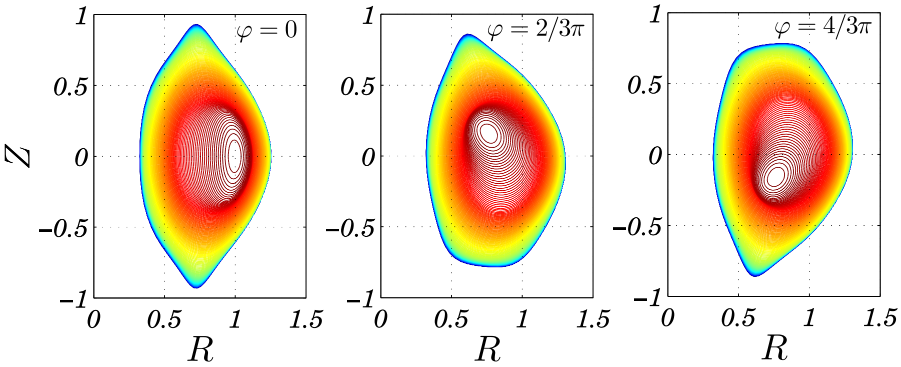

Figure 3.11: Contour of constant pressure surfaces. The shaping of the plasma boundary due to steep pressure gradients and bootstrap contributions is clearly visible.

These equilibrium states computed with the equilibrium VMEC code show two peculiar characteristics. There is no formation of current sheets (due to the absence of the $q = 1$ surface if q is left above unity, but also in the case when q drops below 1). In addition, the radial profile of the helical displacement is smoother than the usual top hat function typical of $m = n = 1$ internal kink modes [25]. A typical 3D helical equilibrium state computed by the VMEC code is shown in figure 3.12, which depicts the Fourier harmonics (poloidal and toroidal) of the cylindrical coordinates R and Z (note that only the $m = 0, 1$ and $n = -1, 1$ Fourier modes are shown). The $m = 0$ and $n = 1$ harmonic yields the helical core amplitude.

We wish now to characterise analytically such helical configurations. The treatment adopted is mathematically different from the approach used for the analysis of nonlinear instability (§ 3.3), since inertia is not included. This is therefore an analysis of the force balance equation (cf. (2.8)):

$$\boldsymbol{J} \times \boldsymbol{B} - \boldsymbol{\nabla} p = 0. \qquad (3.20)$$

In the analytic calculations, we impose an *ad hoc* geometry with a helical core with helicity 1/1. Hence we expand Eq. (3.20) in powers of the smallness parameter ε, obtaining the basic information about the equilibrium fields which give rise to such a configuration. From the

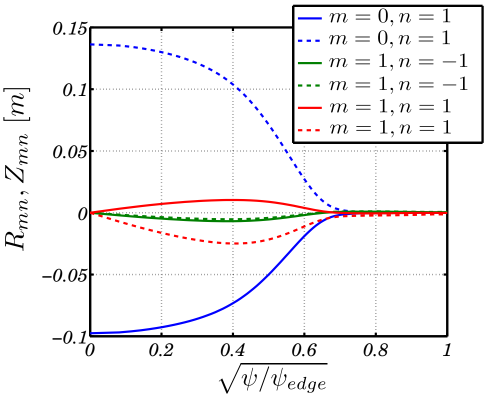

Figure 3.12: R (solid lines) and Z (dashed lines) Fourier components of a VMEC helical equilibrium for a MAST-like plasma. Only the $m = 0$, $n = -1, 1$ modes are shown.

Fourier structure shown in Fig. 3.12, we parametrise our flux surfaces in the Cartesian (X, Y, Z) space in the following manner (r is a flux label (radial variable) and θ the geometric poloidal angle):

$$R = R_0\varepsilon^{-1} + r\cos\theta - \varepsilon\Delta(r) - \varepsilon\xi_0(r)\cos\varphi - \varepsilon^2\xi_1\cos(\theta-\varphi) + \mathcal{O}(\varepsilon^3), \quad (3.21)$$

$$Z = r\sin\theta - \varepsilon\xi_0(r)\sin\varphi - \varepsilon^2\xi_1(r)\sin(\theta-\varphi) + \mathcal{O}(\varepsilon^3), \quad (3.22)$$

$$X = R\sin\varphi, \quad (3.23)$$

$$Y = R\cos\varphi, \quad (3.24)$$

where Δ is the Shafranov shift and $\xi_0(r > r_*) = 0$ with $0 < r_* < a$ (a is the minor radius). This is a simplified parametrisation, but allows us to catch the important underlying physics.

The ordering of the physical quantities involved is given by the ε tag in front of them. With this notation we have that $R_0 \sim \Delta \sim \xi_0 \sim \xi_1 \sim ... \sim 1$. We allow for a helical distorsion of single helicity $n = 1$ and amplitude $\xi_0(r)$, retaining the $m = m + 1$ side harmonic which will play an important role as will be shown later (harmonics $n > 1$ are not strictly important for our analysis, and are therefore neglected). All the Fourier harmonics are required to vanish at the plasma edge. Given the (X, Y, Z) parametrisation, we can calculate the metric tensor which is defined in the usual way $g_{ij} = \sum_{k=1}^{3} \frac{\partial \boldsymbol{X}_k}{\partial q^i}\frac{\partial \boldsymbol{X}_k}{\partial q^j}$, where $\boldsymbol{X} = (X, Y, Z)$ and $q^i = (r, \theta, \varphi)$ (see Appendix **A** § A.1). We assume a magnetic field written in the following manner $\boldsymbol{B} = \boldsymbol{\nabla}F(r) \times \boldsymbol{\nabla}\theta + \boldsymbol{\nabla}F(r) \times \boldsymbol{\nabla}\eta - \boldsymbol{\nabla}\psi(r) \times \boldsymbol{\nabla}\varphi$ where the function $\eta = \eta(r, \theta, \varphi)$ is periodic in its angular arguments with zero average. We want to solve the equilibrium problem, which for a given ξ_0 involves solving ψ, Δ etc. in terms of r. It is more convenient for the purpose of this analysis not to work in a straight field line coordinate system, hence we still consider the angle θ as the true geometric angle. By means of the parametrisation given by Eqs. (3.21)-(3.22), we expand the covariant radial projection of the force balance equation (3.20) in a series in ε. Each order is then set to zero. It is impossible of course to solve all the orders of the expansion, but for the moment we are interested to extract some rough information about the shape of the fields and the mode coupling in such helical configurations, not their exact characterisation. We also note that in order to solve the higher order expansion coefficient of (3.20) which are presently neglected more and more Fourier components in the parametrisation (3.21)-(3.22) have to be taken, reflecting the intrinsically *nonlinear* behaviour of the equilibrium. All physical quantities involved (the Shafranov shift Δ, etc.) are expanded in powers of ε, i.e. for a generic quantity f we set $f = f_0 + \varepsilon f_1 + ...$ We assume within the standard tokamak ordering that $p \sim \varepsilon^2$, i.e. $p = \varepsilon^2 p_2 + ...$ The equation for the function η can obtained by imposing $J^r = 0$:

$$\partial_\theta\left[\frac{g_{\theta\varphi}}{\sqrt{g}}\left(1 - q\partial_\varphi\eta\right) + q\frac{g_{\varphi\varphi}}{\sqrt{g}}\left(1 + \partial_\theta\eta\right)\right] - \partial_\varphi\left[\frac{g_{\theta\theta}}{\sqrt{g}}\left(1 - q\partial_\varphi\eta\right) + q\frac{g_{\theta\varphi}}{\sqrt{g}}\left(1 + \partial_\theta\eta\right)\right] = 0.$$

We have set the following normalisation: $\mu_0 = B_0 = a = 1$, where B_0 is the value of the magnetic field on the axis. The function η is also expanded in powers of ε ($\eta = \varepsilon H_1 + ...$). In order to have a correct expansion of Eq. (3.20) up to order ε, it is required to evaluate η up to order ε^3 (i.e. the expressions for H_1, H_2 and H_3 are needed). The evaluation of H_i ($i = 1, 2, ...$) is rather tedious and not insightful, and is accomplished by using computer algebra calculations, whose details are not shown.

Eq. (2.8) can be recast in the following manner:

$$\mathcal{U} = g_{\varphi\varphi}\frac{\partial_r p}{\partial_r \psi} - \frac{g_{\varphi\varphi}}{\sqrt{g}}\Big[q(1+\partial_\theta\eta)(\partial_\varphi B_r - \partial_r B_\varphi) - (1 - q\partial_\varphi\eta)(\partial_r B_\theta - \partial_\theta B_r)\Big] = 0,$$

and it can be written in an ε-series as follows:

$$\varepsilon^{-2}\mathcal{U}_{-2} + \varepsilon^{-1}\mathcal{U}_{-1} + \mathcal{U}_0 + \varepsilon\mathcal{U}_1 + \mathcal{O}(\varepsilon^2) = 0. \tag{3.25}$$

The first two terms are set to zero by imposing $F_0' = F_1' = rB_0$. The third order term ($\mathcal{U}_0$) gives

$$\left[\frac{2r}{R_0^2}\{(\psi_0')^2 + r\psi_0'\psi_0'' - r^2\} - \frac{r^2}{R_0}(3\Delta_0' + r\Delta_0'') + (2r^2p_2' + rF_2'' - 2F_2')\right] +$$
$$\left[\frac{r^2}{R_0}(3\xi_{0,0}' + r\xi_{0,0}'') + 2(r\xi_{1,0}' + r^2\xi_{1,0}'' - \xi_{1,0})\right]\cos\varphi = 0,$$

from which it immediately follows that the $\cos\varphi$ component of the equation above links ξ_0 to its sideband ξ_1, i.e.:

$$\xi_{1,0} = \frac{r\xi_{0,0}}{2R_0}. \tag{3.26}$$

By averaging in θ and φ we obtain an equation for F_2, where ψ_0, and Δ_0 are still unknown.

The $\cos\theta$ component of $\mathcal{U}_1$ provides the equation for the Shafranov shift Δ_0. If one assumes that the ε^3 corrections to Eqs. (3.21) and (3.22) are of the form $\zeta(r)\cos(m\vartheta - \varphi)$ and $-\zeta(r)\sin(m\vartheta - \varphi)$ respectively (in accordance with VMEC results), the $\cos\varphi$ component provides a link between $\xi_{1,1}$ and $\xi_{0,1}$ in the same manner of Eq. (3.26). The $\cos(\theta - \varphi)$ average gives:

$$(r - \psi_0')[r(r - \psi_0')\xi_{0,0}'' - (\psi_0' + r(2\psi_0'' - 3))\xi_{0,0}'] = 0, \tag{3.27}$$

which can be written in terms of the safety factor $q = r/\psi_0'$ (we recall that $B_0 = 1$ in our normalisations) yielding:

$$\underbrace{(q-1)}_{\mathbf{A}}\underbrace{[r^2(1 - 1/q)\xi_{0,0}'' - \{r/q + r[2(r/q)' - 3]\}\xi_{0,0}']}_{\mathbf{B}} = 0. \tag{3.28}$$

The equation above is fulfilled if either **A**=0 or **B**=0. Three cases are now considered.

(a) Assume a safety factor as shown in figure 3.13-(a). Hence Eq. (3.28) cannot be satisfied by $\mathbf{A} = 0$, so it must be satisfied by $\mathbf{B} = 0$, which gives:

$$\xi_{0,0}(r) = C_0 + C_1 \int^r \frac{d\tilde{r}}{\tilde{r}^3(1-1/q)^2}, \tag{3.29}$$

which is the same expression derived in Ref. [25], i.e. the eigensolution for internal kink modes for the case of a singular surface. But for our case 3.13-(a) there is no $q = 1$ surface, therefore $\xi_{0,0}$ has to be matched smoothly with the vanishing solution for $r > r_*$, implying that $C_0 = C_1 = 0$. Thus no helical cores can exist for the analytic equilibrium treatment undertaken here.

(b) For a safety factor as in Fig. 3.13-(b), Eq. (3.27) can be satisfied by $\mathbf{A} = 0$ at $r = r_*$, but not at any other value of r. Thus, we expect discontinuities in $\xi_{0,0}$ at $r = r_*$. Setting $C_1 = 0$ in (3.29) because of regularity on the magnetic axis, the solution for the helical core assumes an internal kink-like form, i.e. $\xi_{0,0} = C_0$ for $r < r_*$ and $\xi_{0,0} = 0$ for $r > r_*$.

(c) Finally let us assume that the safety factor has a broad region which extends from $r = 0$ up to $r = r_*$, where $q \approx 1$ as in Fig. 3.13-(c). Equation (3.28) is automatically satisfied for $0 < r < r_*$ by $\mathbf{A} = 0$. In which case for our analytic equilibrium treatment **B** can be arbitrary within $0 < r < r_*$, allowing $\xi_{0,0}$ itself to be arbitrary.

This leads us to the following considerations for our analytic equilibrium treatment: in order to have a finite amplitude helical core we must have at leading order either a $q = 1$ resonant point (with $\xi_{0,0}$ a top-hat function), or a flat $q = 1$ over an extended region in the core (with $\xi_{0,0}$ arbitrary). In Chapter **4** it will be shown that a similar condition on the safety factor for the existence of smooth core displacements holds (*infernal modes* problem).

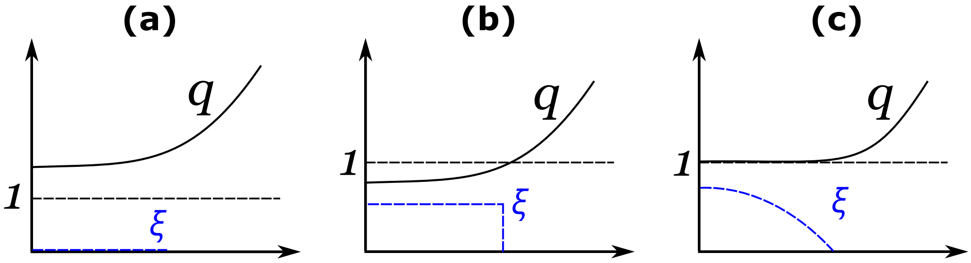

Figure 3.13: Different shapes of safety factor profiles and corresponding radial 1/1 helical fluid displacements.

3.5 Comparison of equilibrium and non-linear simulations for RFX

Saturated states of helicity $m = 1$, $n = 7$ are observed in the RFX device with reversed shear q-profiles and sufficiently high current [7]. Such states have not previously been compared with initial value calculations for saturated non-linear stability (departing from an axisymmetric equilibrium), nor with analytic expressions for the displacement. The initial equilibrium is evaluated using a novel version of the code VMEC, called VMEC2000 [18]. The code uses as a radial variable the normalized (to the edge) poloidal flux rather than the toroidal flux, in order to handle the change of sign in the q profile. The profiles of pressure and q are shown in figure 3.14. The constant pressure surfaces of the axisymmetric equilibrium branch is also shown. A helical core is found by choosing carefully the guess of the magnetic

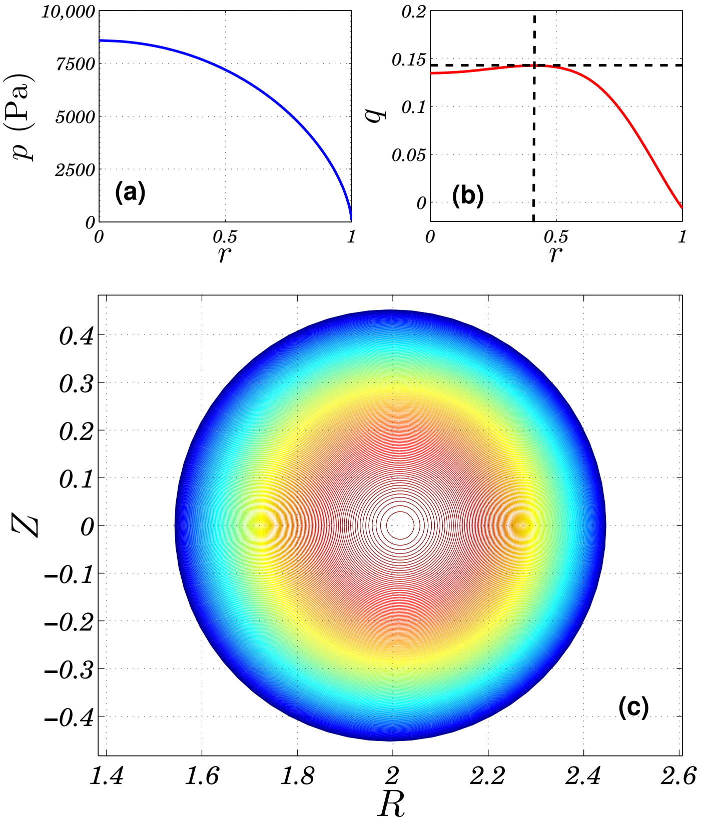

Figure 3.14: **(a)**,**(b)**: Profiles used for the nonlinear runs of XTOR-2F. The blue line shows the pressure profile while the red curve the q profile. The 1/7 resonance is also shown (black horizontal dashed line), as well the position of $q_{max} = 0.14206$ (black vertical dashed line).The radial variable r here is the square root of the normalised poloidal flux ($r = \sqrt{\psi/\psi_{edge}}$). **(c)**: Contours of the constant pressure surfaces at 2D equilibrium from the axisymmetric branch of VMEC2000.

r	ψ	$d\psi/dr$	p	p'	T	TT'
R	Z	g^{rr}	$g^{\theta\theta}$	$g^{r\theta}$	$g^{\varphi\varphi}$	$\sqrt{g}$

Table 3.2: Equilibrium quantities required for XTOR-2F runs. Here g^{ij} are the contravariant components of the metric tensor whose Jacobian is $\sqrt{g}$, T denotes the covariant toroidal component of the magnetic field and $r = \sqrt{|(\psi - \psi_0)/(\psi_{edge} - \psi_0)|}$. The geometric poloidal and toroidal angles are denoted by θ and φ respectively. The prime denote differentiation against the poloidal flux ψ, i.e. $' \equiv d/d\psi$.

axis and by imposing $n = 7$ periodicity in the Fourier modes. However such helical distorsion is dependent on the number of toroidal modes which are allowed in the simulation: with a spectrum of four poloidal modes, retaining only the $n = 7$ mode, the displacement is rather small, while if the $n = 14$ is also included, then it becomes quite large. Our attention in this paper is mainly focused on VMEC2000 simulations with only the $n = 7$ toroidal mode: this is because of the feasibility of the XTOR-2F nonlinear runs and for valid comparisons with the analytic approach. The output of an axisymmetric equilibrium from VMEC2000 is directly interfaced with XTOR-2F, contrarily to previous simulations which were interfaced using the equilibrium code CHEASE.

The coordinate system chosen is (r, θ, φ), where r is defined as the square root of the normalised poloidal flux, θ is the geometric poloidal angle and φ is the toroidal angle. The input quantities required by XTOR-2F are given in Table 3.2 ($' \equiv d/d\psi$ where here ψ denotes the poloidal flux) [66, 69], and where the equilibrium magnetic field has been taken as $\boldsymbol{B} = T\boldsymbol{\nabla}\varphi - \boldsymbol{\nabla}\psi \times \boldsymbol{\nabla}\varphi$. The contravariant components of the metric tensor are indicated by g^{ij} where $g = \det(g^{ij})$. The nonlinear runs are performed with 200 radial grid points, 64 and 48 poloidal and toroidal grid points respectively. In line with the VMEC simulations, the toroidal mode spectrum has only two toroidal mode numbers, namely $n = 0$ and $n = 7$, where the poloidal spectrum ranges from $n - m_{inf}$ to $n + m_{sup}$, with $m_{inf} = 10$ and $m_{sup} = 2$. This is shown in Fig. 3.15. The profiles for the pressure and the q profile used in the nonlinear simulation are already shown in Fig. 3.14. The results of the simulations are shown in figures 3.16 and 3.17, which show respectively the spectrum of the modes in XTOR-2F and the contours of the constant pressure surfaces both from the equilibrium code VMEC2000 and the nonlinear XTOR-2F initial value run (in XTOR-2F we assume an almost incompressible plasma, thus constant flux surfaces must correspond to constant pressure surfaces).

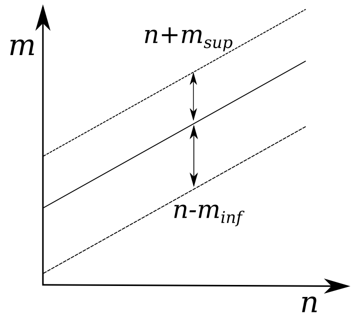

Figure 3.15: Modes spectrum in XTOR-2F.

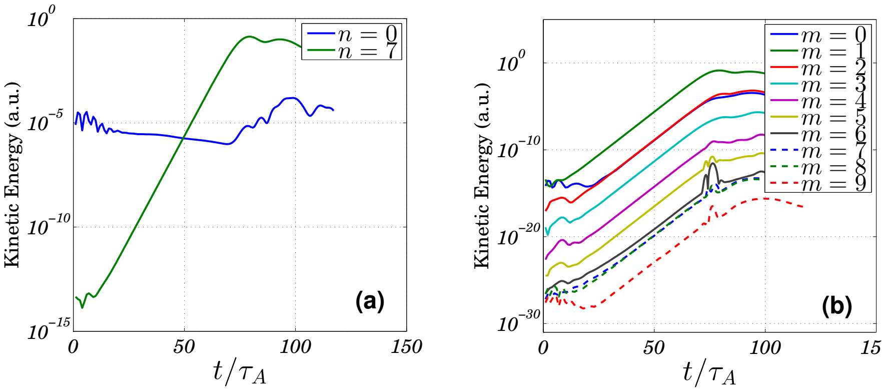

Figure 3.16: (a): Time evolution of the kinetic energy (XTOR-2F units) for the toroidal modes $n = 0$ and $n = 7$. (b): Spectrum of the kinetic energy of the $n = 1$ mode. The fastest growing mode is the $m = 1$, $n = 7$. The time is normalised with respect the Alfvén time $\tau_A = R_0/v_A$ with $v_A^2 = B_0^2/\mu_0\rho$, ρ being the plasma mass density, R_0 the major radius and B_0 the magnetic field on the magnetic axis. The growth rate is given by the derivative of the logarithm of the kinetic energy with respect to time divided by the factor 2.

The XTOR-2F saturated state is taken when the fastest growing mode no longer grows. As indicated in Fig. 3.17, only $n = 0$ and $n = 7$ toroidal modes are taken into account in the equilibrium calculations, and reasonably good agreement between VMEC2000 and XTOR is observed. Fig. 3.18 shows the superposition of constant pressure surfaces from VMEC2000 and XTOR-2F, zoomed in the low-shear region. The snapshot in XTOR-2F is taken when the kinetic energy of $n = 7$ in Fig. 3.16 reaches its maximum (at $t/\tau_A \sim 72$). However the velocity field and consequent inertia enter in the XTOR-2F simulations, but not in the equilibrium model of VMEC. It has been shown in Ref. [24] that around the time of the peak in the kinetic energy is reached, a crescent shape begins to appear in the magnetic surfaces. This would account for the differences seen in the pressure surfaces shown in Figs. 3.17 and 3.18, since, in particular, velocity and inertia does not enter into the physical model of the equilibrium in VMEC2000. Nevertheless, as also pointed out in Ref. [24], the growth of this crescent shape does not affect the magnetic axis position, even though it continues to grow after the peaking of the kinetic energy [24]. The crescent shape does not affect the axial position because $m > 1$ perturbations depend on position approximately as $\xi \sim r^{m-1}$. Hence the main characteristics (i.e. axial-kink amplitude) that we wish to compare between initial value stability, analytic calculations and equilibrium calculations are not significantly affected by the crescent structure. Nevertheless it is clear that the non-linear stability and the equilibrium states are not exactly alike in the transition region between low and high magnetic shear, and this may warrant further study in the future. Finally, the inertia is not so large as to yield a discernible difference between the constant pressure surfaces of Figs. 3.17 and 3.18 and magnetic surfaces.

We note that if VMEC is executed with a mode set of the from $n = 7, 14, 21$, etc.,

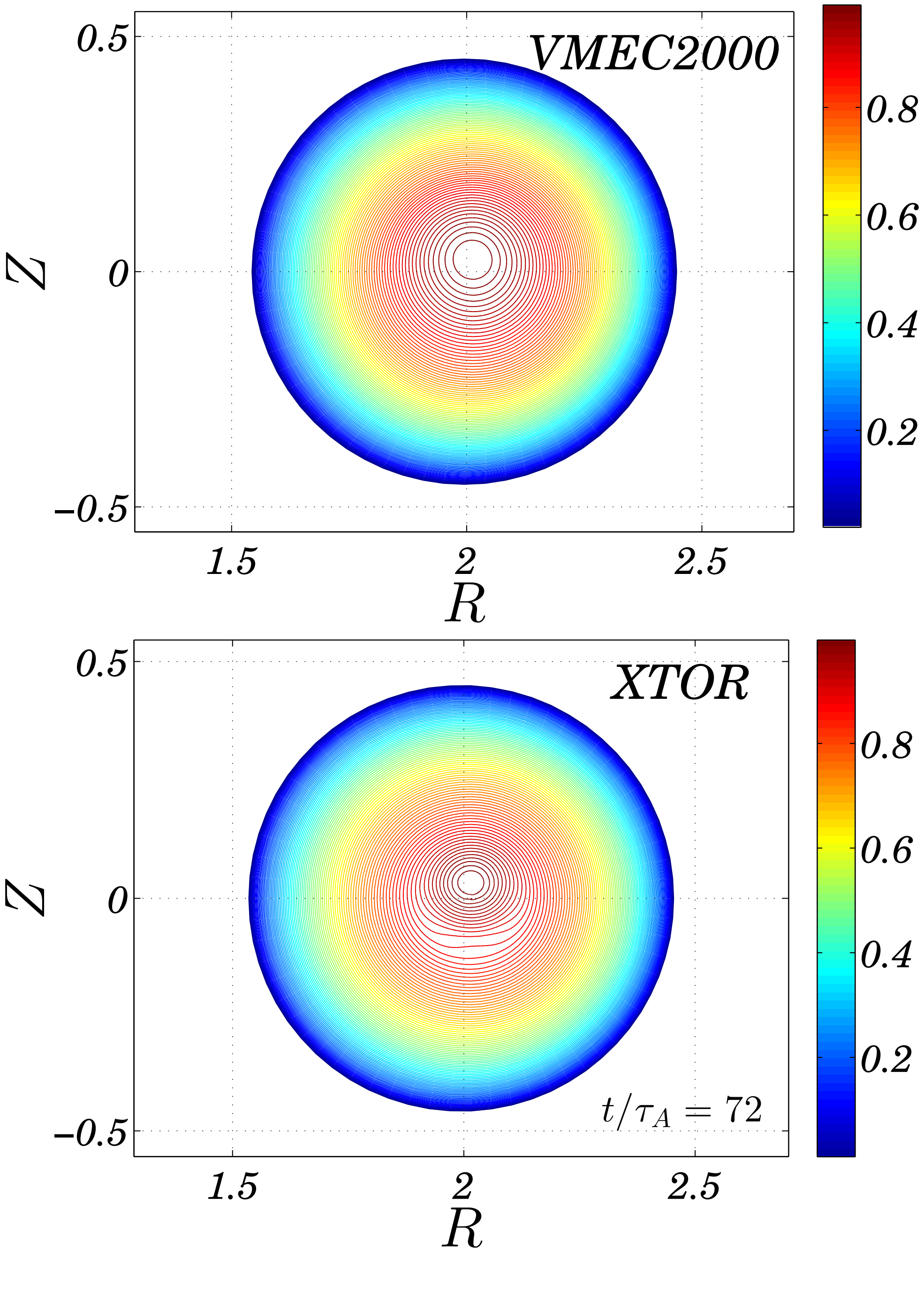

Figure 3.17: Contours of normalised constant pressure surfaces (with respect to its value on the magnetic axis) from VMEC2000 (top) and XTOR-2F (bottom) at $\varphi = \pi/2$ when the kinetic energy of the $n = 7$ mode reaches its maximum (see Fig. 3.16).

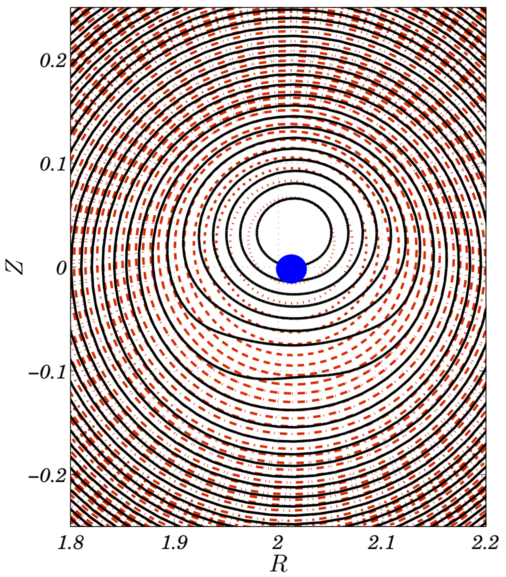

Figure 3.18: Zoom of the constant pressure surfaces shown in Fig. 3.17. The solid black lines correspond to XTOR-2F results, while the dot-dashed lines are the VMEC2000 contours. The blue point indicates the position of the magnetic axis in the axisymmetric case.

a large helical displacement is produced (much larger than that shown in Fig. 3.17). The XTOR-2F code can be run with the same mode set, but there is no appreciable difference in the growth of the mode and in the amplitude of the saturated state from when it is calculated with only the $n = 7$ mode. This is shown in Fig. 3.19. By increasing or decreasing the value of q_{max} we are also able to identify what the most unstable modes are. It is found that in our case, taking $q_{\max} \in [1/8, 1/7]$, the most unstable mode is the $n = 7$ as shown in Fig. 3.20. To conclude, it appears that VMEC agrees with XTOR-2F only when the mode set is taken to be $n = 0$ and $n = 7$. By taking e.g. $n = 7, 14, 21$, etc. in VMEC, it appears that artificially large helical equilibria are produced. Very recently, dedicated VMEC simulations have been undertaken with a large mode set which is not just multiples of $n = 7$. In particular, simulations with $n = 0, 1, 2, ..., 15$ resulted in a helical core similar to the case $n = 0$, $n = 7$ only (cf. Fig 3.17). Again this confirms that the helical state should be small.

In XTOR-2F it is not straightforward to apply the technique for calculating the displacement described in section 3.2 (i.e. δ_h). So, in what follows, displacements from XTOR-2F and VMEC2000 are obtained by evaluating the shift of the peak of the plasma pressure with respect to its equilibrium position in the poloidal plane for $\varphi = 0$ (the geometry of the system is almost circular). The displacement predicted by XTOR-2F gives $\xi_{XTOR} \approx 0.03m$ which is the approximately the same displacement predicted by VMEC2000 for the case $n = 0, 7$ (or indeed in simulations

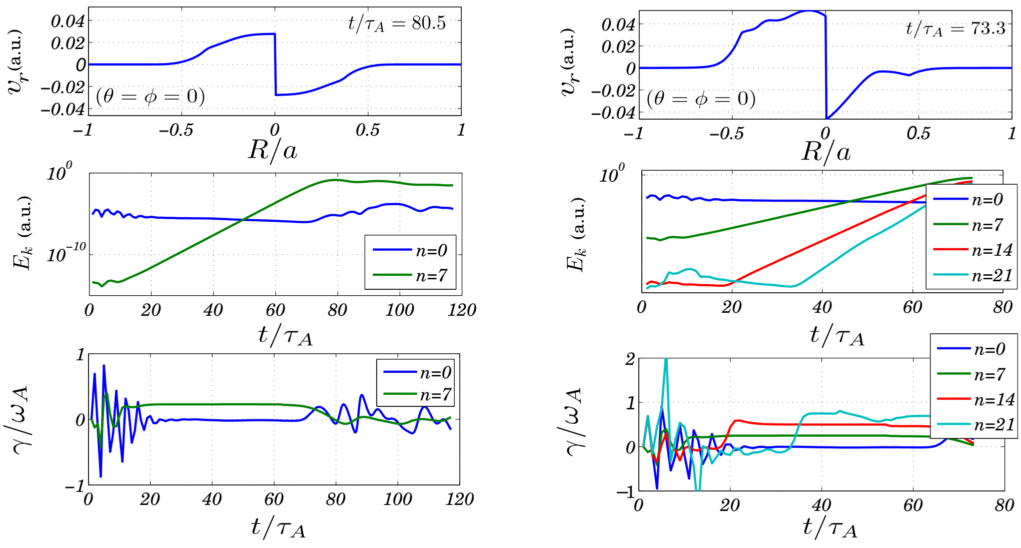

(a) **(b)**

Figure 3.19: Radial velocity versus major radius, kinetic energy and growth rate versus time (same equilibrium profiles as in Fig. 3.16) computed by XTOR-2F for the case $n = 0, 7$ (a) and $n = 0, 7, 14, 21$ (b). Although the code in the case be is running in a VMEC-like configuration, there is no significant difference between (a) and (b).

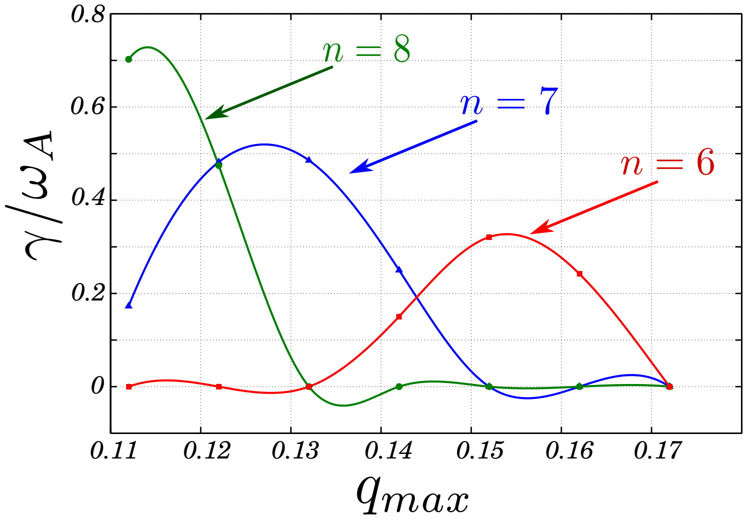

Figure 3.20: Growth rate γ of the $m = 1$ mode for different toroidal mode numbers n in function of q_{max}.

with $n = 0, 1, 2, ..., 15$), $\xi_{VMEC} = 0.03m$ (if one applies formulae (3.16) and (3.17) presented in the previous section then in both cases $a\delta_h \approx 0.036m$).

The growth rate of the unstable $m = 1,\ n = 7$ mode shown in figures 3.16 and 3.17, is approximately $\gamma/\omega_A \sim 0.23$, which is calculated by $\gamma = \frac{1}{2} d \log K/dt$ where K is the kinetic energy of the largest mode plotted in Fig. 3.16. In order to clarify the mechanism behind the generation of a displacement, we apply the analytic results for the prediction of the linear growth rate and the non-linearly saturated perturbed eigen-displacement, namely Eq.(3.3) and (3.13).

The corresponding growth rate, obtained from formulae (2.23), (2.24), (3.3) and (3.5) gives $\gamma/\omega_A \approx 0.32$, which agrees well with the growth rate obtained from the linear phase of XTOR-2F simulations. In order to identify the instability mechanism, we let

$$\delta W = \delta W_{press} + \delta W_{curr},$$

where

$$\begin{aligned}\delta W_{press} &\sim \int_0^{r_s} dr[2(kr)^2\mu_0/(1+(kr)^2)p_0'],\\ \delta W_{curr} &\sim \int_0^{r_s} dr\frac{(kr)^2 B_\vartheta^2/r}{(1+(kr)^2)^2} \times (kQ+1)(kQ(3+k^2r^2)+k^2r^2-1),\end{aligned}$$

which represent respectively the pressure and the current contribution to the total MHD energy. Both pressure and current terms are destabilising (i.e. negative δW) but we deduce that this mode is mainly current driven since $\delta W_{press}/\delta W_{curr} \ll 1$ Finally, since the SHAx configuration is an *almost* resonant $m = 1$ mode, we are permitted to employ the nonlinear analytic predictions (i.e. Eq. (3.14a)) for the displacement. We then compare the analytic growth rate and displacement with equilibrium and nonlinear simulations results. If we employ the analytic growth rate of $\gamma/\omega_A \approx 0.39$ one obtains (by employing Eq. (17) in Ref. [62]) $\xi \approx 0.03m$. Instead we employ the growth rate from the XTOR-2F simulation (see Fig. 3.16) of $\gamma/\omega_A \approx 0.23$, and we obtain (by employing Eq. (17) in Ref. [62]) $\xi \approx 0.018m$. In both cases we have good agreement between numerical simulations (both equilibrium and nonlinear) and analytical theory for the estimate of the linear growth rate and the nonlinear displacement of an $m = 1$ mode. This gives confidence in our analytic identification that the displacement occurs dominantly by a current driven instability (δW_{curr}).

3.6 Summary

This chapter addresses the characterisation, both numerically and analytically, of helical states in tokamaks and RFPs. Both equilibrium and saturated nonlinear approaches are considered. The nonlinear analytic theory of the $m = 1$ saturated kinks has been extended to arbitrary toroidal wave numbers in order to model modes with $n > 1$. In addition, analytic conditions on the magnetic fluxes and the mode spectrum are derived, for which a helical state exists.

A comparison between simulations of fixed and free boundary 3D equilibria and nonlinear saturated ideal MHD instabilities in ITER-like and MAST-like plasmas has been presented. A small $n = 1$ RMP external magnetic perturbation has been allowed in the MAST-like equilibrium calculations ($\delta B_{RMP}/B_{vac} \approx 10^{-4}$) in order to try to improve agreement between 3D equilibrium codes and nonlinear initial value code when $q_{min} < 1$ for tokamak internal kink mode cases. When $q_{min} > 1$ good agreement between VMEC and XTOR-2F results have been found in accordance with analytical predictions for saturated internal kinks [26, 62, 63], and previous numerical results [48, 64]. The amplitude of the displacement of the magnetic axis weakly depends on the choice of an external $n = 1$ (RMP) perturbation. When q_{min} is sufficiently less than unity, the helical displacement shows a strong dependence on the amplitude of $n = 1$ RMP field: a significant reduction/increase of the RMP yields a significant reduction/increase of δ_h. The discrepancy of the approaches when resonant surfaces exist in the plasma is not yet understood.

An RFP-like configuration with a non-monotonic q profile having $q_{max} \approx 1/7$ has also been studied. The SHAx equilibrium has been modelled using the code VMEC2000 retaining only one toroidal mode, namely $n = 7$. Interfacing the output of VMEC2000 with the nonlinear code XTOR-2F, it has been possible to study the behaviour of the ideally saturated $n = 7$ mode: the two codes agree well for the prediction of the displacement of the magnetic axis providing that a large toroidal mode set comprising only of multiples of $n = 7$ are not used in VMEC. The analytical theory of the nonlinear saturation of an ideal $m = 1$ mode has been extended to general toroidal wave numbers k. In the approximation of large aspect ratio ($kr \ll 1$), these results are used to predict the nonlinear saturated displacement of the $n = 7$ mode: the agreement of both equilibrium (VMEC2000) and nonlinear (XTOR-2F) numerical simulations with the analytical prediction given by Eq. (3.14a) is very good.

Connection to the analytic theory shows that the SHAx equilibrium is generated by a 1/7 internal kink, dominantly driven by current gradient and weakly by pressure gradient. Agreement with XTOR-2F initial value code opens the way to begin a resistive treatment which could permit stochastic regions to be generated, possibly also with more than one magnetic axis.

4

Fast growing modes in low-shear tokamaks with non-MHD effects

In this chapter we present the linear theory of resistive instabilities in low shear tokamaks. The main goal is to derive an analytic dispersion relation for resistive instabilities in a low shear tokamak configuration when extra non-MHD effects are considered and to check if fast growing modes (much faster than the conventional linear tearing mode) are still possible. The resistive infernal mode model [L. A. Charlton et al., *Phys. Fluids B* **1**, 798 (1989)] is generalised to include plasma diamagnetism, subsonic equilibrium toroidal flow shear and viscosity. An estimate of the transition point between fast $S^{-3/13}$ *infernal-like* (S is the Lundquist number) and slow $S^{-3/5}$ *tearing-like* scaling is given. In particular a novel $S^{-3/8}$ scaling is found close to the ideal ion-diamagnetic MHD stability boundary. New moderately fast scalings in S are also found when sheared toroidal $\boldsymbol{E} \times \boldsymbol{B}$ flow and viscosity are considered.

4.1 Introduction

As we have seen in the introduction, an intermediate step between the H-mode inductive scenario and the strong reversed scenario is the so called *"hybrid scenario"* [75], which is characterised by low (almost flat with $q > 1$ everywhere) shear in the central region with q_0 close to unity (q_0 is the value of the safety factor on the magnetic axis), and high values of $\beta_N = \langle\beta\rangle a_0 B_T/I_p$ ($\beta = p/(B^2/2\mu_0)$) where a_0 is the plasma minor radius, I_p the plasma current, B_T the toroidal field and $\langle\beta\rangle$ is the volume averaged normalised plasma pressure [6]. As pointed out in [6, 76] these kind of discharges can be characterised by the presence of MHD activity, whose most important modes are typically LLMs [8], global oscillations [77], snakes [78] and NTMs [32] (note that NTMs are not always benign). In particular, TCV hybrid plasmas have been experimentally reported to be prone to global plasma oscillations which are either ideal or resistive [77, 79].

In plasmas with an approximately shear free core, pressure driven MHD instabilities characterised by the coupling between a fundamental helical (m, n) harmonic with its $(m \pm 1, n)$ sidebands [56, 57, 80], are possible. These modes are called *"infernal modes"* and are closely related to the quasi-interchange modes described by Wesson for the special $m = n = 1$ case [34]. When resistive effects are taken into account close to the MHD stability boundary, fast growing resistive modes, which scale as $S^{-3/13}$ (S being the Lundquist number), are found [58]. These *"resistive infernal modes"* show a tearing character on the resonant surface of the $m + 1$ sideband of the main poloidal harmonic m. Such sideband perturbations could be relevant for the triggering of neo-classical tearing modes (NTMs) [33], thus providing the seed island necessary for the development of rapid growing modes (NTMs) [40].

Shear free core plasmas can occur either in the above mentioned hybrid scenario or after a sawtooth crash in baseline scenarios where it is found that $q = 1$ over a large region of the core following a fully reconnected sawtooth crash [52, 53]. For a brief time after the crash (and assuming density peaking in the core [81]) such a configuration is essentially identical to the hybrid scenario mentioned earlier, and as such, infernal modes are expected to be triggered. In particular it has been experimentally observed that after a sawtooth crash, resistive modes can grow on ideal timescales [40, 50]. Furthermore since the coupling involves an ideal MHD harmonic in the core region with a resistive tearing-like sideband at $q = (m \pm 1)/n$, then the effect of plasma diamagnetism should be important because the tearing mode is required to rotate at the electron diamagnetic frequency at that surface [58]. Indeed in TCV hybrid-like operation regimes the presence of modes which rotate in both electron and ion diamagnetic directions have been observed [9].

With these applications in mind, our aim is to extend Charlton's model for *"resistive infernal modes"*, investigating the growth of resistive instabilities with non-MHD effects. Ultimately an attempt is made to find the scaling of the growth rate with respect to S when non-MHD effects are included. The aim is to examine primarily the impact of sheared plasma rotation and diamagnetism on perpendicular dynamics and to see if fast growing resistive modes still occur despite these additional non-MHD effects. These effects were neglected in previous analysis on fast growing resistive modes [58]. Furthermore, a phenomenological perpendicular viscous term [72, 82] is taken into account on the sideband resonant surface where the dispersion relation can be extended in a simple way to accommodate it (we do not aim for an extended treatise of the viscosity since our main dissipative effect remains resistivity).

The first part of this chapter is devoted to an explanation of the setup of the problem and a derivation of the model of the drift-MHD equations which describe the magnetic perturbation. The geometry of the system, the equilibrium fields and the physical model adopted are then presented. We then show a derivation of perturbed physical quantities (plasma pressure, magnetic fluxes and temperature), yielding linearised Faraday-Ohm's law and vorticity equations, i.e. the equations describing the magnetic perturbation in the low-shear ($q' = 0$) and sheared ($q' \neq 0$) regions when additional non-MHD effects are included. Since the self adjointness of the MHD operator is lost, the equations describing the perturbed fluxes are derived directly from the equation of motion [83] rather than performing a δW minimisation [35, 84, 85]. In particular, even if the equations governing the fluid displacement in the low-shear region are already known [35, 58, 84, 86], a detailed derivation of these equations is retained in order to have a unified description across all the plasma, and covering the different physical mechanisms. With an appropriate choice of the rotational transform, an exact analytic treatment of the magnetic perturbation in the sheared region is derived. With this choice we present the approximations needed to obtain the solution in the resistive layer. Eventually the dispersion relation for *infernal resistive modes* is derived and analysed: three dispersion relations in three different regimes are studied in the neighbourhood of the ideal MHD stability boundary. Each regime separately considers the effects of plasma diamagnetism, viscosity with diamagnetic corrections and equilibrium toroidal flows. Novel scalings of growth rates with the Lundquist number S are provided and tabulated, showing the possibility that fast growing resistive perturbations can occur even when non-MHD effects are considered.

4.2 Equilibrium

We adopt the standard tokamak ordering where $B_P/B_T \sim \mathcal{O}(\varepsilon)$ (B_P and B_T denote respectively the poloidal and the toroidal magnetic field strength) and $\beta \sim \mathcal{O}(\varepsilon^2)$. We use a straight field line coordinate system (r, ϑ, φ) where r is a flux label with the dimensions of length, ϑ is a poloidal-like angle such that the magnetic field

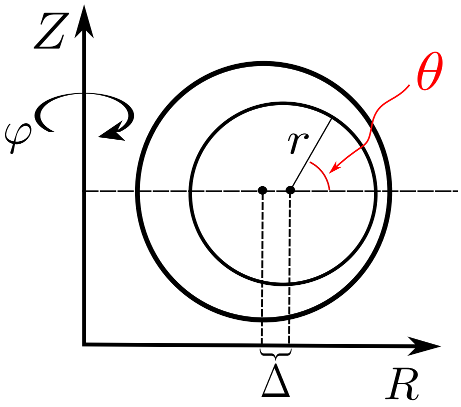

Figure 4.1: Schematic view of the tokamak (r, θ, φ) coordinate system.

lines are straight and φ is the toroidal angle. The contravariant and covariant basis vectors are denoted hereinafter by ∇q^i and $\boldsymbol{e}_{q^i}$ respectively, with $q^i = (r, \vartheta, \varphi)$. The equilibrium geometry of a tokamak of major radius R_0 is defined by shifted circular toroidal surfaces in a large aspect ratio approximation ($\varepsilon = r/R_0 \ll 1$), as shown in Fig. 4.1. The total magnetic field is represented in terms of flux functions [87]:

$$\boldsymbol{B} = \nabla f \times \nabla\vartheta - \nabla\psi \times \nabla\varphi, \tag{4.1}$$

where the vector potential is given by $\boldsymbol{A} = f(r,\vartheta,\varphi)\nabla\vartheta - \psi(r,\vartheta,\varphi)\nabla\varphi$. Hereafter we set $' \equiv \partial/\partial r$. The equilibrium fluxes ψ_0 and f_0 (denoted by the subscript 0) depend only on r, and $q = f_0'/\psi_0'$ with $f_0' \approx B_0 r$ which follows from $B_T \approx R_0 B_0/R$ [16] (B_0 is the magnetic field strength on the axis). Normalising $\mu_0 = 1$, from the Ampére's law $\boldsymbol{J} = \nabla \times \boldsymbol{B}$, where $\boldsymbol{J}$ is the current density, we have $\sqrt{g}J^\varphi = \boldsymbol{\Delta}^*\psi + \boldsymbol{\Theta}^* f$, where the expressions for the operators $\boldsymbol{\Delta}^*$ and $\boldsymbol{\Theta}^*$ are:

$$\boldsymbol{\Delta}^*\chi = \partial_r\left(\frac{g_{\vartheta\vartheta}}{\sqrt{g}}\partial_r - \frac{g_{r\vartheta}}{\sqrt{g}}\partial_\vartheta\right)\chi - \partial_\vartheta\left(\frac{g_{r\vartheta}}{\sqrt{g}}\partial_r - \frac{g_{rr}}{\sqrt{g}}\partial_\vartheta\right)\chi,$$
$$\boldsymbol{\Theta}^*\chi = -\partial_r\left(\frac{g_{r\vartheta}}{\sqrt{g}}\partial_\varphi\chi\right) + \partial_\vartheta\left(\frac{g_{rr}}{\sqrt{g}}\partial_\varphi\chi\right).$$

Defining $J_0 = \boldsymbol{\Delta}^*\psi_0/f_0'$, it can be easily seen that:

$$J_0 = \partial_r\left(\frac{g_{\vartheta\vartheta}}{\sqrt{g}}\iota\right) + \frac{g_{\vartheta\vartheta}}{\sqrt{g}}\iota\frac{f_0''}{f_0'} - \iota\partial_\vartheta\left(\frac{g_{r\vartheta}}{\sqrt{g}}\right), \tag{4.2}$$

which at leading order reads $J_0 = 1/R_0[(r\iota)' + \iota]$. It is easy to show that $J_0' = 1/(mR_0)[(r^2 k_{||}^m)'/r]'$ [92], where $\iota = 1/q$ and $k_{||}^m = m\iota - n$.

In order to compute the metric tensor coefficients, we start with a right handed cylindrical coordinate system (R, Z, φ) in which the flux surfaces are parametrised as follows (see Chapter **2** § 2.3 and Appendix **A** § A.1):

$$\begin{aligned}
&R = R_0 + r\cos\theta - \Delta(r) + \mathcal{O}(\varepsilon^2),\\
&Z = r\sin\theta + \mathcal{O}(\varepsilon^2),
\end{aligned}$$

where θ is the geometric poloidal angle and $\Delta(r) \sim \mathcal{O}(\varepsilon a_0)$ is the Shafranov shift. We first note the length element in the axisymmetric (r, ϑ, φ) coordinate system is given by (cf. Appendix A.1):

$$d\ell^2 = g_{rr}dr^2 + g_{\vartheta\vartheta}d\vartheta^2 + 2g_{r\vartheta}drd\vartheta + R^2 d\varphi^2,$$

where $g_{\varphi\varphi} = R^2$ and $g_{r\varphi} = g_{\vartheta\varphi} = 0$ due to axisymmetry. In a right handed straight field line representation, the most general form of the equilibrium magnetic field is given by the following form $\boldsymbol{B} = \boldsymbol{\nabla} f_0 \times \boldsymbol{\nabla}\vartheta - \boldsymbol{\nabla}\psi_0 \times \boldsymbol{\nabla}\varphi$ where $\vartheta = \theta + \lambda$ is the *rectified* (straight field line) poloidal angle and $\lambda \sim \mathcal{O}(\varepsilon)$ is the rectification parameter. By imposing the condition $J^r = \frac{1}{\sqrt{g}}\frac{\partial}{\partial\vartheta}\left(\frac{g_{\varphi\varphi}}{\sqrt{g}}\frac{\partial f_0}{\partial r}\right) = 0$ (which comes from Eq. (2.8)), we can calculate the elements of the metric tensor, up to $\mathcal{O}(\varepsilon)$, whose expressions are [88]:

$$\begin{aligned}
&g_{rr} = 1 - 2\Delta'\cos\vartheta, \quad g_{r\vartheta} = \left(\frac{r^2}{R_0} + r\Delta' + r^2\Delta''\right)\sin\vartheta,\\
&g_{\vartheta\vartheta} = r^2 + \frac{2r^3}{R_0}\cos\vartheta + 2r^2\Delta'\cos\vartheta,\\
&g_{\varphi\varphi} = R_0^2\left[1 + \frac{2r}{R_0}\cos\vartheta\right], \quad \frac{1}{\sqrt{g}} = \frac{1}{rR_0}\left[1 - \frac{2r}{R_0}\cos\vartheta\right],
\end{aligned} \tag{4.3}$$

where the ratio $g_{\varphi\varphi}/\sqrt{g}$ depends only on the flux label r. A more careful derivation gives [89] ($\langle\ \cdot\ \rangle := \frac{1}{2\pi}\int_0^{2\pi}(\ \cdot\ )d\vartheta$):

$$\langle g_{\varphi\varphi}\rangle' = \langle R^2\rangle' = -rR_0\left(\Delta'' + 3\Delta'/r + 1/R_0\right), \tag{4.4}$$

where the Shafranov shift fulfils the following equation [90]:

$$\Delta'' = \frac{1}{R_0} - \frac{2R_0 p_0'}{rB_0^2}q^2 - \left(\frac{3}{r} + 2q\left(\frac{1}{q}\right)'\right)\Delta',$$

with p_0 the equilibrium pressure profile and q the safety factor profile ($' \equiv d/dr$).

4.3 Physical model and drift MHD equations

Infernal modes depend critically on the safety factor profile q, whose typical profile in hybrid (low-shear) configuration is shown in Fig. 4.2. It is convenient to split the analysis of the instability into three different regions. In the core we impose a large region of **low-shear** (region I) which extends from the magnetic axis up to the radial position r_* where the magnetic shear $\hat{s} = rq'/q$ is almost vanishing, i.e. $q' \approx 0$, and $q \sim m_0/n$. A **sheared region** (region II) where $q' \sim \mathcal{O}(1)$ extends from $r = r_*$ up to the plasma boundary $r = a_0$. The transition point between region I (low shear) and region II (high shear) is marked by r_*, so that $q'(r < r_*) = 0$ and $q'(r > r_*) = \mathcal{O}(1)$. Finally a thin **resonant layer** (region III, shaded in Fig. 4.2) about the radial position $r = r_s$, where the $(m_0 + 1)/n$ resonance of the safety factor occurs, is included. The non-MHD effects considered are diamagnetic flows and viscosity. The additional MHD effect of equilibrium toroidal flow $\boldsymbol{v}_0 = v^\varphi \boldsymbol{e}_\varphi$ is assumed constant in the low-shear region (see Fig. 4.2) and subsonic ($\mathcal{M} \ll 1$, $\mathcal{M}$ is the Mach number) in order to preserve the property $p_0 = p_0(r)$ [91]. Finally, as indicated in figure 4.2 r_0 is the radius at which we force the pressure (assumed parabolic, viz. $p_0 \sim 1 - (r/r_0)^2$) to vanish.

For a fixed toroidal mode number. the Fourier structure of the magnetic perturbation is assumed to be characterised by having a fundamental mode m_0 and two poloidal $m_0 \pm 1$ sideband components which are of order $\mathcal{O}(\varepsilon)$ with respect to the dominant one. In the low-shear region the parallel wave vector $k_{||}^{m_0}$ is taken to be $\mathcal{O}(\varepsilon)$, thus inertial corrections to the m_0 harmonic and the coupling with its sidebands are important. Furthermore in this region ion diamagnetic flow and equilibrium flow shear are taken into account. In the sheared region only non-inertial ideal MHD is required and it will be shown that the Fourier harmonics are decoupled at leading order. The resonant layer physics of the $(m_0 + 1)/n$ sideband is augmented by viscous and diamagnetic (both ion and electron) effects. Sheared $\boldsymbol{E} \times \boldsymbol{B}$ flows are also retained. Each region, which includes different physical mechanisms, is treated separately. Through the matching of the corresponding eigenfunctions a dispersion relation for the magnetic perturbation is derived. We obtain a single equation for the dominant Fourier m_0 component which depends on the stability index $\Delta' := \psi_+'/\psi_+|_{r_s-}^{r_s+}$ [16] by matching the solution in the low-shear region with the solution in the sheared region. Standard tearing theory [83] is used for matching the eigenfunction in the resonant layer with the eigenfunction in the sheared region, providing $\Delta' = \Delta'(\omega)$ (ω is the frequency of the mode) which

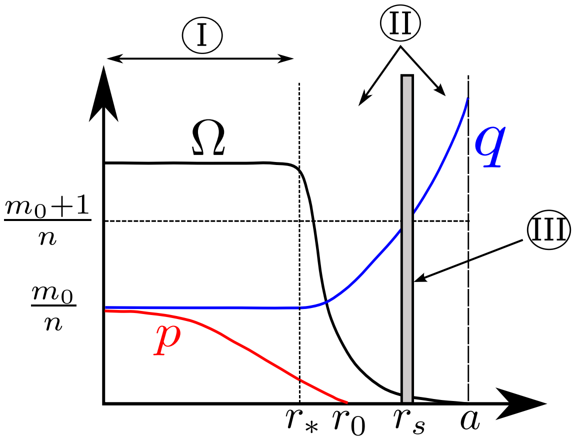

Figure 4.2: Profiles for toroidal rotation frequency, pressure and safety factor. In the low-shear region ($r < r_*$) the q profile is almost resonant ($q \approx m_0/n$). The resonant $m_0 + 1$ surface is labelled by r_s.

eventually leads to the dispersion relation.

In order to model the non-MHD effects, we adopt the following set of drift-MHD equations [67, 82, 92] ($s = i, e$):

$$\partial_t n_s + \boldsymbol{\nabla} \cdot (n_s \boldsymbol{v}_s) = 0 \tag{4.5}$$

$$\varrho \left[\partial_t \boldsymbol{v} + \boldsymbol{v} \cdot \boldsymbol{\nabla} \boldsymbol{v} + \boldsymbol{v}_i^* \cdot \boldsymbol{\nabla} \boldsymbol{v}_\perp\right] = -\boldsymbol{\nabla} p + \boldsymbol{J} \times \boldsymbol{B} + \mu_\perp \boldsymbol{\nabla}^2 \boldsymbol{v} \tag{4.6}$$

$$\partial_t p_s + \boldsymbol{v}_s \cdot \boldsymbol{\nabla} p_s + \tfrac{5}{3} p_s \boldsymbol{\nabla} \cdot \boldsymbol{v}_s = 0 \tag{4.7}$$

$$\boldsymbol{E} + \boldsymbol{v}_e \times \boldsymbol{B} + \frac{\boldsymbol{\nabla} p_e}{e n_0} + 0.71 \frac{\boldsymbol{\nabla}_{||} T_e}{e} = \eta \boldsymbol{J} \tag{4.8}$$

where n_s is the density of the species s ($n_i = n_e = n_0$), the electric field is given by $\boldsymbol{E} = -\boldsymbol{\nabla}\Phi - \partial_t \boldsymbol{A}$, Φ is the electrostatic potential, $\boldsymbol{v}_{i,e}$ are the ion and electron velocities, where for the ions $\boldsymbol{v}_i = \boldsymbol{v}_E + \boldsymbol{v}_{||i} + \boldsymbol{v}_i^*$, with $\boldsymbol{v}_E = \boldsymbol{E} \times \boldsymbol{B}/B^2$, $\boldsymbol{v}_s^* = \boldsymbol{B} \times \boldsymbol{\nabla} p_s/(q_s n_0 B^2)$ (q_s is the charge of the particle of the species s), and for electrons $\boldsymbol{v}_e = \boldsymbol{v}_i - \boldsymbol{J}/e n_0$. The parallel velocity is defined by $\boldsymbol{v}_{||} = (\boldsymbol{v} \cdot \boldsymbol{b})\boldsymbol{b}$, where $\boldsymbol{b} = \boldsymbol{B}/B$ is the unit vector along the magnetic field. The plasma MHD velocity is defined as $\boldsymbol{v} = \boldsymbol{v}_i - \boldsymbol{v}_i^*$, $\varrho = n_0 m_i$ is the mass density, η and $\mu_\perp$ are the plasma resistivity and perpendicular viscosity respectively, which are both taken constant (this is a reasonable approximation since their contribution is non-negligible only in thin layer close to the resonant *tearing* surface $q = (m_0 + 1)/n$). The total plasma pressure p is defined as $p = p_i + p_e$. Finally T_s and n_s are respectively temperature and density of the species s with $\boldsymbol{\nabla}_{||} = \boldsymbol{b}(\boldsymbol{b} \cdot \boldsymbol{\nabla})$, $\boldsymbol{\nabla}^2(\,\cdot\,)$ is the Laplace operator. Finally, the diamagnetic frequency for the species s for a given wave number $\boldsymbol{k}$ is given by $\omega_s^* = \boldsymbol{k} \cdot \frac{\boldsymbol{B} \times \boldsymbol{\nabla} p}{q_s n_s B_0^2}$.

We include a purely phenomenological perpendicular viscous term (as introduced in Ref. [82]) which provides a modest generalisation of the dispersion relation of these resistive modes in hybrid plasmas. A more elaborate treatment of the plasma viscosity has been presented in Ref. [93], however we do not attempt to model parallel dynamics in the long mean free path. Indeed the viscous term enters only in the thin layer of the sideband of the main mode which is treated in slab geometry with a constant background magnetic field, leading us to drop the contribution of possible toroidal effects. Moreover the sideband layer is in a cooler part of the plasma, strengthening the argument that the perpendicular dynamics are dominant over the parallel dynamics in the $q = (m + 1)/n$ region. [1] Our aim is to primarily examine macroscopic perpendicular dynamics, which arrive from the short mean free path equations. In addition to perpendicular viscosity and resistivity, we include the impact of ion and electron diamagnetism and shear flow on the mode growth. We point out that this set of equations is adopted in analogy with the model equations employed by many MHD codes which study core tokamak behaviour such as XTOR-2F [66, 95]. Thus, in the derivation of Eq. (4.6), we employed the *gyro-viscous cancellation* [67, 92, 95]:

---

[1] There are other important dissipative effects beyond diamagnetic-MHD, such as parallel dynamics of wave-particle interaction. An example is the modelling of interchange modes in Alcator C-MOD, where ion Landau damping effects were favoured over viscosity effects as a substitute for diamagnetic effects in the core [94]. Our application differs from that of Ref. [94] in that our main dissipation effect is resistivity.

$$\partial_t \boldsymbol{v}_i + \boldsymbol{\nabla} \cdot \underline{\underline{\Pi}}_{gv} \approx \partial_t \boldsymbol{v} + \boldsymbol{v}_i^* \cdot \boldsymbol{\nabla} \boldsymbol{v}_\perp$$

in which a straight, uniform magnetic field is assumed ($\underline{\underline{\Pi}}_{gv}$ is the gyro-viscous stress tensor). This is a reasonable approximation, since the inertial terms in the low-shear region enter only at leading order where the equilibrium magnetic field is assumed constant (this will be clear in the following sections).

4.4 Derivation of the equations for (Φ, ψ, f, p)

The main objective of this section is to derive a set of coupled equations for the perturbed electric potential Φ and the poloidal magnetic flux ψ, namely the vorticity equation and the Faraday-Ohm's law. Because of the ordering scheme in the low-shear region, the corrections due to perturbed pressure and toroidal magnetic field become important. Thus an expression for these quantities is required. We assume flute-like perturbations (a tilde denotes perturbed quantities and X is a generic physical quantity):

$$|\boldsymbol{B}_0 \cdot \boldsymbol{\nabla} \tilde{X}| \ll |\boldsymbol{B}_0 \times \boldsymbol{\nabla} \tilde{X}|,$$

with a time dependence $exp(-i\omega t)$.

The total perturbed plasma pressure ($\tilde{p} = \tilde{p}_i + \tilde{p}_e$) is written as a sum of an incompressible and a compressible contribution, namely $\tilde{p} = p_1 + \delta p$. At leading order we can neglect the compressible contribution $\boldsymbol{\nabla} \cdot \boldsymbol{v} \approx 0$, so that the equation governing the incompressible part of the total pressure is $(\partial_t + \boldsymbol{v} \cdot \boldsymbol{\nabla}) p_1 = 0$ [92], which gives for the mth Fourier mode (for sake of simplicity we omit to write the subscript n):

$$p_{1,m} = imp_0'/f_0'\xi_m, \tag{4.9}$$

where $\xi = i\tilde{\Phi}/\hat{\omega}$ and $\hat{\omega} = \omega + nv^\varphi$ where v^φ is the equilibrium toroidal flow due to the equilibrium electric field. The perturbed ion pressure is found by linearising eq. (4.7) under the assumption of hydrodynamic like ions $\boldsymbol{\nabla} \cdot \boldsymbol{v}_i \simeq 0$ [96], which gives:

$$\tilde{p}_{i,m} = imp_{i0}'/f_0'\xi_m. \tag{4.10}$$

By subtracting (4.10) from (4.9) we obtain an approximate expression for the electron pressure:

$$\tilde{p}_{e,m} = imp'_{e0}/f'_0\xi_m. \tag{4.11}$$

Finally, writing $\tilde{p}_e = \tilde{n}T_{e0} + n_0\tilde{T}_e$ and imposing quasi-neutrality, from (4.5) and (4.11) the perturbed electron temperature reads:

$$\tilde{T}_{e,m} = imT'_{e0}/f'_0\xi_m. \tag{4.12}$$

By taking the contravariant radial component of the curl of the Faraday-Ohm's law (Eq. (4.8)) we obtain at leading order:

$$\begin{aligned}\left(\partial_t - \frac{[p'_{0e}/n + 0.71T'_{e0}]}{f'_0 e}\partial_\vartheta + \boldsymbol{v}_{MHD}\cdot\boldsymbol{\nabla}\right)\sqrt{g}\tilde{B}^r = \\ - L_{||}\partial_\vartheta\left(\tilde{\Phi} + \frac{\tilde{p}_e}{en} + \frac{0.71\tilde{T}_e}{e}\right) + \eta\sqrt{g}\boldsymbol{\nabla}^2\tilde{B}^r,\end{aligned}$$

where Eqs. (4.11) and (4.12) have been used and $L_{||} = \iota\partial_\vartheta + \partial_\varphi$ is the parallel magnetic operator. Hence, neglecting the contribution from the perturbation of the toroidal flux f which will be shown *a posteriori* to be small, the equation for the mth Fourier component of the perturbed poloidal flux ψ reads:

$$D\psi_m = ik^m_{||}\xi_m, \qquad D = \left(1 - \frac{i\eta}{\hat{\omega} - \hat{\omega}^*_e}\frac{d^2}{dr^2}\right), \tag{4.13}$$

where $\hat{\omega}^*_e = \omega^*_e + \omega^T_e$, $\omega^*_e = -mp'_{0e}/(en_0f'_0)$, and $\omega^T_e = -m0.71T'_{e0}/(ef'_0)$. Since the resistive contribution is important only in a thin layer close to the resonant surface we approximate $\boldsymbol{\nabla}^2 \approx d^2/dr^2$.

We now derive an expression for the perturbation of the toroidal flux f. By taking the covariant φ projection of (4.6) and neglecting the inertial terms we obtain the radial contravariant perturbed current:

$$\tilde{J}^r = 1/\psi'_0[\partial_\varphi\tilde{p} + J^\vartheta_0\sqrt{g}\tilde{B}^r].$$

Using the Ampère's law and eq. (4.13), at leading order we get:

$$\tilde{B}_{\varphi m} = \frac{B_0}{m}\left\{\frac{nr}{mR_0}\partial_r[k^m_{||}rX_m] + q\frac{nR_0p'_0}{B_0^2}X_m - \frac{q}{B_0}F'_0k^m_{||}X_m\right\},$$

having used the relation $\tilde{p}_m \approx -p'_0X_m$ with $X_m = -\partial_\vartheta\xi_m/f'_0$. Therefore, assuming $\beta \sim \mathcal{O}(\varepsilon^2)$ and $k^m_{||} \sim \mathcal{O}(\varepsilon)$ with $q \approx m/n$, we have (F denotes the covariant φ

component of the magnetic field):

$$\tilde{F}_m = \tilde{B}_{\varphi m} = -\frac{R_0 \tilde{p}_m}{B_0}, \tag{4.14}$$

where (4.9) has been used. Equation (4.14) shows that the *mth* Fourier component of the toroidal flux f (cf. Eq. (4.1)) is $f_m \sim \mathcal{O}(\varepsilon^2)\xi_m$, allowing us to approximate $\sqrt{g}\tilde{B}^r \simeq -\partial_\vartheta \psi$. $\tilde{B}_{\varphi m}$ can be also found by means of Eq. (A6) in Ref. [97] under the same assumptions.

The expression for the compressible contribution to the plasma pressure ($\tilde{p} = p_1 + \delta p$) is found by projecting eq. (4.6) along $\boldsymbol{B}/B_0^2$. By means of the Faraday-Ohm's law with no resistive effects ($\psi = L_{||}\xi$) we note that:

$$\frac{\boldsymbol{B}_0}{B_0^2} \cdot \nabla(p_1 + \delta p) - \frac{\tilde{\boldsymbol{B}}}{B_0^2} \cdot \nabla p_0 = -(L_{||}\delta p)/B_{\varphi 0},$$

so that we are left with $\partial_t Z = -(L_{||}\delta p)/B_{\varphi 0}$, where $Z = \boldsymbol{v} \cdot \boldsymbol{B}_0/B_0^2$, $\tilde{B}^r/B_0^2 \simeq \sqrt{g}\tilde{B}^r/(f_0' F_0)$ and $\boldsymbol{B}_0/B_0^2 \cdot \boldsymbol{\nabla} = 1/F_0 L_{||}$ having ignored the resistive term in $\tilde{B}^r$. Therefore at leading order (neglecting longitudinal viscosity) the following expression is derived [98]:

$$\delta p = i\hat{\omega}\varrho F_0 L_{||}^{-1} Z.$$

From $\boldsymbol{\nabla} \cdot \boldsymbol{v}_i \approx 0$ [96] we have $\boldsymbol{B}_0 \cdot \boldsymbol{\nabla} Z = -\boldsymbol{\nabla} \cdot \boldsymbol{v}_{i\perp}$. At leading order, using the expression for the perturbed ion pressure (Eq. 4.10) we write [96]:

$$\boldsymbol{\nabla} \cdot \boldsymbol{v}_{i\perp} = \left(1 - \frac{\omega_i^*}{\hat{\omega}}\right) \boldsymbol{\nabla} \cdot \left(\frac{\boldsymbol{B}_0 \times \boldsymbol{\nabla}\tilde{\Phi}}{B_0^2}\right), \tag{4.15}$$

with $\omega_i^* = m p_{0i}'/(e n_0 f_0')$, under the assumption that ω_i^* and $\hat{\omega}$ do not depend upon the variable r. Thus using (4.15) and recalling that $B_0^\varphi = f_0'/\sqrt{g}$, we eventually find that the compressible contribution to the plasma pressure δp reads [83]:

$$\delta p = -i\left(\hat{\omega} - \omega_i^*\right) \varrho F_0 L_{||}^{-2} \sqrt{g}/f_0' [\tilde{\Phi}, \sqrt{g}/f_0'], \tag{4.16}$$

and the Poison bracket is defined as:

$$[A, B] = 1/\sqrt{g}\left(\partial_r A \partial_\vartheta B - \partial_\vartheta A \partial_r B\right).$$

$L_{||}^{-1}$ denotes the inverse operator of $L_{||}$, such that $L_{||}^{-1} L_{||} = L_{||} L_{||}^{-1} = I_d$, where I_d is the identity operator (here $L_{||}^{-2} = L_{||}^{-1} L_{||}^{-1}$).

Finally the vorticity equation is derived in the following manner. By applying the operator $\boldsymbol{\nabla}\varphi \cdot \boldsymbol{\nabla} \times 1/B^\varphi$ on (4.6), and taking the Fourier poloidal m component for a fixed toroidal number n after linearisation we have (equilibrium quantities are denoted by the subscript 0) [83, 98]:

$$i\sum_{m'}\Big[(m\iota - n)\boldsymbol{\Delta}^*_{m,m'} - (m-m')J'_{0m'} + m'J_{0m'}\partial_r\Big]\psi_{m-m'} + \\ \Big(\sqrt{g}\left[\tilde{p}, R^2/F_0\right] - p'_0\partial_\vartheta\left(R^2\tilde{F}/F_0^2\right) - \sqrt{g}I\Big)_m = H_m \tag{4.17}$$

where the inertial-like quantity I is given by:

$$I = \boldsymbol{\nabla}\cdot\left\{\left[\bar{\varrho}\left(\frac{\partial \boldsymbol{v}}{\partial t} + \boldsymbol{v}_0\cdot\boldsymbol{\nabla}\boldsymbol{v} + \boldsymbol{v}^*_{i0}\cdot\boldsymbol{\nabla}\boldsymbol{v}_\perp\right) - \mu_\perp\boldsymbol{\nabla}^2\boldsymbol{v}_i\right]\times\frac{\boldsymbol{\nabla}\varphi}{B_0^\varphi}\right\}, \tag{4.18}$$

and the H term is defined as:

$$H = L_{||}\left(J_0\sqrt{g}\tilde{B}^\varphi - \boldsymbol{\Theta}^*\tilde{f}\right) + J'_0\partial_\varphi\tilde{f}.$$

Finally, the average is defined as:

$$(\,\cdot\,)_{m'} = 1/(2\pi)\int_0^{2\pi}(\,\cdot\,)\exp(im'\vartheta)d\vartheta,$$

and the explicit formula for $\boldsymbol{\Delta}^*_{m,m'}$ is (we recall that $' \equiv \partial/\partial r$):

$$\boldsymbol{\Delta}^*_{m,m'}\chi = \frac{\partial}{\partial r}\left[\left(\frac{g_{\vartheta\vartheta}}{\sqrt{g}}\right)_{m'}\frac{\partial\chi}{\partial r}\right] - i\,(2m-m')\left(\frac{g_{r\vartheta}}{\sqrt{g}}\right)_{m'}\chi' \\ -(m-m')\left[i\left(\frac{g_{r\vartheta}}{\sqrt{g}}\right)'_{m'} + m\left(\frac{g_{rr}}{\sqrt{g}}\right)_{m'}\right]\chi.$$

We are now ready to solve the generic set of equations (4.13), (4.14) and (4.17) together with the equation for the plasma pressure given by the sum of (4.9) and (4.16) in the *low-shear region*, the *sheared region* and the *resonant layer region* (see Fig. 4.2).

4.5 Low-shear region

In the low-shear region we assume a constant toroidal flow and a generalised parabolic equilibrium pressure profile $p_0 = \bar{p}(1-(r/r_0)^2)$ with $r_0 > r_*$ where the factor r_0 controls the peaking of the pressure (see Fig. 4.2) and $\bar{p}$ denotes the value of the pressure on the magnetic axis. We allow for ion diamagnetic effects. With a parabolic p_0, the ω^* and $\hat{\omega}$ frequencies do not depend upon the radial variable r, so that the differential operators do not act on these quantities. Note that with this pressure profile we have that $\beta = \bar{p}/B_0^2(r_0/a_0)^2$ [86]. The fluid-like displacement ξ is expanded as follows:

$$\tilde{\xi} = \xi_{m_0} e^{im_0\vartheta - in\varphi} + \varepsilon \xi_{m_0\pm1} e^{i(m_0\pm1)\vartheta - in\varphi} + \mathcal{O}(\varepsilon^2)$$

where m_0 is the mode number of the main poloidal harmonic. The ordering adopted here assumes $k_{||}^{m_0} \sim \omega/\omega_A \sim \omega_{i,e}^*/\omega_A \sim \varepsilon$ and $p_0/B_0^2 \sim \varepsilon^2$ where $\omega_A = V_A/R_0$, $V_A = B_0/\sqrt{\bar{\varrho}}$ and $\bar{\varrho}$ is the value of the density on the magnetic axis. Since the density profile is assumed slowly varying, so that a reasonable approximation is to take a constant density implying that ω_A is constant. Thus the pressure gradients are entirely due to temperature gradients. In this region the exact resonances $q = m_0/n$ and $q = (m_0 \pm 1)/n$ are avoided, hence the resistive corrections can be neglected (this yields $D = 1$, cf. Eq. (4.13)) [58]. In addition we assume that the plasma core is sufficiently hot, so that collisional effects, i.e. viscosity, can be dropped. Thus by means of (4.15), the following expression for the inertial term is obtained:

$$(\sqrt{g} I)_{m_0} \approx -\hat{\omega}\left(\hat{\omega} - \omega_i^*\right) \frac{r R_0 \bar{\varrho}}{B_0^2} \mathbb{T}_{m_0}(\xi_{m_0})$$

with $\mathbb{T}_m(\zeta) = 1/r^2 \Big\{ \frac{d}{dr}\left[r^3 \frac{d}{dr}\left(\frac{\zeta}{r}\right)\right] + (1-m^2)\zeta \Big\}$. In the derivation of the above expression it has been assumed that at leading order the magnetic field is straight and uniform, thus fulfilling the requirements of the gyro-viscous cancellation [92].

Using the expressions for the metric tensor coefficients (4.3), it turns out that [98]:

$$q^2\{L_{||}^2 \delta p, \sqrt{g}/f_0'\}_{m_0} = -(\sqrt{g}[\delta p, \sqrt{g}/f_0'])_{m_0}, \tag{4.19}$$

where $\{A, B\} = \partial_r A \partial_\vartheta B + \partial_\vartheta A \partial_r B$ (the details of the derivation are given in Appendix A.2). Thus from Eq. (4.16), with the approximation $T_0/f_0' \simeq R_0/r$, we write:

$$[L_{||}^2 \delta p' \partial_\vartheta(\sqrt{g}/f_0')]_m = -2i\omega(1 - \omega_i^*/\hat{\omega})\varrho R_0/B_0^2 r \Phi_m'',$$
$$[\partial_\vartheta L_{||}^2 \delta p(\sqrt{g}/f_0')']_m = 2i\omega(1 - \omega_i^*/\hat{\omega})\varrho R_0/B_0^2 [\Phi_m' - m^2\Phi_m/r].$$

Thus adding the two equations above and using (4.19) we obtain:

$$(\sqrt{g}[\delta p, \sqrt{g}/f_0'])_{m_0} = -i\omega(1 - \omega_i^*/\hat{\omega})\varrho R_0 2/(rB_0^2)[r^2\Phi_{m_0}'' + r\Phi_{m_0}' - m_0^2\Phi_{m_0}],$$

which eventually leads to:

$$\left(\sqrt{g}\,[\delta p, 1/B_0^\varphi]\right)_{m_0} = \hat{\omega}\left(\hat{\omega} - \omega_i^*\right) \frac{r R_0 \bar{\varrho} 2 q^2}{B_0^2} \mathbb{T}_{m_0}(\xi_{m_0}). \tag{4.20}$$

This result extends the Glasser, Green, Johnson inertia enhancement [68], for the case of extended low shear and with diamagnetic effects.

By using (4.13), from (4.17) three coupled equations are derived which at leading order are written as:

$$
\begin{aligned}
& iL_0^{m_0}(k_{||}^{m_0}\xi_{m_0}) + K_2^{m_0}\xi_{m_0} + \boldsymbol{\Lambda}_\omega \mathbb{T}_{m_0}(\xi_{m_0}) + \\
& \sum_{\pm}\Big(iL_1^{m_0,\mp 1}(k_{||}^{m_0\pm 1}\xi_{m_0\pm 1}) + K_1^{m_0,\mp 1}\xi_{m_0\pm 1}\Big) = 0, && (4.21)\\
& L_0^{m_0\pm 1}\psi_{m_0\pm 1} + K_1^{m_0\pm 1,\pm 1}\xi_{m_0} = 0, && (4.22)\\
& L_0^{m_0-1}\psi_{m_0-1} + K_1^{m_0-1,-1}\xi_{m_0} = 0, && (4.23)
\end{aligned}
$$

where the sum is carried over the neighbouring sidebands, $\boldsymbol{\Lambda}_\omega = r/(R_0\omega_A^2)(\hat{\omega} - \omega_i^*)[\hat{\omega}(1+2q^2)]$, and from (4.3) we have defined the following operators:

$$
\begin{aligned}
L_0^m\zeta &= \frac{i}{R_0}\Big\{k_{||}^m\left[(r\zeta')' - m^2\zeta/r\right] - [(r^2k_{||}^m)'/r]'\zeta\Big\},\\
K_2^m\zeta &= m^2\left[\left(\frac{\langle R^2\rangle}{F_0}\right)'\frac{p_0'}{f_0'} - \frac{p_0'^2R_0}{B_0F_0^2f_0'}\langle R^2\rangle\right]\zeta,\\
L_1^{m,m'}\zeta &= i\Big[(m\iota - n)\boldsymbol{\Delta}^*_{m,m'} - (m-m')J'_{0m'} + m'J_{0m'}\partial_r\Big]\zeta,\\
K_1^{m,m'}\zeta &= \left(\frac{\sqrt{g}}{f_0'}\right)'_{m'}(m-m')^2\frac{p_0'}{f_0'}\zeta - m'(m-m')\left(\frac{\sqrt{g}}{f_0'}\right)_{m'}\left[\frac{p_0'}{f_0'}\zeta\right]'.
\end{aligned}
$$

After some lengthy algebra, we have from (4.14) (for more details see appendix A.2):

$$
K_2^{m_0}\xi_{m_0} \simeq \frac{2p_0'm_0^2}{rB_0^2}\left[\frac{R_0p_0'q^2}{B_0^2} + \frac{r}{R_0}\left(\frac{1}{q^2} - 1\right)\right]\xi_{m_0}, \tag{4.24}
$$

$$
\left(k_{||}^{m_0\mp 1}L_1^{m_0,\pm 1} + K_1^{m_0,\pm 1}\right)\xi_{m_0\mp 1} \simeq \mp\frac{m_0p_0'}{rB_0^2}r^{\pm m_0}\left(r^{1\mp m_0}\xi_{m_0\mp 1}\right)', \tag{4.25}
$$

having used the fact that $k_{||}^{m_0\pm 1}$ is a constant and the relation (cf. Eq. (4.2)):

$$
\frac{1}{2\pi}\int_0^{2\pi}J_0e^{\pm i\vartheta}d\vartheta = \frac{\iota r}{2R_0}\left[\Delta'' + \frac{3\Delta'}{r} - \frac{1}{R_0}\right] = -\frac{p_0'q}{B_0^2}.
$$

After introducing the fluid displacements $X_{m_0} = -\partial_\vartheta\xi_{m_0}/f_0'$, $X_\pm = -\partial_\vartheta\xi_{m_0\pm 1}/f_0'$, Eqs. (4.21), (4.22) and (4.23) can also be written in a compact form as [35, 99]:

$$
\begin{aligned}
\frac{d}{dr}\left[r^3Q\frac{dX_{m_0}}{dr}\right] + r\left[(1-m_0^2)Q - \frac{\alpha^2}{2q^2} + \frac{\alpha r}{R_0q^2}\left(\frac{1}{q^2} - 1\right)\right]X_{m_0} + \\
\frac{\alpha}{2q^2}\left[\frac{r^{-m_0}}{m_0+1}\left(r^{2+m_0}X_+\right)' - \frac{r^{m_0}}{m_0-1}\left(r^{2-m_0}X_-\right)'\right] = 0 \qquad (4.26)
\end{aligned}
$$

$$
\left[r^{-1\mp 2m_0}\left(r^{2\pm m_0}X_\pm\right)'\right]' = \pm\frac{m_0 \pm 1}{2}\left[\alpha r^{\mp m_0}X_{m_0}\right]' \tag{4.27}
$$

where $Q = \delta q^2/q^4 - \hat{\omega}(\hat{\omega} - \omega_i^*)(1 + 2q^2)/(m_0^2\omega_A^2)$, $\delta q = q - m_0/n$ and $\alpha = -(2R_0p_0'q^2)/B_0^2$. We also used the relation [92]:

$$\frac{k_{||}}{r}\left\{\frac{d}{dr}\left[r\frac{d}{dr}\left(k_{||}\xi\right)\right] - \frac{m^2k_{||}}{r}\xi - \frac{d}{dr}\left[\frac{1}{r}\frac{d(r^2k_{||})}{dr}\right]\xi\right\} = \\ \frac{1}{r^2}\left\{\frac{d}{dr}\left[r^3k_{||}^2\frac{d}{dr}\left(\frac{\xi}{r}\right)\right] - (m^2-1)k_{||}^2\xi\right\}.$$

Equations (4.26) and (4.27) form a coupled system for the magnetic perturbation in the low-shear region which are to be matched with the eigen-solution in the sheared region. This matching will eventually give the dispersion relation. It is also important to note that the factor Q contains all the non-ideal terms in the low-shear region. We stress the point that since the m_0/n resonance is avoided, the only non-negligible non-ideal effect is the ion diamagnetism. Viscosity and resistivity will instead enter the problem via the $(m_0 + 1)/n$ sideband.

4.6 Sheared region

It is convenient to describe the sideband magnetic perturbation in terms of the fluid displacement X. This is linked to the poloidal flux by the relation (cf. (4.13)):

$$\psi_m = -(f_0'k_{||}^m/m)X_m. \tag{4.28}$$

In the external region, the leading order of equation (4.21) is given by $L_0^{m_0}\psi_{m_0} = 0$ which can be written as:

$$\frac{d}{dr}\left[r^3\left(k_{||}^{m_0}\right)^2\frac{dX_{m_0}}{dr}\right] - r(m_0^2-1)\left(k_{||}^{m_0}\right)^2X_{m_0} = 0. \tag{4.29}$$

We multiply the previous expression by X_{m_0} and we integrate between r_* and a [92], imposing the boundary condition $X_{m_0}(a_0) = 0$ and assuming no strong radial excursions. Since $k_{||}^{m_0}(r_*) \sim \mathcal{O}(\varepsilon)$, it then follows that at leading order $X_{m_0} = 0$. In this region, the equations for the sidebands are then given by $L_0^{m_0\pm1}\psi_{m_0\pm1} = 0$ which can be written in a form similar to (4.29) with the obvious substitution $m_0 \to m_0 \pm 1$ [35, 99]. An exact analytic solution for X_+ can be found for ι profiles defined as $\iota(r) = \iota_1 + \iota_2(r/r_s)^\lambda$. The constants ι_1 and ι_2 are chosen such that $\iota(r_*) = n/m_0 - \delta q$ and $\iota(r_s) = n/(m_0+1)$. If $r_* \ll r_s$ then:

$$(m_0+1)\iota - n \approx n/m_0[1-(r/r_s)^\lambda] \tag{4.30}$$

which corresponds to the model safety factor used in Ref. [84]. Introducing the variable $z = (r/r_s)^\lambda$, the equation for the $m = m_0 + 1$ sideband is written in this convenient form:

$$\frac{d}{dz}\left[z^{2/\lambda+1}\left(1-z\right)^2\frac{dX_+}{dz}\right]-\frac{m^2-1}{\lambda^2}z^{2/\lambda-1}\left(1-z\right)^2X_+=0. \tag{4.31}$$

When the equation above is augmented by finite β effects, an analytic solution is derived in Ref. [83] for the particular case $\lambda = 2$ with parabolic pressure p. A solution with a general λ for a logarithmic pressure profile is given in Appendix A.3. When $z < 1$, i.e. $r < r_s$, the solutions of (4.31) can be expressed as a combination of hypergeometric functions [83, 100, 101]:

$$\begin{aligned} X_+ = z^{(m-1)/\lambda}(1-z)^{-1}\Big(&A_1^*F(a,b;a+b+1;z)+\\ &B_1^*z^{-a-b}F(-b,-a;1-a-b;z)\Big) \end{aligned} \tag{4.32}$$

where we defined $a = (m-\bar{m})/\lambda$, $b = (m+\bar{m})/\lambda$, $\bar{m} = \sqrt{m^2+2\lambda+\lambda^2}$ and for convenience $A_1^* = A_1\frac{ab\Gamma(a)\Gamma(b)}{\Gamma(1+a+b)}$ and $B_1^* = B_1\frac{ab\Gamma(-a)\Gamma(-b)}{\Gamma(1-a-b)}$. If $(r_*/r_s)^\lambda \ll 1$, far from the resonant surface, i.e. for $z \ll 1$, it is easy to see that

$$X_+ \sim \left(\frac{r}{r_*}\right)^{m_0} + C_0\left(\frac{r}{r_*}\right)^{-(2+m_0)} \tag{4.33}$$

where $C_0 = (r_*/r_s)^{-2m_0-2}B_1^*/A_1^*$, which recovers the asymptotic behaviour found in proximity of r_* [84]. Conversely, when $z > 1$, i.e. $r > r_s$, the solution of (4.31) reads [83, 100, 101]:

$$\begin{aligned} X_+ = z^{-(1+\bar{m})/\lambda}(z-1)^{-1}\Big(&A_2^*F\left(b,-a;1+b-a;1/z\right)+\\ &B_2^*z^{b-a}F(-b,a;1+a-b;1/z)\Big) \end{aligned} \tag{4.34}$$

where $A_2^* = -A_2\frac{ab\Gamma(-a)\Gamma(b)}{\Gamma(1-a+b)}$ and $B_2^* = -B_2\frac{ab\Gamma(a)\Gamma(-b)}{\Gamma(1+a-b)}$. The constant B_2^* is found by imposing the condition $X_+(a_0) = 0$, which eventually gives:

$$B_2^* = -\left(\frac{r_s}{a_0}\right)^{2\bar{m}}\frac{F(b,-a;1-a+b;(r_s/a_0)^\lambda)}{F(-b,a;1+a-b;(r_s/a_0)^\lambda)}A_2^*,$$

which can be written as $B_2 = D_0A_2$ where [83]

$$D_0 = -\left(\frac{r_s}{a_0}\right)^{2\bar{m}}\frac{F(b,-a;1-a+b;(r_s/a_0)^\lambda)}{F(-b,a;1+a-b;(r_s/a_0)^\lambda)}\times\frac{\Gamma(-a)\Gamma(b)\Gamma(1+a-b)}{\Gamma(a)\Gamma(-b)\Gamma(1-a+b)}.$$

Defining $\Delta' := \psi'_+/\psi_+|_{r_s-}^{r_s+}$ [16], expressing (4.32) and (4.34) in terms of ψ by means of (4.28), after some straightforward algebra making use of the approximate formula for the hypergeometric function in the limit $|1-z| \ll 1$ namely (Ref. [102] p. 555):

$$F(a,b;a+b+1,z) \simeq \frac{\Gamma(a+b+1)}{\Gamma(a)\Gamma(b)}\{1/(ab)-(z-1)\times \\ \times[\ln(1-z)-\Psi(1)-\Psi(2)+\Psi(a+1)+\Psi(b+1)]\},$$

where Ψ is the Digamma function (Ref. [102] p. 253), we can express the ratio B_1/A_1 as a function of Δ':

$$B_1/A_1 = -\frac{A_0 - \frac{D_0}{1+D_0}(A_0+B_0+\bar{m}) - r_s\Delta'}{B_0 - \frac{D_0}{1+D_0}(A_0+B_0+\bar{m}) - r_s\Delta'}, \tag{4.35}$$

where A_0 and B_0 represent respectively the logarithmic jumps across r_s of the regular and diverging eigenfunctions at the origin ad are given by:

$$A_0 = m+\bar{m}-(m^2-\bar{m}^2)/\lambda[\Psi(-a)-\Psi(a)] = -\frac{(\pi\cot\pi a)}{\lambda}(m^2-\bar{m}^2), \tag{4.36}$$

$$B_0 = (\pi\cot\pi b)(m^2-\bar{m}^2)/\lambda. \tag{4.37}$$

For the sake of simplicity we assume that $(r_s/a_0)^{2\bar{m}} \ll 1$, hence the quantities involving D_0 can be neglected, so that the parameter C_0 is written as:

$$C_0 = -\frac{\Gamma(-a)\Gamma(-b)\Gamma(1+a+b)}{\Gamma(a)\Gamma(b)\Gamma(1-a-b)}\frac{A_0-r_s\Delta'}{B_0-r_s\Delta'}\left(\frac{r_*}{r_s}\right)^{-2m_0-2}.$$

The parameter Δ' will be computed by solving the equation for X_+ in the resistive resonant layer as shown in the next section.

4.6.1 WKB approach for more general q profiles

When we have a more generic q profile, the WKB approximation can be used for the evaluation of the coefficients A_0, B_0 and G_0 [29]. The analysis is split into two regions, one far away from r_s, called outer region and a one close to such surface, called inner region. Assuming that ψ_m varies more rapidly than the equilibrium quantities [29], in the outer region the equation governing the magnetic perturbation can be written as $\delta^2\psi_m'' = U\psi_m$ where $U = 1/r^2 + \langle R_0J_0\rangle'/[m(m\iota-n)]$ and $\delta = 1/m$ (finite β effects can also be retained, see Appendix B, § B.2.2) . Far from the rational surface, treating δ as a smallness parameter [29], the WKB solution to leading order in δ reads:

$$\psi_m^{out} = \sum_{\pm} A^{\pm}_{\lessgtr}\exp\left[\pm m\left(\int_{r_s}^{r}\frac{d\tilde{r}}{\tilde{r}} + \int^{r}\frac{\tilde{r}^2\langle R_0J_0\rangle' d\tilde{r}}{2m(m\iota-n)}\right)\right],$$

where the subscript $>$ ($<$) refers to $r>(<)r_s$, having used the relation $\sqrt{U} \approx 1/r + r\langle R_0 J_0\rangle'/[2m(m\iota - n)]$. If $r \ll r_s$ then

$$\psi_m^{out} = A^+_{\lessgtr}(r/r_s)^m + A^-_{\lessgtr}(r/r_s)^{-m}, \tag{4.38}$$

while when the resonant surface is approached, introducing the variable $z = 2m/(r_s q_s')(q - m/n)$ [29] the inner limit of the outer solution is:

$$\psi_m^{out} = \begin{cases} A^+_<|z|^\Lambda e^{-|z|/2} + A^-_<|z|^{-\Lambda}e^{|z|/2}, & z<0 \\ A^+_> z^\Lambda e^{z/2} + A^-_> z^{-\Lambda}e^{-z/2}, & z>0, \end{cases}$$

where $\Lambda = -q_s\langle R_0 J_0\rangle_s'/(2nq_s')$. Boundary layer theory is used in the inner region. The equation governing the poloidal flux ψ_m in the inner region is $d^2\psi_m^{in}/dz^2 - (1/4 + \Lambda/z)\psi_m^{in} = 0$ [29] whose solution is written as a combination of Whittaker functions (ref [102] p. 503):

$$\psi_m^{in} = \begin{cases} \Gamma(1-\Lambda)W_{\Lambda,1/2}(|z|) + B_< M_{\Lambda,1/2}(|z|), & z<0 \\ \Gamma(1+\Lambda)W_{-\Lambda,1/2}(z) + B_> M_{-\Lambda,1/2}(z), & z>0. \end{cases}$$

Asymptotic matching between the inner and outer solutions gives $A^+_< = \Gamma(1-\Lambda)$, $A^-_> = \Gamma(1+\Lambda)$, $A^-_< = B_</\Gamma(1-\Lambda)$ and $A^+_> = B_>/\Gamma(1+\Lambda)$. Imposing the boundary condition $\psi_m(a_0) = 0$ we obtain $B_> = -\Gamma^2(1+\Lambda)(r_s/a_0)^{2m}$; thus if $(r_s/a_0)^{2m} \ll 1$, the term proportional to $B_>$ can be dropped. Therefore $B_<$ is expressed as a function of the tearing stability index [29]:

$$B_< = \pi\Lambda\cot(\pi\Lambda) + r_s\Delta'/(2m), \tag{4.39}$$

and the following replacements have to be performed:

$$C_0 = B_</\Gamma^2(1-\Lambda)(r_s/r_*)^{2m}, \tag{4.40}$$
$$A_0 = 2(m_0+1)[-C_1\bar{C}/(2+2m_0+C_1) - \pi\Lambda\cot(\pi\Lambda)], \tag{4.41}$$
$$B_0 = 2(m_0+1)[\bar{C}(2+2m_0-C_1)/C_1 - \pi\Lambda\cot(\pi\Lambda)], \tag{4.42}$$

where $C_1 = mr_*\iota'(r_*)/(m\iota(r_*)-n)$ and $\bar{C} = \Gamma^2(1-\Lambda)(r_*/r_s)^{2m}$ $(m = m_0+1)$. If the magnetic shear is small on the surface $r = r_*$, the previous expressions can be simplified giving $A_0 = -2m\pi\Lambda\cot(\pi\Lambda)$, $B_0 = -\frac{4m\Gamma^2(1-\Lambda)(r_*/r_s)^{2m}}{\hat{s}_*}$.

4.7 Resonant $(m_0+1)/n$ layer region

In the limit $r\partial/\partial r \gg 1$, introducing the layer variable $x = (r-r_s)/r_s$, from (4.13) and (4.17) we obtain two coupled differential equations [67, 103] which in Fourier representation $\hat{\xi}(k) = \mathcal{F}\xi(x) = 1/\sqrt{2\pi}\int_{-\infty}^{\infty}\xi(x)\exp[-ikx]dx$ can be combined in one single equation for the $m = m_0 + 1$ harmonic which reads [72, 103, 104]:

$$\frac{d}{dk}\left(\frac{k^2}{1+\delta_\eta k^2}\frac{d\hat{\xi}}{dk}\right) - \delta_0\delta_I k^2\hat{\xi} - \delta_0\delta_\mu k^4\hat{\xi} = 0 \tag{4.43}$$

where $\delta_0 = -(\hat{\omega} - \omega_i^*)_s/(m\hat{s}_s\omega_A/q_s)^2$ (the subscript s means that the quantity is evaluated at $r = r_s$), $\delta_\eta = iS^{-1}\omega_A/(\hat{\omega} - \omega_e^* - \omega_e^T)_s$, $\delta_I = \hat{\omega}_s(1 + 2q_s^2)$ and $\delta_\mu = i(\mu_\perp/r_s^2)/\bar{\varrho}$, $S = \tau_R/\tau_A$ is the Lundquist number where $\tau_R = r_s^2/\eta$ and $\tau_A = 1/\omega_A$. The solution of (4.43) must fulfil the boundary condition

$$\lim_{k\to\infty}\hat{\xi}(k) = 0. \tag{4.44}$$

and can be chosen having definite parity, i.e. even ($\hat{\xi}_e$) or odd ($\hat{\xi}_o$).

The solution procedure broadly follows the approach of Ref. [72], matching the solutions obtained in the regions $k \gg 1$ and $0 < k \ll 1$ in the *constant* $-\ \psi$ approximation limit ($\delta_0\delta_I \ll \delta_\eta$) provided by the condition $\delta\Delta' \ll 1$ [105], viz. for sufficiently small diamagnetic frequencies, where δ is the layer thickness. When $k \ll 1$ the approximate equation for $\hat{\xi}$ is (we set $d/dk \sim 1/k$) [72]:

$$\frac{d}{dk}\left(\frac{k^2}{1+\delta_\eta k^2}\frac{d\hat{\xi}}{dk}\right) = 0 \tag{4.45}$$

whose solution is $\hat{\xi} = -c_0/k + c_0\delta_\eta k + c_1$. For k large we have:

$$\frac{d^2\hat{\xi}}{dk^2} - \delta_\eta\delta_0\delta_j k^\gamma\hat{\xi} = 0 \tag{4.46}$$

where $\gamma = 2$ and $\delta_j = \delta_I$ in the resistive regime, while $\gamma = 4$ and $\delta_j = \delta_\mu$ in the viscous-resistive regime. The resistive/viscous solutions of (4.46) which fulfil (4.44) are $\hat{\xi} \sim D_{-1/2}(\sqrt{2}\delta_*^R k)$ and $\hat{\xi} \sim k^{1/2}K_{1/6}(\delta_*^V k^3/3)$ respectively, where [72, 104]:

$$\delta_*^R = (\delta_0\delta_I\delta_\eta)^{1/4}, \tag{4.47}$$

$$\delta_*^V = (\delta_\eta\delta_0\delta_\mu)^{1/6}; \tag{4.48}$$

D and K denote the parabolic cylinder and modified Bessel functions respectively. Matching the solution of (4.45) with the solution of (4.46) in the limit $k \gg 1$ and

$k \ll 1$ respectively, the following expression close to the origin in k space is obtained[2]:

$$\hat{\xi} \simeq \begin{cases} 1 + \dfrac{1}{k}\left[\dfrac{2\Gamma(3/4)}{\Gamma(1/4)}\dfrac{(\delta_0\delta_I)^{1/4}}{\delta_\eta^{3/4}}\right] = 1 + \Delta_R/k, & \text{(resistive)}, \\ 1 + \dfrac{1}{k}\left[\dfrac{6^{2/3}\Gamma(5/6)}{\Gamma(1/6)}\dfrac{(\delta_0\delta_\mu)^{1/6}}{\delta_\eta^{5/6}}\right] = 1 + \Delta_V/k, & \text{(visco-resistive)}, \end{cases}$$

where $\Delta_R = 2\Gamma(3/4)/\Gamma(1/4)\delta_0^{1/4}\delta_I^{1/4}\delta_\eta^{-3/4}$ and $\Delta_V = 6^{2/3}\Gamma(5/6)/\Gamma(1/6)\delta_0^{1/6}\delta_\mu^{1/6}\delta_\eta^{-5/6}$. Thus the even (e) and odd (o) functions are written as $\hat{\xi}_{e,o} \sim (1+\Delta_{R,V}|k|^{-1})[sign(k)]^p$ where $p=0$ for the even solution and $p=1$ for the odd one. We explicitly invert $\hat{\xi}_o$ via the following relations [106]:

$$\mathcal{F}^{-1}\left(1/k\right) = -i\sqrt{\pi/2}sign(x), \qquad \mathcal{F}^{-1}(sign(k)) = \sqrt{2/\pi}/(ix),$$

giving $\xi_o(x) \sim 1/x + \pi\Delta_{R,V}/2sign(x)$. Adopting the notation employed in Ref. [83] using also (4.13), in the outer region we can write $\xi^{out}_{\lessgtr} = \Xi_0/x(1+\Delta_{c,p}|x|)$ where the logarithmic term in ψ has been neglected [83] and $r_s\Delta' = \Delta_c + \Delta_p$ where $<$ $(>)$ stands for $x < (>) 0$. The inner solution for ξ^{in} is written as a combination of even and odd functions $\mathcal{E}_\pm$ which have to be matched with the outer solution:

$$\xi^{in}_{>} = \mathcal{E}_+ + \mathcal{E}_- = \Xi_0\Big(1/|x| + \Delta_c\Big) \tag{4.49}$$

$$\xi^{in}_{<} = \mathcal{E}_+ - \mathcal{E}_- = -\Xi_0\Big(1/|x| + \Delta_p\Big) \tag{4.50}$$

where $\mathcal{E}_+ = \mathcal{F}^{-1}\hat{\xi}_e$ and $\mathcal{E}_- \sim 1/|x| + \pi\Delta_{R,V}/2$. Subtracting (4.50) from (4.49) we get $2\mathcal{E}_- = \Xi_0(2/|x| + \Delta_c + \Delta_p)$, which finally gives the dispersion relation:

$$r_s\Delta' = \begin{cases} \pi\Delta_R, & \text{(resistive)}, \\ \pi\Delta_V, & \text{(visco-resistive)}. \end{cases} \tag{4.51}$$

After matching the parameter $r_s\Delta'$ in the sheared region with $r_s\Delta'$ calculated in the resonant layer region, we then simplify substituting (4.51) into (4.35) to yield B_1 in terms of A_1. In order to obtain the final dispersion relation, a further match between the solution in the low-shear and sheared region is required, as shown in

---

[2] Let us take the Fourier transform, in one dimension, of the function f (which is assumed to be well behaved) defined as $\hat{f} = 1/\sqrt{2\pi}\int_{-\infty}^{\infty}\exp[-ikx]f(x)dx$. We note that for large k the exponential is highly oscillating, therefore we have almost no contributions to the integral unless the variable x is in the neighbourhood of the origin. Thus we are left with

$$\hat{f}(k \gg 1) \approx \frac{1}{\sqrt{2\pi}}\int_{-\infty}^{+\infty} dx \exp[ikx]f(x \ll 1).$$

Hence the behaviour for large k in the Fourier space is translated in real space into the behaviour for small x and vice versa.

the next section.

4.8 Eigenfunctions and eigenvalues

In the preceding section, we have an equation for the eigenfunctions in the low-shear region (cf. Eqs. (4.27)) and in the high shear region (cf. Eqs. 4.32), (4.34) and (4.51)). In order to obtain a dispersion relation, we match smoothly these equations at r_*, which is the radial position close to the transition point between high and low shear regions. Integrating (4.27) and assuming regularity at $r = 0$, we get:

$$X_+ = \tilde{A}_+ r^{m_0} + r^{-2-m_0}\frac{m_0+1}{2}\int_0^r \alpha\tilde{r}^{1+m_0}X_{m_0}d\tilde{r}. \tag{4.52}$$

We note that the first integral of (4.27) for X_- gives:

$$(r^{2-m_0}X_-)' = \tilde{A}_- r^{1-2m_0} - \frac{m_0-1}{2}\alpha r^{1-m_0}X_{m_0}.$$

By imposing X_- to be regular on the magnetic axis, it follows necessarily that $\tilde{A}_- = 0$. Therefore matching (4.52) with the eigensolution X_+ in the sheared region across $r = r_*$ (viz. imposing continuity for X_+ and X_+' [3]), we find:

$$\tilde{A}_+ = r_*^{-2-2m_0}\boldsymbol{\Lambda}^{\omega}_{m_0,n}\int_0^{r_*}\alpha r^{1+m_0}X_{m_0}dr,$$

where $\boldsymbol{\Lambda}^{\omega}_{m_0,n} = [(m_0+1)/2](2+m_0+\boldsymbol{C})/(m_0-\boldsymbol{C})$ and $\boldsymbol{C} = r_*X_+'(r_{*+})/X_+(r_{*+})$ [35]; hence, the following expression for the main m_0 harmonic which fulfils the regularity conditions at the origin, is obtained [35, 58]:

$$\frac{d}{dr}\left[r^3 Q\frac{dX_{m_0}}{dr}\right] + r\left[(1-m_0^2)Q + \frac{\alpha r}{R_0 q^2}\left(\frac{1}{q^2}-1\right)\right]X_{m_0} + \\ r_*^{-2-2m_0}\frac{\boldsymbol{\Lambda}^{\omega}_{m_0,n}}{q^2}\alpha r^{m_0+1}\int_0^{r_*}\alpha r^{1+m_0}X_{m_0}dr = 0. \tag{4.53}$$

Making use of (4.33), we obtain $\boldsymbol{C} = m_0\frac{1-(1+2/m_0)C_0}{1+C_0}$, thus $\boldsymbol{\Lambda}^{\omega}_{m_0,n} = (m_0+1)/(2C_0)$, where C_0 is evaluated using (4.35) with $r_s\Delta'$ given by (4.51).

---

[3] Let us call $B = \frac{m_0+1}{2}\int_0^r \alpha\tilde{r}^{1+m_0}X_{m_0}d\tilde{r}$ so that $X_+ = \tilde{A}_+ r^{m_0} + r^{-2-m_0}B$. Hence we have:

$$(2+m)X_+(r_{*+}) = (2+m)[r_*^{m_0}\tilde{A}_+ + r_*^{-2-m_0}B],$$
$$r_*X_+(r_{*+})' = m_0 r_*^{m_0}\tilde{A}_+ - (2+m_0)r_*^{-2-m_0}B.$$

If we sum the two expressions above we obtain $X_+(r_{*+}) = 2(m+1)r_*^m\tilde{A}_+/[2+m+r_*X'(r_{*+})/X(r_{*+})]$ which is plugged in the equation for $X(r_{*+})$ giving $\tilde{A}_+ = Br^{-2-2m}(2+m+\boldsymbol{C})/(m-\boldsymbol{C})$ with $\boldsymbol{C} = r_*X'(r_{*+})/X(r_{*+})$.

Equation (4.53) generalises the resistive infernal mode analytic results of Charlton et al. to include η, $mu_\perp$, ω^* effects and shear flow. These additional effects are contained in the quantities Q and $\mathbf{\Lambda}^{\omega}_{m_0,n}$. Q contains the effect of the inertia of the main m_0 mode and the effect of diamagnetic ions in the low shear region. The parameter $\mathbf{\Lambda}^{\omega}_{m_0,n}$ contains the layer physics which includes resistivity, viscosity and diamagnetic effects (for ions and electrons) at the $q = (m_0+1)/n$ resonant surface. In the next sections we examine in more detail the cases $m_0 = n$ and $m_0 \neq n$.

4.8.1 Case $m_0 = n$

This situation corresponds to a value of q in the low shear region close to unity. The pressure profile in the low shear region is taken as $p = \bar{p}(1-(r/r_0)^2)$ for $0 \leq r \leq r_0$, with $r_* \leq r_0 \leq a_0$, and $p = 0$ elsewhere [86] (cf. Fig. 4.2) where the coefficient r_0 is used to control the peaking of the pressure. A parabolic pressure profile in the low-shear region implies constant ω^* frequencies. Dropping the $(1/q^2 - 1)$ term, which is small for $m_0 = n$, Eq. (4.53) can be solved analytically by using the method of variation of parameters imposing the integral condition [86]:

$$\int_0^{r_*} \alpha r^{m_0+1} X_{m_0} dr = 1. \tag{4.54}$$

The solution therefore reads (q is the value of the safety factor in the low-shear region):

$$X_{m_0} = -\frac{2R_0\bar{p}}{a^2B_0^2}\frac{q^2\mathbf{\Lambda}_{m_0,n}r_*^{-2m_0}}{Q(m_0+1)}\left[r^{m_0-1} - r^{m_0+1}/r_*^2\right].$$

Plugging the equation above into Eq. (4.54), the following eigenvalue relation is obtained:

$$\frac{\hat{\omega}(\hat{\omega}-\omega_i^*)}{\omega_A^2} = \frac{n^2}{1+2q^2}\left[\left(\frac{\delta q}{q}\right)^2 - \frac{2\varepsilon_*^2\mathbf{\Lambda}^{\omega}_{m_0,n}\beta_p^2}{(m_0+1)^2(m_0+2)}\right], \tag{4.55}$$

where $\varepsilon_* = r_*/R_0$ and $\beta_p = \bar{p}q^2/(B_0^2\varepsilon_0^2)(a_0/r_0)^4$ with $\varepsilon_0 = a_0/R_0$. Hence the eigenvalue relation can be written as ($\omega_A = 1$):

$$\hat{\omega}(\hat{\omega}-\omega_i^*) = \frac{n^2}{1+2q^2}\left[\delta q^2 + \beta_p^2 G_0\frac{B_0 - r_s\Delta'}{A_0 - r_s\Delta'}\right], \tag{4.56}$$

where we define:

$$G_0 = \begin{cases} \dfrac{\varepsilon_*^2 (r_*/r_s)^{2m_0+2}}{(m_0+1)(m_0+2)} \dfrac{\Gamma(a)\Gamma(b)\Gamma(1-a-b)}{\Gamma(-a)\Gamma(-b)\Gamma(1+a+b)}, & \text{(4.57a)} \\ \dfrac{\varepsilon_*^2 \hat{s}_*/(\hat{s}_* - 2)}{(m_0+1)(m_0+2)}. & \text{(4.57b)} \end{cases}$$

Expression (4.57a) holds if ι is given by (4.30), so that A_0 and B_0 are given by (4.36) and (4.37) respectively. When the WKB approach is used, then G_0 is given by (4.57b) (for small shear we can simplify (4.57b) as $G_0 = -\frac{\varepsilon_*^2 \hat{s}_*}{2(m_0+1)(m_0+2)}$) and A_0 and B_0 are given by (4.41) and (4.42). If $r_s \Delta' \to \infty$ (ideal MHD limit), the eigenfrequencies are given by:

$$\hat{\omega} = \omega_i^*/2 \pm \sqrt{(\omega_i^*)^2/4 + \alpha_*}; \tag{4.58}$$

where

$$\alpha_* = n^2/3[\delta q^2 + \beta_p^2 G_0]. \tag{4.59}$$

We can relate α_* to the growth rate of the ideal MHD mode (zero diamagnetic effects) if we write $\gamma_{MHD}^2 = -\alpha_*$. The stability condition becomes $(\omega_i^*)^2/4 - \gamma_{MHD}^2 > 0$ (it is immediate to recognise the stabilising effect of diamagnetic ions). The stability boundary ($Im(\omega) = 0$) is identified by just β_p and $\delta q_c = -\beta_p^2 G_0$. Note that these relations hold also if $m_0 \neq n$, with $m_0/n \approx 1$.

4.8.2 Case $m_0 > n$

For $q > 1$ in the low-shear region, Equation (4.53) can be solved analytically for parabolic pressure profiles [86]. The solution which is vanishing on the surface $r = r_*$ is [86]:

$$X_{m_0} = \frac{\sigma}{\kappa} \left(\frac{r_*^{m_0} J_{m_0}(\sqrt{\kappa/Q}r)}{r J_{m_0}(\sqrt{\kappa/Q}r_*)} - r^{m-1} \right),$$

where $\sigma = 16\beta_p^2 r_*^{-2-2m_0} \mathbf{\Lambda}^{\omega}_{m_0,n}/R_0^2$, $\kappa = 4\beta_p(1/q^2-1)/(q^2 R_0^2)$ and $J_m(z)$ denotes the Bessel function of first kind of order m and argument (in general complex) z (Ref. [102] p. 355):

$$J_m(z) = (\tfrac{1}{2}z)^m \sum_{n=0}^{\infty} \frac{(-\frac{1}{4}z^2)^n}{n!\Gamma(m+n+1)}. \tag{4.60}$$

We assume that the quantity $\frac{\kappa/Qr_*^2}{4(m+1)}$ is small: this is reasonable if we consider a case for which $\kappa a_0^2/Q \sim \mathcal{O}(1)$ (consistent with the ordering of the various terms in eq. (4.53)), with r_*/a_0 sufficiently small. Therefore taking the first two terms in (4.60), from the integral condition (eq. 4.54) we obtain the same dispersion relation as the $m_0 = n$ case, namely eq. (4.55). We note that for plasmas with $q \approx 1$ in the core, the factor κ is $\mathcal{O}(\varepsilon^2)$ smaller than for $q \neq 1$ plasmas, therefore the approximation of the Bessel function with its two first terms in the series holds even better.

In the next sections we evaluate the growth rates for the resistive mode in a neighbourhood of the ideal stability boundary.

4.9 Analysis of the dispersion relation

We focus on the $m_0 = n$ case since this is the most relevant for tokamak hybrid scenarios with $q_{min} \approx 1$. We start the analysis of the dispersion relation assuming vanishing diamagnetic effects with zero viscosity and no equilibrium toroidal flows [58]. We conveniently write $r_s\Delta' = \bar{S}^{3/4}\gamma^{5/4}$, where $\bar{S} = [2\pi\Gamma(3/4)/\Gamma(1/4)]^{4/3}[(1+2q^2)/\hat{s}_s^2]^{1/3}S$. Hereafter we set $\gamma = -i\omega$. In the limit of large $r_s\Delta'$, from (4.56) we obtain the following dispersion relation [58]:

$$\gamma^{5/4}(\gamma^2 + \alpha_*) = \gamma_{inf}^{13/4}, \tag{4.61}$$

where α_* is given by (4.59) and we denote with γ_{inf} the growth rate of the resistive infernal mode close to ideal marginal stability for which $\gamma_{MHD}^2 = 0$, i.e.:

$$\gamma_{inf} = \Xi^{4/13}\bar{S}^{-3/13}, \tag{4.62}$$

where $\Xi = \frac{n^2}{3}\beta_p^2 G_0(B_0 - A_0)$.

If $\alpha_* = 0$ ($\gamma_{MHD}^2 = 0$), the fast $S^{-3/13}$ scaling is recovered [58]. Assuming β_p fixed, we write $\delta q^2 = \delta q_c^2 + \Delta^2$, where δq_c is the critical value for which $\alpha_* = 0$ ($\delta q_c^2 + \beta_p^2 G_0 = 0$). If $\Delta \approx 0$, then $\gamma \sim \gamma_{inf} \sim S^{-3/13}$ which recovers the results of Ref. [58]. If δq is increased, i.e. Δ increases, the system undergoes a transition from *infernal* ($S^{-3/13}$) to *tearing* ($S^{-3/5}$) behaviour [58, 107]. We infer that the transition point in δq from the *infernal-like* to the *tearing-like* behaviour occurs when $\gamma \simeq n\Delta/\sqrt{3}$ (i.e. $\gamma \simeq \sqrt{\alpha_*}$) [58], which approximately reads:

$$\Delta \approx \frac{\gamma_{inf}}{2^{4/13}}\sqrt{\frac{3}{n^2}}, \tag{4.63}$$

as shown in figure 4.3.

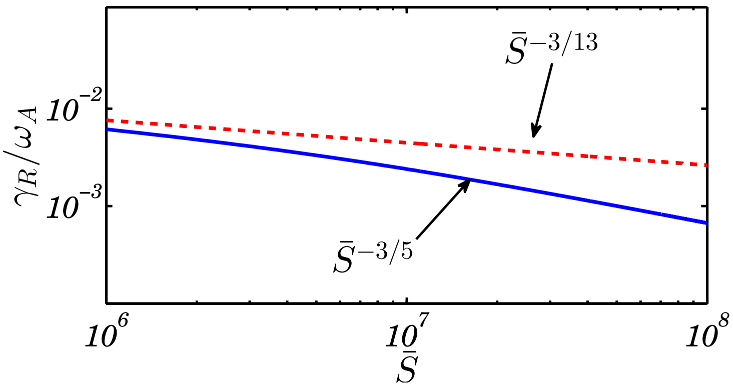

Figure 4.3: Growth rate of the purely growing (zero diamagnetic effects) resistive $m_0 = n = 4$ mode calculated from eq. (4.61) with $\delta q = 0.007$, $\lambda = 3.6$, $r_*/a_0 = 0.55$, $r_s/a_0 = 0.9$, $\varepsilon = 0.3$. If $\Delta = 0$ (ideal marginal stability, cf. (4.63)) the fast $S^{-3/13}$ scaling is recovered (dashed line line). If (4.63) is used to calculate $\Delta(S)$ with $\bar{S} = 10^8$, a transition to the $S^{-3/5}$ scaling occurs (solid line).

As δq is increased further ($\alpha_* \gg \gamma^2$), then (4.56) reduces to the dispersion relation for tearing modes [107]. Indeed if δq increases, the coupling in the low-shear region becomes weaker and the modes $m_0 + 1$, m_0 and $m_0 - 1$ become independent of each other. The coupling is lost, so that $B_1 = 0$ (because of regularity of the sideband on the magnetic axis) which implies that $r_s\Delta' = A_0$, yielding the standard dispersion relation for tearing modes in a cylindrical configuration (in this case for the $m_0 + 1$ mode) [107]. Thus the mode becomes stable if $A_0 < 0$. We recall that A_0 is the logarithmic jump of the m_0+1 sideband across the resonant layer. Hence the stability of the system is determined by the stability of the sideband to tearing. We note that in order to avoid unphysical divergencies in $\mathbf{\Lambda}^{\omega}_{m_0,n}$, we must include the effects of small shear at the transition point r_*. This gives $\mathbf{\Lambda}^{\omega}_{m_0,n} \sim 1 + 2k_{||}/k'_{||}$. Then, for large δq, Eq. (4.56) which gives the growth rate for the m_0 mode, reduces to $\omega^2 = n^2\delta q^2/(1 + 2q^2) > 0$, indicating a stable mode.

Equation (4.56), allows us also to derive an analytic expression of the threshold for the resistive mode (zero diamagnetic effects). The definition of the threshold by the condition $\gamma = 0$ ($r_s\Delta' = 0$) yields $\delta q^2 + \beta_p^2 G_0 B_0/A_0 = 0$. The behaviour of the growth rate (ideal and resistive) as function of β_p is shown in figure 4.4. Note that we employed (4.58) to show the stabilising effect of core diamagnetic ions on the ideal mode. Note also that for a fixed value of δq, if β_p is sufficiently bigger than the critical poloidal $\beta_{p,c}$ for which $\gamma_{MHD} = 0$, then the resistive mode scales as S^0, thus the growth rate of the resistive mode is the ideal growth rate [108]. It important to stress the fact that if $\beta_p \approx \beta_{p,c}$ the fast resistive infernal scaling ($S^{-3/13}$) is found, while if β_p is further decreased, then the transition to the tearing behaviour ($S^{-3/5}$) occurs [108]. Figure 4.5 shows the growth rate γ against δq with non vanishing resistivity and with diamagnetic effects turned on (both ion and electron). The

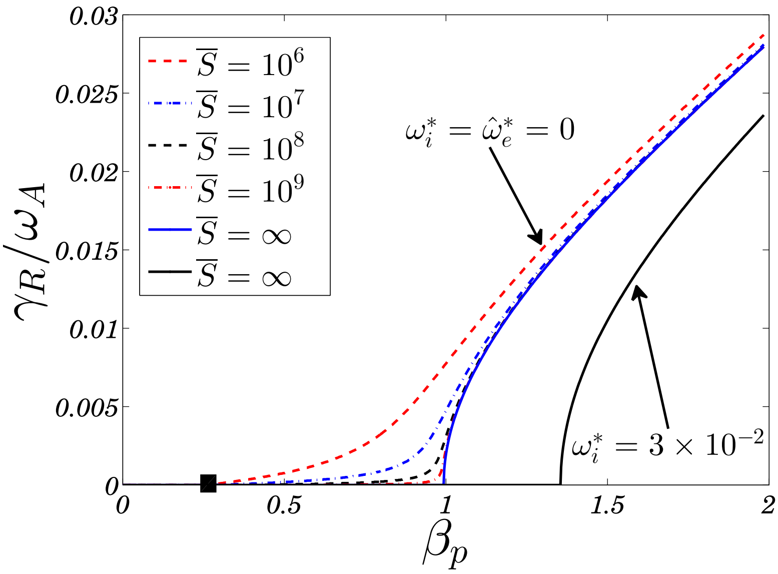

Figure 4.4: Growth rate of ideal (solid lines) and resistive (purely growing, zero diamagnetic effects, dashed lines) for the $m_0 = n = 4$ mode with the same profiles as in figure 4.3 and $\omega_i^* = 3 \times 10^{-2}$. The stabilising effect of diamagnetic ions on the ideal mode (Eq.(4.58)) is evident. The resistive threshold (black square on figure) is found at $\beta_p \approx 0.267$ is most clearly exhibited by the $\gamma_R = 0$ point of the red line ($S = 10^6$).

impact of such non-MHD effects are thus studied in the next sections where the generalised dispersion relation is analysed.

4.9.1 Resistive infernal modes with diamagnetic effects

Now that the main results for resistive infernal modes of [58] have been recovered (in particular the $S^{-3/5}$ and the $S^{-3/13}$), we add new physics and obtain novel results. The effect of diamagnetism is considered first. We conveniently set $r_s\Delta' = \bar{S}^{3/4}[\gamma(\gamma - \lambda_i)(\gamma - \lambda_e)^3]^{1/4}$, where $\lambda_i = -i\omega_i^*$ and $\lambda_e = -i\hat{\omega}_e^*$ ($\bar{S}$ has been defined in the previous section).

In the limit of large $r_s\Delta'$, from (4.56) we obtain the following dispersion relation (the subscripts s and ℓ indicate that the quantity is evaluated at the resonant surface or in the low shear region respectively):

$$\underbrace{\gamma(\gamma - \lambda_{i,s})(\gamma - \lambda_{e,s})^3}_{\text{layer region}}\underbrace{[\gamma(\gamma - \lambda_{i,\ell}) + \alpha_*]^4}_{\text{low-shear region}} = \gamma_{inf}^{13}. \tag{4.64}$$

We will consider two particular cases: one for which $\alpha_* = 0$, so that $\gamma_{MHD}^2 = 0$,

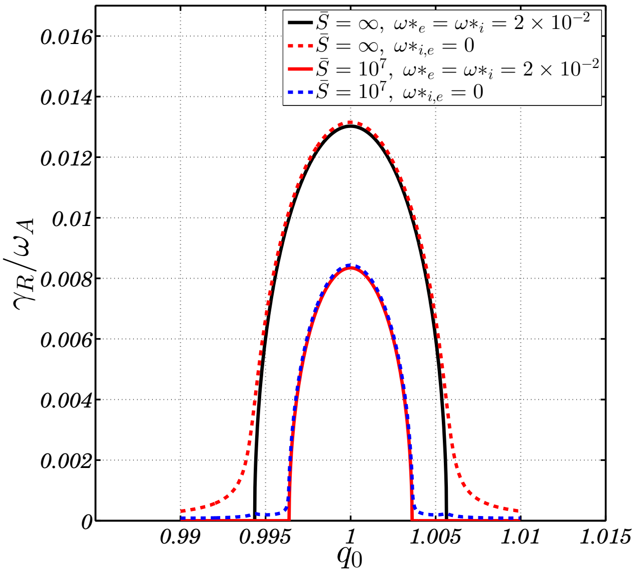

Figure 4.5: Growth rate of ideal (solid lines) and resistive (dashed lines) for the $m_0 = n = 4$ mode with the same profiles as in figure 4.3 with $\beta_p = 0.8$. Diamagnetic ions stabilise the resistive mode as well. The impact of plasma diamagnetism is discussed in section 4.9.1.

and another for which $\alpha_* = -(\omega_i^*)^2/4$ so that $\gamma_{MHD}^2 = (\omega_i^*)^2/4$. The first case corresponds to ideal marginal stability when diamagnetic effects are neglected, while the second corresponds to marginal stability of an ideal mode when ω_i^* corrections are taken into account. We refer to the latter case as the *diamagnetic ideal stability boundary*. It is also important to note in (4.64) the different ω^* effects which come from the layer and the low-shear region contribution, since they give rise to new rotating branches in the mode spectrum. The physical roots of eq. (4.64) must satisfy the condition $Re[(\delta_*^R)^2] > 0$ in order to have spatially localised modes [67, 105] (i.e. an existing Fourier transform). This condition is equivalent to the condition either $|\arg\delta_*^R| < \pi/4$ or $|\arg\delta_*^R| > 3\pi/4$ [109], where δ_*^R is given by (4.47)). Roots with $Re[(\delta_*^R)^2] < 0$ can be however regularised by some extra physics not included in the model [104, 105]. Hereinafter we set $r_0 = a$ and $\lambda_{i,s} = \lambda_{i,\ell} = \lambda_i$. If $|\gamma_{MHD}^2| \gg |\gamma(\gamma-\lambda_i)|$, it is easy to see that (4.64) reduces to the dispersion relation for drift-tearing modes [67, 96, 110].

If $\alpha_* = 0$, the dispersion relation reads:

$$\gamma(\gamma-\lambda_i)(\gamma-\lambda_e)^{3/5} = \gamma_{inf}^{13/5}. \tag{4.65}$$

When diamagnetic effects are weak, i.e. $\gamma_{inf} \gg \lambda_{i,e}$, the solution of (4.65) reads:

$$\gamma \simeq \left(\tfrac{3}{13}\lambda_e + \tfrac{5}{13}\lambda_i\right) + \Xi^{4/13}\bar{S}^{-3/13}. \tag{4.66}$$

We consider again $\alpha_* = 0$, but with strong diamagnetic effects, namely $\gamma_{inf} \ll \lambda_{i,e}$. The unstable roots are written as $\gamma = \lambda_i + \delta$, $\gamma = \lambda_e + \delta$, $\gamma = \delta$ where δ is the growth rate, which is much smaller than the diamagnetic frequencies. These roots are referred to as ion, electron and kink respectively [111]. Thus in the limit $\alpha_* = 0$, the approximate solution of (4.65) reads [109, 110]:

$$\gamma \simeq \begin{cases} \lambda_e + \dfrac{\Xi^{4/3}}{[\lambda_e(\lambda_e - \lambda_i)]^{5/3}}\,\bar{S}^{-1}, & \gamma_I \approx \lambda_e \\ \lambda_i + \dfrac{\Xi^{4/5}}{\lambda_i(\lambda_i - \lambda_e)^{3/5}}\,\bar{S}^{-3/5}, & \gamma_I \approx \lambda_i \\ -\dfrac{\Xi^{4/5}}{\lambda_i(-\lambda_e)^{3/5}}\,\bar{S}^{-3/5}, & |\gamma_{R,I}| \ll |\lambda_{i,e}| \end{cases} \tag{4.67}$$

with $\gamma_R = Re(\gamma)$ and $\gamma_I = Im(\gamma)$, where the electron diamagnetic frequency $\hat{\omega}_e^*$ has been taken with a positive sign, while the ion diamagnetic frequency ω_i^* has been taken negative. The unstable roots found analytically are correctly recovered for large $\bar{S}$ from the numerical solution of (4.65) as shown in Fig. 4.6. The real part of the coefficient $(\delta_*^R)^2$ has been evaluated numerically and it is found to be positive for all the modes, although the modes rotating with the ion diamagnetic frequency have $(\delta_*^R)^2 \ll 1$. Therefore we deduce that although $\alpha_* = 0$, so that the mode is nominally close the ideal stability boundary, the presence of strong diamagnetic effects makes the mode move towards the stability region. Hence the fast growth typical of the infernal mode is lost and the instability shows a *drift-tearing* character.

Taking now $\alpha_* = -(\omega_i^*)^2/4$ the dispersion relation yields:

$$\gamma(\gamma - \lambda_i)(\gamma - \lambda_e)^3(\gamma - \lambda_i/2)^8 = \gamma_{inf}^{13}. \tag{4.68}$$

If diamagnetism is weak, i.e. $|\lambda_{i,e}| \ll |\gamma_{inf}|$, then the growth rate is given by Eq. (4.66) with $\gamma \sim S^{-3/13}$, otherwise for strong diamagnetic effects, in the vicinity of the diamagnetic-ideal stability boundary ($\alpha_* = -(\omega_i^*)^2/4$) we have solutions:

$$\gamma \simeq \begin{cases} \lambda_e + \dfrac{\Xi^{4/3}}{\left[\lambda_e(\lambda_e - \lambda_i)(\lambda_e - \frac{\lambda_i}{2})^8\right]^{1/3}}\,\bar{S}^{-1}, & \gamma_I \approx \lambda_e \\ \lambda_i + \dfrac{256\Xi^4}{\lambda_i^9(\lambda_i - \lambda_e)^3}\,\bar{S}^{-3}, & \gamma_I \approx \lambda_i \\ \dfrac{\lambda_i}{2} + \dfrac{\Xi^{1/2}}{[\frac{\lambda_i^2}{4}(\lambda_e - \frac{\lambda_i}{2})^3]^{1/8}}\,\bar{S}^{-3/8}, & \gamma_I \approx \dfrac{\lambda_i}{2}. \end{cases} \tag{4.69}$$

Figure 4.7 shows the unstable roots evaluated numerically from (4.68). The same considerations on $(\delta_*^R)^2$ (cf. Eq. (4.47)) hold also in this case. The various scalings

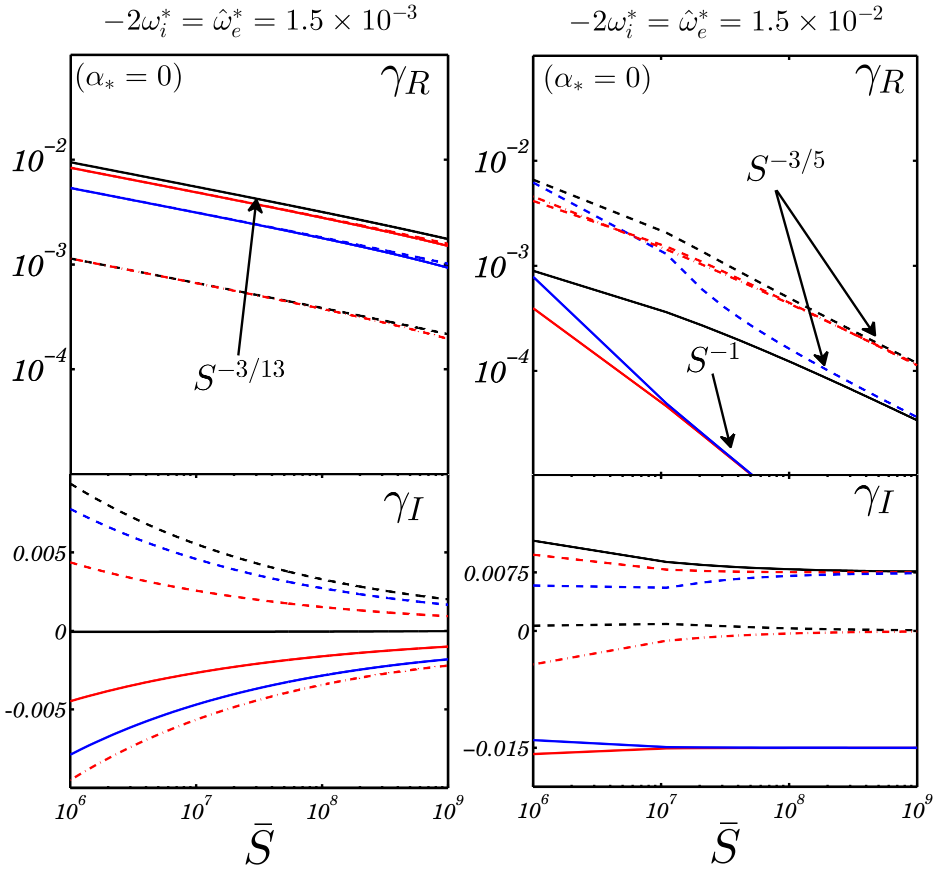

Figure 4.6: Real ($\gamma_R = Re(\gamma)$) and imaginary ($\gamma_I = Im(\gamma)$) parts of the unstable solutions of (4.65) as function of the Lundquist number in a neighbourhood of ideal MHD stability ($\alpha_* = \gamma^2_{MHD} = 0$) for the $m_0 = n = 4$ mode with $\delta q = 0.01$, $\lambda = 3.6$, $r_*/a = 0.5$, $r_s/a = 0.9$, $\varepsilon = 0.3$ and $\omega_i^* = -\hat{\omega}_e^*/2$. The left picture refers to the case $\hat{\omega}_e^* = 1.5 \times 10^{-3}$ while the right one to $\hat{\omega}_e^* = 1.5 \times 10^{-2}$. The same roots in the upper and lower graphs have the same line type. The corresponding scalings in S are also shown.

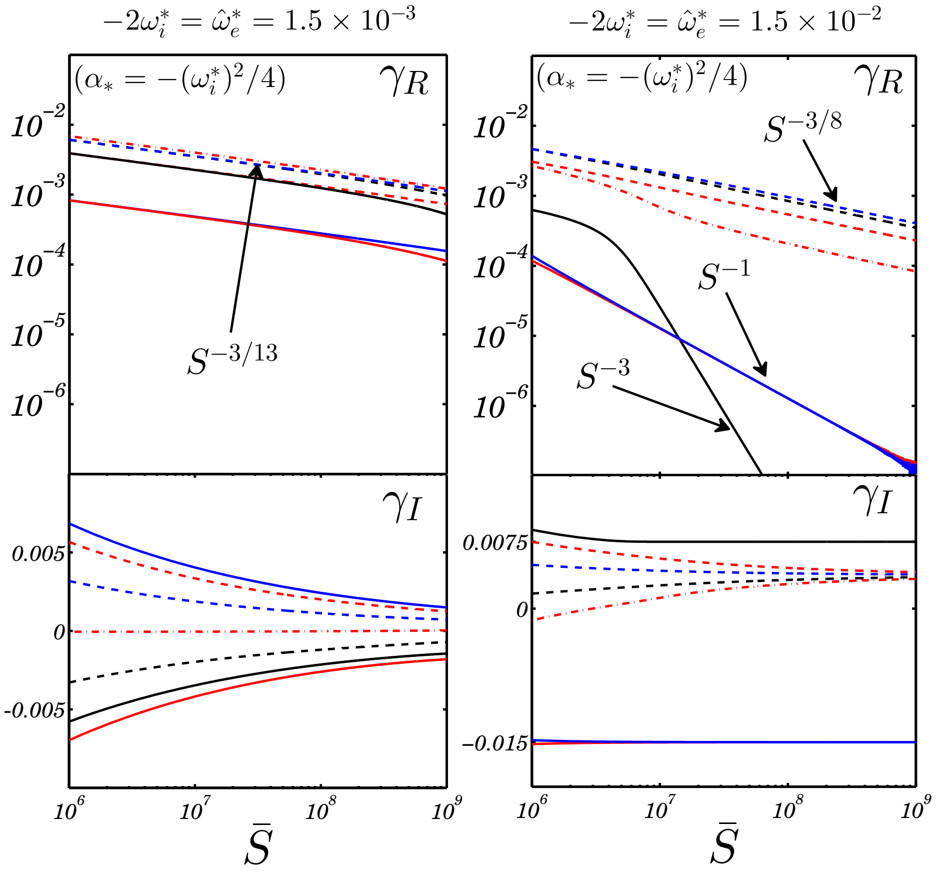

Figure 4.7: Real ($\gamma_R = Re(\gamma)$) and imaginary ($\gamma_I = Im(\gamma)$) parts of the unstable solutions of (4.68) as function of the Lundquist number in a neighbourhood of diamagnetic ideal stability ($\alpha_* = -(\omega_i^*)^2/4$). Same parameters as in Fig. 4.6.

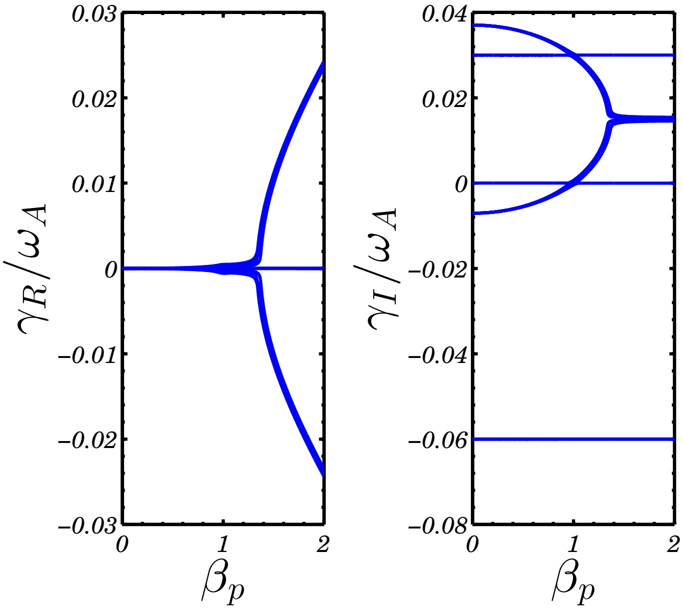

Figure 4.8: Real ($\gamma_R = Re(\gamma)$) and imaginary ($\gamma_I = Im(\gamma)$) parts of the solutions of (4.70) as function of β_p for the mode $m_0 = n = 4$. Same profiles as in figure 4.3 with $\hat{\omega}_e^* = -2\omega_i^* = 6 \times 10^{-2}$.

of the growth rate (and the respective rotation frequencies) with weak or strong diamagnetic effects, either at the ideal stability boundary or at the ideal-diamagnetic stability boundary are listed in Table 4.1.

Independently of the value taken by α_*, in the case of strong diamagnetic effects ($\gamma_{inf} \ll \lambda_{i,e}$), we can identify the thresholds of the three branches (kink, ion and electron) by setting $r_s\Delta' = 0$ (viz. zero growth rate) and solving eq. (4.56). Under the assumption that $r_0 = a$ and the ion diamagnetic frequency is constant through the plasma volume, Eq. (4.56) can be written in the following form:

$$r_s\Delta'(\gamma - \lambda_+)(\gamma - \lambda_-) = (\gamma - \delta_+)(\gamma - \delta_-)A_0 \tag{4.70}$$

where $\lambda_\pm = \lambda_i/2 \pm [-(\omega_i^*)^2/4 - \alpha_*]^{1/2}$, $\delta_\pm = \lambda_i/2 \pm [-(\omega_i^*)^2/4 - \alpha_* + n^2/3\beta_p^2 G_0(1 - B_0/A_0)]^{1/2}$ ($r_s\Delta'$ and α_* have been already defined in the previous sections). In the ideal limit ($r_s\Delta' \to \infty$) then we get $(\gamma - \lambda_+)(\gamma - \lambda_-) = 0$ which reduces to (4.58). Numerical solution of eq. (4.70) are shown in figure 4.8: because diamagnetic effects are considered, the stability threshold for the ideal mode is located at $\beta_p \approx 1.35$ (see Fig. 4.4). The mode is however destabilised by the presence of finite resistivity. In the limit of large $\bar{S}$ a perturbative approach can be used to solve the dispersion relation. Assuming $\lambda_\pm$ purely imaginary (i.e. $\alpha_* \geq -(\omega_i^*)^2/4$) and sufficiently large diamagnetic frequencies with respect to the growth rate of the pure resistive infernal mode, the corresponding roots of (4.70) can be written as $\gamma = \delta$, $\gamma = \lambda_i + \delta$, $\gamma = \lambda_e + \delta$,

$\gamma = \lambda_+ + \delta$ and $\gamma = \lambda_- + \delta$ where $\delta \ll |\lambda_{i,e,\pm}|$ is the growth rate. The following thresholds are found setting $\delta = 0$ leading to

$$\begin{aligned}
&\delta_+\delta_- = 0, && \text{(kink)}\\
&(\lambda_i - \delta_+)(\lambda_i - \delta_-) = 0, && \text{(ion)}\\
&(\lambda_e - \delta_+)(\lambda_e - \delta_-) = 0, && \text{(electron)}.
\end{aligned}$$

For the ion and kink roots the stability threshold reads $\delta q^2 + \beta_p^2 G_0 B_0/A_0 = 0$, while the electron branch has stability threshold $\lambda_e(\lambda_e - \lambda_i) + \frac{n^2}{3}(\delta q^2 + \beta_p^2 G_0 B_0/A_0) = 0$. For the $\lambda_\pm$ branch no threshold in β_p is found. The two cases considered in the section of resistive infernal modes are given by $\lambda_+ = \lambda_i$, $\lambda_- = 0$ ($\alpha_* = 0$) and $\lambda_+ = \lambda_- = \lambda_i/2$ ($\alpha_* + (\omega_i^*)^2/4 = 0$). When diamagnetic effects are weak it is easy to see that the expression for the thresholds reduce to the threshold of a resistive mode evaluated in the previous section.

To conclude the resistive infernal mode model [58] has now been generalised to include diamagnetic effects. Fast growing modes with a growth proportional to $S^{-3/13}$ which rotate at low frequency in a combination of ion and electron direction, have been found when diamagnetic corrections are small. Close to the ideal MHD stability boundary, the effect of plasma diamagnetism destroys the extremely fast $S^{-3/13}$ scaling and it is replaced by three branches which grow slower and rotate at different frequency. These branches show a typical tearing scaling, namely the kink and the ion branch scale as $S^{-3/5}$ while the electron branch scales as S^{-1}. Close to the diamagnetic ideal stability boundary the $S^{-3/13}$ scaling is also lost, but a new intermediate scaling proportional to $S^{-3/8}$ with a rotation frequency equal to $\lambda_i/2$ has been found, giving the possibility of moderately fast growing modes which rotate at frequency $\omega_R \sim \lambda_i/2$. Other scalings are possible when the ion diamagnetic frequency is allowed to vary between the low-shear region and the resonant layer region.

4.9.2 Visco-Resistive infernal modes

In our model viscosity enters only when resistivity is taken into account on the sideband resonant surface. We write $r_s\Delta' = \nu_\mu^{1/6}(\gamma - \lambda_i)^{1/6}(\gamma - \lambda_e)^{5/6}\bar{S}^{5/6}$ [72, 112, 113], where the effects of viscosity enters through $\nu_\mu = \mu_\perp/(\varrho r_s^2)$ and also we define a normalised Lundquist number $\bar{S} = 6^{4/5}[\pi\Gamma(5/6)/\Gamma(1/6)]^{6/5}\hat{s}_s^{-2/5}S$.

When diamagnetic effects are weak the dispersion relation reads $\gamma(\gamma^2 + \alpha_*) = \gamma_v^3$

$$\gamma_v = \Xi^{1/3}\nu_\mu^{-1/18}\bar{S}^{-5/18}.$$

When $\alpha_* = 0$ a new moderately fast $S^{-5/18}$ scaling is found. If we write $\delta q^2 = \delta q_c^2 + \Delta^2$

(δq_c has been already defined) with fixed β_p, it is easy to see that when the q profile is shifted rigidly up, i.e. Δ increases, the *visco-tearing*-like scaling $\gamma \sim \nu_\mu^{-1/6} S^{-5/6}$ [72, 113] is recovered. The transition point in Δ from the moderately fast $S^{-5/18}$ scaling to the *visco-tearing* behaviour occurs when $\gamma \simeq \sqrt{\alpha_*}$ [58] which gives

$$\Delta \approx 2^{-1/3} \gamma_\nu \sqrt{3/n^2}. \tag{4.71}$$

When diamagnetic corrections are retained, the dispersion relation reads:

$$(\gamma - \lambda_i)^{1/6} (\gamma - \lambda_e)^{5/6} [\gamma(\gamma - \lambda_i) + \alpha_*] = \gamma_v^3. \tag{4.72}$$

We focus our attention on the case $\alpha_* = 0$, i.e. close to ideal MHD stability boundary, thus (4.72) becomes

$$\gamma (\gamma - \lambda_i)^{7/6} (\gamma - \lambda_e)^{5/6} = \gamma_v^3. \tag{4.73}$$

When diamagnetic effects are weak, i.e. $\gamma_{inf} \gg \lambda_{i,e}$, the solution of (4.73) is:

$$\gamma \simeq \left(\tfrac{5}{18}\lambda_e + \tfrac{7}{18}\lambda_i\right) + \Xi^{1/3} \nu_\mu^{-1/18} \bar{S}^{-5/18}. \tag{4.74}$$

In limit of strong diamagnetic effects, i.e. $\gamma_{inf} \ll \lambda_{i,e}$, the roots of eq. (4.73) are:

$$\gamma \simeq \begin{cases} \lambda_e + \dfrac{\Xi^{6/5} \nu_\mu^{-1/5}}{\lambda_e^{6/5} (\lambda_e - \lambda_i)^{7/5}} \bar{S}^{-1}, & \gamma_I \approx \lambda_e \\ \lambda_i + \dfrac{\Xi^{6/7} \nu_\mu^{-1/7}}{\lambda_i^{6/7} (\lambda_i - \lambda_e)^{5/7}} \bar{S}^{-5/7}, & \gamma_I \approx \lambda_i \\ \dfrac{\Xi \nu_\mu^{-1/6}}{(-\lambda_i)^{7/6} (-\lambda_e)^{5/6}} \bar{S}^{-5/6}, & |\gamma_{R,I}| \ll |\lambda_{i,e}| \end{cases} \tag{4.75}$$

We note that in this particular case we are far from the diamagnetic-stability boundary, thus a slow growth of the mode is expected. Figure 4.9 shows the unstable roots of eq. (4.73). We note for this case ($\alpha_* = 0$) the slow scaling against S of the growth rate of the unstable modes: indeed these roots behave as S^σ where $\sigma \approx -1$. We omit the calculations for the case $\alpha_* = -(\omega_i^*)^2/4$ (diamagnetic ideal stability boundary), which are essentially the same already presented in the *resistive infernal modes* section. It is however interesting to note that in the case for which $\alpha_* = -(\omega_i^*)^2/4$, with strong diamagnetic effects ($\gamma_{inf} \ll \lambda_{i,e}$), two roots appear: one rotates in the electron direction and the growth scales as S^{-1}, while the other one rotates in the ion direction with frequency $\omega_i^*/2$ and the growth rate scaling is $S^{-5/12}$.

In conclusion, the effect of plasma viscosity on resistive modes with diamagnetic

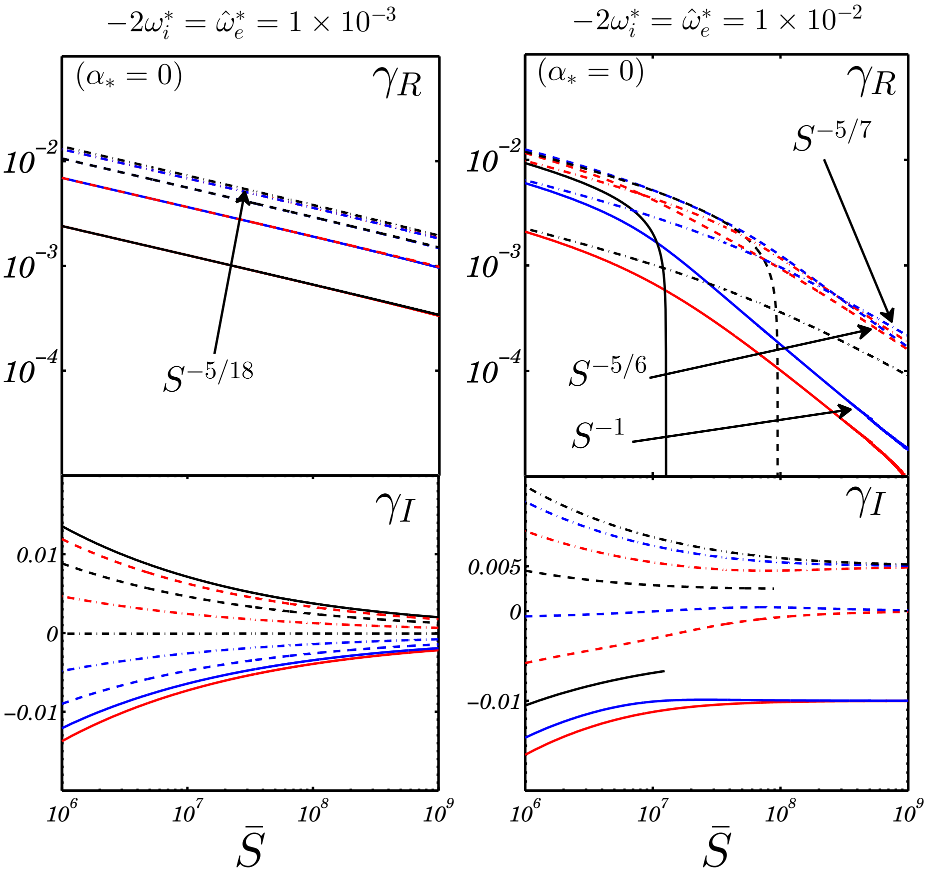

Figure 4.9: Real ($\gamma_R = Re(\gamma)$) and imaginary ($\gamma_I = Im(\gamma)$) parts of the unstable solutions of (4.73) as function of the Lundquist number for $\alpha_* = \gamma^2_{MHD} = 0$ (ideal MHD stability boundary) with $\nu_\mu = 10^{-9}$ and the same parameters of Fig. 4.6. The left picture refers to the case $\hat{\omega}^*_e = 1\times10^{-3}$ while the right one to $\hat{\omega}^*_e = 1\times10^{-2}$. Since the black solid line represents a mode which becomes stable for $\bar{S} \gtrsim 10^{7.3}$, the rotation frequency γ_I is not reported. The same argument applies for the black dashed line. The same line types for the real and imaginary parts of γ/ω_A indicate the same root. The scaling in S of the fastest growing mode of its branch are shown.

corrections has been studied: close to the ideal MHD stability boundary it is found that when the diamagnetic frequencies are much smaller than the growth rate of the mode, the scaling $S^{-3/13}$ is lost and it is replaced by a moderately fast scaling proportional to $S^{-5/18}$. The mode rotates at small frequency, since the dispersion relation comprises a combination of the electron and the ion diamagnetic frequencies. When the ω^* effects are increased in amplitude, the $S^{-5/18}$ scaling is lost and is replaced by three slow growing branches which rotate either with zero frequency ($S^{-5/6}$) or in the electron direction (S^{-1}) or in the ion direction ($S^{-5/7}$) as shown in eq. (4.75) and in Fig. 4.9. The various scalings of the growth rate (and the respective rotation frequencies) for weak and strong diamagnetic effects, either at the ideal stability boundary or at the ideal-diamagnetic stability boundary are listed in Table 4.2. We note that although Visco-Resistive modes scale as $\gamma \approx S^{-1}$ (i.e. indicating simple resistive diffusion, thus growing on slow timescales), the multiplying factor ν_μ^q (although q is small) is still a large correction, enhancing the growth rate, so that this mode could be in principle distinguished from pure slow resistive diffusion.

4.9.3 Rotating-Resistive infernal modes

In this section we introduce the effects of toroidal $\boldsymbol{E} \times \boldsymbol{B}$ rotation. It will be found that $\boldsymbol{E} \times \boldsymbol{B}$ toroidal rotation does not affect stability unless we have finite resistivity and the rotation profile is sheared. For the sake of simplicity diamagnetic corrections are dropped and we set $\alpha_* = 0$ (hence we are always in the neighbourhood of ideal-MHD stability boundary). Moreover the toroidal flow v^φ is assumed positive. Using $r_s\Delta' = \bar{S}^{3/4}(\gamma - \Omega_s)^{5/4}$ where $\Omega = inv^\varphi$ ($\bar{S}$ has already been defined in the section for the resistive infernal modes), the dispersion relation in a neighbourhood of ideal MHD stability ($\gamma_{MHD}^2 = 0$) reads:

$$(\gamma - \Omega_\ell)^2 (\gamma - \Omega_s)^{5/4} = \gamma_{inf}^{13/4}, \tag{4.76}$$

where the subscripts ℓ and s indicate that the quantity is evaluated in the low shear region or at the resonant surface respectively. We always assume that $\Omega_\ell > \Omega_s$. We note that an unsheared strongly subsonic toroidal rotation does not enter the problem since its only effect is to Doppler shift the frequency [67]. In analogy with the previous sections, we distinguish the case in which the toroidal rotation is much smaller than the growth rate of the mode: consequently the growth rate is

$$\gamma \simeq \left(\tfrac{5}{13}\Omega_s + \tfrac{8}{13}\Omega_\ell\right) + \Xi^{4/13}\bar{S}^{-3/13}. \tag{4.77}$$

When the rotation effect becomes important (viz. $|\gamma_{inf}| \ll |\Omega_\ell|$), then the growth rate reads

$$\gamma \simeq \begin{cases} \Omega_\ell + \dfrac{\Xi^{1/2}}{(\Omega_\ell - \Omega_s)^{5/8}} \bar{S}^{-3/8}, & \gamma_I \approx \Omega_\ell \\ \Omega_s + \dfrac{\Xi^{4/5}}{(\Omega_s - \Omega_\ell)^{8/5}} \bar{S}^{-3/5}, & \gamma_I \approx \Omega_s \end{cases} \tag{4.78}$$

The unstable roots of (4.76) are shown in Fig. 4.10. It is thus seen that shear flow can modify the resistive infernal growth rate scaling in S from $S^{-3/13}$ to a moderately fast scaling $S^{-3/8}$.

If $\alpha_* \neq 0$, the more general expression for the dispersion relation reads:

$$\hat{\gamma}_s^{5/4}(\hat{\gamma}_\ell^2 + \alpha_*) = [\hat{\gamma}_\ell^2 - n^2/3(\delta q^2 + \beta_p^2 G_0 B_0/A_0)] A_0 \bar{S}^{-3/4},$$

where $\hat{\gamma}_{s/\ell} = \gamma - \Omega_{s/\ell}$. The above expression can be recast in the following form:

$$(\gamma - \Omega_s)^{5/4} (\gamma - \Omega_+)(\gamma - \Omega_-) = \frac{A_0}{\bar{S}^{3/4}} [(\gamma - \Omega_\ell)^2 + \tfrac{n^2}{3}(\delta q^2 + \beta_p^2 G_0 \tfrac{B_0}{A_0})],$$

where $\Omega_\pm = \Omega_\ell \pm \sqrt{-\alpha_*}$. Assuming $\Omega_\pm$ purely imaginary , i.e. $\alpha_* > 0$, and strong toroidal $\boldsymbol{E} \times \boldsymbol{B}$ flows ($\gamma_{inf} \ll \Omega_{s,\ell}$) we identify three branches: the branch which has rotation frequency Ω_s has threshold $(\Omega_s - \Omega_\ell)^2 + \frac{n^2}{3}(\delta q^2 + \beta_p^2 G_0 \frac{B_0}{A_0}) = 0$, while the two remaining branches $\Omega_\pm$ have no thresholds.

In conclusion, when the effect of toroidal flows is rather small then the eigenfrequency of the mode shows the same fast $S^{-3/13}$ scaling of the resistive mode [58]. With a strong toroidal flow ($|\gamma_{inf}| \ll |\Omega_\ell|$), this scaling is lost and an intermediate scaling proportional to $S^{-3/8}$ is found. Such mode rotates with the toroidal frequency of the low-shear region. The existence of this moderately fast resistive branch is due to the combined effects of a sheared $\boldsymbol{E} \times \boldsymbol{B}$ toroidal rotation and non negligible resistivity on the resonant $m_0 + 1$ surface. Also a tearing-like scaling ($S^{-3/5}$) is found: the rotation frequency of this mode is the toroidal frequency evaluate on the resonant $q = (m_0 + 1)/n$ surface. The scalings of the growth rate (and the respective rotation frequencies) against the Lundquist number S, calculated at the ideal stability boundary, are summarised in Table 4.3.

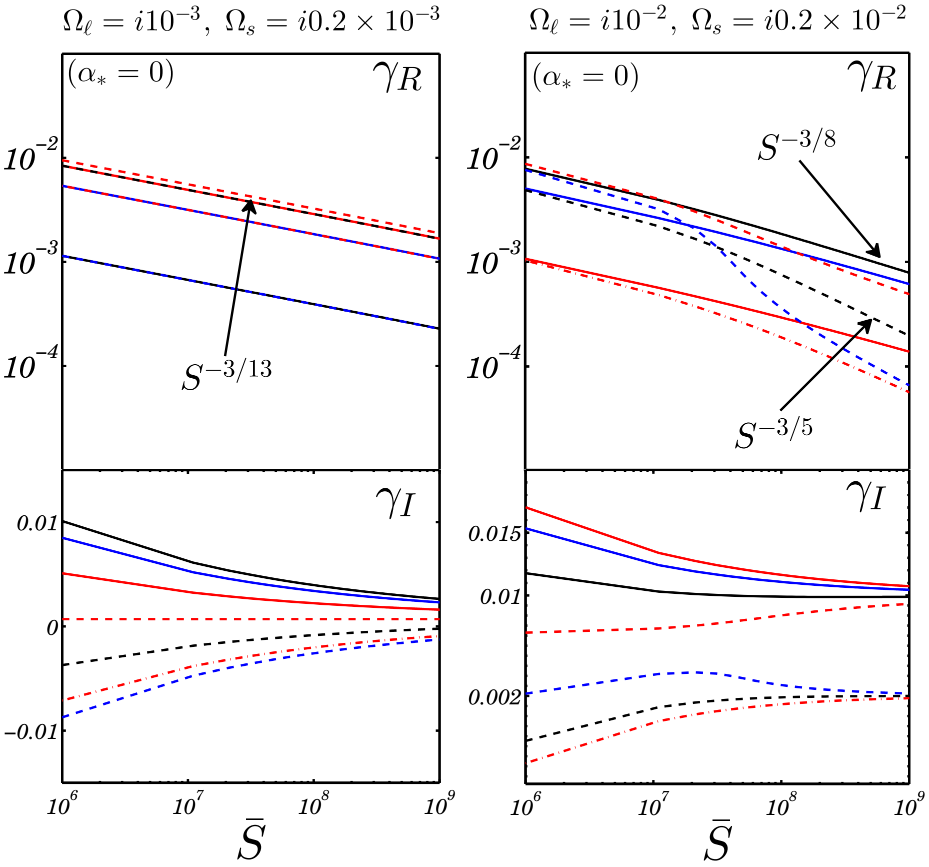

Figure 4.10: Real ($\gamma_R = Re(\gamma)$) and imaginary ($\gamma_I = Im(\gamma)$) parts of the unstable solutions of (4.76) as function of the Lundquist number in the neighbourhood of ideal MHD stability for the $m_0 = n = 4$ mode with $\delta q = 0.01$, $\lambda = 3.6$, $r_*/a = 0.5$, $r_s/a = 0.9$, $\varepsilon = 0.3$ and $\Omega_\ell = 5\Omega_s$. The left picture refers to the case $i\Omega_\ell = -10^{-3}$ while the right one to $i\Omega_\ell = -10^{-2}$.

I: Resistive-Diamagnetic	$\gamma_I \approx \lambda_e$	$\gamma_I \approx \lambda_i$	$\lvert\gamma_{R,I}\rvert \ll \lvert\lambda_{i,e}\rvert$	$\gamma_I \approx \lambda_i/2$	${}^3\!/_{13}\lambda_e + {}^5\!/_{13}\lambda_i$
Weak diamagnetic effects ($\gamma_{inf} \gg \lvert\lambda_{i,e}\rvert$):					
Ideal stab. bound. ($\alpha_* = 0$)	-	-	-	-	$S^{-3/13}$
Strong diamagnetic effects ($\gamma_{inf} \ll \lvert\lambda_{i,e}\rvert$):					
Ideal stab. bound. ($\alpha_* = 0$)	S^{-1}	$S^{-3/5}$	$S^{-3/5}$	-	-
Ideal-diamagnetic stab. bound. ($\alpha_* = -(\omega_i^*)^2/4$)	S^{-1}	S^{-3}	-	$S^{-3/8}$	-

Table 4.1: Growth rate scalings versus $S \propto \bar{S}$ for the Resistive-Diamagnetic mode at ideal ($\alpha_* = 0$) and ideal-diamagnetic stability boundary ($\alpha_* = -(\omega_i^*)^2/4$).

II: Visco-Resistive	$\gamma_I \approx \lambda_e$	$\gamma_I \approx \lambda_i$	$\lvert\gamma_{R,I}\rvert \ll \lvert\lambda_{i,e}\rvert$	$\gamma_I \approx \lambda_i/2$	${}^5\!/_{18}\lambda_e + {}^7\!/_{18}\lambda_i$
Weak diamagnetic effects ($\gamma_{inf} \gg \lvert\lambda_{i,e}\rvert$):					
Ideal stab. bound. ($\alpha_* = 0$)	-	-	-	-	$\nu_\mu^{-1/18} S^{-5/18}$
Strong diamagnetic effects ($\gamma_{inf} \ll \lvert\lambda_{i,e}\rvert$):					
Ideal stab. bound. ($\alpha_* = 0$)	$\nu_\mu^{-1/5} S^{-1}$	$\nu_\mu^{-1/7} S^{-5/7}$	$\nu_\mu^{-1/6} S^{-5/6}$	-	-
Ideal-diamagnetic stab. bound. ($\alpha_* = -(\omega_i^*)^2/4$)	$\nu_\mu^{-1/5} S^{-1}$	$\nu_\mu^{-1} S^{-5}$	-	$\nu_\mu^{-1/12} S^{-5/12}$	-

Table 4.2: Growth rate scalings versus $S \propto \bar{S}$ and ν_μ for the Visco-Resistive mode at ideal ($\alpha_* = 0$) and ideal-diamagnetic stability boundary ($\alpha_* = -(\omega_i^*)^2/4$).

III: Rotating-Resistive	$\gamma_I \approx \Omega_\ell$	$\gamma_I \approx \Omega_s$	${}^5\!/_{13}\Omega_s + {}^8\!/_{13}\Omega_\ell$
Weak $\boldsymbol{E} \times \boldsymbol{B}$ flow ($\gamma_{inf} \gg \lvert\Omega_{\ell,s}\rvert$):			
Ideal stab. bound. ($\alpha_* = 0$)	-	-	$S^{-3/13}$
Strong $\boldsymbol{E} \times \boldsymbol{B}$ flow ($\gamma_{inf} \ll \lvert\Omega_{\ell,s}\rvert$):			
Ideal stab. bound. ($\alpha_* = 0$)	$S^{-3/8}$	$S^{-3/5}$	-

Table 4.3: Growth rate scalings versus $S \propto \bar{S}$ for the Rotating-Resistive mode at the ideal stability boundary ($\alpha_* = 0$).

4.10 Summary

This chapter presents a derivation of an analytic expression for the growth rate for *infernal modes* with additional non-MHD effects. Charlton's resistive quasi-interchange model [58] is extended with the inclusion of plasma diamagnetism, viscosity and equilibrium MHD toroidal flows. Viscosity and electron diamagnetic effects are retained only at the resistive toroidal sideband resonant ($q = (m+1)/n$) surface, in addition to equilibrium toroidal flows and ion diamagnetic corrections which are taken into account also in the core region.

The stabilising effects of ω_i^* in the core (assuming constant diamagnetic frequency in the core [8]) has been shown, leading to an increased threshold for the ideal mode. The rotational transform has been chosen in a such way that an analytic treatment of the magnetic perturbation in the sheared region is tractable, which yields three dispersion relations, corresponding to three different regimes. Each regime considers separately plasma diamagnetism, the combined effect of viscosity, diamagnetic corrections, and equilibrium toroidal flows.

When layer physics are considered, additional non-ideal effects tend to reduce the extremely fast ($\sim S^{-3/13}$) growth rate of resistive modes in low shear plasmas [58] close to the ideal MHD stability boundary, but realistic modes of operation are identified that are not inconsistent with fast NTM seeding. A family of modes are obtained, some of which rotate in the electron diamagnetic direction, and others in the ion diamagnetic direction. Both types of modes have been observed simultaneously in TCV [9] during hybrid-like operation. An analytic estimate of the transition point between *infernal-like* and *tearing-like* behaviour for resistive modes with and without viscous effects is given in the absence of diamagnetic effects and toroidal rotation. Intermediate scalings between the *infernal-like* and *tearing-like* behaviour are found: in particular, a novel scaling proportional to $S^{-3/8}$ has been found close to the diamagnetic ideal stability boundary. This scaling occurs either when strong ω^* effects are allowed in the core, or when $\boldsymbol{E} \times \boldsymbol{B}$ equilibrium toroidal flows are retained.

Depending on diamagnetic frequency amplitudes, different scalings in S have been derived in conjunction with the effects of viscosity and equilibrium toroidal flows. The effects of density gradients with flat temperature profile for the $m_0 = n = 1$ have also been assessed (see appendix A.4). Employing the WKB approach [29] a more general dispersion relation with a generic q-profile can be derived.

Generalised pressure profiles which lead to $\omega_i^*(r_*) \neq \omega_i^*(r_{m_0+1})$ will require further study as well as the full dispersion relation which considers all these effects simultaneously. Further work on the non-linear dynamics of these instabilities could be addressed numerically. The more general case with $\omega_i^*(r_*) \neq \omega_i^*(r_{m_0+1})$, where all non-ideal effects are taken into account may be also addressed numerically, as well as the problem of the implications that these instabilities have on the development of fast triggering of NTMs, resistive global oscillations and saturated equilibria in ITER like operating scenarios in which non linearity becomes important. To conclude, resistive infernal modes [58] have been generalised to include diamagnetism, viscosity and the equilibrium $\boldsymbol{E} \times \boldsymbol{B}$ toroidal sheared flows. While each of these tends to slow the extremely fast resistive scaling ($\gamma \sim S^{-3/13}$) of Ref. [58], moderately fast growing resistive modes remain.

5

XTOR-2F numerical simulations of infernal modes and comparison with analytic results

In this chapter we present a numerical study of pressure driven magnetohydrodynamic instabilities in a low-shear tight aspect ratio configuration. We have shown in the previous chapter that when the magnetic shear is sufficiently small over an extended region in the core, enhanced instability occurs due to toroidal coupling of poloidal sidebands. Numerical simulations have been performed with the initial value code XTOR-2F both in the ideal and resistive MHD frame. Two-fluid effects (plasma diamagnetic flows) have been retained in addition to viscosity. The predictions of the XTOR-2F code on the amplitude of the growth rate and on the rotation frequency of the modes have been compared with analytic linear theory of *infernal modes*, which was outlined in the previous chapter. Qualitative agreement has been found between numerical and analytical results, in spite of the tight aspect ratio configuration. The new intermediate scaling $\gamma \sim S^{-3/8}$, predicted by the linear theory [114], is recovered by the numerical results. Finally, a study of the nonlinear evolution of the magnetic island of the tearing sideband has been performed and the results from the simulations are compared with Rutherford's theory.

5.1 Introduction

It has been shown in the previous chapters that the hybrid tokamak operating regime (weakly reversed or almost flat q close to but above unity in the core region) is of particular interest in present day tokamaks and for future ITER operation, allowing longer sawteeth-free plasma discharges [6]. In Chapter **4** we show that infernal modes, that are MHD instabilities characterised by the coupling due to the pressure gradient between a (m, n) Fourier mode (almost resonant with $q = m/n$) and its poloidal sidebands (due to toroidicity) with wave number $(m \pm 1, n)$, can occur [56, 58, 86, 114]. The coupling occurs in the low shear region, where the safety factor is close to a rational, namely $q = m/n + \delta q$. The destabilisation is due to the combined effect of the pressure gradient and the closeness of q to the resonance m/n, i.e. for an increase of β and a reduction of δq the mode is expected to be more unstable.

If resistivity is allowed on the $q = m/n$ surface, the $(m + 1)$ sideband typically exhibits a tearing character on that surface. Due to the coupling in the low shear region, the final dispersion relation differs from the usual tearing mode results, and a large variety of resistive scalings appears: far from the ideal stability boundary the character is essentially *tearing* in the behaviour, namely $\gamma \sim \eta^{3/5}$ where γ is the growth rate of the mode. When the ideal stability boundary is approached, the scaling of the growth rate dramatically changes to $\gamma \sim \eta^{3/13}$ [58, 114]. In the region of strong ideal instability the growth of the mode is almost independent of η, having an ideal character while preserving reconnection dynamics at the $q = m/n$ surface on ideal timescales. The existence of such fast growing resistive modes has been confirmed numerically in the related literature [58, 115].

In Chapter **4** it has been shown that when the layer associated with the $m + 1$ infernal mode sideband is augmented by non-MHD effects (plasma diamagnetism, equilibrium flows, viscous effects, etc.) novel scalings for γ are found [114]. These modes are required to rotate either in the ion or in the electron direction, depending on the branch considered and the presence of such modes has been observed experimentally [9]. When ω^* effects are taken into account, a reduction of the growth rate of the mode, either ideal or resistive, is expected [114]. Complete stabilisation of the ideal mode, for ω_i^* frequency almost constant in the plasma core, has been also suggested [8, 116].

The aim of this chapter is to investigate numerically, by means of the initial value code XTOR-2F [66, 95], the behaviour of such instabilities and compare the simulation results with the linear theory [35, 58, 86, 114] which has been extended in order to include non-MHD effects as presented in the previous chapter. The comparison between theory and simulations shows reasonable agreement both in the ideal and resistive case. The two fluid effects predicted in the analytical model (the novel scaling against η and the mode rotation) have been numerically confirmed by the simulations. The novel moderately fast scaling $\gamma \sim S^{-3/8}$ predicted by the linear theory, is recovered by numerical simulations for sufficiently large Lundquist number (small resistivity) and diamagnetic effects. Finally, the behaviour of the nonlinear evolution of the island width in the pure resistive case (no ω^* effects) is presented and compared with the analytic prediction from Rutherford's theory [30]. It is seen that after the fast growth during the linear phase, when the mode enters in the nonlinear stage, the island exhibits a slower growth in accordance with Rutherford's predictions.

The chapter is organised as follows: the first section describes briefly the physical modes employed and the dispersion relation, when additional non-MHD effects are taken into account in the sideband resonant layer (a brief reminder of the results presented in Chapter **4**) [114], which will be employed for comparison with the magnitude of the eigenfrequencies of the modes computed with the XTOR-2F code. After that, the results of the XTOR-2F simulations are presented: the first part is focused on ideal dynamics with and without the presence of ω_i^* effects. The second part deals with resistive dynamics, and scalings against the Lundquist number, obtained by varying the strength of ω^* effects. These results are compared with analysis [114]. In addition to comparing the linear simulations with the linear analysis, the non-linear XTOR results are compared with the Rutherford equation [30].

5.2 XTOR-2F physical model for low shear plasmas with diamagnetic effects

The physical model adopted in the nonlinear XTOR-2F simulations is given by the set of equations (4.5), (4.6) and (4.7) where Eq. (4.8) is replaced by:

$$\partial_t \boldsymbol{B} = \boldsymbol{\nabla} \times (\boldsymbol{v} \times \boldsymbol{B}) + \boldsymbol{\nabla} \times \left(\frac{\boldsymbol{\nabla}_{||} p_e}{e n_0} \right) - \boldsymbol{\nabla} \times (\eta \boldsymbol{J}), \tag{5.1}$$

in which the plasma resistivity is allowed to vary over space and time in contrast with the linear theory developed in the previous chapter, and the parallel temperature gradient has been neglected assuming a large parallel heat conductivity. The phenomenological contribution from plasma viscosity is retained in the numerical simulations. We note that also in the physical model implemented in the XTOR-2F code the *gyro-viscous cancellation* has been employed [67, 92, 95] in the derivation of Eq. (4.6). Indeed it is easy to prove analytically that for the problem of *infernal modes*, corrections due to a more exact treatment of $\boldsymbol{\nabla} \cdot \underline{\underline{\Pi}}_{gv}$ are of higher order in Eq. (4.18) [114]. A self-consistent derivation of the momentum equation has been presented in [93], but it has not been implemented in XTOR-2F and it is not used for fusion application in any code [95].

Equations (4.5)-(4.7) and (5.1) are chosen in order to have a direct comparison between the analytic linear theory and the results from numerical XTOR-2F calculations. As shown in Appendix **C** § C.2, the XTOR-2F code evolves the full resistive MHD equations extended to include bi-fluid effects resulting from the Braginskii equations: these equations can be straightforwardly derived from Eqs. (4.5)-(4.7) and (5.1) and their explicit form can be found in Refs. [66, 95]. In the XTOR-2F code, in contrast to the analytic model, the plasma resistivity is allowed to vary over the plasma radius, although it is kept constant in time. The resistivity profile is taken such that the equilibrium toroidal electric field is constant over the plasma radius (even for "ideal" simulations, a small amount of viscosity needs to be added in order to achieve numerical stability). The electron diamagnetic frequency is chosen to have the same absolute value as the ion diamagnetic frequency, but with the opposite sign, and both are taken constant in time and over the minor radius. Time dependencies are normalised with respect to the Alfvén time ($\tau_A = R_0/v_A$ ($\omega_A = 1/\tau_A$), where $v_A = B_0/\sqrt{\mu_0 \varrho_0}$) The resistive time is defined as $\tau_R = \mu_0 r_s^2/\eta$; hence we have $S = \tau_R/\tau_A$. Based on the model outlined here, the linear theory of infernal modes is developed in the next section. Now we provide a summary of the linear theory of *infernal modes* developed in Chapter **4**.

5.2.1 Choice of equilibrium profiles parametrisation of analytic solutions for comparison against XTOR-2F

In this section we briefly summarise the results of the linear theory of infernal modes, developed in Chapter **4**, for tokamaks with an almost flat q profile close to m_0/n in the core. In particular we point out what are the equations relevant for the comparison with XTOR-2F simulations. In Chapter **4** we derived a dispersion relation for an analytic safety factor and then we generalised it to an arbitrary q by using the WKB approach. The analytic safety factor given by (4.30) generates unphysical negative currents in the region which extends from $q = (m_0 + 1)/1$ up to the plasma edge. Hence in this region for the XTOR-2F simulations, the safety factor has been tailored in order to have positive currents. However, we decided not to have an abrupt transition between low and high shear. Therefore the safety factor in the central core region is well approximated by Eq. (4.30), but in the external region this formula does not give the shape of q. Hence the parameters which are related to the safety factor properties in the core region are given by the expressions derived in the exact analytic treatment of the dispersion relation, while in contrast the parameters which are dependent on the shape of q in the external region close to the boundary are computed in the framework of the WKB approximation.

We now summarise the linear theory of infernal modes. For a fixed toroidal mode number, the Fourier structure of the magnetic perturbation is assumed to be characterised by having a fundamental mode with wave number (m_0, n) and two small ($\sim \varepsilon$) poloidal $(m_0 \pm 1, n)$ sidebands. In the low-shear region, the (m_0, n) Fourier mode has a small parallel wave number, i.e. $k_{||} \sim \mathcal{O}(\varepsilon)$, so that inertial corrections, ion diamagnetic flow and the coupling with its sidebands have a non negligible effect. In the high-shear region only non-inertial ideal MHD is required and at leading order the Fourier harmonics are decoupled. Standard tearing theory [83] is used to treat the resonant layer of the $(m_0+1)/n$ sideband, where diamagnetic effects (both for ions and electrons) are retained.

The equilibrium geometry for the analytic expansion is given by nested circular slightly shifted toroidal surfaces in the large aspect ratio approximation ($\varepsilon = a/R_0 \ll 1$). Standard tokamak ordering $B_P/B_T \sim \mathcal{O}(\varepsilon)$ and $\beta \sim \mathcal{O}(\varepsilon^2)$ is adopted. A parabolic pressure profile in the low-shear region is assumed, i.e. (r is a flux label):

$$p = p_0(1-(r/r_0)^2), \quad 0 \le r \le r_0, \tag{5.2}$$

with $r_* \le r_0 \le a$. The analytic theory does not care about the shape of the pressure for $r > r_*$, so that in XTOR-2F simulations p for $r > r_*$ can be of any shape. The position of the resonant surface of the sideband and the transition point between low and high shear regions are denoted by $r = r_s$ and $r = r_*$ respectively, while the magnetic shear is defined as $\hat{s} = rq'/q$. Hereafter the symbols s and $*$ indicate that the quantity is calculated at $r = r_s$ and $r = r_*$ respectively.

By solving the linearised equations for the fluid displacements, and matching the eigensolutions of each Fourier harmonic in the three regions across the transition point $r = r_*$ (imposing continuity and smoothness in the first derivative for X_{m_0+1}) and then matching asymptotically the ideal MHD solution for X_{m_0+1} to the resonant layer solutions, the dispersion relation is derived:

$$\hat{\omega}(\hat{\omega} - \omega_i^*) = \frac{n^2}{1+2q^2}\left[\delta q^2 + \beta_p^2 G_0 \frac{B_0 - r_s\Delta'}{A_0 - r_s\Delta'}\right]. \tag{5.3}$$

The layer physics is contained in $r_s\Delta'$ which is computed by means of (4.35) and (4.51). The quantity β_p is evaluated at the transition point $r = r_*$: we note that with a parabolic pressure in the low shear region, β_p is almost constant for $0 \le r \le r_*$. The quantities A_0, B_0 and G_0 are given by Eqs. (4.41), (4.42) and (4.57b). The quantity G_0 is related to the shape of the eigenfunction and of the safety factor in the region $r < r_s$, while the parameters A_0 and B_0 are a measure of the amplitude of the jump of the eigenfunction across $r = r_s$. For sake of simplicity we set $m = m_0 + 1$.

Equations (4.41) and (4.42) can be written as $A_0 = -C_1\bar{C}/(1 + C_1/2m) + r_s\Delta'_{tear}$ and $B_0 = 2m\bar{C}(2m - C_1)/C_1 + r_s\Delta'_{tear}$, where $\bar{C}$ and C_1 have been defined in Chapter

4 § 4.6.1, and $r_s\Delta'_{tear}$ is the tearing stability index, given by [29, 114]:

$$r_s\Delta'_{tear} = -2m\pi\Lambda\cot(\pi\Lambda), \tag{5.4}$$

with $\Lambda = -q_s\langle R_0 J_0\rangle'_s/(2nq'_s)$. We shall now assume for $r < r_s$, the following form for the rotational transform (cf. (4.30)):

$$\iota = 1/q \approx n/m_0\{1 + 1/m[1 - (r/r_s)^\lambda]\}; \tag{5.5}$$

hence we can replace the general formula for G_0 with a more appropriate one:

$$G_0 = \frac{\varepsilon_*^2(r_*/r_s)^{2m}}{m(m+1)}\frac{\Gamma(\xi)\Gamma(\zeta)\Gamma(1-\xi-\zeta)}{\Gamma(-\xi)\Gamma(-\zeta)\Gamma(1+\xi+\zeta)}, \tag{5.6}$$

where $\xi = (m - \bar{m})/\lambda$ and $\zeta = (m + \bar{m})/\lambda$, $\bar{m} = \sqrt{m^2 + 2\lambda + \lambda^2}$. The expression above for G_0 is less sensitive than Eq. (4.57b) to the value of $\hat{s}_*$, thus it is more reliable when the transition between the low and high shear regions is not abrupt. In principle we should replace also the quantities A_0 and B_0, but they are strongly dependent upon the overall shape of the ι profile. Since the ι profile chosen in the numerical simulations strongly deviates from Eq. (5.5) in the region far from r_*, a good estimate of A_0 and B_0 is nevertheless given by the expressions (4.41) and (4.42). In the next sections, the predictions of the linear theory of the infernal mode problem will be compared with the results of the XTOR-2F code.

5.3 Numerical simulations for a low-shear MAST-like configuration

Numerical simulations for a MAST-like equilibrium, whose profiles are shown in Fig. 5.1 ($I^* = \langle J^\varphi/R\rangle/\langle R^{-1}\rangle$ where $\langle\ \cdot\ \rangle = \oint_{\psi=\text{const}}(\ \cdot\ )d\vartheta$), are performed by using the initial value code XTOR-2F [66]. The pressure profile in the central region is equal to the profile used in the analytic calculations, while the q profile is chosen in order to avoid the formation of unphysical negative toroidal currents, which are possible with a rotational transform of the form (4.30). The equilibrium is interfaced with XTOR-2F through the CHEASE code [69], which provides the required quantities (listed in Table 3.2) for the stability calculation.

We note that since the q profile does not present a sharp transition between low and high shear region, it is quite difficult to estimate the location of r_*. Low-shear and high-shear regions are defined where $\hat{s} \lesssim 0.1$ and $\hat{s} \gtrsim 1$ respectively. For the q profile shown in Fig. 5.1, the transition occurs in the region $0.6 \lesssim r/a \lesssim 0.7$, i.e. where $0.1 \lesssim \hat{s} \lesssim 1$. We point out that r_* determines the shape of the eigenfunctions. Note that r_* was identified in Ref. [35] by variations of the growth rate γ with

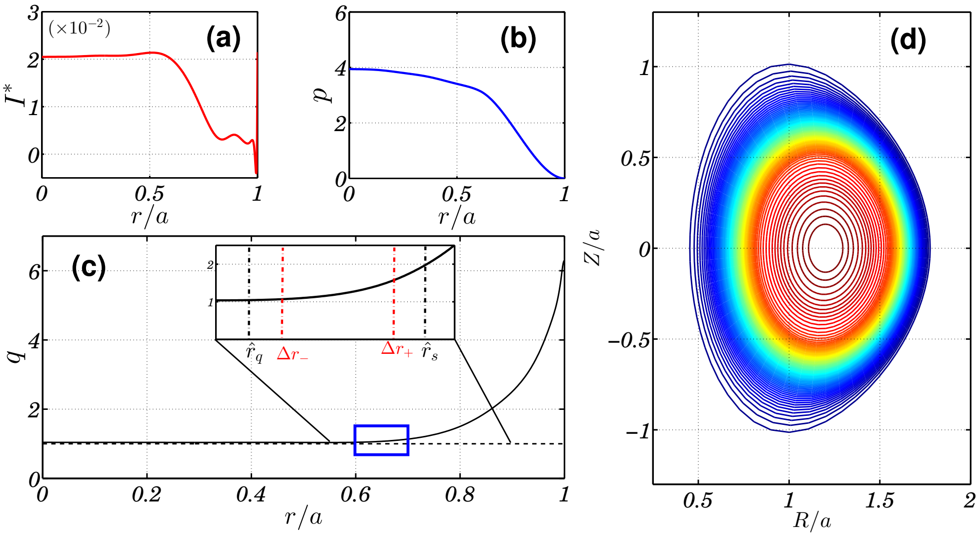

Figure 5.1: Equilibrium profiles for a MAST-like configuration with $\beta = 2.88\%$ and $q_{min} = 1.0223$: (a) Surface averaged toroidal current density; (b) Plasma pressure (I^* and p are normalised with respect to CHEASE internal units); (c) Safety factor (d) Contour plot of the constant pressure surfaces. Here $r = \sqrt{|(\psi - \psi_0)/(\psi_{edge} - \psi_0)|}$, ψ is the poloidal flux and the subscript 0 indicates that the quantity is evaluated on the magnetic axis. In figure (c), the $q = 1$ level is shown by the horizontal dashed line while the blue box indicates the approximate region where a transition point $r = r_*$ exists between low and high shear regions. We defined $\hat{r}_q = r_q/a$ and $\hat{r}_s = r_s/a$.

respect to r_*. This was argued to be valid because it represents a variation of the eigenfunction that yields the maximum growth rate. Nevertheless γ was found to depend fairly weakly on r_*.

We represent the ι profile in the region $r_q/a + \Delta r_+ < r/a < r_s/a - \Delta r_-$, as shown in Fig. 5.1, with the expression (5.5), where $\Delta r_\pm$ are chosen to vary in between 0 and 0.1. In addition, by varying the parameter $\Delta r_\pm$ we obtain an estimate for λ in Eq. (5.5) which can vary between 6.3 and 7. The quantity G_0 is not strongly affected by the variation of λ within this range, thus for the calculations that follow, we set $\lambda \approx 6.7$ corresponding to $\Delta r_+ = 0.05$ and $\Delta r_- = 0.075$ with $r_q/a = 0.6$. The value of λ calculated above is then used in Eqs. (5.3) and (5.6) for analytic comparison. We stress the point that we are interested in the qualitative, rather than quantitative, description of the behaviour of the perturbation. The aspect ratio has been chosen to be small in order to enhance the toroidal coupling between the modes. We point out that (5.3) and (5.6) were derived for a cylindrical plasma in the limit of large aspect ratio, and therefore some non-negligible deviations between the simulations and the analytical predictions are expected. This is mainly because of shaping effects (mainly elongation) and the tight aspect ratio ($\varepsilon = 0.643$ from CHEASE calculations) of the configuration.

The pressure profile is taken to be parabolic, as indicated by Eq. (5.2) with

$r_0/a = 1$, in the region which extends from the magnetic axis to $r \approx r_q$. At the plasma edge the pressure gradient has been diminished in order to prevent the formation of unphysical modes due to an insufficiently well resolved spectrum in XTOR-2F calculations. We choose $r_*/a \approx 0.65$ and β_p is evaluated at the surface $r/a \approx 0.7$. In the scans with respect to β_p, the latter is varied by changing p_0.

The XTOR-2F simulations are performed in the ideal and resistive MHD frame with the inclusion of ion and electron diamagnetic effects. Other additional effects like neoclassical corrections, externally driven flows etc. are switched off. The diamagnetic frequencies both for ions and electrons are taken to be constant throughout the plasma volume and they have the same absolute value. By taking constant diamagnetic frequencies we loose the reconnection screening effect due to sheared diamagnetic flows. The analysis of such effects is not implemented in the analytical model adopted and it is beyond the scope of the present thesis. We employed different values in the numerical discretisation for some particular cases ($q_{min} = 1.0223$), in order to check if the modes observed were physical or not. Denoting N_r, N_θ and N_φ the number of points in the radial, poloidal and toroidal direction respectively, we used three different discretisations: ($N_r = 100$,$N_\theta = 48$, $N_\varphi = 12$), ($N_r = 200$, $N_\theta = 64$, $N_\varphi = 24$) and ($N_r = 300$, $N_\theta = 96$, $N_\varphi = 48$). Simulations show that the unstable mode persists and grows at the same rate, independently of the discretisation employed. Hence hereafter we choose to set the numerical discretisation in the radial direction consisting of 201 points, while the poloidal and toroidal grid points are 64 and 24 respectively. The Fourier decomposition takes into account only two toroidal mode numbers, namely $n = 0$ and $n = 1$, with a poloidal mode window of 11 modes, $n - 4 < m < n + 7$. Since it has been shown that higher toroidal harmonics ($n > 1$) are at least two orders of magnitude smaller compared to the $n = 1$ [115], we do not expect a large difference in the results of the simulations when higher toroidal mode numbers $n > 1$ are retained (both in the linear and nonlinear stage). The chosen value for the normalised viscosity is $\bar{\mu}_\perp = \tau_A \mu_\perp / a^2 = 5 \times 10^{-6}$. For each mode, the growth rate calculated in the simulations is defined as $\gamma = -i\omega = \frac{1}{2} d \ln E_k/dt$ where E_k is the kinetic energy defined as $E_k = (d\boldsymbol{\xi}/dt)^2/2$. Typical experimental MAST parameters are $n_0 \approx 10^{20}\ m^{-3}$, $B_0 \approx 0.6\ T$, $R_0 \approx 0.84\ m$ and aspect ratio $\varepsilon \approx 0.64$, thus the Alfvén time is approximately $\tau_A \approx 6.42 \times 10^{-7} s$. It is noted that MAST geometry, with its strong toroidicity, has been chosen in order to ensure strongly unstable infernal modes. Parameter variation, and comparison with analytical expressions is therefore more robust. In the following sections we present the XTOR-2F results of the ideal and resistive simulations and a comparison with the analytic theory for the case $m_0 = n = 1$.

5.3.1 Ideal simulations

First the ideal MHD dynamics of the $m_0 = n = 1$ mode without ω_i^* effects are examined. The typical behaviour of the kinetic energy of an unstable infernal mode is shown in Fig. 5.2: the mode grows linearly for about 1000 τ_A and then enters in the non-linear regime. The nonlinear regime is characterised by an oscillating behaviour whose amplitude decreases with time [115]. We point out from Fig. 5.2-d that $E_{k,m_0}/E_{k,m_0+1} \sim \varepsilon^{-2}$, implying $X_{m_0+1}/X_{m_0} \sim \mathcal{O}(\varepsilon)$. Figure 5.3 shows the Poincaré cross section at time $t/\tau_A = 1171$, i.e. when the peak in the kinetic energy occurs: the interchange-like pattern of the flux surfaces is clearly visible [24]. Note that the shift of the flux surfaces depends on the value of q_{min} (the closer q_{min} to unity, the larger the displacement).

From the linear theory (cf. Eq. (5.3)), if $r_s\Delta' \to \infty$ (ideal MHD limit), the growth rate of the mode is given by $\hat{\gamma} = \hat{\gamma}_{MHD}$ ($\hat{\gamma} = \gamma/\omega_A$), where (for $m_0 = n = 1$):

$$\hat{\gamma}_{MHD}^2 \simeq -n^2/3[\delta q^2 + \beta_p^2 G_0]. \tag{5.7}$$

In order to have a comparison between analytical estimates of the ideal growth rate with the numerical ones, we decided to perform two sets of simulations. In the first set we keep $\delta q = 0.052$ fixed and change the pressure, with β varying from 2.5% to 5%. The comparison of the growth rate between the XTOR-2F simulations and the analytic estimate computed by Eqs. (5.3) and (5.6) are shown in Fig. 5.4: the stability threshold computed analytically is reasonably close to the threshold found numerically. As explained before, the deviations from analytical results are expected mainly due to the tight aspect ratio of the configuration, and shaping effects.

It is well known that in tight aspect ratio toroidal geometry, stability thresholds are not as sharply defined as in large aspect ratio theory [73]. We can have unstable $m_0 = n = 1$ internal kinks when the minimum in q is further above unity. This is also valid for other modes, like double tearings and external kinks [117]. In Chapters **3** we performed simulations for internal kinks and the shape of the eigenfunction that we measure is close to the top-hat function. When q becomes more flat in the core the effect of inertia is enhanced over an extended region in the core, so that the eigenfuction structure is forced to appear infernal-mode-like, i.e. smoother in the core (see Fig 5.5). Although the reconnection rate and the velocity flows are comparable to the ones measured for internal kinks, in the infernal mode simulations of this chapter, the pattern of the flux surfaces are bean shaped indicating a quasi-interchange like behaviour. In addition the crucial difference with the internal kinks is that for infernal modes the coupling with the poloidal sidebands gives rise to tearing-like islands which grow on extremely fast timescales ($\gamma \sim S^{-3/13}$ at ideal stability boundary, see next section) according with previous works [58]. This feature is typical of infernal modes and not of internal kinks.

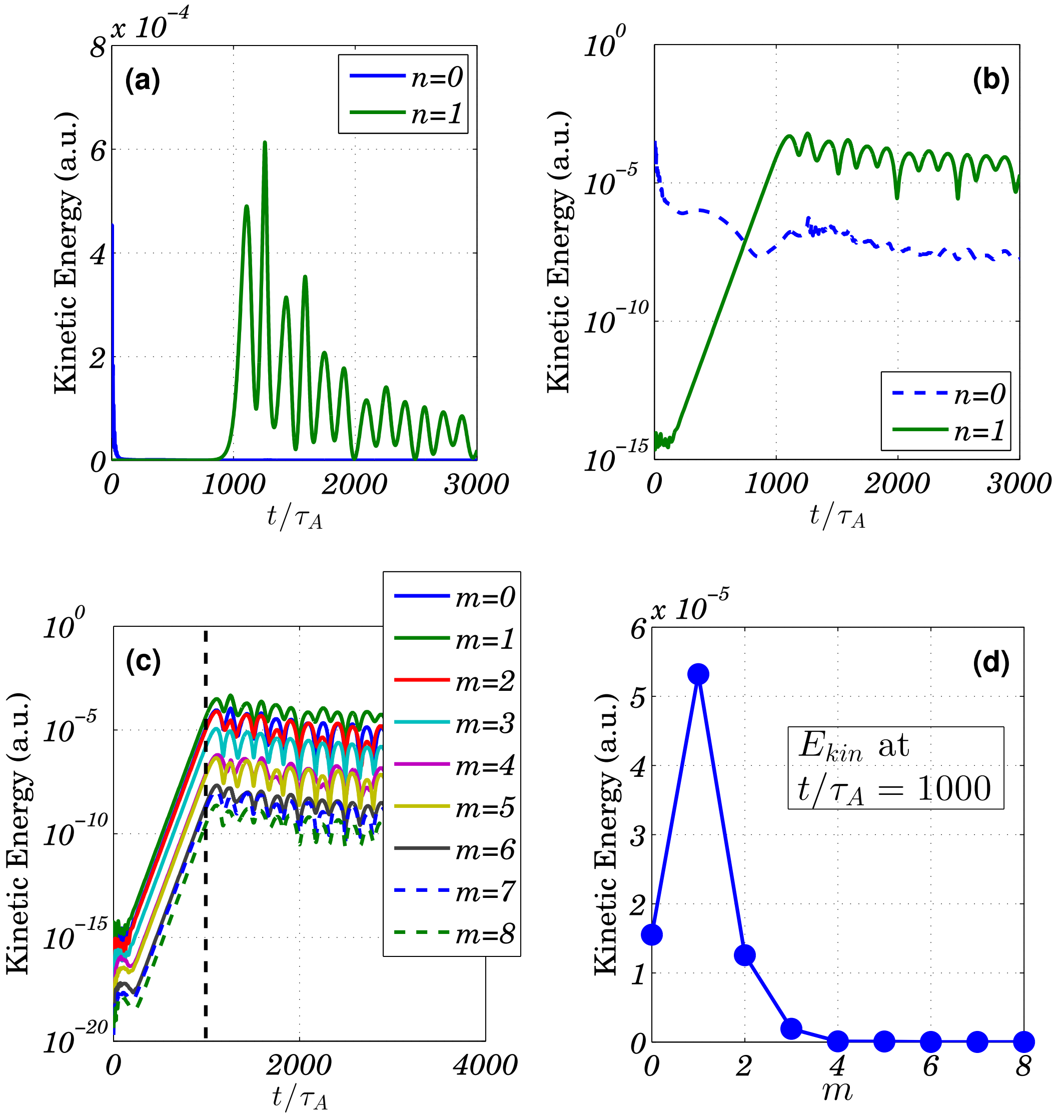

Figure 5.2: Spectrum of the kinetic energy E_k for a MAST-like equilibrium with the same parameters as in Fig. 5.1: Kinetic energy of the $n = 0$ and $n = 1$ mode (linear (a) and logarithmic (b)); (c) Spectrum of the kinetic energy versus time of the poloidal number of the $n = 1$ mode; (d) Spectrum of the kinetic energy against poloidal number for $n = 1$ at $t/\tau_A = 1000$. The amplitude of the $m = 1$ sidebands (which is of the same magnitude) clearly indicates that coupling occurs.

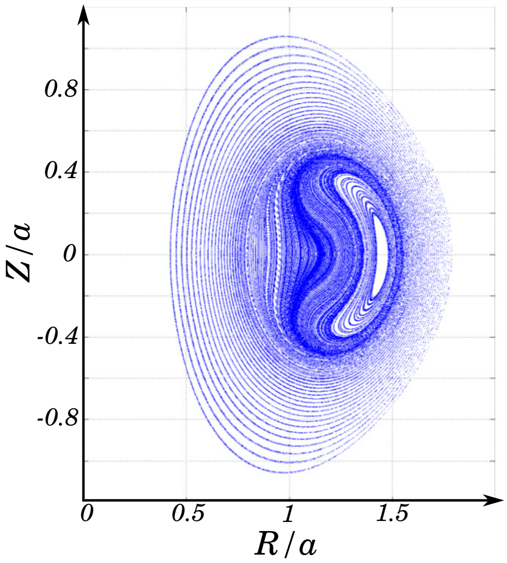

Figure 5.3: Poincaré plot at time $t/\tau_A = 1000$ at $\varphi = 0$ (equilibrium parameters as in Fig. 5.1), when the kinetic energy reaches the maximum value. A cold bubble forms in the central region [16, 34]. A similar pattern was found in Ref. [24]. In the nonlinear regime the shift of the core bounces back and the forth again as indicated also by the behaviour of the kinetic energy shown in figure 5.2.

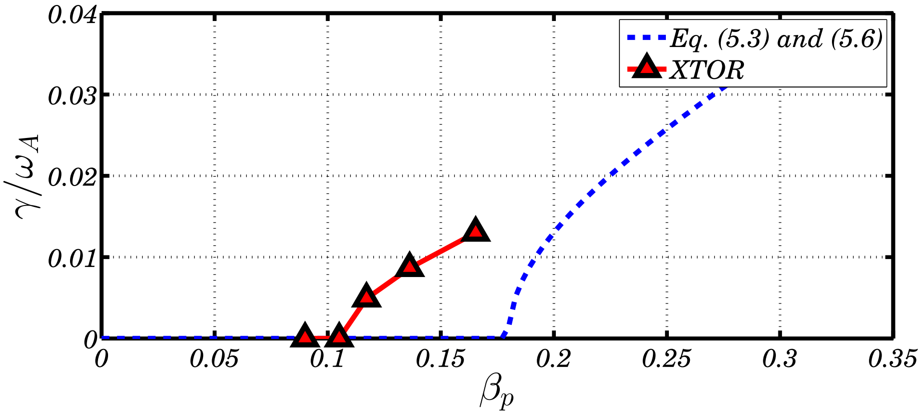

Figure 5.4: Growth rate of the $n = 1$ mode versus β_p. The broken curve represents the analytical results from (5.3) and (5.6); the red triangles are the results from the XTOR-2F simulations. Qualitative agreement between linear theory and numerical simulations is found. The discrepancy between numerical and analytical threshold is attributed to toroidal effects, which are known, at least for the $m = 1$ internal kink mode, to strongly affect this value.

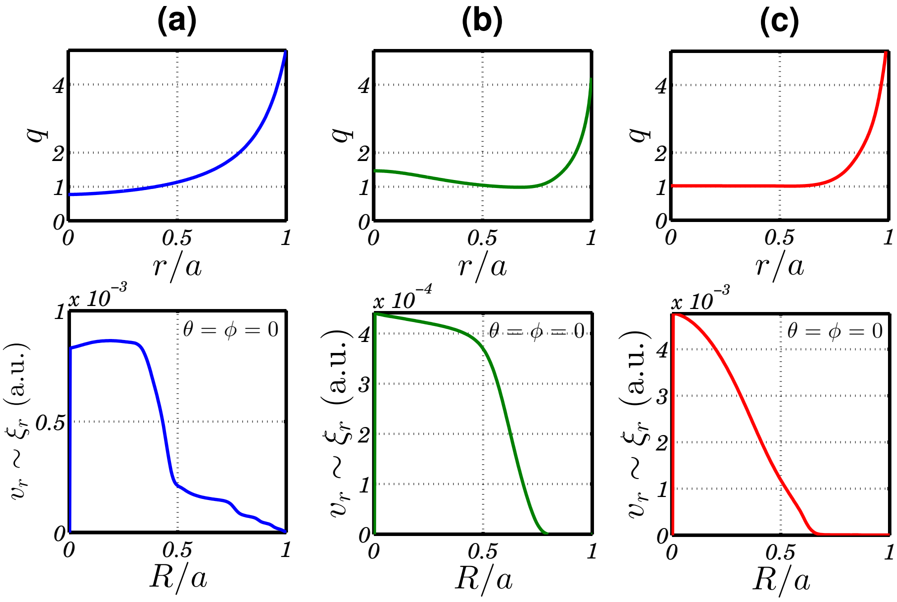

Figure 5.5: Safety factor (top, CHEASE equilibrium) and radial velocities (bottom, $v_r \sim \xi_r/\gamma$ from ideal XTOR-2F simulations) of the $m_0 = n = 1$ mode for three different type of q profiles: (a) monotonic (circular, low β, moderate $\varepsilon \sim 0.4$), (b) weak-reversed (ITER-like, see Chapter 3), (c) ultra-flat (MAST-like, $q_{min} \sim 1.0156$).

A second set of simulations has been performed by keeping $\beta \approx 3\%$ fixed and by varying q_{min}. The behaviour of the instability both with and without the inclusion of ω^* effects is examined. The parameter q_{min} is varied by shifting the safety factor up and down rigidly, within the interval $0 \leq \delta q \leq 0.05$, where $\delta q = q_{min} - 1$ and the value of β_p does not change significantly due to the variations in δq. We know from the linear theory that when ω_i^* effects are taken into account, the eigenfrequency of the mode acquires a real part indicating that the mode starts to rotate, namely (the hat indicates that the quantity is normalised with respect to the alfvénic frequency):

$$\hat{\omega} = \hat{\omega}_i^*/2 + \sqrt{(\hat{\omega}_i^*)^2/4 - \hat{\gamma}_{MHD}^2}. \tag{5.8}$$

The mode rotates in the ion direction in the poloidal plane (i.e. counterclockwise) and, as shown in the XTOR simulation in Figure 5.6, the topology of the magnetic surfaces is not altered, i.e. they are still nested: the ion diamagnetic rotation frequency imposed in the XTOR-2F simulation, shown in Fig. 5.6, is $|\omega_i^* \tau_A| = 6.43 \times 10^{-3}$. When diamagnetic effects are turned on, the spectrum of E_k is similar to Fig. 5.2 with only a reduction of the linear growth rate. Indeed, as seen in figure 5.6, the core displacement is visibly reduced compared to simulations with $\omega_i^* = 0$ (cf. Fig. 5.3) when the peak in the kinetic energy is reached. From (5.8) we therefore expect that the mode rotates with half of the diamagnetic frequency. The frequency calculated from numerical results is $\omega_{rot} \approx 1.42 \times 10^{-3}$ whereas the analytic rotation frequency reads $\omega_{rot} = \omega_i^* \tau_A/2 \approx 3.215 \times 10^{-3}$. If ω_i^* is increased further, then the discrepancy with the analytic estimate becomes smaller: for a simulation with $|\omega_i^* \tau_A/2| = 1.6075 \times 10^{-2}$ the simulated rotation frequency is $\omega_{rot} \approx 1.2 \times 10^{-2}$.

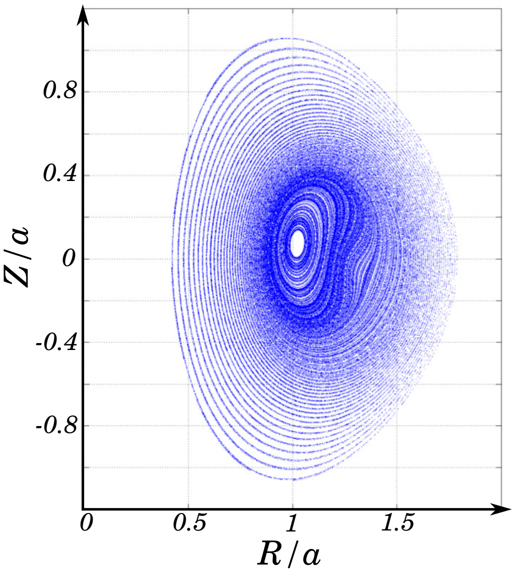

Figure 5.6: Poincaré plot at time $t/\tau_A \approx 1280$ at $\varphi = 0$ (equilibrium parameters as in Fig. 5.1). The diamagnetic frequency is set in the simulation to $|\omega_i^* \tau_A| = 6.43 \times 10^{-3}$. The displacement of the core is visibly reduced compared to Fig. 5.3 and the magnetic axis starts rotating in the ion direction, i.e. counterclockwise.

In addition, from Eq. (5.8), we infer that the presence of ion diamagnetic flows would imply a stabilisation of the mode. The nonlinear amplitude is certainly reduced (compare Figs 5.3 and 5.6), but in addition linear stability boundaries are also affected. This is shown in figure 5.7 where the growth rate calculated by means of Eqs. (5.6), (5.7) and (5.8), and plotted against q_{min}, is compared with the result from XTOR-2F simulations. The growth rate diminishes when q drops below unity as shown in Fig. 5.7, in agreement with Eq. (5.3). A reasonable agreement is found both for the thresholds of the ideal mode with and without ω_i^* corrections, and for the magnitude of the growth rate. The ion stabilisation effect is clearly visible, although it appears less pronounced compared with analytic predictions. In the next section the numerical simulations are extended to include the plasma resistivity, and a comparison with the linear theory is presented.

5.3.2 Resistive simulations

When resistivity is allowed at the $q = 2$ surface, the resonant mode will exhibit a tearing character with the formation of a magnetic island as shown in Fig. 5.8. The

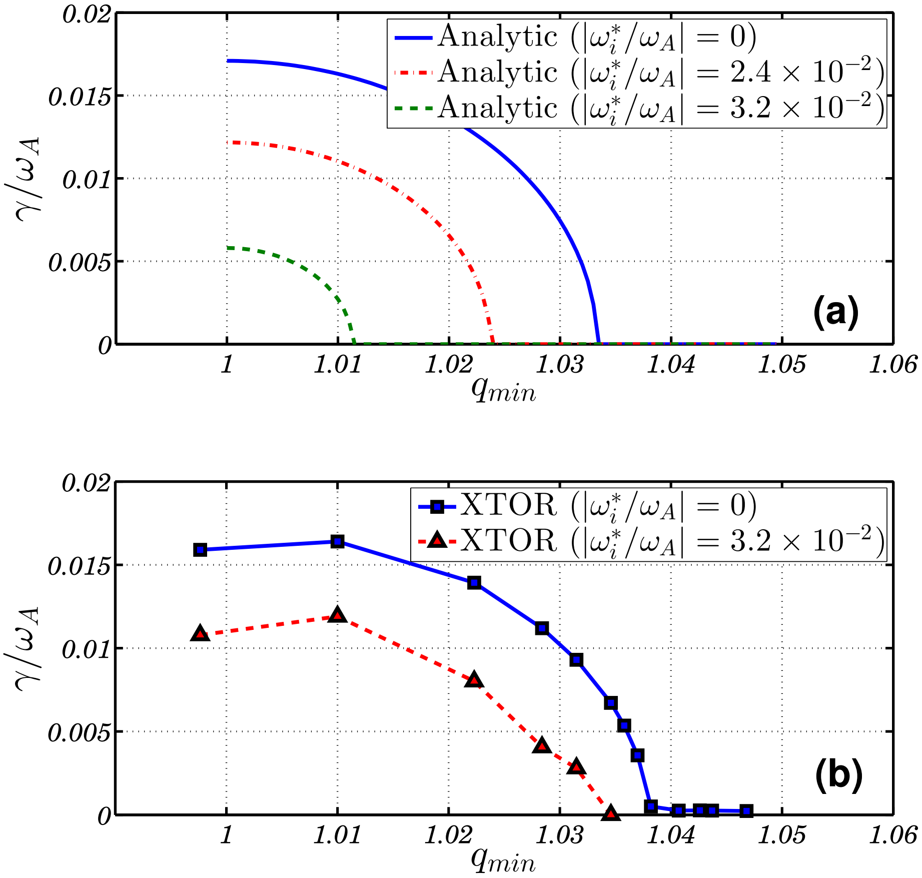

Figure 5.7: Growth rate of the ideal $n = 1$ mode with respect to q_{min}: (a) Analytical growth rate from formulae (5.3), (5.6), (5.7) and (5.8) where $\beta_p \approx 0.1152$; (b) Growth rate from XTOR-2F simulations. The dot-dashed curve (red in (a)) represents the growth rate calculated analytically where the factor $\omega_i^*/2$ is set equal to the rotation frequency calculated from the XTOR-2F simulation (in the XTOR-2F simulation $\omega_i^* \tau_A/2 = 1.6075 \times 10^{-2}$). If one uses the same ω^* frequency as the one as input for XTOR-2F, the ion diamagnetic stabilisation appears stronger in the analytic calculations (green dashed curve in (a)).

behaviour of the kinetic energy and the spectrum for a pure resistive mode (no ω^* corrections) is similar to the one shown in Fig. 5.2. We point out that resistive simulations are carried out by maintaining q_{min} always above unity, in order to prevent the formation of a $m = n = 1$ resistive mode at the $q = 1$ surface.

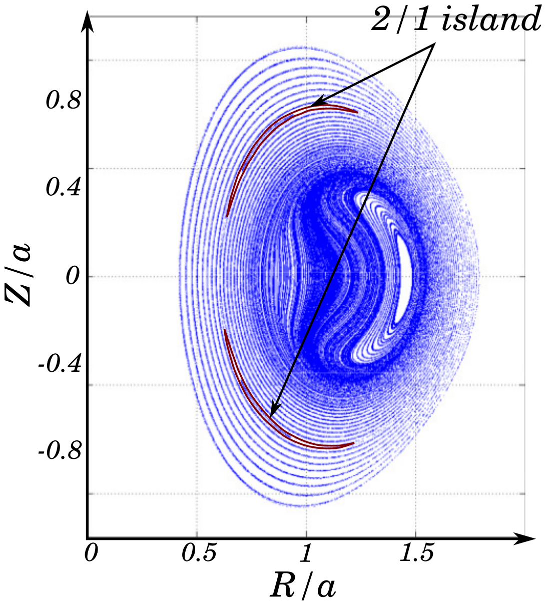

Figure 5.8: Poincaré plot at time $t/\tau_A \approx 1114$ at $\varphi = 0$ (same equilibrium parameters as in Fig. 5.1). The Lundquist number on the magnetic axis is $S = 10^6$, while ω^* effects are switched off. The position of the 2/1 island has been highlighted. Note that the magnetic island develops on ideal timescales. It is shown later that for this configuration the growth rate γ depends rather weakly on resistivity. Thus the mode is classified as being essentially ideal, while it is preserving the tearing character at the $q = 2$ surface.

When diamagnetic effects are dropped, the dispersion relation (5.3) reads (see the previous chapters) [58, 114]:

$$\hat{\gamma}^{5/4}(\hat{\gamma}^2 - \hat{\gamma}^2_{MHD}) = \hat{\gamma}^{13/4}_{inf}, \tag{5.9}$$

where γ_{inf} denotes the growth rate of the resistive infernal mode at the ideal stability boundary ($\gamma_{MHD} = 0$):

$$\hat{\gamma}_{inf} = \left(\frac{n^2\beta_p^2 G_0(B_0 - A_0)}{1 + 2q_*^2}\right)^{4/13} \bar{S}^{-3/13}. \tag{5.10}$$

If $\gamma^2_{MHD} \gg \gamma^2 > 0$ (which has to be checked *a posteriori*), i.e. a condition for which β_p (δq) is sufficiently large (small), the growth rate becomes independent at leading order of the value of plasma resistivity, i.e. $\gamma \sim S^0$. This is because the mode is in the region of strong ideal instability. On the other hand, if $|\gamma^2_{MHD}| \gg \gamma^2$ with $\gamma^2_{MHD} < 0$, i.e. we are in the ideal stability region, the scaling of the resistive mode will be *tearing-like*, namely $\gamma \sim S^{-3/5}$.

The stability threshold in δq (for fixed $\beta_p \approx 0.1$) of the resistive mode, found by using Eqs. (5.3), (4.41), (4.42), (5.4) and (5.6), is $\delta q_{crit} \approx 0.05$. The tearing stability index for this equilibrium configuration, calculated by means of Eq. (5.4), is $r_s\Delta'_{tear} \approx -3.5$ and it is not strongly affected by the variation of q_{min}. Thus we do not expect any growth of the usual 2/1 tearing mode if either the q profile is sufficiently far from the 1/1 resonance or β_p is sufficiently low, namely we are *tearing stable* in the cylindrical limit of the analysis employed for the 2/1 mode. Indeed in Fig. 5.9, where the behaviour of the growth rate of the resistive mode is shown with respect to q_{min}, we see that no resistive modes develop beyond $q_{min} = 1.05$. Diminishing δq, the mode enters in the strong instability region and the growth rate becomes asymptotically independent of the resistivity. When we are close to the

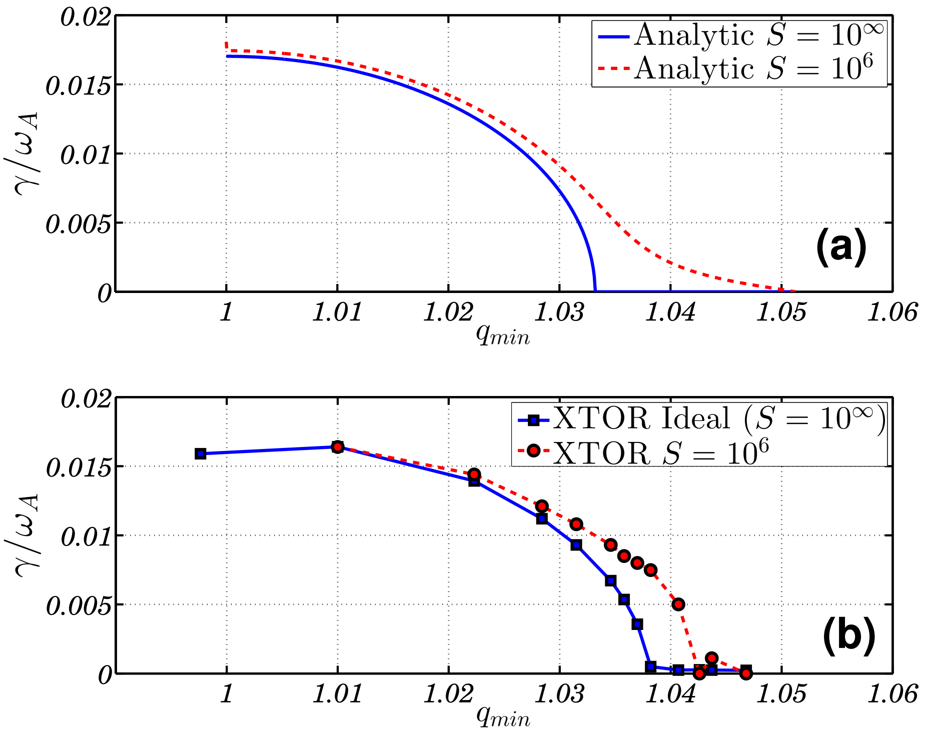

Figure 5.9: (a) Analytic growth rate ideal (blue solid line) and resistive (red dashed line) with q_{min} from the equilibrium parameters as in Fig. 5.2, and with $\beta_p \approx 0.115$ (the resistive threshold is found for $\delta q \approx 0.05$); (b) Ideal (blue squares) and resistive (red dots) growth rate from XTOR-2F simulations (equilibrium parameters as in Fig. 5.2) with no ω^* effects. The value of the Lundquist number on the magnetic axis is $S = 10^6$ (the value of S on the resonant surface is $S \approx 3.5 \times 10^5$). It is clearly visible that for sufficiently small values of δq, the growth rate becomes asymptotically independent of the plasma resistivity. Close to marginal stability, the effects of resistivity on growth rate and stability boundary is strong.

ideal stability boundary ($\gamma_{MHD} = 0$), the effects of resistivity strongly affect the growth rate and the stability boundary. The scaling with respect to the Lundquist number is found to be $\gamma \sim S^{-3/13}$, as shown in Fig. 5.10. The agreement between numerical results and analytical calculations is rather good, even though the aspect ratio is small.

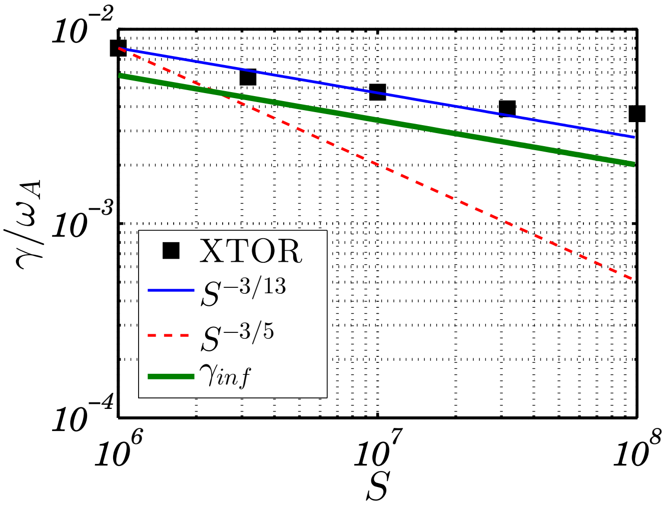

Figure 5.10: Growth rate of the infernal-resistive mode, close to the ideal stability boundary, wrt the Lundquist number S with $q_{min} = 1.037$ and $\beta_p = 0.1152$. The results from XTOR-2F simulations (black squares) are in reasonable agreement with the expected $S^{-3/13}$ dependence shown by the thin blue solid line. The thick green solid line shows the analytic estimate of γ_{inf} obtained by using Eq. (5.10).

When diamagnetic effects are allowed on the resonant $q = 2$ surface, Eq. (5.9) is modified in the following manner [114]:

$$\left[\hat{\gamma}(\hat{\gamma} + i\hat{\omega}_i^*)(\hat{\gamma} + i\hat{\omega}_e^*)^3\right]_s [\hat{\gamma}(\hat{\gamma} + i\hat{\omega}_i^*) - \hat{\gamma}_{MHD}^2]_\ell^4 = \hat{\gamma}_{inf}^{13}, \tag{5.11}$$

where the subscript s (ℓ) indicates that the diamagnetic frequency has to be evaluated for the mode resonant (almost resonant) with the $q = 2$ ($q = 1$) surface. If γ_{MHD}^2 is sufficiently large and positive definite, then the dispersion relation at leading order reads $\hat{\gamma}(\hat{\gamma} + i\hat{\omega}_{i,\ell}^*) - \hat{\gamma}_{MHD}^2 = 0$, i.e. the dispersion relation reduces to the one for ideal modes. Indeed Fig. 5.11 clearly shows that if the mode is in the ideal instability region, the growth rate has a weak dependence on the plasma resistivity. On the other hand, if γ_{MHD}^2 is large but negative, Eq. (5.11) reduces to the standard dispersion relation for drift-tearing modes [67, 96, 110].

A modification of the ideal stability boundary is expected once diamagnetic effects are switched on, according to Eq. (5.8). We identify the *ideal diamagnetic stability boundary* where the growth rate of the ideal mode with ω^* effects is vanishing. When the diamagnetic effects are weak, the growth rate of the mode is given by Eq. (5.10),

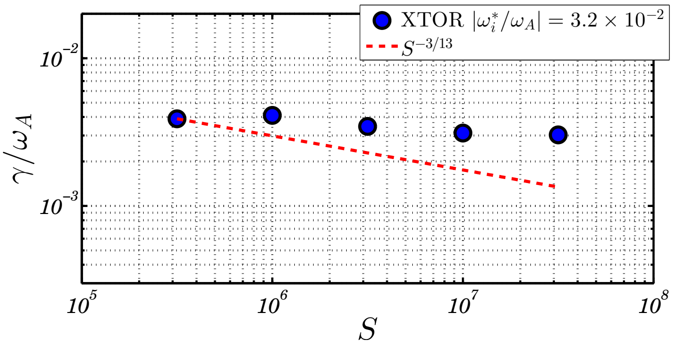

Figure 5.11: Growth rate against the Lundquist number from a starting equilibrium with the same profiles as in Fig. 5.2 but with $q_{min} = 1.0315$ and $\beta \approx 2.834\%$. The diamagnetic frequency is $|\omega_i^*/\omega_A| = 0.032$. The growth rate of the mode shows a weak dependence upon the plasma resistivity, as expected since we are sufficiently far from the ideal diamagnetic stability boundary (see Fig. 5.7).

and the mode rotates with a frequency equal to $\omega_{rot} \approx \frac{1}{13}(\omega_{i,s}^* + 3\omega_{e,s}^* + 4\omega_{i,\ell}^*)$. If ω^* effects are increased further, we might expect that the ideal diamagnetic stability boundary is crossed and the growth rate changes from the fast ($\sim S^{-3/13}$) scaling to a moderately fast ($\sim S^{-3/8}$) scaling, first identified in Ref. [114]. Finally, the standard *drift-tearing* scaling [67, 96, 110, 111] is recovered when the diamagnetic effects are increased further.

From XTOR-2F results, when diamagnetic effects are included, and when the plasma parameters are those of the earlier section, the stability boundary occurs for $0.0129 < |\omega_i^*/\omega_A| < 0.0161$. Figure 5.12 shows the behaviour of the growth rate with different values of the diamagnetic frequencies. The growth rate diminishes with an increase of the diamagnetic effects as expected from the linear theory, and appears to exhibit a transition from extremely fast ($\sim S^{-3/13}$ for $|\omega^*/\omega_A| = 0$) to moderately fast ($\sim S^{-3/8}$ for $|\omega^*/\omega_A| \approx 1.61 \times 10^{-2}$ and $S \gtrsim 10^7$). This is in accordance with the analytic predictions in Chapter **4** since we can approximate $\gamma_{inf} \ll \omega^*$. Eventually the transition to the *drift-tearing* regime is expected when $\omega^* \gg |\gamma_{MHD}^2|$. We are able to measure the rotation frequency for the case $|\omega_i^* \tau_A| = 1.6 \times 10^{-2}$ with $S = 2 \times 10^6$ on the magnetic axis, which gives $\omega_{rot}\tau_A \approx 10^{-3}$, indicating a slowly (compared to to the diamagnetic frequency) rotating mode. Unfortunately it has not been possible to check the rotation frequency of the modes for higher Lundquist numbers, i.e. when the moderately fast scaling occurs, because the amplitude of the modes becomes too small.

5.3.3 Evolution of the island width

After the linear phase, where the 2/1 magnetic island is driven unstable by the linear coupling due to toroidicity with the 1/1 mode, the island evolves non-linearly. We

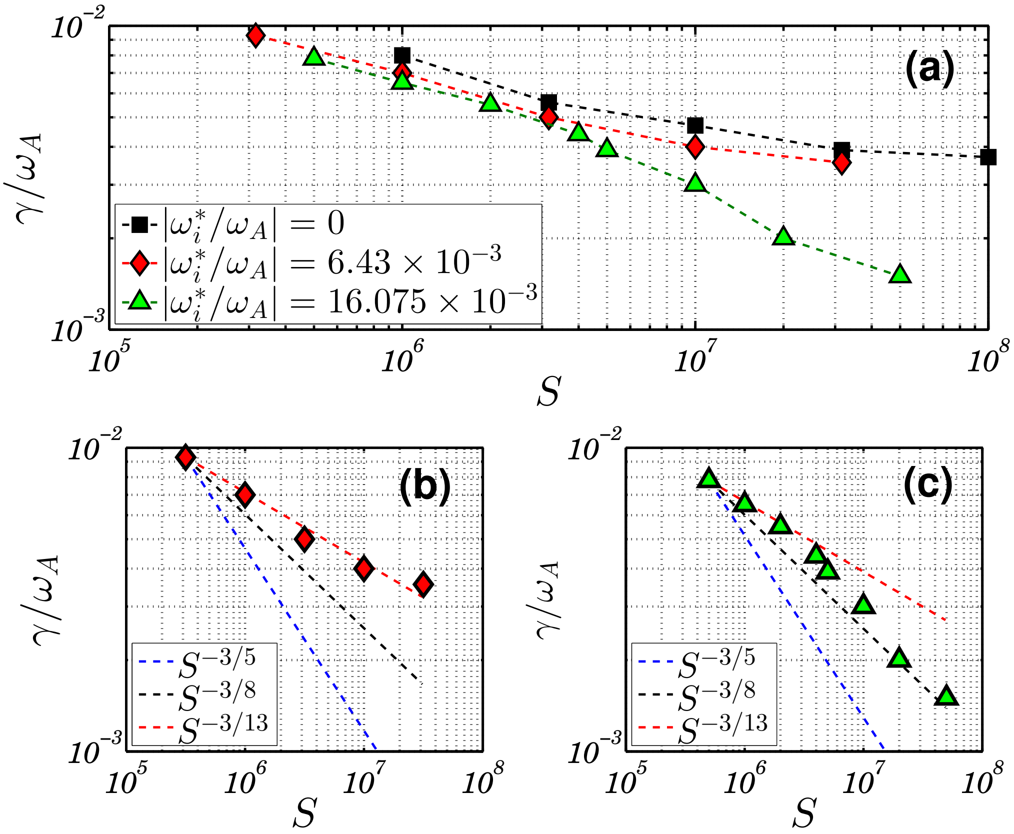

Figure 5.12: Growth rate wrt the Lundquist number from a starting equilibrium with the same profiles as in Fig. 5.2 for different values of the diamagnetic frequencies $|\omega_i^*/\omega_A| = 0, 6.43 \times 10^{-3}, 16.075 \times 10^{-3}$ (a); (b) corresponds to $|\omega_i^*/\omega_A| = 6.43 \times 10^{-3}$ and (c) corresponds to $|\omega_i^*/\omega_A| = 16.075 \times 10^{-3}$. The reduction of the growth rate is visible as well as the change of the scaling with respect S for sufficiently large values of the Lundquist number.

now examine the evolution of the width of the island in absence of diamagnetic effects. The equilibrium considered has the profiles, for p and q, shown in Fig. 5.2 with $q_{min} = 1.0223$ and $\beta = 2.88\%$. Thus in accordance with Figs. 5.7 and 5.9 we are in the region of strong instability. Hereafter the resistivity and density values on the magnetic axis are taken such that $S = 10^6$.

When the nonlinear stage is reached, the kinetic energy of the 1/1 mode shows an oscillating behaviour whose amplitude is slowly decreasing in time, as shown in Figure 5.13. The magnetic energy of the mode is also highly oscillating but it has a less regular pattern. On the other hand, the magnetic energy of the 2/1 sideband oscillates less, and eventually saturates (the kinetic energy manifests an oscillating behaviour in phase with the 1/1 mode). Figure 5.15 shows the Poincaré plot of the flux surfaces when the evolution enters in the nonlinear phase. The 1/1 mode exhibits an oscillating behaviour which repeats every $250\tau_A$. The magnetic island located at the $q = 2$ surface, after the very rapid growth during the linear phase, is monotonically increasing in size with time.

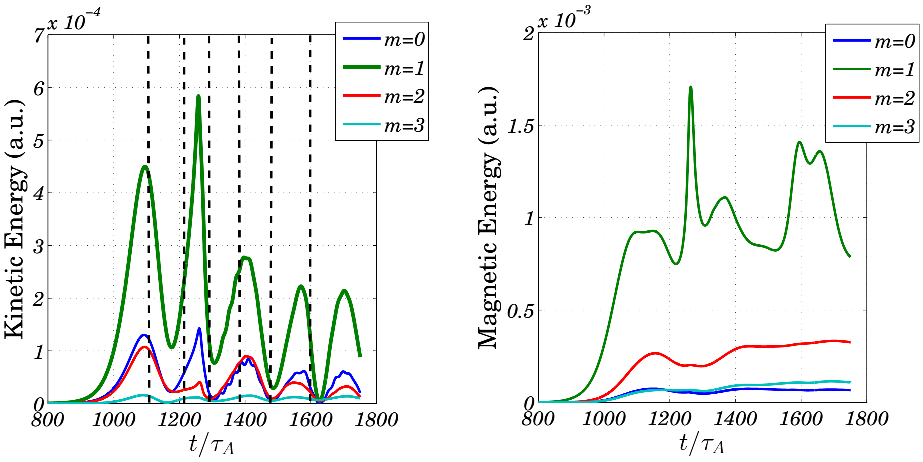

Figure 5.13: Evolution of the kinetic energy (left) and magnetic energy (right) of the $n = 1$ mode with the same parameters as in Fig. 5.2. The magnetic energy of the $m = 2$ mode saturates indicating a persistent $m = 2$ mode. The dashed vertical lines on the left panel indicate the time at which each snapshot of the Poincaré cross section in Fig. 5.15 is taken.

The behaviour of the pressure during the nonlinear phase is rather regular with the peak of the pressure following the position of the magnetic axis of the bean shaped flux surfaces. Figure 5.14 shows the evolution of the pressure profile plotted as a function the major radius where the snapshots correspond to those of the Poincaré plots in Fig. 5.15. The ion diamagnetic frequency ω_i^* is set to zero, so the mode does not rotate in the poloidal plane (hence the asymmetry of p with respect to R due to the 1/1 mode does not change direction).

We note that although only two toroidal modes are retained, namely the $n = 0$

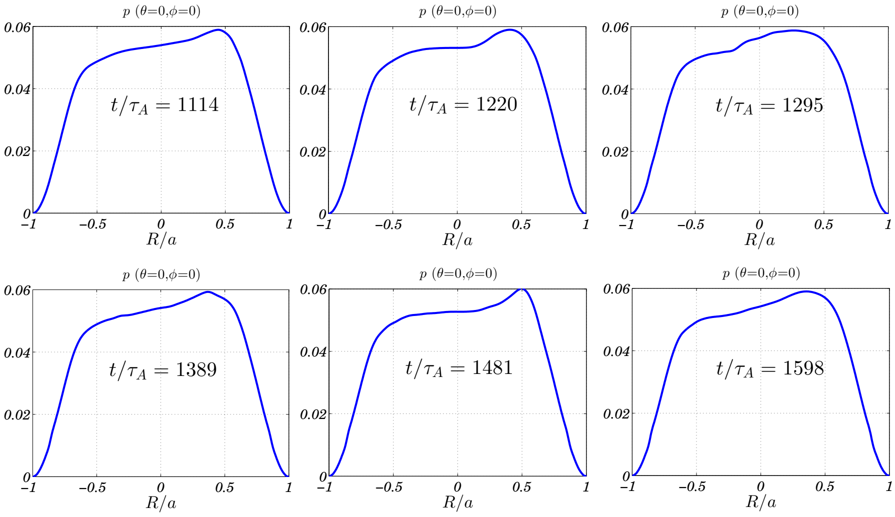

Figure 5.14: Normalised pressure profile (XTOR-2F units) evolution during the nonlinear phase. The pressure is shifted outwards and inwards following the position of the magnetic axis.

and the $n = 1$, the evolution of the physical quantities (the kinetic and magnetic energies and the island width, the shift of the 1/1 mode) are apparently similar to the numerical results presented in previous papers [115]. However we stress here the point that the 2/1 island shown in Fig. 5.8 (in contrast with Ref. [115]) is driven by the linear coupling with the 1/1 mode due to toroidicity. When the 2/1 island becomes larger than the resistive layer, i.e. when it enters in the nonlinear regime, the evolution of the magnetic island width is given by the well known Rutherford equation [16, 30, 32]:

$$\frac{a}{r_s}\frac{d\hat{w}}{d\hat{t}} = 1.66\frac{r_s\Delta'_{tot}}{S}, \tag{5.12}$$

where $\hat{w} = w/a$ is the normalised island width, $\hat{t} = t/\tau_A$ and the Lundquist number is evaluated on the surface $r = r_s$ (it is assumed that S is almost constant across the resistive layer). The coupling of the 2/1 with the 1/1 mode which occurs in the plasma core, alters the shape of the eigenfunction at the resonant 2/1 surface (where the treatment is cylindrical in nature), leading to a modification of the slope of the poloidal flux across this point, namely a modification in $r_s\Delta'$. Thus the expression of $r_s\Delta'_{tot}$ contains a coupling contribution Δ'_{coupl}, as well as the standard contribution of a cylindrical plasma Δ'_{tear} given by equation (5.4) [29], and the Glasser, Green, Johnson contribution $\Delta'_{GGJ} = -6.35(q^2-1)L_q^2/(rL_p)\beta/w$ where $L_q = q/(dq/dr)$ and $L_p = -p/(dp/dr)$ [33]. Hence:

$$r_s\Delta'_{tot} = r_s\Delta'_{tear} + r_s\Delta'_{coupl} + r_s\Delta'_{GGJ}.$$

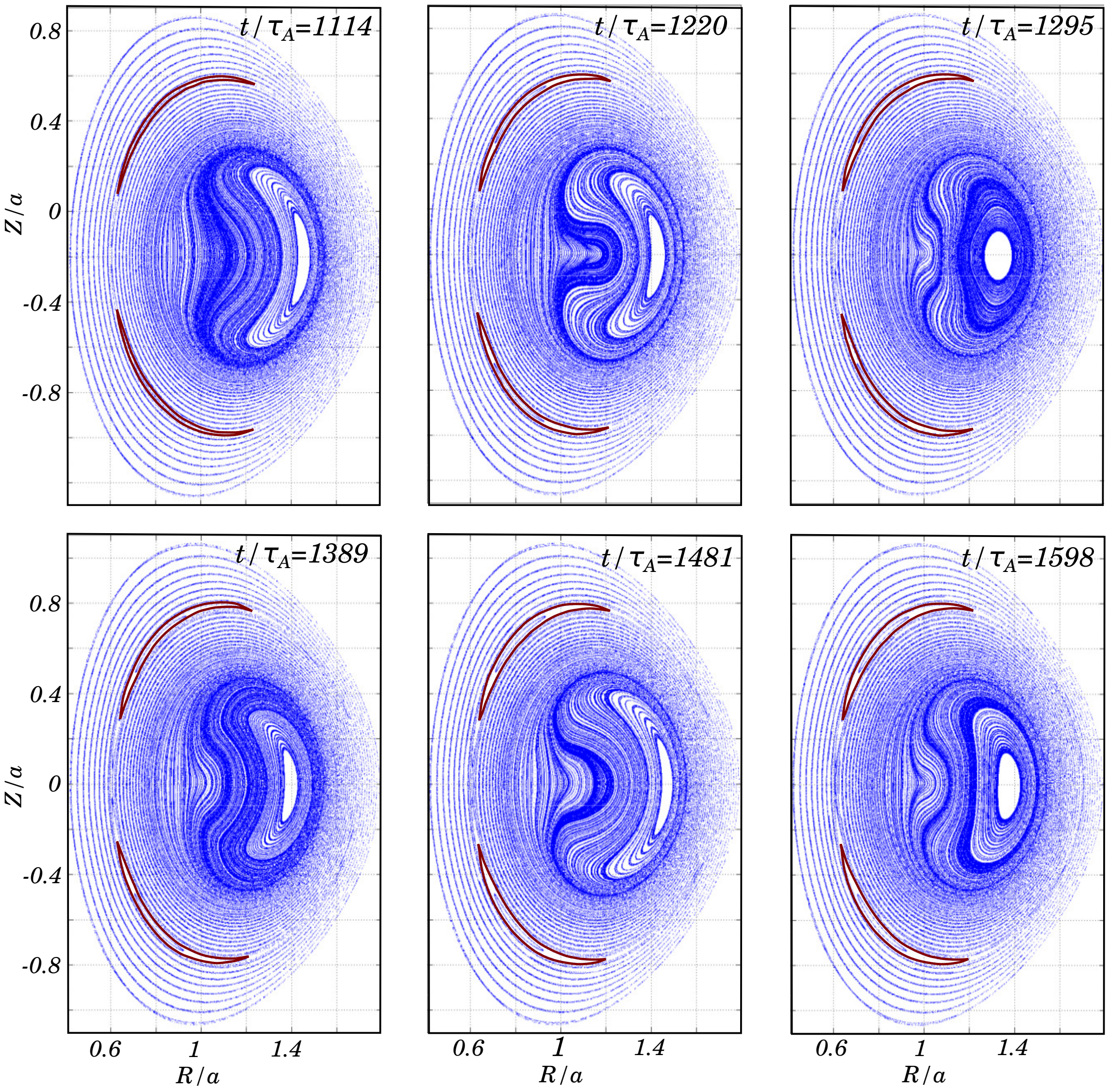

Figure 5.15: Poincaré plots at $\varphi = 0$ with the same parameters as in Fig. 5.13. The linear phase ends approximately at $t/\tau_A = 1114$. When the modes enter in the nonlinear regime, the oscillating behaviour, shown in Fig. 5.2, of the main $m_0 = 1$ mode is clearly visible, while the 2/1 magnetic island shows a monotonic growth in time (the contours of the 2/1 island have been highlighted).

Other terms arising from quasi-linear corrections, bootstrap contribution, etc. are discarded, since we are interested in the nonlinear behaviour before saturation, not on the saturation mechanism itself. Moreover these additional corrections are not included in our XTOR-2F calculations. The contribution due to the "*tearing*" and the GGJ terms can be computed analytically giving $r_s\Delta'_{tear} \approx -3.5$ and $r_s\Delta'_{GGJ} \approx -0.9$. Although the coupling is nominally weak ($\mathcal{O}(\varepsilon)$), we expect that Δ'_{coupl} will contribute significantly to the total Δ'_{tot}. In the absence of diamagnetic effects, the parameter $r_s\Delta'_{tot}$ is easily computed once the linear growth rate of the 2/1 mode is known, i.e.:

$$r_s\Delta'_{tot} = \bar{S}^{3/4}\hat{\gamma}^{5/4}. \tag{5.13}$$

The growth rate γ is computed either from the linear phase in XTOR or from the analytic estimate (for large growth rate they match reasonably well, see Fig. 5.9). Note that during the linear phase, the growth rate of the 2/1 mode is identical to the 1/1 mode. Thus we assume $r_s\Delta'_{tot} \approx 6.18$ (fixed, thin island).

In figure 5.16, which shows the temporal evolution of the magnetic island width, two phases are clearly visible. The phase just before the nonlinear stage is characterised by a rapid growth of the island width until $t/\tau_A \approx 1100$ (this is still the linear stage, as we can see from the plot of the kinetic energy in Fig. 5.13). The magnetic energy of the $m = 2$ mode (cf. Fig. 5.13) peaks at about $t/\tau_A \approx 1150$ and decreases until $t/\tau_A \approx 1200$. From $t/\tau_A \approx 1200$ the growth of the island width exhibits a Rutherford-like behaviour, where the slope of the time evolution is in good agreement with Eq. (5.12). The two phases are consistent with Fig. 5.13 when the 2/1 mode is rising rapidly from $t/\tau_A \approx 800$ until $t/\tau_A \approx 1200$, with a subsequent decrease of the magnetic energy, which is followed by a slower growth. Note that in the nonlinear simulations, $\omega^*_{i,e}$ was set to zero, so that modes rotating in the electron direction, such as those shown in Fig. 5 of Ref. [9], are absent.

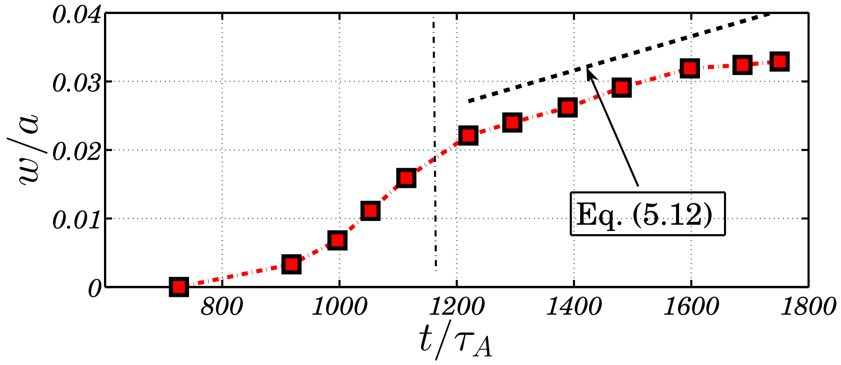

Figure 5.16: Magnetic island width with respect to time (parameters as in Fig. 5.13). The behaviour of the evolution of the magnetic island width shows two growths before reaching saturation. Rutherford's equation (5.12) together with Eq. (5.13) qualitatively gives the slope of the growth from $t/\tau_A \approx 1200$ until the saturation.

The nonlinear evolution of the magnetic island width and the results obtained from XTOR-2F simulations of figures 5.15 and 5.16 could be consistent with experimental TCV data [40] of strong NTM seeding by sawteeth. Measurements of a 2/1 island, growing within 100 τ_A after a sawtooth crash, were experimentally reported, as well as a 3/2 island which is detected within $800\mu s$ after a sawtooth event [40]. Although the full explanation of the 3/2 NTM seeding and evolutions needs additional nonlinear physics, magnetic measurements suggest that the 3/2 mode could be generated by the 2/2 subharmonic via toroidal coupling [40]. Indeed a large 2/2 subharmonic during a sawtooth collapse is also consistent with previous numerical simulations [118]. A calculation with $n = 2$ modes in XTOR-2F, as in the analytic dispersion relation, shows that the 2/2 mode is also strongly unstable, and a 3/2 island is also triggered as shown in Fig. 5.17. The argument on timescales and relevance to TCV holds also for the $n = 2$ mode.

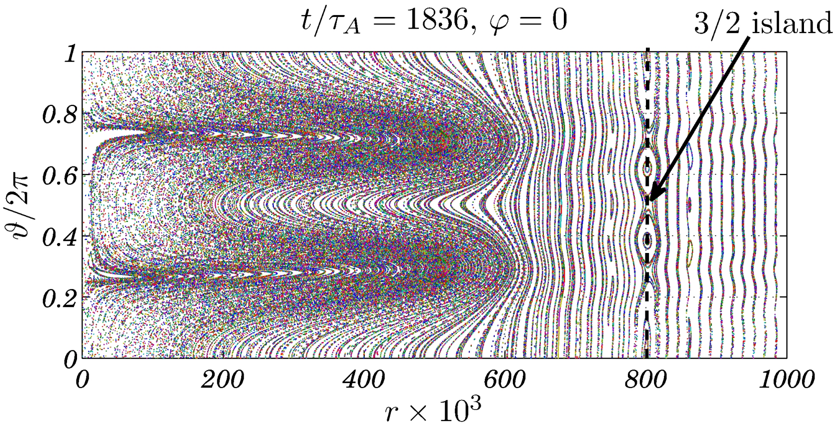

Figure 5.17: Poincaré plot of the magnetic field lines with the same input profiles as in Fig. 5.15, but where only the $n = 2$ mode has been retained. The linear phase goes from $t/\tau_A = 0$ up to $t/\tau_A = 1680$. The linear growth rate of the $n = 2$ mode is $\gamma/\omega_A \approx 0.012$. The vertical dashed line indicates the position of the $q = 3/2$ surface.

We point out that the coupling with the 1/1 mode is the key ingredient for the seeding and evolution of the island width. Indeed we just analysed a situation where the tearing 2/1 mode is stable ($\Delta' < 0$), but the coupling with the 1/1 mode drives it unstable. We stress the point that we considered a configuration for which $q_{min} > 1$ (no $q = 1$ resonance) so that the resistivity only matters at the 2/1 surface. A separate analysis as to be carried out when $q_{min} < 1$, for which the resistive 1/1 mode develops. Hence the 2/1 island width would be expected to diminish on resistive times if the q profile were raised or lowered sufficiently far from the 1/1 resonance after the end of linear phase. When δq is large (i.e. q is far from the resonance), the 1/1 and the 2/1 modes are no longer coupled, and in this situation the 2/1 *standard tearing mode* is intrinsically stable. More advanced work would include a bootstrap contribution, so that once the island has been seeded and evolved via the 1/1 coupling, a subsequent large island can remain in place regardless of the dynamics of the 1/1 mode.

5.4 Summary

In this chapter an extensive study of MHD instabilities in a low shear MAST-like configuration has been presented. Numerical simulations performed with the XTOR-2F code, both in the ideal and resistive MHD frame with the inclusion of diamagnetic flows, have been compared with analytic linear theory of infernal modes [114]. Additional effects such as $\boldsymbol{E} \times \boldsymbol{B}$ sheared flows, neoclassical corrections, energetic ions, etc. have been neglected. Since the infernal modes are characterised by coupled poloidal sidebands due to the combined effect of pressure gradient and toroidicity, the aspect ratio has been kept sufficiently small in the simulation in order to enhance the coupling.

The results of the linear theory have been successfully compared, with reasonable agreement, with numerical XTOR-2F simulations. The impact of ω^* effects on the scaling of the growth rate as a function of S and on the mode rotation have been confirmed by the XTOR-2F code. The study of ideal MHD dynamics has been carried out by performing a scan both in β_p (with a fixed δq) and δq (with fixed β_p). When a constant diamagnetic frequency ω_i^* is taken into account the mode tends to be stabilised and starts to rotate in the ion direction. The numerical threshold and the magnitude of the growth rate of the mode are found to be in qualitative agreement with the analytic estimate, as well as the rotation frequency when ion diamagnetic effects are present. The discrepancies can be attributed to shaping effects, which have not been taken into account in the analytic treatment, and to the tight aspect ratio of the configuration considered.

Resistive dynamics have been studied by varying δq from 0 to 0.05 with a fixed value of $\beta_p \approx 0.1$ at the $r = r_*$ surface. The comparison between analytic and numerical growth rate close to the ideal (without ω_i^* effects) stability boundary shows good agreement. In addition it has been possible to provide an analytical estimate for the threshold of the resistive mode, which appear to be consistent with XTOR-2F results. No growth of the resistive tearing mode occurs for sufficiently large values of δq (i.e. in the resistive stability region of the infernal mode). This is also in agreement by having a negative Δ'_{tear}.

Various scalings with respect to the Lundquist number are found by tuning the strength of two-fluid effects: close to the ideal stability boundary, the growth rate tends to decrease with an increase of the ω^* frequencies. The growth of the mode converts from the extremely fast $\gamma \sim S^{-3/13}$ scaling to a moderately fast $\gamma \sim S^{-3/8}$ growth and is then expected to eventually turn into the standard drift-tearing scaling as ω^* is increased.

A preliminary study of the nonlinear evolution of the width of the magnetic island of the tearing $(m_0 + 1, n)$ sideband has been performed. The numerical results show two distinct phases: right before the early nonlinear stage we have a rapid growth, which is subsequently followed by a second phase in which the growth reduces and the island width evolves according to Eq. (5.12), a modified Rutherford equation that includes a coupling contribution to the 1/1 mode.

6

Conclusions

Understanding plasma dynamics in tokamak fusion relevant scenarios is of crucial importance for the success of the entire fusion program. This thesis addresses the problem of equilibrium properties and MHD stability of hybrid plasmas, both in tokamak and RFP configurations. This work has two main outcomes: the first is a characterisation of the properties of equilibrium helical states and the connection that they have with non-linearly saturated ideal modes frequently observed in hybrid-like tokamaks and RFPs [7, 8]. The second outcome is a description of fast growing resistive instabilities (when the safety factor is sufficiently flat) and the impact that non-MHD effects have on the growth of such modes, related in particular to the problem of the fast seeding of NTMs.

Chapter **3** presents an analytic theory of non-linearly saturated $m = 1$ modes (with an arbitrary toroidal mode number n), and analytic conditions for which a helical state exists. Comparisons between 3D VMEC equilibria calculations and XTOR-2F nonlinear simulations of saturated ideal MHD instabilities have been presented. We examined both tokamak and RFP plasmas, where VMEC results were computed in fixed and free boundary conditions. Hybrid ITER-like and MAST-like plasmas have been examined: VMEC and XTOR-2F agree reasonably well when $q_{min} > 1$ in accordance with analytical predictions for saturated internal kinks [26, 62, 63]. When $q_{min} < 1$, the helical state in the 3D equilibrium calculations decreases and eventually disappears, in contrast with XTOR-2F and analytic results. It is found that if a small $n = 1$ RMP external magnetic perturbation is included in the equilibrium calculations, the displacement resulting from VMEC calculations approaches the amplitude of the saturated kink computed with XTOR. It is also found that when q is above unity the amplitude of the displacement of the magnetic axis depends weakly on the strength of the external RMP field. When q_{min} is less than unity, the position of the magnetic axis is strongly dependent upon the $n = 1$ RMP field applied: a significant reduction/increase of the RMP yields a significant reduction/increase of δ_h. In contrast with the cases where $q_{min} > 1$, the discrepancy of the VMEC and XTOR-2F approaches when resonant surfaces exist in the plasma is not still understood.

Beyond tokamak physics, an RFP configuration with a non-monotonic q profile having $q_{max} \approx 1/7$, has also been studied. This configuration gives rise to the SHAx equilibrium state, and has been previously modelled using the VMEC code [7]. By using the XTOR-2F code in the ideal frame, it has been possible to study the behaviour of the ideally saturated $n = 7$ mode. It has been found that XTOR-2F agrees well for the prediction of the displacement of the magnetic axis with the VMEC code when only one toroidal mode, i.e. $n = 7$, is retained in XTOR-2F and VMEC. The numerical results are compared with very good agreement with the analytical theory of the nonlinear saturation of an ideal $m = 1$ mode (cf. Eq. (3.14a) in Chapter **3**), in the approximation of large aspect ratio. Connection to linear theory shows that the driving mechanism of the SHAx equilibrium is a 1/7 internal kink, caused by the combined effect of current and pressure gradients, but dominantly by the current.

Chapter **4** presents a derivation of an analytic expression for the growth rate for *infernal modes* with additional non-MHD effects (cf. Eq. (4.56)). Charlton's resistive quasi-interchange model [58] has been extended with the inclusion of plasma diamagnetism and equilibrium MHD toroidal flows, both retained throughout the entire plasma volume, and viscosity, which is taken into account only at the resistive sideband resonant surface. The sideband magnetic perturbation can be analytically described exactly with a careful choice of the rotational trasform. An approximate WKB generalisation has also been derived. It is found that the ideal mode is stabilised when core ω_i^* corrections (with constant ω_i^*) are considered. Considering separately plasma diamagnetism, the effect of viscosity and equilibrium toroidal flows, three dispersion relations, corresponding to three different regimes, are derived. Various scalings of the growth rate γ against the Lundquist number S have been found.

Focusing in particular on the effect of plasma diamagnetism, it has been found that for sufficiently weak non-MHD effects, the fast growth ($\gamma \sim S^{-3/13}$ at the ideal stability boundary) of the mode is preserved. This could be consistent with the fast growth of NTM seeding in realistic modes of operation. With strong ω^* effects, the extremely fast growth rate of the resistive mode is reduced but, close to the ideal MHD stability boundary, a novel moderately fast scaling proportional to $S^{-3/8}$, i.e. intermediate between the *infernal* and the *tearing* behaviour, has been identified. A similar scaling has also been found close to the ideal boundary when equilibrium toroidal flows are taken into account. These modes tend to rotate either in the electron diamagnetic direction, or in the ion diamagnetic direction, in agreement with TCV experiments during hybrid-like operation [9]. The effects of density gradients with flat temperature profile, relevant in the post sawtooth scenario, for the $m_0 = n = 1$ have also been assessed (see Appendix A.4).

A comparison between the linear theory of Chapter **4** and numerical XTOR-2F simulations is given in Chapter **5**, where an extensive study of *infernal type* MHD instabilities in a low shear MAST-like configuration has been presented. The goal of the comparison is to confirm numerically the novel analytic results (ideal and resistive growth rates, mode rotation, scaling wrt S). After agreement was made between linear analytic and numerical simulations, this enabled us to confidently undertake nonlinear simulations of infernal resistive modes. A MAST-like configuration is preferable because of the enhanced coupling due to the tight aspect ratio of the machine. Numerical simulations are performed both in the ideal and resistive MHD frame with the inclusion of diamagnetic flows, neglecting additional effects such as $\boldsymbol{E} \times \boldsymbol{B}$ sheared flows, neoclassical corrections, energetic ions, etc. In the ideal limit, the stabilising effect of core diamagnetic ions has been shown, together with demonstrating that the mode rotation is in the ion direction. The stability threshold, the growth rate and the rotation frequency of the mode calculated with XTOR-2F are found to be in good agreement with the analytic estimate. Shaping and finite aspect ratio effects are considered to be responsible for the deviations in the simulations with respect to the linear theory predictions.

When resistivity is turned on, the comparison between analytic and numerical growth rate close to the ideal (without ω_i^* effects) stability boundary shows good agreement. The stability boundary of the resistive mode is also showing good agreement with analytical predictions. The impact of ω^* effects on the growth of the resistive mode has been assessed numerically, and various scalings with respect to the Lundquist number are found by tuning the strength of two-fluid effects. We first notice that an increase of the ω^* frequencies tends to reduce the growth rate close to the ideal stability boundary, as predicted by the linear theory. In addition the transition from the extremely fast $\gamma \sim S^{-3/13}$ scaling to the moderately fast $\gamma \sim S^{-3/8}$ growth, when strong diamagnetic effects are considered, has been confirmed in XTOR-2F simulations. Finally a preliminary study of the nonlinear evolution of the width of the magnetic island of the tearing sideband has been performed, showing two distinct phases. First, in the linear phase the growth of the resistive sideband experiences a rapid increase followed then by a second phase in which the island width evolves on resistive timescales according to Rutherford's theory [30]. This appears to be consistent with experimental measurements of NTM evolution following a sawtooth crash in TCV [40].

In conclusion, the present thesis presents a study of equilibrium and stability properties of tokamak and RFP hybrid plasmas. The first part provides a characterisation of helical 3D equilibrium states based on equilibrium calculations and nonlinear stability simulations in the ideal MHD frame. In addition, analytical criteria for the existence of helical equilibrium cores were given. In the second part of the thesis, the problem of the fast growth of resistive modes in shear free tokamak plasmas, in relation to the NTM seeding problem, is investigated analytically and numerically. Agreement between numerical and analytic approaches is very good. Future extensions of the present work should include an analysis using the XTOR-2F code of the resistive dynamics of RFP plasmas, modelling the plasma behaviour which leads to the formation of the helical SHAx state, from the initially axisymmetric configuration. The agreement of the analytic theory with the XTOR-2F initial value code opens the way to begin a resistive treatment which could permit stochastic regions to be generated and also more than one magnetic axis. Finally, the connection between infernal-like instabilities and the development of fast triggering of NTMs, resistive global oscillations and saturated equilibria in ITER-like operating scenarios should be continued. A possible extension would include the nonlinear dynamics of the resistive island when bootstrap corrections are considered, thus enabling more realistic modelling of NTM triggering by strong 1/1 modes in configurations with extended regions of low shear.

A

Mathematical derivations

A.1 Curvilinear coordinate systems

We now present some general information about curvilinear coordinates [83, 119]. Let us take a point P in space, characterised by its three Cartesian coordinates x, y and z. The three unit vectors along the three axes, orthogonal to each other, are denoted by $\boldsymbol{i}$, $\boldsymbol{j}$ and $\boldsymbol{k}$. Assume that P lies on a surface. It is convenient to introduce a unit vector denoted by $\boldsymbol{e}_1$ normal to the surface in P, and then two vectors $\boldsymbol{e}_2$ and $\boldsymbol{e}_3$ tangent to the surface. It is possible to introduce three curves (q^1, q^2, q^3) passing through P, tangent to $\boldsymbol{e}_1$, $\boldsymbol{e}_2$, $\boldsymbol{e}_3$ respectively. These lines are called coordinate lines and are shown in Fig. A.1.

Therefore we have a coordinate system in which any point in space is described by the following relations:

$$\boldsymbol{x} = \boldsymbol{x}\left(q^1, q^2, q^3\right),$$

where $\boldsymbol{x} = (x, y, z)$. The coordinate lines are linked to the Cartesian coordinates by the relation $q^i = q^i\,(x, y, z)$ $(i = 1, 2, 3)$. We define the length s between two adjacent points by (we use Einstein notation):

$$ds^2 = dx^2 + dy^2 + dz^2 = g_{rs} dq^r dq^s, \qquad g_{rs} = \frac{\partial \boldsymbol{x}}{\partial q^r} \cdot \frac{\partial \boldsymbol{x}}{\partial q^s} = g_{sr},$$

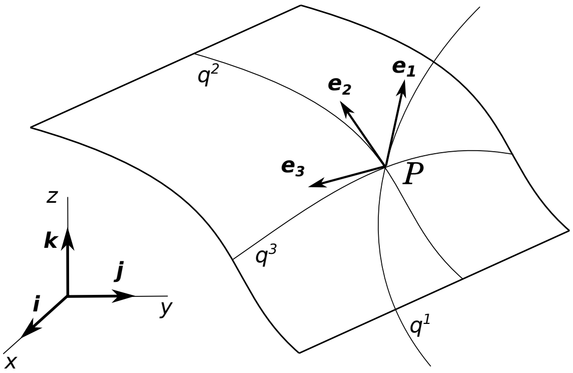

Figure A.1: Curvilinear coordinate system (q^1, q^2, q^3) adapted on a constant q^1 surface. Inspired by Ref. [119].

where g_{rs} denote the covariant components of the metric tensor. The contravariant components are defined in an analogous manner:

$$g^{rs} = \frac{\partial q^r}{\partial x}\frac{\partial q^s}{\partial x} + \frac{\partial q^r}{\partial y}\frac{\partial q^s}{\partial y} + \frac{\partial q^r}{\partial z}\frac{\partial q^s}{\partial z} = g^{sr}.$$

It is easy to check that $\sum_{n=1}^{3} g_{rn} g^{ns} = \delta_r^s$ where δ_r^s is the Kronecker delta. Let us now introduce two sets of three vectors:

$$\hat{\boldsymbol{e}}_r = \frac{\partial x}{\partial q^r}\boldsymbol{i} + \frac{\partial y}{\partial q^r}\boldsymbol{j} + \frac{\partial z}{\partial q^r}\boldsymbol{k}, \qquad \hat{\boldsymbol{e}}^r = \frac{\partial q^r}{\partial x}\boldsymbol{i} + \frac{\partial q^r}{\partial y}\boldsymbol{j} + \frac{\partial q^r}{\partial z}\boldsymbol{k}, \qquad r = 1, 2, 3$$

The set $\hat{\boldsymbol{e}}_r$ is the covariant basis, while the set $\hat{\boldsymbol{e}}^r$ is the contravariant basis which is denoted in a compact form as $\hat{\boldsymbol{e}}^r = \boldsymbol{\nabla} q^r$. It immediately follows that $\hat{\boldsymbol{e}}_r \cdot \hat{\boldsymbol{e}}_s = g_{rs}$ and $\hat{\boldsymbol{e}}^r \cdot \hat{\boldsymbol{e}}^s = g^{rs}$. It is important to note that the covariant (contravariant) vectors are not necessarily orthogonal. The following relations hold:

$$\hat{\boldsymbol{e}}^1 = \boldsymbol{\nabla} q^1 = (\hat{\boldsymbol{e}}_2 \times \hat{\boldsymbol{e}}_3)/\sqrt{g}, \tag{A.1}$$

$$\hat{\boldsymbol{e}}_1 = \sqrt{g}(\hat{\boldsymbol{e}}^2 \times \hat{\boldsymbol{e}}^3) = \sqrt{g}(\boldsymbol{\nabla} q^2 \times \boldsymbol{\nabla} q^3), \tag{A.2}$$

and equivalent expressions for the other vectors are obtained by circular permutations. The determinant of the metric tensor matrix is denoted by g ($\det(g_{ij}) = g$, $\det(g^{ij}) = 1/g$) and it is defined by:

$$\hat{\boldsymbol{e}}_1 \cdot (\hat{\boldsymbol{e}}_2 \times \hat{\boldsymbol{e}}_3) = \sqrt{g}, \tag{A.3}$$

$$\hat{\boldsymbol{e}}^1 \cdot \left(\hat{\boldsymbol{e}}^2 \times \hat{\boldsymbol{e}}^3\right) = \boldsymbol{\nabla} q^1 \cdot \left(\boldsymbol{\nabla} q^2 \times \boldsymbol{\nabla} q^3\right) = 1/\sqrt{g}, \tag{A.4}$$

which is related to the volume element $d^3 r$ by the relation $d^3 r = dxdydz = \sqrt{g} dq^1 dq^2 dq^3$. The coordinate system $(\hat{\boldsymbol{e}}_1, \hat{\boldsymbol{e}}_2, \hat{\boldsymbol{e}}_3)$ is right handed when $\sqrt{g} > 0$. Finally we have $\hat{\boldsymbol{e}}_r \cdot \hat{\boldsymbol{e}}^s = \hat{\boldsymbol{e}}_r \cdot \boldsymbol{\nabla} q^s = \delta_r^s$. We can now define for a generic vector $\boldsymbol{V}$

its covariant (V_r) and contravariant (V^r) components:

$$\boldsymbol{V} = V_r \boldsymbol{\nabla} q^r = V^r \hat{\boldsymbol{e}}_r. \tag{A.5}$$

The scalar and cross product between two vectors $\boldsymbol{V}$ and $\boldsymbol{W}$ are given by:

$$\begin{aligned} &\boldsymbol{V} \cdot \boldsymbol{W} = V^j W_j = V_j W^j = g_{jk} V^k W^j, \\ &(\boldsymbol{V} \times \boldsymbol{W})^i = \frac{1}{\sqrt{g}} \varepsilon^{ijk} V_j W_k, \qquad (\boldsymbol{V} \times \boldsymbol{W})_i = \sqrt{g} \varepsilon_{ijk} V^j W^k, \end{aligned}$$

where $\varepsilon^{ijk} = \varepsilon_{ijk}$ is the Levi-Civita symbol.

Gradient, divergence and curl operators are written as follows:

$$(\boldsymbol{\nabla} u)_i = \frac{\partial u}{\partial q^i}, \quad \boldsymbol{\nabla} \cdot \boldsymbol{V} = \frac{1}{\sqrt{g}} \frac{\partial}{\partial q^i} \left(\sqrt{g} V^i \right), \qquad (\boldsymbol{\nabla} \times \boldsymbol{V})^i = \frac{1}{\sqrt{g}} \varepsilon^{ijk} \frac{\partial V_k}{\partial q^j}.$$

A.2 Derivation of equations (4.19), (4.24) and (4.25)

Eq. (4.19)

We start deriving equation (4.19). At leading order we have (cf. Eq. (4.3)) $\sqrt{g}/f_0' = R_0/B_0[1 + 2r/R_0 \cos\vartheta]$ Using the fact that the safety factor is almost flat and $q \approx m/n$, the following expression is obtained:

$$\begin{aligned} &[L_{||}^2 \delta p' \partial_\vartheta (\sqrt{g}/f_0')]_m = \sum_{m'} [\partial_\vartheta (\sqrt{g}/f_0')]_{m'} [(m-m')\iota - n]^2 \delta p'_{m-m'} = \\ &\iota^2 \sum_{m'} \underbrace{(m')^2 [\partial_\vartheta (\sqrt{g}/f_0')]_{m'}}_{[\partial_\vartheta^3 (\sqrt{g}/f_0')]_{m'}} \delta p'_{m-m'} = \iota^2 \sum_{m'} [-\partial_\vartheta (\sqrt{g}/f_0')]_{m'} \delta p'_{m-m'} = \\ &-\iota^2 [\delta p' \partial_\vartheta (\sqrt{g}/f_0')]_m. \end{aligned}$$

Analogously we have:

$$\begin{aligned} &[\partial_\vartheta L_{||}^2 \delta p (\sqrt{g}/f_0')']_m = \sum_{m'} \underbrace{(-im') \delta p_{m-m'}}_{(\partial_\vartheta \delta p)_{m-m'}} \underbrace{[(m-m')\iota - n]^2}_{\iota^2 (m')^2 \rightarrow -\iota^2 \partial \vartheta^2} (\sqrt{g}/f_0')'_{m-m'} = \\ &\iota^2 \sum_{m'} (\partial_\vartheta \delta p')_{m'} (\sqrt{g}/f_0')'_{m-m'} = \iota^2 [(\partial_\vartheta \delta p)(\sqrt{g}/f_0')']_m, \end{aligned}$$

where we used the fact that $\partial_\vartheta^2 (\sqrt{g}/f_0')' = -(\sqrt{g}/f_0')'$. Eventually we obtain Eq. (4.19).

Eq. (4.24)

In order to derive Eq. (4.24), we first note that at leading order $\sqrt{g}[p, R^2/F] \approx -p_0' R^2/T_0^2 \partial_\vartheta \tilde{F} + \sqrt{g}[\tilde{p}, R^2/F_0]$. Taking the Fourier m component and expressing the pressure in terms of the displacement ξ, it is easy to see that:

$$
\begin{aligned}
&(\sqrt{g}[p, R^2/F])_m \approx -m^2 \frac{p_0'^2 R_0}{r B_0^4} \xi_m - i m \tilde{p}_m \langle R^2/T_0^2 \rangle' = \\
&-m^2 \frac{p_0'^2 R_0}{r B_0^4} \xi_m + m^2 \frac{p_0'}{f_0'} \left[\frac{\langle R^2 \rangle'}{F_0} - \frac{\langle R^2 \rangle F_0'}{F_0^2} \right] \xi_m .
\end{aligned}
$$

Using the Grad-Shafranov equation and the fact that at leading order we have $\psi_0' \approx r F_0/(q R_0)$, we obtain $F_0 = R_0 B_0 [1 - \int dr (p_0'/B_0^2 + 2r/(q^2 R_0^2))]$. Thus, by means of 4.4, at leading order the expression for $K_2^{m_0}$ reduces to equation (4.24).

Eq. (4.25)

The derivation of (4.25) is more tricky. At leading order we have $(\sqrt{g}/f_0')_{\pm 1} = r/B_0$, thus it is easy to see that:

$$
K_1^{m_0, \pm 1} \zeta = \frac{(m_0 \pm 1)}{B_0} \left[\mp \frac{p_0'}{f_0'} r^{\pm m_0} \left(r^{1 \mp m_0} \zeta \right)' \mp \left(\frac{p_0'}{f_0'} \right)' \zeta \right] .
$$

Since we have that $J_{0,\pm 1} = q p_0'/B_0^2$, using the assumption that q is almost flat, we obtain the following expression:

$$
\begin{aligned}
&i L_1^{m_0, \pm 1} k_{||}^{m_0 \mp 1} \xi + K_1^{m_0, \pm 1} \xi = \\
&- \left[k_{||}^{m_0} \Delta_{\pm 1}^{*} k_{||}^{m_0 \mp 1} \xi \pm \frac{(m_0 \mp 1)}{B_0} \Big\{ \frac{p_0'}{f_0'} r^{\pm m_0} \left(r^{1 \mp m_0} \xi \right)' \Big\} \right] + \\
&\left[- \Big\{ (m_0 \mp 1) \left(\frac{p_0'}{f_0'} \right)' q \mp \frac{p_0'}{B_0^2} q \partial_r \Big\} k_{||}^{m_0 \mp 1} \mp \frac{(m_0 \mp 1)}{B_0} r \left(\frac{p_0'}{f_0'} \right)' \right] \xi = \\
&- \left[k_{||}^{m_0} \Delta_{\pm 1}^{*} k_{||}^{m_0 \mp 1} \xi \pm \frac{(m_0 \mp 1)}{B_0} \Big\{ \frac{p_0'}{f_0'} r^{\pm m_0} \left(r^{1 \mp m_0} \xi \right)' \Big\} \right] + \\
&k_{||}^{m_0} \Big[\pm \frac{p_0'}{B_0^2} \xi' - \left(\frac{p_0'}{B_0^2} \right)' (m_0 \mp 1) \xi \Big] \pm \frac{p_0'}{B_0^2} \Big\{ \mp \xi' + \frac{m_0 \mp 1}{r} \xi \Big\}
\end{aligned}
$$

Neglecting the term proportional to $\Delta^*_{\pm 1}$ (which is of higher order), some straightforward manipulations show that the expression above can be written as:

$$\begin{aligned}
& iL_1^{m_0,\pm 1} k_{||}^{m_0 \mp 1}\xi + K_1^{m_0,\pm 1}\xi = \\
& \mp \frac{(m_0 \mp 1)}{B_0}\frac{p_0'}{f_0'} r^{\pm m_0}\frac{d}{dr}\left(r^{1\mp m_0}\xi\right) - \frac{p_0'}{rB_0^2} r^{\pm m_0}\frac{d}{dr}\left(r^{1\mp m_0}\xi\right) = \\
& \mp \frac{m_0}{rB_0^2} p_0' r^{\pm m_0}\frac{d}{dr}\left(r^{1\mp m_0}\xi\right),
\end{aligned}$$

hence we have Eq. (4.25).

A.3 Finite β corrections to Eq. (4.31)

In the region $r_* < r < a$ (a is the minor radius), we assume a rotational transform of the form:

$$\iota = n/m + S(1 - (r/r_s)^\lambda),$$

where S is a number. Introducing the variable $z = (r/r_s)^\lambda$, the equation for the perturbed fluid displacement which accounts for finite β corrections is [83]:

$$\frac{d}{dz}\left[z^{2/\lambda+1}\left(1-z\right)^2 \frac{d\tilde{X}_{m,n}}{dz}\right] - [\frac{m^2-1}{\lambda^2}\left(1-z\right)^2 + U_0]z^{2/\lambda-1}\tilde{X}_{m,n} = 0, \qquad (A.6)$$

where $U_0 = 2rp'/B_0^2 n^2/(mS\lambda)^2$. Note that an equation similar to (A.6), where the replacements $\lambda \to -\lambda$ and $U_0 \to S(m/n)^2 U_0$ have to be performed, can be derived with a safety factor of the form $q = m/n(r/r_s)^\lambda$. This equation can be solved in the exterior region ($r > r_*$) for a generic λ assuming a logarithmic pressure profile $p = -p_0 \log(r/a)$ (with a parabolic pressure profile an analytic expression is found only for $\lambda = 2$, see Ref. [83]).

The solution for $z < 1$ (i.e. $r < r_s$), reads [83]:

$$\begin{aligned}
\tilde{X}_{m,n} = z^{-1/\lambda+\bar{U}}(1-z)^{-1/2(1+\tilde{U})}[&A^+_< F(a, b, ; c, z) \\
&+ A^-_< z^{-2\bar{U}} F(a+1-c, b+1-c; 2-c; z)] \qquad (A.7)
\end{aligned}$$

where $a = \sigma - \bar{m}/\lambda$, $b = \sigma + \bar{m}/\lambda$, $c = 1 + 2\bar{U}$, with $\sigma = 1/2[1 - \tilde{U} + 2\bar{U}]$ where $\tilde{U} = \sqrt{1 + 4U_0}$ and $\bar{U} = \sqrt{U_0 + m^2/\lambda^2}$. If we assume that the quantity U_0 is sufficiently small the behaviour of $\tilde{\psi}_{m,n}$ for $r \ll r_s$ is given by Eq. (4.38) (it will be shown later that this expression holds also for $r > r_s$).

Using the linear transformation formulae for the hypergeometric functions, we are able to find the asymptotic behaviour of (A.7) in proximity of the resonant surface $r = r_s$, namely:

$$\tilde{\psi}_{m,n} \sim |x|^{1/2(1-\tilde{U})} \left[1 + \tilde{D}\lambda^{\tilde{U}}|x|^{\tilde{U}}\right], \tag{A.8}$$

where $x = (r - r_s)/r_s$, $s = 1/2[1 + \tilde{U}]$ and

$$\tilde{D} = \frac{\left[\frac{\Gamma(1+2\bar{U})\Gamma(-\tilde{U})}{\Gamma(\sigma-\bar{m}/\lambda)\Gamma(\sigma+\bar{m}/\lambda)} + \frac{\Gamma(1-2\bar{U})\Gamma(-\tilde{U})}{\Gamma(1-\tilde{\sigma}-\bar{m}/\lambda)\Gamma(1-\tilde{\sigma}+\bar{m}/\lambda)}\frac{A_<^-}{A_<^+}\right]}{\left[\frac{\Gamma(1+2\bar{U})\Gamma(-\tilde{U})}{\Gamma(\tilde{\sigma}-\bar{m}/\lambda)\Gamma(\tilde{\sigma}+\bar{m}/\lambda)} + \frac{\Gamma(1-2\bar{U})\Gamma(\tilde{U})}{\Gamma(\bar{\sigma}-\bar{m}/\lambda)\Gamma(\bar{\sigma}+\bar{m}/\lambda)}\frac{A_<^-}{A_<^+}\right]},$$

with $\bar{\sigma} = 1/2[1 + \tilde{U} - 2\bar{U}]$, $\tilde{\sigma} = 1/2[1 + \tilde{U} + 2\bar{U}]$.

When $z > 1$ (i.e. $r > r_s$), we introduce the variable $\hat{x} = 1 - 1/z$. Hence the solution of (A.6) which is vanishing at the plasma boundary ($\tilde{X}_{m,n}(a) = \tilde{\psi}_{m,n}(a) = 0$) reads:

$$\begin{aligned}\tilde{X}_{m,n} \sim \hat{x}^{-1/2(1+\tilde{U})}(1-\hat{x})^{(1+\lambda+\bar{m})/\lambda}[&F(\hat{a},\hat{b};\hat{c};\hat{x}) \\ &+ D_0\hat{x}^{\tilde{U}}F(\hat{a}+1-\hat{c},\hat{b}+1-\hat{c};2-\hat{c};\hat{x})]\end{aligned} \tag{A.9}$$

where $\hat{a} = \sigma + \bar{m}/\lambda$, $\hat{b} = \hat{\sigma} + \bar{m}/\lambda$, $c = 1 - \tilde{U}$, with $\hat{\sigma} = 1/2[1 - \tilde{U} - 2\bar{U}]$ and

$$D_0 = -\frac{F(\hat{a},\hat{b};\hat{c};1-(r_s/a)^\lambda)[1-(r_s/a)^\lambda]^{\tilde{U}}}{F(\hat{a}+1-\hat{c},\hat{b}+1-\hat{c};2-\hat{c};1-(r_s/a)^\lambda)}.$$

Close to $r = r_s$, the behaviour for $\tilde{\psi}_{m.n}$ resulting from Eq. (A.9) is given by:

$$\tilde{\psi}_{m,n} \sim |x|^{1/2(1-\tilde{U})} \left[1 + D_0\lambda^{\tilde{U}}|x|^{\tilde{U}}\right]. \tag{A.10}$$

A.4 Effects of density gradients on the infernal mode

In the present appendix we generalise the equations for infernal modes, with the inclusion of density gradients. While pressure enters the perturbed force operator, the density enters the inertia (in the standard perturbed equations, the density profile in the inertia is contained in the Alvén frequency ω_A). Density gradients could play an important role in a post sawtooth-like scenario. Indeed after a sawtooth, in the full reconnection model, the q profile is raised above unity and the temperature becomes flat inside the $q = 1$ surface. However residual density gradients could remain [81], allowing the presence of a pressure gradient in the central region (this is because

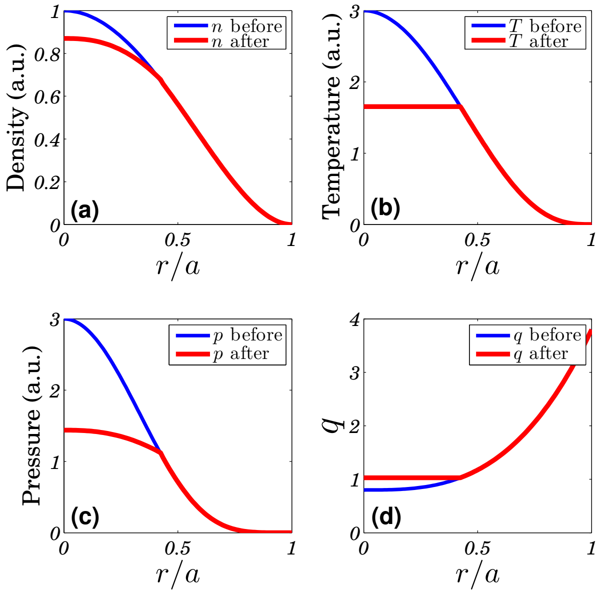

Figure A.2: Profiles for density (a), temperature (b), pressure (c) and safety factor (d) before (blue) and after (red) a sawtooth crash, assuming full reconnection and allowing for density gradients.

$p \sim \varrho T$). This is shown in Fig. A.2.

Neglecting presently diamagnetic effects and equilibrium toroidal flows, Eq. (4.53) is augmented by the density gradient terms, giving for $m_0 = n = 1$, $q = 1 + \delta q$ ($\omega_A = 1$) [84]:

$$rQ(r)\frac{d^2X_1}{dr^2} + \left(3Q(r) + r\hat{\gamma}^2\varrho_0'\right)\frac{dX_1}{dr} + \hat{\gamma}^2\varrho_0' X_1 + \alpha\mathbf{\Lambda}^{\omega}_{1,1}/r_*^4 = 0, \tag{A.11}$$

where we normalised $\omega_A = B_0/(R_0\sqrt{\bar{\varrho}}) = 1$ (B_0 and ϱ are the values of magnetic field and density on the magnetic axis), $Q(r) = \varrho_0\hat{\gamma}^2 + \delta q^2$, $\hat{\gamma} = \sqrt{3}\gamma$, and X_1 fulfils the integrability condition $\int_0^{r^*}\alpha r^2 X_1 dr = 1$. Under the assumption $p_0 \sim \varrho_0 = 1-(r/a_0)^2$ (flat temperature profile) in the low shear region, the following equation is derived:

$$x(1-x)\frac{d^2X_1}{dx^2} + [2-3x]\frac{dX_1}{dx} - \frac{X_1}{2} - \frac{R_0\bar{p}}{B_0^2}\frac{\mathbf{\Lambda}^{\omega}_{1,1}}{\hat{\gamma}^2 r_*^4} = 0$$

where $x = \hat{\gamma}^2\left(r/a\right)^2/(\hat{\gamma}^2 + \delta q^2)$ ($x_* = x(r = r_*)$), whose solution, regular at $r = 0$ with $X_1(r_*) = 0$, is [102]:

$$X_1 = \frac{2R_0\bar{p}}{B_0^2}\frac{\mathbf{\Lambda}^{\omega}_{1,1}}{\hat{\gamma}^2}\left[\frac{F(1+1/\sqrt{2}, 1-1/\sqrt{2}; 2; x)}{F(1+1/\sqrt{2}, 1-1/\sqrt{2}; 2; x_*)} - 1\right]$$

leading to the following dispersion relation (we recall that the dispersion relation is obtained by imposing the condition $\int_0^{r_*}\alpha r^2 X_1 dr = 1$):

$$1 + 2\beta_p^2\varepsilon^2\frac{\mathbf{\Lambda}^{\omega}_{1,1}}{\hat{\gamma}^2}\left[\frac{F(1+1/\sqrt{2},1-1/\sqrt{2};3;x_*)}{F(1+1/\sqrt{2},1-1/\sqrt{2};2;x_*)} - 1\right] = 0.$$

If $\hat{\gamma} = 0$, it is easy to see that for a fixed δq, the critical value of β_p corresponds to β_{crit} found in section **4.8.1** (this is to be expected because the inertia is zero at the stability boundary); if $\delta q = 0$, the growth rate is slightly increased with respect to the one evaluated using eq. (4.58). We note that if we assume both pressure and density to be parabolic, i.e. $\varrho_0 = \bar{\varrho}(1-(r/a)^2)$ and $T_0 = \bar{T}(1-(r/a)^2)$, the total pressure can be well approximated in the central region $p = \bar{p}(1-2(r/a)^2)$. Hence the results just obtained hold with the replacement $\bar{p} \to 2\bar{p}$.

We note that for $m_0 = n \neq 1$, Eq. (A.11) is augmented by the term $\hat{\gamma}^2\varrho_0 r(1-m_0^2)X_{m_0}$ and it is recast in the following form (here $\hat{\gamma}^2 = \gamma^2(1+2q_s^2)/(m_0^2\omega_A^2)$):

$$\begin{aligned} x(1-x)\frac{d^2X_{m_0}}{dx^2} + [2-3x]\frac{dX_{m_0}}{dx} - \left(\frac{1}{2} + \frac{(1-m_0^2)}{4}\frac{(x-1)}{x}\right)X_{m_0} \\ - \frac{R_0\bar{p}}{B_0^2}\frac{\mathbf{\Lambda}^{\omega}_{m_0,n}}{\hat{\gamma}^2 r_*^{2+2m_0}}\left(\frac{\hat{\gamma}^2/a^2}{\hat{\gamma}^2+\delta q^2}\right)^{-\frac{m_0-1}{2}} x^{(m_0-1)/2} = 0. \end{aligned} \tag{A.12}$$

The two independent solutions Y_1 and Y_2 of the homogeneous part of the equation above can be easily expressed in terms of hypergeometric functions (Ref. [102] p. 564):

$$\begin{aligned} Y_1 &= x^{(m_0-1)/2}F(a+m_0, b+m_0; 1+m_0; x), \\ Y_2 &= x^{(m_0-1)/2}\Big[F(a+m_0, b+m_0; 1+m_0; x)\log(x) \\ &+ \sum_{n=1}^{\infty} x^n\frac{(a+m_0)_n(b+m_0)_n}{(1+m_0)_n n!}[\Psi(a+m_0+n) - \Psi(a+m_0) \\ &+ \Psi(b+m_0+n) - \Psi(b+m_0) - \Psi(m_0+1+n) \\ &+ \Psi(m_0+1) - \Psi(n+1) + \Psi(1)] - \sum_{n=1}^{m_0}\frac{(n-1)!(-m_0)_n}{(1-a-m_0)_n(1-b-m_0)_n}x^{-n}, \end{aligned}$$

where $a = \left(1-m_0-\sqrt{1+m_0^2}\right)/2$, $b = \left(1-m_0+\sqrt{1+m_0^2}\right)/2$, Ψ is the Digamma function (Ref. [102] p. 253) and $(z)_n = \Gamma(z+n)/\Gamma(z)$ is the Pochhammer symbol. The general solution of (A.12) can be written by using the variation of parameters method:

$$X_{m_0} = c_1 Y_1 + c_2 Y_2 - Y_1 \int_0^x \frac{Y_2(x')f(x')}{W(x')}dx' + Y_2 \int_0^x \frac{Y_1(x')f(x')}{W(x')}dx' \tag{A.13}$$

where $W(x) = Y_2'(x)Y_1(x) - Y_1'(x)Y_2(x)$ is the Wronskian of Y_1 and Y_2, c_1 and c_2 are constants and $f(x) = -\frac{R_0\bar{p}}{B_0^2}\frac{\mathbf{\Lambda}^{\omega}_{m_0,n}}{\hat{\gamma}^2 r_*^{2+2m_0}}\left(\frac{\hat{\gamma}^2/a^2}{\hat{\gamma}^2+\delta q^2}\right)^{-\frac{m_0-1}{2}} x^{(m_0-1)/2}$. The dispersion relation is eventually found (numerically) by means of (4.54).

B

Coupled internal modes in tokamaks with a helical core

B.1 Geometry and fluxes with equilibrium helical cores

Using the formalism introduced in Chapter **3** § 3.4.3, we analyse the stability of ideal and resistive modes when coupling effects induced by the presence of helical cores are retained. The helical core produces oscillations in the metric tensor. Therefore an unstable internal mode (ideal or resistive) can couple with a sub-mode. In case of resistive modes, the tearing stability parameter Δ' is modified, so that modes which are nominally stable can be driven unstable. The starting point of the analysis is the description of equilibrium helical geometry. We assume an equilibrium helical core of helicity 1/1 and amplitude ξ, hence the flux surfaces are parametrised in the following manner:

$$X = [R_0 + r\cos(\vartheta+\lambda) + \Delta_s(r) + \xi(r)\cos\varphi]\sin\varphi \tag{B.1}$$

$$Y = [R_0 + r\cos(\vartheta+\lambda) + \Delta_s(r) + \xi(r)\cos\varphi]\cos\varphi \tag{B.2}$$

$$Z = r\sin(\vartheta+\lambda) + \xi(r)\sin\varphi \tag{B.3}$$

where Δ_s is the Shafranov shift, ϑ is a poloidal-like angle where the magnetic field lines appear straight, φ is the toroidal angle and $\lambda(r,\vartheta,\varphi)$ is the rectification parameter.

The quantities Δ_s and ξ are assumed to be of order ε, while $R_0 \sim \mathcal{O}(\varepsilon^{-1})$. In this coordinate system, the magnetic field is written as $\boldsymbol{B} = \boldsymbol{\nabla} F(r) \times \boldsymbol{\nabla}\vartheta - \boldsymbol{\nabla}\psi(r) \times \boldsymbol{\nabla}\varphi$, thus:

$$B^r = -(\partial_\theta \psi' + \partial_\varphi F)/\sqrt{g}), \quad B^\vartheta = \psi'/\sqrt{g}, \quad B^\varphi = F'/\sqrt{g}.$$

The constraint $J^r = 0$ provides us the following expression for the rectification parameter λ (correct up to order ε):

$$\lambda(r, \vartheta, \varphi) = (r/R_0 - \Delta_s') \sin\vartheta - \xi' \sin(\vartheta - \varphi). \tag{B.4}$$

The constants of integration have been chosen in order to guarantee the periodicity of the function λ in its angular arguments up to $\mathcal{O}(\varepsilon^3)$. Hence, we can calculate the metric tensor up to order ε for such helical equilibrium (higher order corrections to the metric tensor are not important for following analysis):

$$\begin{aligned}
&g_{rr} = 1 + 2\left[\Delta_s' \cos\vartheta + \xi' \cos(\vartheta - \varphi)\right], \\
&g_{\vartheta\vartheta} = r^2 + 2r^2\left[(r/R_0 - \Delta_s')\cos\vartheta - \xi' \cos(\vartheta - \varphi)\right], \\
&g_{r\vartheta} = \left[r^2/R_0 - r\left(\Delta_s' + r\Delta_s''\right)\right]\sin\vartheta + r\left(\xi' + r\xi''\right)\sin(\vartheta - \varphi), \\
&g_{r\varphi} = \xi \sin(\vartheta - \varphi), \;\; g_{\vartheta\varphi} = r\left(\xi + r\xi'\right)\cos(\vartheta - \varphi), \\
&g_{\varphi\varphi} = R_0^2\left[1 + 2r/R_0 \cos\vartheta\right], \;\; 1/\sqrt{g} = (rR_0)^{-1}\left[1 - 2r/R_0\cos\vartheta\right].
\end{aligned}$$

By using the expressions above, we can show that $F' = rB_0(1 + \mathcal{O}(\varepsilon^2))$. The equilibrium helical displacement ξ is taken in the following form:

$$\xi(r) = \begin{cases} \xi_{ax}\left[1 - \left(\dfrac{r}{r_*}\right)^\alpha\right], & r < r_* \\ 0, & r > r_* \end{cases} \tag{B.5}$$

where $\xi_{ax} \sim \mathcal{O}(\varepsilon)$, as we assumed previously, and $\alpha > 0$. Eq. (B.5) implies that the coupling can occur only in the region $r < r_*$. Using the results obtained in Chapter **3** § 3.4.3, we assume a flat safety factor profile over a large region which extends from the magnetic axis up to $r = r_*$. The Fourier components of the current density explicitly read:

$$\begin{aligned}
&J^r_{m,n} = i\sum_{m',n'}\sum_{m'',n''}\langle 1/\sqrt{g}\rangle_{\boldsymbol{k}'}\Big\{ - i[(m - m')\langle\bar{g}_{r\varphi}\rangle_{\boldsymbol{k}''} + (n - n')\langle\bar{g}_{r\theta}\rangle_{\boldsymbol{k}''}]\times \\
&\times((m - m' - m'')\psi_{\tilde{\boldsymbol{k}}} - (n - n' - n'')F_{\tilde{\boldsymbol{k}}}) + [(m - m')\langle\bar{g}_{\theta\varphi}\rangle_{\boldsymbol{k}''} + \\
&(n - n')\langle\bar{g}_{\theta\theta}\rangle_{\boldsymbol{k}''}]\psi'_{\tilde{\boldsymbol{k}}} + [(m - m')\langle\bar{g}_{\varphi\varphi}\rangle_{\boldsymbol{k}''} + (n - n')\langle\bar{g}_{\theta\varphi}\rangle_{\boldsymbol{k}''}]F'_{\tilde{\boldsymbol{k}}}\Big\},
\end{aligned} \tag{B.6}$$

for the contravariant radial component, and:

$$
\begin{aligned}
J^{\varphi}_{m,n} = & \sum_{m',n'} \sum_{m'',n''} \langle 1/\sqrt{g}\rangle_{\boldsymbol{k}'} \Big\{ \partial_r [-i\langle \bar{g}_{r\theta}\rangle_{\boldsymbol{k}''}((m-m'-m'')\psi_{\tilde{\boldsymbol{k}}} - (n-n'-n'')F_{\tilde{\boldsymbol{k}}}) \\
& + \langle \bar{g}_{\theta\theta}\rangle_{\boldsymbol{k}''}\psi'_{\tilde{\boldsymbol{k}}} + \langle \bar{g}_{\theta\varphi}\rangle_{\boldsymbol{k}''}F'_{\tilde{\boldsymbol{k}}}] - i(m-m')[-i\langle \bar{g}_{rr}\rangle_{\boldsymbol{k}''}((m-m'-m'')\psi_{\tilde{\boldsymbol{k}}} \\
& -(n-n'-n'')F_{\tilde{\boldsymbol{k}}}) + \langle \bar{g}_{r\theta}\rangle_{\boldsymbol{k}''}\psi'_{\tilde{\boldsymbol{k}}} + \langle \bar{g}_{r\varphi}\rangle_{\boldsymbol{k}''}F'_{\tilde{\boldsymbol{k}}}] \Big\},
\end{aligned}
\tag{B.7}
$$

for the contravariant toroidal component, where $\bar{g}_{ij} = g_{ij}/\sqrt{g}$, $\tilde{\boldsymbol{k}} = (m-m'-m'', n-n'-n'')$, $\boldsymbol{k}' = (m', n')$, $\boldsymbol{k}'' = (m'', n'')$, with:

$$
\langle \,\cdot\, \rangle_{\tilde{\boldsymbol{k}}''} = (\,\cdot\,)_{m'',n''} = \tfrac{1}{4\pi^2}\int_0^{2\pi} d\theta d\varphi(\,\cdot\,)\exp[i(m''\theta - n''\varphi)].
$$

If the wave vector over which we are averaging is not specified in the angular brackets, it is implicitly assumed that $\langle \,\cdot\, \rangle = (\,\cdot\,)_{0,0}$. We assume the presence of two coupled modes: one has wave vector $\boldsymbol{k}_0 = (m_0, n_0)$, while the other has $\boldsymbol{k}_1 = (m_0 \pm 1, n_0 \pm 1)$.

First we want to specify the amplitudes of the toroidal and poloidal fluxes for different Fourier harmonics. This is achieved by projecting the force balance equation along the magnetic field, which yields ($\iota = 1/q$):

$$
\tilde{p}_{m,n} = p_0' \frac{m\tilde{\psi}_{m,n} - n\tilde{F}_{m,n}}{F_0'(m\iota - n)}.
\tag{B.8}
$$

The linearised covariant toroidal projection of Eq. (2.8) (cf Chapter **2**) gives:

$$
\tilde{J}^{r}_{m,n} = -\frac{i}{\psi_0'}\Big\{ n\tilde{p}_{m,n} + \sum_{m',n'} (J_0^{\vartheta})_{m',n'}[(m-m')\tilde{\psi}_{\tilde{\boldsymbol{k}}} - (n-n')\tilde{F}_{\tilde{\boldsymbol{k}}}] \Big\},
\tag{B.9}
$$

where we have defined $\tilde{\boldsymbol{k}} = (m-m', n-n')$. Equation (B.9) provides a relation between the toroidal and the poloidal perturbation of the magnetic field. It is easy to see that $(J_0^{\vartheta})_{\pm1,\pm1} \sim \mathcal{O}(\varepsilon)\langle J_0^{\vartheta}\rangle \sim \mathcal{O}(\varepsilon^3)$. The leading order of (B.6) gives:

$$
\begin{aligned}
J^{r}_{m,n} = & \, i/(rR_0)\Big\{ nr/R_0\psi'_{m,n} + mR_0/rF'_{m,n} - i[m\langle \bar{g}_{r\varphi}\rangle_{\pm1} + n\langle \bar{g}_{r\theta}\rangle_{\pm1}]\times \\
& \times[(m\pm1)\tilde{\psi}_{m\mp1,n\mp1} - (n\pm1)\tilde{F}_{m\mp1,n\mp1}] + [m\langle \bar{g}_{\theta\varphi}\rangle_{\pm1} + n\langle \bar{g}_{\theta\theta}\rangle_{\pm1}]\tilde{\psi}'_{m\mp1,n\mp1} \\
& + [m\langle \bar{g}_{\varphi\varphi}\rangle_{\pm1} + n\langle \bar{g}_{\theta\varphi}\rangle_{\pm1}]\tilde{F}'_{m\mp1,n\mp1} \Big\}.
\end{aligned}
\tag{B.10}
$$

Under the assumption that $(\tilde{\psi}, \tilde{F})_{m_0\pm1,n_0\pm1} \sim \mathcal{O}(\varepsilon)\tilde{\psi}_{m_0,n_0}$, because of the ordering $\langle \bar{g}_{ij}\rangle_{\pm1} \sim \mathcal{O}(\varepsilon^2)$, it follows that $\tilde{J}^{r}_{m_0,n_0} = i/(rR_0)\Big\{ n_0 r/R_0\tilde{\psi}'_{m_0,n_0} + m_0R_0/r\tilde{F}'_{m_0,n_0} + \mathcal{O}(\varepsilon^3)\psi_{m_0,n_0}\Big\}$. Thus, we obtain from equation (B.9) that $\tilde{F}_{m_0,n_0} \sim \mathcal{O}(\varepsilon^2)\tilde{\psi}_{m_0,n_0}$. With the same procedure, we also find that $\tilde{F}_{m\pm1,n\pm1} \sim \mathcal{O}(\varepsilon^2)\tilde{\psi}_{m\pm1,n\pm1}$.

The equation for the perturbed poloidal flux is obtained by linearising the $\nabla\varphi$

projection of the curl of Eq. (2.8) (the subscript 0 and a tilde indicate equilibrium and perturbed quantities respectively) [88]:

$$\boldsymbol{B}_0 \cdot \boldsymbol{\nabla} \tilde{J}^{\varphi} + \tilde{\boldsymbol{B}} \cdot \boldsymbol{\nabla} J_0^{\varphi} - \boldsymbol{J}_0 \cdot \boldsymbol{\nabla} \tilde{B}^{\varphi} - \tilde{\boldsymbol{J}} \cdot \boldsymbol{\nabla} B_0^{\varphi} = 0. \tag{B.11}$$

The analysis to split into two regions: a core region where the coupling occurs ($r < r_*$, flat q) and an exterior region where the magnetic shear is large and the modes are uncoupled ($r > r_*$, $q' \sim \mathcal{O}(1)$). Eventually the eigensolutions are matched smoothly (i.e. continuous with continuous first derivative) across $r = r_*$:

$$[\![\tilde{\psi}]\!]_{r_*} \quad = [\![\tilde{\psi}']\!]_{r_*} \quad = 0.$$

We now proceed in the evaluation of the eigenfunctions in the interior and exterior region. Hereafter we denote with r_s the position of the $q = (m_0 \pm 1)/(n_0 \pm 1)$ surface.

B.2 Interior and exterior eigenfunctions

B.2.1 Interior region

We recall that in the interior region, where the equilibrium helical displacement is allowed to vary over the radial variable, we must have an almost flat q profile close to unity (cf. Chapter **3** § 3.4.3). Thus $\langle J_0^{\varphi} \rangle' = 0$. The last two terms in Eq. (B.11) can be dropped since they are proportional to the perturbed toroidal flux, which is a small order correction to $\psi_{m,n}$ (both for the main and the coupled modes). We also note that $\langle J_0^{\varphi} \rangle_{\pm 1} = 0$. Therefore Eq. (B.11) reduces to:

$$\tilde{J}^{\varphi}_{m,n} = 0. \tag{B.12}$$

We start assuming a positive tearing stability index Δ' of the (m_0, n_0) mode, corresponding thus to an unstable mode. The leading order of Eq. (B.12) for the mode $\tilde{\psi}_{m_0,n_0}$ reads:

$$r[r\tilde{\psi}'_{m,n}]' - m^2 \tilde{\psi}_{m,n} = 0, \tag{B.13}$$

whose solution regular on the magnetic axis is

$$\tilde{\psi}_{m,n} = A\,(r/r_s)^m \tag{B.14}$$

where A is an arbitrary constant with the dimension of a magnetic flux, which is imposed *a posteriori*.

In order to derive an expression for $\tilde{\psi}_{m_0 \pm 1, n_0 \pm 1}$, we multiply Eq. (B.11) by $\sqrt{g}$, and by means of (B.7), we obtain at leading order the following expression (for sake of simplicity we set $m = m_0 \pm 1$ and $n = n_0 \pm 1$):

$$
\begin{aligned}
\tilde{J}^{\varphi}_{m,n} &= \frac{1}{rR_0}\Big\{[r/R_0\tilde{\psi}'_{m,n}]' - m^2\frac{1}{rR_0}\tilde{\psi}_{m,n}\Big\} \\
&+\frac{1}{rR_0}\Big\{\partial_r[-i\langle\bar{g}_{r\theta}\rangle_{\pm1}(m\mp1)\tilde{\psi}_{m\mp1,n\mp1} + \langle\bar{g}_{\theta\theta}\rangle_{\pm1}\tilde{\psi}'_{m\mp1,n\mp1}] \\
&-im[-i\langle\bar{g}_{rr}\rangle_{\pm1}(m\mp1)\tilde{\psi}_{m\mp1,n\mp1} + \langle\bar{g}_{r\theta}\rangle_{\pm1}\tilde{\psi}'_{m\mp1,n\mp1}]\Big\}\exp[i\Delta\phi],
\end{aligned}
\tag{B.15}
$$

where $\Delta\phi$ is the phase difference between the two modes, which is taken either 0 or π. For sake of simplicity we set $\Delta\phi = 0$ (this factor can be absorbed into the definition of ξ_{ax}, viz. $\xi_{ax} \to \xi_{ax}\exp[i\Delta\phi]$). By means of (B.5), (B.7) and (B.14), Eq. (B.15) yields:

$$
r[r\tilde{\psi}'_{m,n}]' - m^2\tilde{\psi}_{m,n} + f_{\pm}(r) = 0, \tag{B.16}
$$

where the function $f_{\pm}(r)$ is defined as follows:

$$
f_{\pm}(r) = \begin{cases} \dfrac{\alpha(2+\alpha)(\alpha+2m-2)(m-1)A\xi_{ax}}{2r_*}\,(r/r_*)^{m+\alpha-2}, & m = m_0+1, \\ \dfrac{\alpha(2-\alpha)(\alpha+2m)(m+1)A\xi_{ax}}{2r_*}\,(r/r_*)^{m+\alpha}, & m = m_0-1, \end{cases}
$$

showing that $\tilde{\psi}_{m,n} \sim \mathcal{O}(\varepsilon)\tilde{\psi}_{m_0,n_0}$.

Two cases are considered: the case for which $\alpha \neq 2$ and the case for which $\alpha = 2$. When $\alpha \neq 2$, the solution of Eq. (B.16) reads:

$$
\tilde{\psi}_{m,n} = B\left(\frac{r}{r_s}\right)^m + \begin{cases} \delta_+\,(r/r_*)^{m+\alpha-2}, & m = m_0+1 \\ \delta_-\,(r/r_*)^{m+\alpha}, & m = m_0-1 \end{cases} \tag{B.17}
$$

where $\delta_+ = \frac{[\alpha(\alpha+2)(m-1)]A\xi_{ax}}{(2-\alpha)r_*}$ and $\delta_- = \frac{[(m+1)(\alpha-2)]A\xi_{ax}}{r_*}$. We note that the solution is well behaved on the magnetic axis since $m \geq 2$ and $\alpha > 0$.

In the case for which $\alpha = 2$, if $m = m_0 - 1$ then $f(r)_- = 0$, implying that the coupling is lost. In contrast, if $m = m_0 + 1$ the solution regular on the magnetic axis can be written as:

$$
\tilde{\psi}_{m,n} = B\left(\frac{r}{r_s}\right)^m + \delta_+\left(\frac{r}{r_*}\right)^m\left[1 - 2m\log\left(\frac{r}{r_*}\right)\right], \tag{B.18}
$$

where $\delta_+ = \frac{2A\xi_{ax}}{mr_*}(m-1)$. The constant of integration are determined by matching the solutions in the interior and exterior regions.

B.2.2 Exterior region

The solution in the exterior region is found by means of the same approach used in Chapter **4** § 4.6. Away from the resonant $q = m/n$ surface, the equation for the magnetic perturbation for a finite β plasma can be written as $\delta^2[\tilde{\psi}''_{m,n} + 1/r\tilde{\psi}'_{m,n}] = U\tilde{\psi}_{m,n}$ where $U = 1/r^2 + \langle R_0 J_0\rangle'/[rm(m\iota - n)] + 2(n/m)^2 p'/(rB_0^2(m\iota - n))$ $(\delta = 1/m)$ [29]. Using the WKB approximation, if $r \ll r_s$, the approximate solution in proximity of the transition point $r = r_*$ is given by Eq. (4.38). In the inner region we have $d^2\tilde{\psi}_m^{in}/dz^2 + (-1/4 - \lambda/z + (1/4 - \kappa^2)/z^2)\tilde{\psi}_m^{in} = 0$ [29], where $z = 2m(r - r_s)/r_s$, $\lambda = -q_s\langle R_0 J_0\rangle'_s/(2nq'_s)$ and $\kappa = 1/2\tilde{U}$ with $\tilde{U} = \sqrt{1 + 4U_0}$ and $U_0 = 2p'q_s^2/(r_s B_0^2(q'_s)^2)$. The quantity $\tilde{U}$ is supposed to be positive and slightly less than unity, i.e. $-U_0 \ll 1$. Thus the inner solution, which matches the solution in the outer region, is:

$$\tilde{\psi}_{m,n}^{in} = \begin{cases} C_< W_{\lambda,\kappa}(|z|) + B_< M_{\lambda,\kappa}(|z|), & z < 0 \\ C_> W_{-\lambda,\kappa}(z) + B_> M_{-\lambda,\kappa}(z), & z > 0 \end{cases} \tag{B.19}$$

where M and W are the Whittaker functions (ref [102] p. 503). Asymptotic matching between the inner and outer solutions gives $C_< = A_<^+$, $C_> = A_>^-$, $B_< = A_<^-\Gamma(1/2 - \lambda + \kappa)/\Gamma(1 + 2\kappa)$ and $B_> = A_>^+\Gamma(1/2 + \lambda + \kappa)/\Gamma(1 + 2\kappa)$. Imposing the boundary condition $\tilde{\psi}_{m,n}(a) = 0$, we obtain $B_> = -\Gamma(1/2 + \lambda + \kappa)/\Gamma(1 + 2\kappa)(r_s/a)^{2m} C_>$. The parameters A_z^+ and A_z^- are found by matching Eq. (4.38) with (B.17) and (B.18) after the imposition of continuity of $\tilde{\psi}_{m,n}$ and its derivative across r_*. For the case $m = m_0 + 1$, we have the following expressions:

$$A_<^- = (r_*/r_s)^m \, \alpha(2 + \alpha)(m - 1)/(2m)\frac{A\xi_{ax}}{r_*}, \tag{B.20}$$

$$A_<^+ = B + \left(\frac{r_s}{r_*}\right)^m \frac{\alpha(\alpha + 2)(\alpha + 2m - 2)(m - 1)}{2m(2 - \alpha)}\frac{A\xi_{ax}}{r_*}, \tag{B.21}$$

for $\alpha \neq 2$ and

$$A_<^- = (r_*/r_s)^m \, 2(m - 1)/m\frac{A\xi_{ax}}{r_*}, \tag{B.22}$$

$$A_<^+ = B, \tag{B.23}$$

for $\alpha = 2$.

Conversely when $m = m_0 - 1$ and $\alpha \neq 2$ the following expressions are derived:

$$A_<^- = (r_*/r_s)^m \, \alpha(2 - \alpha)(m + 1)/(2m)\frac{A\xi_{ax}}{r_*}, \tag{B.24}$$

$$A_<^+ = B + (r_s/r_*)^m \, (\alpha - 2)(\alpha + 2m)(m + 1)/(2m)\frac{A\xi_{ax}}{r_*}. \tag{B.25}$$

B.3 Dispersion relation for ideal and resistive modes

B.3.1 Ideal modes

For ideal modes we allow for a finite β effects, thus the asymptotic behaviour close to the resonant surface ($z \ll 1$) of (B.19) is:

$$\tilde{\psi}^{<}_{m,n} \sim |x|^{1/2-\kappa}[1 + \eta_{-}|x|^{2\kappa}], \tag{B.26}$$

$$\tilde{\psi}^{>}_{m,n} \sim |x|^{1/2-\kappa}[1 + \eta_{+}|x|^{2\kappa}], \tag{B.27}$$

where $x = (r - r_s)/r_s$ and $\eta_{\pm} = (2m)^{2\kappa}\left\{\frac{\Gamma(-2\kappa)\Gamma(1\pm\lambda+\kappa)}{\Gamma(2\kappa)\Gamma(1\pm\lambda-\kappa)} + \frac{\Gamma^2(1/2\pm\lambda+\kappa)}{\Gamma(2\kappa)\Gamma(1/2+2\kappa)}\chi_{\pm}\right\}$, with $\chi_{+} = -\left(r_s/a\right)^{2m}$ and $\chi_{-} = B_{<}/C_{<}$. The expression above is then matched with the solution in the inertial layer, which behaves asymptotically for large x as [83, 120, 121]:

$$\tilde{\psi}_{m,n} = \Psi_0|x|^{1/2-\kappa}[1 + \hat{\gamma}^{-2\kappa}\Delta_{-}|x|^{2\kappa}] \pm \Psi_1|x|^{1/2-\kappa}[1 + \hat{\gamma}^{-2\kappa}\Delta_{+}|x|^{2\kappa}] \tag{B.28}$$

where $\pm$ stands for $x \gtrless 0$, Ψ_0 and Ψ_1 are constants, $\hat{\gamma} = \gamma/m\omega_A$ (γ is the growth rate and ω_A the Alfvén frequency) and $\Delta_{\pm} = \frac{\Gamma(\kappa)}{\Gamma(-\kappa)}\frac{\Gamma^2(1/2-\kappa/2\pm1/4)}{\Gamma^2(1/2+\kappa/2\pm1/4)}$. By matching (B.28) with (B.26) and (B.27), one obtains the dispersion relation as in Ref. [83] (Eq. 5.65) with the obvious substitution $\Delta_{p,c} \to \eta_{\pm}$. If a logarithmic pressure profile in the exterior region is employed, by using Eqs. (A.7) and (A.9), we can derive the same dispersion relation with the replacements $\eta_{+} \to D_0\lambda^{\tilde{U}}$ and $\eta_{-} \to \tilde{D}\lambda^{\tilde{U}}$, where D_0 and $\tilde{D}$ are defined in Appendix A.3.

B.3.2 Resistive modes

The dispersion relation for resistive kink modes is given by Eq. (6.40) in Ref. [83] with the substitution $\Delta_{p,c} \to \eta_{\pm}$ as in the ideal case. When we consider tearing modes, we drop the finite β corrections and set $\kappa = 1/2$. Continuity across r_s implies that $C_{<} = C\Gamma(1-\lambda)$ and $C_{>} = C\Gamma(1+\lambda)$, where the constant C is a measure of the amplitude of the mode at the resonant $q = m/n$ surface. According to (4.39), the parameter $B_{<}$ is thus expressed in the following manner:

$$r_s\Delta' = -2m[\pi\lambda\cot(\pi\lambda) - (B_{<} + B_{>})/C]. \tag{B.29}$$

where we recall that $B_{>}$ stabilising but rather small. The solutions for the Fourier modes of Eq. (B.11) are smoothly matched with (4.38), providing us an expression for $B_{<}/C$ which is used to evaluate (B.29).

For the case $\alpha = 2$, equation (B.29) becomes (the subscript (+) refers to the case

$m = m_0 + 1$, while the subscript $(-)$ to the case $m = m_0 - 1$):

$$r_s\Delta'_{\pm} = r_s\Delta'_{Tear} + \Gamma(1-\lambda)\left(\frac{r_*}{r_s}\right)^m \alpha(2\pm\alpha)(m\mp 1)\frac{Y\xi_{ax}}{r_*} - 2m\Gamma^2(1+\lambda)(r_s/a)^{2m}, \quad \text{(B.30)}$$

with $Y = A/C \sim \mathcal{O}(\varepsilon^{-1})$ where $r_s\Delta'_{Tear} = -2m(\pi\lambda)\cot(\pi\lambda)$ is the tearing stability parameter when coupling does not occur. Note that the correction to Δ' due to the coupling is of order of unity if one assumes that $r_*/r_s \sim Y\xi_{ax}/r_* \sim \mathcal{O}(1)$. If r_* becomes sufficiently small, i.e. the region where coupling occurs shrinks, then the second term in l.h.s. of (B.30) diminishes becoming eventually negligible. Thus (B.30) reduces to the standard dispersion relation for tearing modes.

The stability of the mode is thus determined by the relative strength and phase of the modes and by the amplitude of the helical displacement (Y, ξ_{ax}). We note that for the case $m = m_0 + 1$, for a fixed value of λ, the dependence upon the parameter α, namely the shape of the helical distorsion, translates into a shift of the $r_s\Delta'_+$ level curves. Figures B.1 and B.2 show the contours of $r_s\Delta'_{\pm}$ (cf. (B.30)) for the mode $(3,2)$, as a function of Y and ξ_{ax}, for $\lambda = 0.25, 0.5, 0.75$ and fixed $\alpha = 2.5$ for the case $m = m_0 + 1$, and $\alpha = 1.5, 1.9, 2.1, 2.5$ and fixed $\lambda = 0.5$ for the case $m = m_0 - 1$. We note that $\lambda = 0.5$ corresponds to the marginally stable cylindrical tearing mode ($r_s\Delta'_{tear} = 0$), while for $\lambda < 0.5$ we are in the stability region and for $\lambda > 0.5$ we are in the unstable domain of the cylidrical tearing. We see that the stability is affected by the amplitude of ξ_{ax} and Y, making unstable (or stable) an otherwise stable (or unstable) mode.

When $\alpha = 2$, if $m = m_0 - 1$ coupling does not occur, while if $m = m_0 + 1$ the tearing stability $r_s\Delta'_+$ index is given by:

$$r_s\Delta'_+ = r_s\Delta'_{Tear} + \Gamma(1-\lambda)\left(\frac{r_*}{r_s}\right)^m 4(m-1)\frac{Y\xi_{ax}}{r_*} - 2m\Gamma^2(1+\lambda)(r_s/a)^{2m}, \quad \text{(B.31)}$$

whose behaviour is similar to the one already shown in Figs. B.1 and B.2.

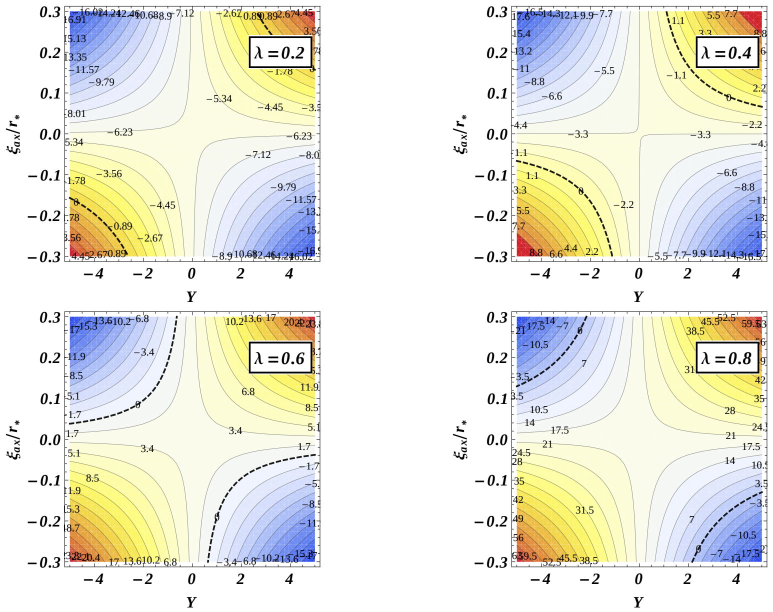

Figure B.1: Constant $r_s\Delta'_+$ contours for the $(3,2)$ mode as function of ξ_{ax} and the relative mode amplitude Y, for different values of λ. The thick dashed line is the $r_s\Delta'_+ = 0$ level curve. We set the transition point in $r_*/a = 0.5$, the resonant surface in $r_s/a = 0.75$, whilst $\alpha = 2.5$.

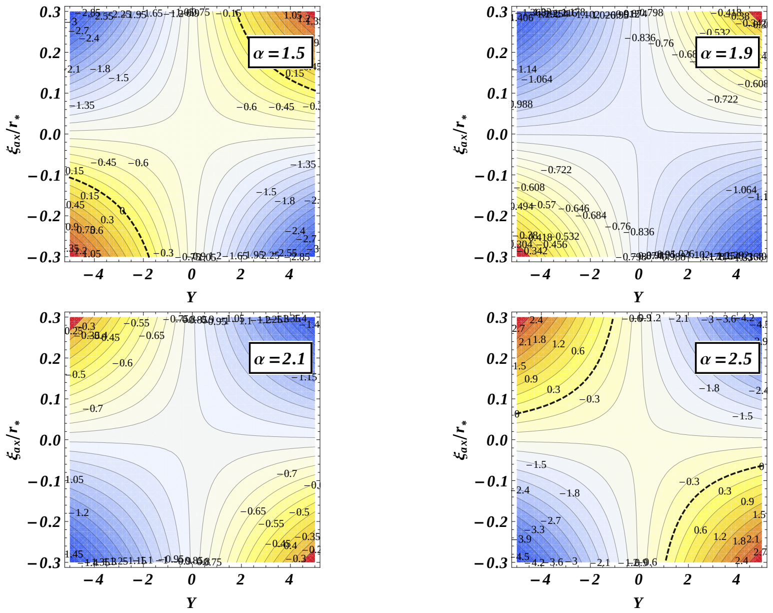

Figure B.2: Constant $r_s\Delta'_-$ contours for the $(3,2)$ mode as function of ξ_{ax} and the relative mode amplitude Y, for different values of α with fixed λ. The thick dashed line is the $r_s\Delta'_- = 0$ level curve. (same parameter in as Fig. B.1 for r_* and r_s) . We set here $\lambda = 1/2$, corresponding to the marginal stability boundary of the tearing mode ($r_s\Delta'_{Tear} = 0$).

C

Numerical codes

In this appendix we describe the two main codes used in the present thesis, i.e. the 3-D equilibrium code VMEC and the initial value stability code XTOR-2F. In the following sections the details of the numerical procedures employed by both codes are outlined as well as their interface, which is presented at the end of the present appendix.

C.1 VMEC

The VMEC code is based on the minimisation of the plasma energy (see section 2.3). A moment expansion of the plasma equilibrium is performed, resulting in a finite set of coupled nonlinear ordinary differential equations [18] for the Fourier components of the inverse mapping $\boldsymbol{x} = \boldsymbol{x}(r, \theta, \varphi)$ with r being a flux label normalised to unity at the plasma edge, θ and φ the geometric poloidal and toroidal angles respectively. The Jacobian in such coordinate system is $\sqrt{g} = [\boldsymbol{\nabla} r \cdot \boldsymbol{\nabla}\theta \times \boldsymbol{\nabla}\varphi]^{-1}$. It is convenient for numerical reasons to introduce a function $\lambda = \lambda(r, \theta, \varphi)$, periodic in its angular arguments, such that the magnetic field is written as $\boldsymbol{B} = \boldsymbol{\nabla}\Phi \times \boldsymbol{\nabla}(\theta + \lambda) - \boldsymbol{\nabla}\psi \times \boldsymbol{\nabla}\varphi$, where Φ is the toroidal flux function and $2\pi\psi$ the usual poloidal flux enclosed by a surface which extends from the magnetic axis $r = 0$ (where $\boldsymbol{\nabla}\psi = 0$) to a surface labelled by r.

The pressure and the toroidal current (alternatively rotational transform) profiles are needed as VMEC input, together with the edge value of the toroidal flux. Its key feature is the fact the a guess for the magnetic axis is needed at the beginning of the numerical calculations. For tokamak/RFP plasmas, depending on the choice of such guess, under particular conditions for the current profile (namely q profile), a bifurcation in the equilibrium could occur: one branch gives the standard axisymmetric equilibrium described by the Grad-Shafranov equation. The other branch describes a 3-D helical equilibrium state. The code can work in fixed and free boundary configuration: in the first case the shape of the outermost flux surface is fixed during all minimisation steps. In the second case the position of the plasma boundary is obtained by imposing continuity of the total pressure $(|B|^2/2\mu_0 + p)$ at the plasma-vacuum interface $r = 1$ and imposing a vanishing normal component of the vacuum field on such surface; thus accounting for the vacuum field, the energy functional becomes $W = \int_{\text{plasma}} \left(\frac{|B|^2}{2\mu_0} + \frac{p}{\Gamma-1}\right) d^3\boldsymbol{x} + \int_{\text{vacuum}} \frac{|B_{\text{vac}}|^2}{2\mu_0} d^3\boldsymbol{x}$. Nested flux surfaces are imposed in the numerical calculation, so that the condition $p = p(r)$ is assumed.

The MHD force balance is given by $\boldsymbol{F} = -\boldsymbol{\nabla} p + \boldsymbol{J} \times \boldsymbol{B}$. The minimisation of the plasma energy W (Eq. (2.12) in Chapter **2** § 2.3) is performed with respect to the parameter τ, i.e.:

$$
\begin{aligned}
&\frac{dW}{d\tau} = -\int \left[F_R \frac{\partial R}{\partial \tau} + F_Z \frac{\partial Z}{\partial \tau} + F_\lambda \frac{\partial \lambda}{\partial \tau}\right] dr d\theta d\varphi \\
&- \int_{r=1} d\theta d\varphi \left[R\left(\frac{|B|^2}{2\mu_0} + p\right)\left(\frac{\partial R}{\partial \theta}\frac{\partial Z}{\partial \tau} - \frac{\partial Z}{\partial \theta}\frac{\partial R}{\partial \tau}\right)\right],
\end{aligned}
$$

where the force projections read:

$$
\begin{aligned}
\mu_0 F_R = &\frac{\partial}{\partial r}\left(P\frac{\partial Z}{\partial \theta}\right) - \frac{\partial}{\partial \theta}\left(P\frac{\partial Z}{\partial r}\right) + \frac{\partial}{\partial \theta}\left(\sqrt{g}B^\theta \boldsymbol{B} \cdot \boldsymbol{\nabla} R\right) + \\
&\frac{\partial}{\partial \varphi}\left(\sqrt{g}B^\varphi \boldsymbol{B} \cdot \boldsymbol{\nabla} R\right) + \frac{\sqrt{g}}{R}\left[P/R - R^2(B^\varphi)^2\right] = \mu_0\sqrt{g}R\boldsymbol{\nabla}\varphi \times \boldsymbol{\nabla} Z \cdot \boldsymbol{F} \\
\mu_0 F_Z = &\frac{\partial}{\partial \theta}\left(P\frac{\partial R}{\partial r}\right) - \frac{\partial}{\partial r}\left(P\frac{\partial R}{\partial \theta}\right) + \frac{\partial}{\partial \theta}\left(\sqrt{g}B^\theta \boldsymbol{B} \cdot \boldsymbol{\nabla} Z\right) + \\
&\frac{\partial}{\partial \varphi}\left(\sqrt{g}B^\varphi \boldsymbol{B} \cdot \boldsymbol{\nabla} Z\right) = \mu_0\sqrt{g}R\boldsymbol{\nabla} R \times \boldsymbol{\nabla}\varphi \cdot \boldsymbol{F} \\
\mu_0 F_\lambda = &\frac{\partial B_\varphi}{\partial \theta} - \frac{\partial B_\theta}{\partial \varphi} = -\mu_0\sqrt{g}\boldsymbol{B} \times \boldsymbol{\nabla} r \cdot \boldsymbol{F}/|B|^2,
\end{aligned}
$$

with $P = R(\mu_0 p + |B|^2/2)$. If we define $(x_1, x_2, x_3) = (R, \lambda, Z)$ where λ replaces the toroidal angle variable , the inverse mapping $\boldsymbol{x} = \boldsymbol{x}(r, \theta, \varphi)$ can be expressed as a function of the flux coordinates in the following manner:

$$x_j = \sum_{m,n} X_j^{m,n}(r)\exp[i(m\theta - n\varphi)],$$

where $j = (1, 2, 3)$ and the reality condition on x_j is translated into $X_j^{m,n} = (X_j^{-m,-n})^*$ (the asterisk denotes complex conjugation).

The variation of the total potential energy then becomes

$$\frac{dW}{d\tau} = -\int \left(F_j^{mn}\right)^* \frac{\partial X_j^{mn}}{\partial \beta} dV,$$

with

$$F_j^{m,n} = \frac{1}{V'(r)} \int\int F_j \exp\left[-i\left(m\theta - n\zeta\right)\right] d\theta d\zeta,$$

where $V'(r) = \int d\theta d\varphi |\sqrt{g}|$. The Fourier decomposition of the energy integral allows us to write the net force a system of second order operators in the radial variable r. A minimum in potential energy is sought via the method of steepest descent. The steepest descent method consists of finding the local minimum of a function $F(\boldsymbol{x})$ whose gradient is known in a neighbourhood of a point $\boldsymbol{a}$. For a sufficiently small ϵ, we have that $F(\boldsymbol{a}) \geq F(\boldsymbol{b})$ where $\boldsymbol{b} = \boldsymbol{a} - \epsilon \boldsymbol{\nabla} F(\boldsymbol{a})$. Thus one starts with a guess of the local minimum located, say, in $\boldsymbol{x}_0$ and moves from $\boldsymbol{x}_i$ to $\boldsymbol{x}_{i+1}$ by minimising along the line from $\boldsymbol{x}_i$ in the direction of the local downhill gradient $-\boldsymbol{\nabla} f(\boldsymbol{x}_i)$ [122]. Hence the following expression is applied iteratively:

$$\boldsymbol{x}_{i+1} = \boldsymbol{x}_i - \epsilon_i \boldsymbol{\nabla} F(\boldsymbol{x}_i),$$

where ϵ_i is allowed to vary during every iteration. Eventually the sequence $\boldsymbol{x}_i$ will converge to the local minimum.

The energy functional is negative definite when we decide to advance $\partial(R, Z, \lambda)/\partial\tau = (F_R, F_Z, F_\lambda)$, which therefore determines the descent path. This path is given by

$$\frac{\partial X_j^{m,n}}{\partial \tau} = F_j^{m,n}.$$

The system of second order differential operators in r above, corresponds to a set of parabolic differential equation, whose convergence can be accelerated by converting them to hyperbolic equations [18] via a second-order Richardson scheme:

$$\frac{\partial^2 X_j^{m,n}}{\partial \tau^2} + \frac{1}{\beta}\frac{\partial X_j^{m,n}}{\partial \tau} = F_j^{m,n},$$

where the optimum value of β, which minimises the number of iterations required to reach the steady state in τ is $\beta^{-1} \simeq -d(\ln \int |F|^2 dV)/d\tau$ and $dV = V'dr$. Particular attention must be taken in the treatment of the magnetic axis. Indeed this is a singular point for which $\boldsymbol{\nabla}\psi = 0$. We first notice that since the function λ is periodic in θ and φ, we must have $X_2^{0,0} = 0$. The magnetic axis must be independent of the poloidal angular variable, thus $X_j^{m,n} = 0$ $(j = 1, 3)$ when $m \neq 0$. Since the net force is a second order operator in r, this implies that also the Fourier coefficients must be second order in r. Therefore $\partial X_1^{0,n}/\partial r = \partial X_3^{0,n}/\partial r$. The final constraint is $\partial X_2^{0,m}/\partial\theta = 0$. The full details of the numerical description of the VMEC code can be found in Ref. [18].

The VMEC code is the natural tool for studying the equilibrium 3-D properties of non axisymmetric plasmas, in particular stellarator plasmas, though it is used also for 2D equilibrium calculations for tokamaks and RFPs. The equilibrium surfaces for stellarator (W7-X), tokamak (MAST) and RFP (RFX) plasmas computed with VMEC are shown in Fig. C.1. This numerical tool is also of extreme importance for analysing non axisymmetric helical cores which can develop in nominally axisymmetric plasmas such as tokamaks and RFPs (this has been presented in Chapter **3**).

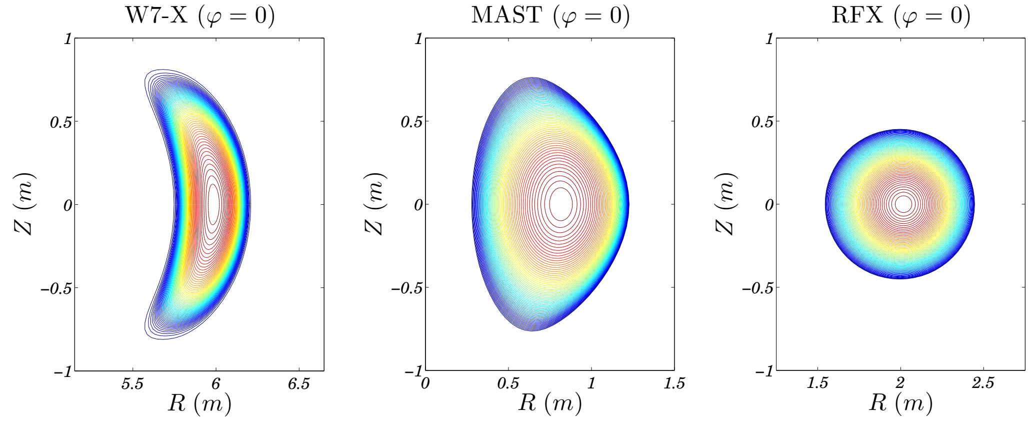

Figure C.1: Contour plot of the flux surfaces computed with the VMEC code for different magnetic confinement systems (stellarator, tokamak and RFP).

C.2 XTOR-2F

XTOR-2F solves the full set resistive MHD equations in toroidal geometry, extended by the full bi-fluid equations resulting from the Braginskii equations [66, 123]:

$$\varrho\partial_t \boldsymbol{v} + \boldsymbol{v} \cdot \boldsymbol{\nabla}\boldsymbol{v} + \boldsymbol{v}_i^* \cdot \boldsymbol{\nabla}\boldsymbol{v} = -\boldsymbol{\nabla}p + \boldsymbol{J} \times \boldsymbol{B} + (\boldsymbol{\nabla}\nu\boldsymbol{\nabla})\boldsymbol{v}, \tag{C.1}$$

$$\partial_t \boldsymbol{B} = \boldsymbol{\nabla} \times (\boldsymbol{v} \times \boldsymbol{B}) + \alpha\boldsymbol{\nabla} \times \frac{\boldsymbol{\nabla}_{||}p_e}{\varrho} - \boldsymbol{\nabla} \times \eta(\boldsymbol{J} - \boldsymbol{J}_{\mathrm{boot}}), \tag{C.2}$$

$$\begin{aligned}\partial_t p + \boldsymbol{v} \cdot \boldsymbol{\nabla}p + \Gamma p\boldsymbol{\nabla} \cdot \boldsymbol{v} = -\alpha\Gamma\frac{p_i}{\varrho}\boldsymbol{\nabla}p \cdot \boldsymbol{\nabla} \times \frac{\boldsymbol{B}}{B^2} + \boldsymbol{\nabla} \cdot (\chi_\perp\boldsymbol{\nabla}p) + \\ \boldsymbol{\nabla} \cdot \left[\boldsymbol{B}\left(\frac{\chi_{||}}{B^2}(\boldsymbol{B} \cdot \boldsymbol{\nabla})p\right)\right] + H,\end{aligned} \tag{C.3}$$

with either condition given by Eq. (2.3) in Chapter **2** § 2.1, or:

$$\partial_t\varrho + \boldsymbol{v} \cdot \boldsymbol{\nabla}\varrho + \varrho\boldsymbol{\nabla} \cdot \boldsymbol{v} = -\alpha\boldsymbol{\nabla}p_i \cdot \boldsymbol{\nabla} \times \frac{\boldsymbol{B}}{B^2} + \boldsymbol{\nabla} \cdot (D_\perp\boldsymbol{\nabla}\varrho) + S, \tag{C.4}$$

where the current density is given by (2.6). The ion velocity is written as $\boldsymbol{v}_i = \boldsymbol{v} + \boldsymbol{v}_i^* + \boldsymbol{v}_p$, where $\boldsymbol{v}_i^* = \alpha\frac{\boldsymbol{B}\times\boldsymbol{\nabla}p_i}{\varrho B^2}$, $\boldsymbol{v} = \frac{\boldsymbol{E}\times\boldsymbol{B}}{B^2} + \boldsymbol{v}_{i||}$ and $\boldsymbol{v}_p$ represents the polarisation drift velocity. It has been assumed that $p_i = p_e = p/2$. The quantity $\alpha = (\Omega_{ci}\tau_A)^{-1}$ tunes the strength of the diamagnetic effects. The quantities η and ν are plasma resistivity and viscosity respectively. The resistivity can be chosen to vary either according to Spitzer's law ($\eta \sim T^{-3/2}$) or in order to keep the toroidal electric field constant over space. In the equations for p and ϱ, the parameters $D_\perp$, $\chi_\perp$ and $\chi_{||}$ are the perpendicular and parallel diffusion coefficients, where H and S are the heat and density sources. Neoclassical effects can be included in the bootstrap contribution of the current density $\boldsymbol{J}_{\mathrm{boot}}$, which is taken to vary according to Ref. [28].

In XTOR-2F normalisations, the magnetic axis is defined by the dimensionless number R_0. The plasma minor radius is normalised such that $a = 1$, where a is the half size of the plasma cross-section at $Z = 0$, consistent with CHEASE metrics [66]. The magnetic field unit is set by $B_{\varphi,0} = R_0$. The plasma mass density is normalised with respect to its central value ϱ_0 and the time is expressed in terms of Alfvénic units τ_A. With such normalisations the Lundquist number S is simply the inverse of the resistivity, i.e. $S = \eta^{-1}$. The physical quantities are Fourier decomposed both in the poloidal (with θ being the geometric poloidal angle) and the toroidal direction (with φ being the geometric toroidal angle), while linear staggered finite differences on a staggered mesh (the derivative of a quantity discretised on the integer mesh r_l is evaluated on the half-integer mesh $r_{l+1/2}$, and vice versa) are used in the radial coordinate $r \sim \sqrt{\psi}$ which labels the equilibrium poloidal magnetic flux surfaces. The Jacobian in such coordinate system is $\sqrt{g}$. The radial mesh in XTOR is obtained from the solution of the Grad-Shafranov equation, i.e. Eq. (2.11), providing the required expressions for the metric tensor coefficients g^{ij}. The input quantities for XTOR-2F include also pressure, flux profiles and R and Z for each flux surface (the details of the input quantities will be given in the next chapter). Since XTOR-2F is designed for the study of internal modes, no plasma-vacuum interface is assumed, viz. an infinitely conducting wall located at the plasma surface is assumed. We stress the point that the XTOR-2F plasma boundary is axisymmetric. Therefore we have the following boundary conditions for the perturbed quantities (denoted by a tilde) at the plasma edge [123]:

$$\begin{aligned}
&\tilde{v}^r_{edge} = 0, \quad \partial_r \tilde{v}^\theta_{edge} = 0, \quad \partial_r \tilde{v}^\varphi_{edge} = 0, \\
&\partial_r \tilde{B}_{\varphi,edge} = 0, \quad E_{\varphi,0,edge} = \eta_0 J_{\varphi,0,edge} = \eta_{edge}(t) J(t)_{\varphi,edge} = E_{||},
\end{aligned}$$

where the subscript 0 denotes equilibrium quantities, and $E_{||}$ is the loop voltage.

Now we outline the numerical method implemented in XTOR-2F. First we write the set of equations (C.1)-(C.4) in this compact manner:

$$\dot{\boldsymbol{x}} = \boldsymbol{F}(\boldsymbol{x}), \tag{C.5}$$

where $\boldsymbol{x} = (v^r, \sqrt{g}v^\theta, v^\varphi, B^r, \sqrt{g}B^\theta, B^\varphi, p)$ (the superscript indicates the contravariant component of the vector), and $\boldsymbol{F}$ is the RHS of Eqs. (C.1)-(C.4). The poloidal contravariant components of the velocity and the magnetic field are multiplied by the Jacobian in order to remove the singularity on the magnetic axis. It is known that the application of the MHD equation to tokamaks is a very stiff problem: there is coexistence on the same scale of very fast (compressible Alfvén) and very slow (resonant shear Alfvén) modes. In addition the relevant physics is slow compared to the basic time scale (the Alfvén time) because of the good confinement in tokamaks. Therefore relevant studies must address long time behaviour. The implicit time advance is chosen to address the stiff problem. Finally, every implicit time step is performed by an iterative Newton–Krylov method (NITSOL package). When the Newton-Krylov method is applied, it is important to avoid the exact evaluation of the Jacobian matrix required at every implicit time advance step. This problem is eliminated by using the matrix-free method [124], in which the matrix coefficient are not stored explicitly, but the matrix is accessed by evaluating matrix-vector products (in XTOR-2F the Jacobian matrix is evaluated by numerical differentiation).

If the subscript n labels the time step, the system represented by equation (C.5) is advanced in time by an amount Δt by setting:

$$\boldsymbol{x}_{n+1} - \boldsymbol{x}_n = \Delta t \boldsymbol{F}\left[\frac{\boldsymbol{x}_{n+1} + \boldsymbol{x}_n}{2} + \Theta(\boldsymbol{x}_{n+1} - 2\boldsymbol{x}_n + \boldsymbol{x}_{n-1})\right],$$

where Θ is a numerical constant. At every time step this equation is inverted to give $\boldsymbol{x}_{n+1}$. The expression above can be rearranged to give $G(\Delta_n, \bar{\boldsymbol{x}}) \equiv \Delta_n - \Delta t \boldsymbol{F}\left[(\frac{1}{2} + \Theta)\Delta_n + \bar{\boldsymbol{x}}\right]$ with $\Delta_n = \boldsymbol{x}_{n+1} - \boldsymbol{x}_n$ and $\bar{\boldsymbol{x}} = (1 - \Theta)\boldsymbol{x}_n + \Theta \boldsymbol{x}_{n-1}$. This expression is solved for Δ_n by means of a preconditioned Newton-Krylov method:

$$M^{-1}\left[L(\Delta_n^k,\bar{\boldsymbol{x}})(\Delta_n^{k+1}-\Delta_n^k)+G(\Delta_n^k,\bar{\boldsymbol{x}})\right]=0,$$

where M^{-1} is the pre-conditioner and k labels the steps in the Newton-Krylov method. $L(\Delta_n^k,\bar{\boldsymbol{x}})$ is the MHD operator linearised about $\bar{\boldsymbol{x}}$. With an efficient pre-conditioner M^{-1}, the number of iterations is greatly reduced. The pre-conditioner M^{-1} is chosen to be physical, i.e the linearised MHD operator is used to construct the pre-conditioner for the implicit solver, and it is written as:

$$M^{-1}=\underbrace{M_\eta^{-1}}_{\text{Resistive}}\times\underbrace{M_D^{-1}}_{\text{Diffusion}}\times\underbrace{M_\chi^{-1}}_{\text{Transport}}\times\underbrace{M_{MHD}^{-1}}_{\text{Ideal}}.$$

The pre-conditioner is inverted by an exact LU method in the Fourier representation, limiting the time spent in preconditioning to $1/3\div 1/2$ the total CPU time of the simulation. The details of the numerical description of XTOR-2F can be found in Refs. [66, 123].

C.3 VMEC/XTOR-2F interface

The natural way to assess the stability properties of plasmas which give rise to helical cores, is to interface the equilibrium computed with VMEC with the stability code XTOR-2F. The interface for the XTOR-2F code is the 2D equilibrium solver CHEASE [69]. Therefore an interface between VMEC and CHEASE is required. First the poloidal flux Ψ is computed, after the plasma pressure p and its derivative with respect to Ψ are computed. Finally the quantities $TdT/d\Psi$, I^* and $I_{||}$ are evaluated, where T is the covariant toroidal component of the magnetic field ($\boldsymbol{B} = T\boldsymbol{\nabla}\varphi - \boldsymbol{\nabla}\Psi \times \boldsymbol{\nabla}\varphi$, φ is the ignorable toroidal angle) and:

$$I^* = \frac{\oint_{s_{const}} j_\varphi(\sqrt{g}/R)d\chi}{\oint_{s_{const}}(\sqrt{g}/R)d\chi}, \qquad I_{||} = \frac{\oint_{s_{const}} \boldsymbol{J}\cdot\boldsymbol{B}\sqrt{g}d\chi}{\oint_{s_{const}} \boldsymbol{B}\cdot\boldsymbol{\nabla}\varphi\sqrt{g}d\chi},$$

where j_φ is the toroidal current density ($j_\varphi = \boldsymbol{J}\cdot\boldsymbol{\nabla}\varphi/|\boldsymbol{\nabla}\varphi|$), χ is a poloidal-like angle, $\sqrt{g}$ is the Jacobian and all the quantities are function of the variable $s = \sqrt{\frac{|\Psi_{edge}-\Psi|}{|\Psi_{edge}-\Psi_0|}}$ (Ψ_0 and Ψ_{edge} are respectively the values of the poloidal flux on the magnetic axis and at the plasma boundary). When all the required equilibrium quantities are computed, together with the plasma boundary, the CHEASE code can compute the equilibrium which will be used by the XTOR-2F code.

The equilibrium computed by VMEC can be directly interfaced with XTOR-2F, without passing through the CHEASE code. The physical quantities required by XTOR-2F are shown in Table 3.2. After computing p, $dp/d\Psi$ and $dT/d\Psi$, instead of using these quantities as input for CHEASE, the R and Z Fourier components of the VMEC equilibrium are transformed in real space and the elements of the metric tensor used in XTOR-2F are computed in the coordinate system (s,θ,φ), where s and φ have been defined above, while θ is the geometric poloidal angle. First the radial and poloidal derivatives of R and Z are computed. This allows to derive the expressions of g_{ij} as defined in Appendix A § A.1. By using the fact that $g^{ss} = R^2 g_{\theta\theta}/g$, $g^{\theta\theta} = R^2 g_{ss}/g$, $g^{\phi\phi} = 1/R^2$ and $g^{s\theta} = -R^2 g_{s\theta}/g$ where $\sqrt{g} = R[g_{ss}g_{\theta\theta} - g_{s\theta}^2]^{1/2}$, we can calculate the metric coefficients g^{ij}. This allows us to directly prepare the equilibrium used by XTOR-2F. This is particularly useful when RFP equilibria are considered.

The way back, from CHEASE to VMEC, is rather similar when CHEASE is interfaced with VMEC. First the toroidal flux is computed and consequently the expressions for plasma pressure p and covariant toroidal current density J^φ (or alternatively the rotational transform ι), where all these quantities are function of the toroidal flux. Finally the polynomial coefficients for ι and for J^φ are easily evaluated via numerical polynomial fitting routines and the boundary is decomposed in Fourier harmonics, which eventually allows VMEC to compute the equilibrium.

Bibliography

[1] T. J. M. Boyd and J. J. Sanderson, **The Physics of Plasmas** (CUP Cambridge, 2003), p. 8.

[2] J. D. Lawson, Proc. Phys. Soc. B **70**, 6 (1957).

[3] N. A. Krall and A. W. Trivelpiece, **Principles of Plasma Physics** (McGraw-Hill, 1973), p. 22.

[4] R. J. Hastie, Astrophysics and Space Science **256**, 177 (1997).

[5] R. J. Buttery, S. Günter, G. Giruzzi, T. C. Hender, D. Howell1, G. Huysmans, R. J. La Haye, M. Maraschek, H. Reimerdes, O. Sauter, C. D. Warrick, H. R. Wilson and H. Zohm, Plasma Phys. Control. Fusion **42**, B61 (2000).

[6] C. Gormezano, A. C. C. Sips, T. C. Luce, S. Ide, A. Becoulet, X. Litaudon, A. Isayama, J. Hobirk, M.R. Wade, T. Oikawa, R. Prater, A. Zvonkov, B. Lloyd, T. Suzuki, E. Barbato, P. Bonoli, C. K. Phillips, V. Vdovin, E. Joffrin, T. Casper, J. Ferron, D. Mazon, D. Moreau, R. Bundy, C. Kessel, A. Fukuyama, N. Hayashi, F. Imbeaux, M. Murakami, A. R. Polevoi and H. E. St John Nucl. Fusion **47**, S285 (2007).

[7] R. Lorenzini, E. Martines, P. Piovesan, D. Terranova, P. Zanca, M. Zuin, A. Alfier, D. Bonfiglio, F. Bonomo, A. Canton, S. Cappello, L. Carraro, R. Cavazzana, D. F. Escande, A. Fassina, P. Franz, M. Gobbin, P. Innocente, L. Marrelli, R. Pasqualotto, M. E. Puiatti, M. Spolaore, M. Valisa, N. Vianello, P. Martin & RFX-mod team and collaborators, Nat. Phys. **5**, 570 (2009).

[8] I. T. Chapman, M. -D. Hua, S. D. Pinches, R. J. Akers, A. R. Field, J. P. Graves, R. J. Hastie, C. A. Michael and the MAST Team, Nucl. Fusion **50**, 045007 (2010).

[9] H. Reimerdes, I. Furno, F. Hofmann , An. Martynov, A. Pochelon and O. Sauter, Plasma Phys. Control. Fusion **48**, 1621 (2006).

[10] P. Buratti, M. Baruzzo, R.J. Buttery, C.D. Challis, I.T. Chapman, F. Crisanti, L. Figini, M. Gryaznevich, T.C. Hender, D.F. Howell, Nucl. Fusion **52**, 023006 (2012).

[11] J. P. Freidberg, **Ideal Magnetohydrodynamics** (Plenum Press, New York & London, 1987).

[12] H. Grad and H. Rubin, Proceedings of the 2nd UN Conf. on the Peaceful Uses of Atomic Energy, Vol. **31** (IAEA Geneva, 1958) , p. 190.

[13] V. D. Shafranov, **Reviews of Plasma Physics**, Vol. 2 ed. M. A. Leontovich, (New York: Consultants Bureau, 1966), p. 103.

[14] L. S. Solov'ev, Sov. Phys.-JETP **26**, 400 (1968).

[15] H Lütjens, Magnetohydrodynamic stability of internal kink modes in tokamaks: application of an equilibrium code using bicubic finite elements, *PhD thesis no. 1105, École Polytechniqye Fèdèrale de Lausanne (EPFL), CH-1015 Lausanne, Switzerland*, 1992.

[16] J. A. Wesson, **Tokamaks** (Oxford UK, Oxford U. P. 2011).

[17] W. A. Cooper, J. P. Graves, A. Pochelon, O. Sauter and L. Villard, Phys. Rev. Lett. **105**, 035003 (2010).

[18] S. P. Hirshman and J. C. Whitson, Phys. Fluids **26**, 3553 (1983).

[19] D. Biskamp, **Nonlinear Magnetohydrodynamics** (CUP Cambridge, 1993).

[20] I. B. Bernstein, E. A. Frieman, M. D. Kruskal and R. M. Kulsrud, Proc. Roy. Soc. A **244**, 17 (1958).

[21] Miyamoto K 1997 **Fundamentals of Plasma Physics and Controlled Fusion** (Iwanami Book Service Centre, Tokyo)

[22] W. Newcomb, Ann. Phys. **10**, 232 (1960).

[23] R. J. Hastie, T. C. Hender, B. A. Carreras, L. A. Charlton and J. A. Holmes , Phys. Fluids **30**, 1756 (1987).

[24] H J. A. Holmes, B. A. Carreras, L. A. Charlton, V. E. Lynch, R. J. Hastie and T. C. Hender, Phys. Fluids **31**, 1202 (1988).

[25] M. N. Rosenbluth, P. Y. Dagazian and P. H. Rutherford, Phys. Fluids **16**, 1894 (1973).

[26] M. N. Bussac, R. Pellat, D. Edery and J. L. Soule, Phys. Rev. Lett. **35**, 1638 (1975).

[27] R. J. Goldston, P. H. Rutherford, **Introduction to Plasma Physics** (IOP London, 1995).

[28] O. Sauter, R. J. La Haye, Z. Chang, D. A. Gates, Y. Kamada, H. Zohm, A. Bondeson, D. Boucher, J. D. Callen, M. S. Chu, T. A. Gianakon, O. Gruber, R. W. Harvey, C. C. Hegna, L. L. Lao, D. A. Monticello, F. Perkins, A. Pletzer, A. H. Reiman, M. Rosenbluth, E. J. Strait, T. S. Taylor, A. D. Turnbull, F. Waelbroeck, J. C. Wesley, H. R. Wilson and R. Yoshino, Phys. Plasmas **4**, 1654 (1997).

[29] C. C. Hegna and J. D. Callen, Phys. Plasmas **1**, 2308 (1994).

[30] P. H. Rutherford, Phys. Fluids **16**, 1903 (1973).

[31] P. H. Furth, J. Killeen and M. N. Rosenbluth, Phys. Fluid **6**, 459 (1963).

[32] R. B. White, D. A. Monticello, M. N. Rosenbluth and B. V. Waddell, Phys. Fluids **20**, 800 (1977).

[33] R. J. La Haye, Phys. Plasmas **13**, 055501 (2006).

[34] J. Wesson, Plasma Phys. Control. Fusion **28**, 243 (1986).

[35] R. J. Hastie and T. C. Hender, Nucl. Fusion **28**, 585 (1988).

[36] A. W. Edwards, D. J. Campbell, W. W. Engelhardt, H. -U. Fahrbach, R. D. Gill, R. S. Granetz, S. Tsuji, B. J. D. Tubbing, A. Weller, J. Wesson, and D. Zasche, Phys. Rev. Lett. **57**, 210 (1986).

[37] Z. Chang, J. D. Callen, E. D. Fredrickson, R. V. Budny, C. C. Hegna, K. M. McGuire, M. C. Zarnstorff, and TFTR group, Phys. Rev. Lett. **74**, 4663 (1995).

[38] Z. Chang, E. D. Fredrickson, J. D. Callen, K. M. McGuire, M. G. Bell, R. V. Budny, C. E. Bush, D. S. Darrow, A. C. Janos, L. C. Johnson, H. K. Park, S. D. Scott, J. D. Strachan, E.J. Synakowski, G. Taylor, R. M. Wieland, M. C. Zarnstorff and S.J. Zweben, Nucl. Fusion **34**, 1309 (1994).

[39] M. Maraschek, S. Günter, H. Zohm and the ASDEX Upgrade Team, Plasma Phys. Control. Fusion **41**, L1 (1999).

[40] G. P. Canal, B. P. Duval, F. Felici, T. P. Goodman, J. P. Graves, A. Pochelon, H. Reimerdes, O. Sauter, D. Testa and the TCV Team, Nucl. Fusion **53**, 113026 (2013).

[41] G. P. Canal, Sawtooth generated magnetic islands and the properties of the snowflake divertor, *PhD thesis no. 6272, École Polytechniqye Fèdèrale de Lausanne (EPFL), CH-1015 Lausanne, Switzerland*, 2014.

[42] C. E. Kessel, Nucl. Fusion **34**, 1221 (1994).

[43] R. Fitzpatrick, Phys. Plasmas **2**, 825 (1995).

[44] A. H. Glasser, J. M. Greene and J. L. Johnson, Phys. Fluids **18**, 875 (1975).

[45] H. R. Wilson, J. W. Connor, R. J. Hastie and C. C. Hegna, Phys. Plasmas **3**, 248 (1996).

[46] M. F. F. Nave, E. Lazzaro, R. Coelho, P. Belo, D. Borba, R. J. Buttery, S. Nowak, F. Serra and EFDA-JET Contributors, Nucl. Fusion **43**, 179 (2003).

[47] W. A. Cooper, J. P. Graves and O. Sauter, Plasma Phys. Control. Fusion **53**, 024002 (2011).

[48] D. Brunetti, W. A. Cooper, J. P. Graves, F. Halpern, C. Wahlberg, H. Lütjens and J. F. Luciani, J. Phys.: Conf. Ser. **401**, 012003 (2012).

[49] D. Brunetti, J. P. Graves, W. A. Cooper and D. Terranova, Nucl. Fusion **54**, 064017 (2014).

[50] J. P. Graves, I. T. Chapman, S. Coda, M. Lennholm, M. Albergante and M. Jucker, Nature Commun. **3**, 624 (2012).

[51] R. J. Buttery, T. C. Hender, G. T. A. Huysmans, R. J. La Haye, P. U. Lamalle, M. Mantsinen, C. Petty, O. Sauter, and H R Wilson, *Controlled Fusion and Plasma Physics* (Proc 26th EPS Maastricht) 23J p 121 (1999).

[52] B. B. Kadomtsev, Sov. J. Plasma Phys. **1**, 389 (1975).

[53] F. Porcelli, D. Boucher and M. N. Rosenbluth, Plasma Phys. Control. Fusion **38**, 2163 (1996).

[54] H. Reimerdes, O. Sauter, T. Goodman, and A. Pochelon, Phys. Rev. Lett. **88**, 105005 (2002).

[55] D. P. Brennan, E. J. Strait, A. D. Turnbull, M. S. Chu, R. J. La Haye, T. C. Luce, T. S. Taylor, S. Kruger and A. Pletzer, Phys. Plasmas **9**, 2998 (2002).

[56] J. Manickam, N. Pomphrey and A. M. M. Todd, Nucl. Fusion **27**, 1461 (1987).

[57] L. E. Zakharov, Nucl. Fusion **18**, 335 (1978).

[58] L. A. Charlton, R. J. Hastie and T. C. Hender, Phys. Fluids B **1**, 798 (1989).

[59] J. Kamleitner, S. Coda, J. Decker, J. P. Graves and the TCV team, *Suprathermal electron dynamics and MHD instabilities in a tokamak*, submitted to Plasma Phys. Control. Fusion.

[60] O. Gruber, R. C. Wolf, R. Dux, C. Fuchs, S. Günter, A. Kallenbach, K. Lackner, M. Maraschek, P. J. McCarthy, H. Meister, G. Pereverzev, F. Ryter, J. Schweinzer, U. Seidel, S. Sesnic, A. Stäbler, J. Stober and the ASDEX Upgrade Team, Phys. Rev. Lett. **83**, 1787 (1999).

[61] O. Gruber, A. C. C. Sips, A. Staebler, R. Dux, J. Hobirk, L. D. Horton, C. F. Maggi, A. Manini, M. Maraschek, R. Neu, ASDEX Upgrade Team and Y. S. Na, Phys. Plasmas **12**, 056127 (2005).

[62] K. Avinash, Phys. Rev. Lett. **59**, 2647 (1987).

[63] K. Avinash, Phys. Fluids B **2**, 2373 (1990).

[64] J. P. Graves, D. Brunetti, I. T. Chapman, W. A. Cooper, H. Reimerdes, F. Halpern, A. Pochelon, O. Sauter, the TCV team and the MAST team, Plasma Phys. Control. Fusion **55** 014005 (2013).

[65] M. N. Bussac and R. Pellat, Phys. Rev. Lett. **59**, 2650 (1987).

[66] H. Lütjens and J. F. Luciani, J. Comput. Phys. **229**, 8130 (2010).

[67] G. Ara, B. Basu, B. Coppi, G. Laval, M.N. Rosenbluth, B.V. Waddell, Ann. Phys. **112**, 443 (1978).

[68] A. H. Glasser, J. M. Greene and J. L. Johnson, Phys. Fluids **18**, 875 (1975).

[69] H. Lütjens, A. Bondeson and O. Sauter, Comput. Phys. Commun. **97**, 219 (1996).

[70] D. V. Anderson, W. A. Cooper, R. Gruber, S. Merazzi and U. Schwenn, **Scientific Computing on Supercomputers II** (Springer Us, 1990), p. 159.

[71] W. A. Cooper, J. P. Graves, O. Sauter, J. Rossel, M. Albergante, S. Coda, B. P. Duval, B. Labit, A. Pochelon, H. Reimerdes and the TCV team, Plasma Phys. Control. Fusion **53**, 124005 (2011).

[72] F. Porcelli, Phys. Fluids **30**, 1734 (1987).

[73] H. Lütjens and J. F. Luciani, Phys. Plasmas **4**, 4192 (1997).

[74] D. Pfefferlé, J. P. Graves, W. A. Cooper, C. Misev, I. T. Chapman, M. Turnyanskiy and S. Sangaroon, Nucl. Fusion **54**, 064020 (2014).

[75] A. Staebler, A. C. C. Sips, M. Brambilla, M. Bilato, R. Dux, O. Gruber, J. Hobirk, L. D. Horton, C. F. Maggi, A. Manini, M. Maraschek, A. Mück, Y. -S. Na, R. Neu, G. Tardini, M. R. Wade and ASDEX Upgrade Team, Nucl. Fusion **45**, 617 (2005).

[76] C. Gormezano, A. Becoulet, P. Buratti, L. Carraro, F. Crisanti, B. Esposito, G. Giruzzi, R. Guirlet, G. T. Hoang, E. Joffrin, X. Litaudon, T. Luce, V. Pericoli-Ridolfini, O. Sauter, A. C. C. Sips, A. Tuccillo and the JET EFDA Contributors, Plasma Phys. Control. Fusion **46**, B435 (2004).

[77] V. S. Udintsev, O. Sauter, E. Asp, E. Fable, T. P. Goodman, G. Turri, J. P. Graves, A. Scarabosio, G. Zhuang, C. Zucca and the TCV Team, Plasma Phys. Control. Fusion **50**, 124052 (2008).

[78] A. Weller, A. D. Cheetham, A. W. Edwards, R. D. Gill, A. Gondhalekar, R. S. Granetz, J. Snipes and J. A. Wesson, Phys. Rev. Lett. **59**, 2303 (1987).

[79] Y. Camenen, F. Hofmann, A. Pochelon, A. Scarabosio, S. Alberti, G. Arnoux, P. Blanchard, S. Coda, T. P. Goodman, M. A. Henderson, E. Nelson-Melby, L. Porte and O. Sauter, Nucl. Fusion **47**, 586 (2007).

[80] B. N. Kuvshinov, Sov. J. Plasma Phys. **15**, 526 (1989).

[81] I. T. Chapman, R. Scannell, W. A. Cooper, J. P. Graves, R. J. Hastie, G. Naylor and A. Zocco, Phys. Rev. Lett. **105**, 255002 (2010).

[82] R. Fitzpatrick and F. L. Waelbroeck, Phys. Plasmas **12**, 022307 (2005).

[83] A. B. Mikhailovskii, **Instabilities In A Confined Plasma** (IoP Publishing, Bristol, UK, 1998).

[84] F. L. Waelbroeck and R. D. Hazeltine, Phys. Fluids **31**, 1217 (1988).

[85] H. J. de Blank and T. J. Schep, Phys. Fluids B **3**, 1136 (1991).

[86] C. Wahlberg and J. P. Graves, Phys. Plasmas **14**, 110703 (2007).

[87] W. D. D'haeseleer, W. N. G. Hitchon, J. D. Callen and J. L. Shohet, **Flux Coordinates and Magnetic Field Structure** (Springer-Verlag, New York, 1991).

[88] E. Lazzaro and P. Zanca, Phys. Plasmas **10**, 2399 (2003).

[89] A. B. Mikhailovskii, Nucl. Fusion **14**, 483 (1974).

[90] J. M. Greene, J. L. Johnson and K. E. Weimer, Phys. Fluids **14**, 671 (1971).

[91] C. Wahlberg, Plasma Phys. Control. Fusion **51**, 085006 (2009).

[92] R. D. Hazeltine and J. D. Meiss, **Plasma Confinement** (Addison-Wesley, Redwood City, CA, 1992).

[93] J. J. Ramos, Phys. Plasmas **12**, 112301 (2005).

[94] Y. In, J. J. Ramos, R. J. Hastie, P. J. Catto, A. E. Hubbard, I. H. Hutchinson, E. Marmar, M. Porkolab, J. Snipes, S. Wolfe, G. Taylor and A. Bondeson, Phys. Plasmas **7**, 5087 (2000).

[95] D. Meshscheriakov, P. Maget, H. Lütjens, P. Beyer and X. Garbet, Phys. Plasmas **19**, 092509 (2012).

[96] R. D. Hazeltine and D. W. Ross, Phys Fluids **21**, 1140 (1978).

[97] J. W. Connor, S. C. Cowley, R. J. Hastie, T. C. Hender, A. Hood and T. J. Martin, Phys. Fluids **31**, 577 (1988).

[98] A. B. Mikhailovskii, **Reviews of Plasma Physics** vol. 9, ed. M. A. Leontovich (Consultants Bureau, New York, 1986).

[99] C. G. Gimblett, R. J. Hastie and T. C. Hender, Phys. Plasmas **3**, 3369 (1996).

[100] N. N. Lebedev, **Special Functions and Their Applications** (Dover, New York, 1972).

[101] B. N. Kuvshinov and A. B. Mikhailovskii, Sov. J. Plasma Phys. **16**, 639 (1991).

[102] M. Abramowitz and I. A. Stegun, **Handbook of Mathematical Functions** (Dover, New York, 1968).

[103] S. Migliuolo, Nucl. Fusion **33**, 1721 (1993).

[104] D. Grasso, M. Ottaviani and F. Porcelli, Phys. Plasmas **8**, 4306 (2001).

[105] S. Migliuolo, F. Pegoraro and F. Porcelli, Phys. Fluids B **3**, 1338 (1991).

[106] M. J. Lighthill, **Introduction to Fourier Analysis and Generalized Functions** (Cambridge U. P., Cambridge, 1958).

[107] H. P. Furth, P. H. Rutherford and H. Selberg, Phys. Fluids **16**, 1054 (1973).

[108] L. A. Charlton, B. A. Carreras and V. E. Lynch, Phys. Fluids B **2**, 1574 (1990).

[109] R. D. Hazeltine, D. Dobrott and T.S. Wang, Phys Fluids **18**, 1778 (1975).

[110] D. Biskamp, Nucl. Fusion **18**, 1059 (1978).

[111] R. B. White, **Theory of Toroidally Confined Plasmas** (ICP, London, 2006).

[112] F. Porcelli and S. Migliuolo, Phys. Fluids **29**, 1741 (1986).

[113] A. Bondeson A and J. R. Sobel, Phys. Fluids **27**, 2028 (1984).

[114] D. Brunetti, J. P. Graves, W. A. Cooper and C. Wahlberg, Plasma Phys. Control. Fusion **56**, 075025 (2014).

[115] F. Wang, G. Y. Fu, J. A. Breslau, K. Trizt and J. Y. Liu, Phys. Plasmas **20**, 072506 (2013).

[116] G. T. A. Huysmans, S. E. Sharapov, A. B. Mikhailovskii and W. Kerner, Phys. Plasmas **8**, 4292 (2001).

[117] A. D. Turnbull, F. Troyon, Nucl. Fusion **29**, 1887 (1989).

[118] F. D. Halpern, H. Lütjens and J. F. Luciani, Phys. Plasmas **18**, 102501 (2011).

[119] R. Balescu, **Transport Process In Plasmas Vol. II, Neoclassical transport theory** (Elsevier Science Publisher B.V., 1988).

[120] D. Correa-Restrepo, Plasma Phys. Control. Fusion **27**, 565 (1985).

[121] Jr T. M. Antonsen, A. Ferreira and J. J. Ramos, Plasma Physics **24**, 197 (1982).

[122] W.H. Press, B. P. Flannery, S. A. Teukolsky, W. T. Wetterling, **Numerical recipes** (CUP Cambridge, 1986), p. 302.

[123] H. Lütjens, J. F. Luciani, J. Comput. Phys. **227**, 6944 (2008).

[124] D. A. Knoll and D. E. Keyes, J. Comput. Phys. **193**, 357 (2004).

Acknowledgements

These four years of PhD have been a very tough, but fruitful period, and many are the people I wish to thank. First of all I thank my supervisors, Jon and Tony, who guided me and my research during these four years, making possible my Phd. I thank them for the long fruitful discussions, for the careful guidance, for their availability, having their office always open for asking questions and clarifying doubts. I thank Federico for having helped me with all the physical and numerical problems I encountered, for having always had time to talk about physics, for all the pleasant chats we had.

I thank David for being a great colleague to work with, for all the ideas and discussions we shared during this period. I thank my good friends Fabio and Claudio for all the time we spent together laughing, talking and complaining about physics, making these four years funny and enjoyable. I thank my friends Luca and Alberto, hoping that we will continue to collaborate in the scientific world. I thank my dearest friend Daniele, who supported and helped me in these four long and intense years, for all the laughs, for the great moments we spent together. I thank the CRPP magic group for all the unforgettable moments that we spent playing cards.

I want to thank the all CRPP lab and in particular my fellow PhD students and postdocs (who already left and who just started this adventure) Alexandre, Andreas, Anna, Annamaria, Antoine, Cedric, Christoph, Falk, Fabio (R), Farah, Federico, Gabriele, Hamish, Himank, Joaquim, Jonathan, Josef, Joyeeta, Julien, Karim, Kevin, Kim, Lucia, Madhu, Matteo, Paola, Pedro, Umar, Zhouji.

Voglio ringraziare in modo particolare Marta, che mi è stata accanto e mi ha supportato/sopportato durante tutto il periodo di preparazione della tesi, per l'infinita pazienza. Finally I thank my parents, my mother and my father, Ivana and Roberto, for their love and continuous support that they always gave me.

Lausanne, June 9 2015 D. B.

Daniele Brunetti

Personal Data

Professional address: EPFL SB CRPP CRPP-TH PPB 312 (Bâtiment PPB)
Station 13 CH-1015, Lausanne
☎(Office): +41 21 693 3480
📱 +41 0762675369, +39 3343087160
email: daniele.brunetti@epfl.ch
Nationality: Italian
Place and Date of Birth: Milan, Italy — 20 October 1985
Gender: Male

Work Experience

Dates: April 2011 - *Current*
Occupation or position held Doctoral Assistant (Ph.D student)
Name and address of the employer: EPFL SB CRPP CRPP-TH
Station 13 CH-1015, Lausanne

Education

November 2010 Master Degree *cum laude* in Physics,
Universitá degli studi di Milano, Milan
Thesis: "Identification of the Magnetic Structure of Tearing Perturbations from Electron Cyclotron Emission Signals" (italian)
— Advisor: Prof. Enzo Lazzaro

December 2007 Bachelor Degree in Physics,
Universitá degli studi di Milano, Milan
Thesis: "Born-Raman Controversy on Specific Heat" (italian)
— Advisor: Prof. Luigi Galgani

June 2004 **Liceo Classico "G. Carducci"**, Milan

Extracurricola experience

Mobility trip:	Culham, JET	2013
Teaching assistant:	Swiss Institute of Technology (EPFL): Physique Numérique I/II	2011-2014

Languages

English: Fluent (Written/Spoken)
Italian: Mothertongue
French: Basic Knowledge

COMPUTER SKILLS

Scientific software: Linux, Matlab, Mathematica, Word, LaTeX, Beamer
Programming languages: Fortran, C++, Bash

INTERESTS

Reading, cinema, art, music

LIST OF PLUBLICATIONS

First author

- D. Brunetti et al., *Extended MHD simulations of infernal mode dynamics and coupling to tearing modes*, Plasma Phys. Control. Fusion **57** (5), 054002 (2015).
- D. Brunetti et al., *Fast growing resistive two fluid instabilities in hybrid-like tokamak configuration*, Plasma Phys. Control. Fusion **56** (7), 075025 (2014).
- D. Brunetti et al., *Ideal saturated MHD helical structures in axisymmetric hybrid plasmas*, Nucl. Fusion **54** (6), 064017 (2014).
- D Brunetti et al., *MHD properties in the core of ITER-like hybrid scenarios*, J. Phys.: Conf. Ser. **401**, 012003 (2012).
- D. Brunetti et al., *Interpretation of tearing mode physics from ECE temperature fluctuations associated with magnetic islands and Mirnov signals*, Eur. Phys. J. D **64**, 405 (2011).

Co-author

- W. A. Cooper et al. *Free boundary Equilibrium in 3D Tokamaks with Toroidal Rotation*, accepted for publication in Plasma Phys. Control. Fusion.
- W. A. Cooper et al., *An approximate single fluid 3-dimensional magnetohydrodynamic equilibrium model with toroidal flow*, Plasma Phys. Control. Fusion **56** (9), 094004 (2014).
- I.T. Chapman et al., *Three-dimensional distortions of the tokamak plasma boundary: boundary displacements in the presence of saturated MHD instabilities*, Nucl. Fusion **54** (8), 083007 (2014).
- W.A. Cooper et al., *Bifurcated helical core equilibrium states in tokamaks*, Nucl. Fusion **53** (7), 073021 (2013).
- J. P. Graves et al., *Magnetohydrodynamic helical structures in nominally axisymmetric low-shear tokamak plasmas*, Plasma Phys. Control. Fusion **55** (1), 014005 (2013).
- S. Nowak et al., *Interpretation of the effects of electron cyclotron power absorption in pre-disruptive tokamak discharges in ASDEX Upgrade* Phys. Plasmas **19** (9), 092508 (2012).
- B. Esposito et al., *Avoidance of disruptions at high β_N in ASDEX Upgrade with off-axis ECRH*, Nucl. Fusion **51** (8), 083051 (2011).

CONFERENCES' CONTRIBUTIONS

- D. Brunetti et al., *Extended MHD simulations for low shear tokamak plasmas and coupling to tearing modes*, contributed talk at 19th Workshop on MHD Stability Control - A US-Japan Workshop November 3-5, 2014, Auburn, Alabama.

- D. Brunetti et al., *Extended MHD simulations for low shear tokamak plasmas and coupling to tearing modes*, contributed poster at 56th Annual Meeting of the APS Division of Plasma Physics October 27-31, 2014, New Orleans, Louisiana.
- D. Brunetti et al., *Fast growing instabilities and non-linear saturated states in hybrid tokamak and RFP plasmas* , invited talk at Theory of Fusion Plasmas, Joint Varenna - Lausanne International Workshop, 1 - 5 September 2014, Varenna, Italy.
- D. Brunetti et al., *Resistive instabilities in low magnetic shear tokamak configuration*, contributed poster at 15th European Fusion Theory Conference, 23 - 26 September 2013, Merton College, Oxford, UK.
- D. Brunetti et al., *Saturated helical congurations in tokamak hybrid plasmas*, contributed poster at 531st Wilhelm and Else Heraeus Seminar, 3D versus 2D in Hot Plasmas, 30th April - 2nd May 2013 Physikzentrum Bad Honnef, Germany.
- D. Brunetti et al., *MHD properties in the core of ITER-like hybrid scenarios*, contributed poster at Theory of Fusion Plasmas, Joint Varenna - Lausanne International Workshop, 27 - 31 August 2012, Varenna, Italy.

PERSONAL INFORMATION

I am currently a Ph.D student in the Doctoral Program in Physics (EDPY) at the EPFL-CRPP, Lausanne. After graduation at the university of Milan with a work on plasma physics on the identification of tearing perturbations from ECE signals, I am currently involved in the numerical study of non axisymmetric equilibrium tokamak plasmas and non- linear MHD core dynamics both in tokamak an RFPs configurations. Besides this, I am also involved in the analytical and numerical study of core tokamak instabilities beyond the MHD frame.